Proceedings of the Eleventh UK Conference on Boundary Integral Methods (UKBIM 11)

10-11 July 2017
Nottingham Conference Centre
Nottingham Trent University




Edited by David J. Chappell

Nottingham Trent University: Publications

Proceedings of the Eleventh UK Conference on Boundary Integral Methods (UKBIM 11)

Published by Nottingham Trent University: Publications
Nottingham Trent University, 50 Shakespeare Street, Nottingham NG1 4FQ

2017
ISBN 978-0-9931112-9-7 (paperback)
ISBN 978-1-912253-00-5 (eBook)

Dedicated to the memory of Professor Henry Power,
a former member of the UKBIM Scientific Committee.

Henry made many outstanding contributions to the development of the BEM
and will be truly missed by all his friends in the BEM community.

Preface

Over the past 50 years or so, boundary integral methods have become established for solving a wide variety of problems in science and engineering. UK based researchers have been active and made substantial contributions in the theory and development of boundary integral formulations, as well as their analysis, discretisation and numerical solution. The UKBIM conference series aims to provide a forum where recent developments in boundary integral methods can be discussed in an informal atmosphere. The first UK conference on boundary integral methods (UKBIM) was held at the University of Leeds in 1997. Subsequent UKBIM conferences have taken place in Brunel (1999), Brighton (2001), Salford (2003), Liverpool (2005), Durham (2007), Nottingham (2009), Leeds (2011), Aberdeen (2013) and Brighton (2015). The success of these events has made the conference a regular event for researchers based in the UK, and elsewhere, who are working on all aspects of boundary integral methods.

This book contains the abstracts and papers presented at the Eleventh UK Conference on Boundary Integral Methods (UKBIM 11), held at Nottingham Trent University in July 2017. The work presented at the conference, and published in this volume, demonstrates the wide range of work that is being carried out in the UK, as well as from further afield. I am grateful to the members of the scientific committee for their advice and support during the past year, and to all the authors and reviewers for their hard work in producing the high quality peer-reviewed papers for this book.

Acknowledgements

I would like to thank the local organising committee (Janis Bajars, Jonathan Crofts, Rebecca Martin and Gregor Tanner) for their help in organising this conference and putting together this proceedings book. I would also like to thank Abi Middleham from the Nottingham Conference Centre for helping to make sure everything runs smoothly. Finally, I would like to gratefully acknowledge the financial support received from the *London Mathematical Society* (`https://www.lms.ac.uk`) via a Scheme 1 Conference Grant.

David J. Chappell, Nottingham UK, July 2017

Scientific Committee

Prof. Ke Chen	University of Liverpool
Prof. Derek Ingham	University of Sheffield
Prof. Daniel Lesnic	University of Leeds
Dr Paul Harris	University of Brighton
Dr Oleksandr Menshykov	University of Aberdeen
Prof. Sergey Mikhailov	Brunel University
Prof. Jon Trevelyan	Durham University
Prof. Luiz Wrobel	Brunel University

Journal Special Issue

Authors will have the opportunity to submit an extended version of their paper to be peer reviewed for a special issue of the International Journal of Mechanical Sciences to be guest edited by Dr Oleksandr Menshykov. Further details will be given during the conference.

Contents

Chapter 1

Abstract only submissions

I. Invited Plenary Talk:
The Unified Transform for elliptic PDEs and for water waves

Thanasis Fokas

DAMTP, Centre for Mathematical Sciences,
University of Cambridge,
Wilberforce Road
Cambridge
UK

Abstract. *The unified transform (also referred to as the Fokas method) will be reviewed. In particular, it will be shown that this transform yields unexpected results even for such classical problems as the heat equation. Details will be presented for the analysis of elliptic PDEs in the interior of a polygon and for the problem of water waves with moving boundaries, with emphasis on the numerical solution of the so-called global relation.*

II. Function extension with radial basis functions for solving non-homogeneous PDEs

Fredrik Fryklund

Department of Numerical Analysis, KTH Royal Institute of Technology,
Stockholm
Sweden

Abstract. *In many applications it is desirable to solve partial differential equations on irregular domains with high accuracy and speed. Integral equation based methods offer this ability for homogeneous elliptic PDEs. For the non-homogeneous Poisson equation the solution would involve evaluating a volume potential over the irregular domain, which is difficult to do accurately. Instead the problem can be split in two parts: In the first the given right hand side function is extended to a rectangular domain, discretized with a uniform grid; a problem well suited for fast spectral solvers. The second part consists of solving Laplace's equation on the irregular domain with modified boundary conditions. For this, a boundary integral method with special techniques for highly accurate numerical integration of singular and nearly singular integrands is employed.*

The success of our method relies on a technique to efficiently compute a high-regularity extension of a function to a domain embedding the given irregular domain. To do so, the domain is tiled with overlapping partitions. In any partition that intersects the original boundary, an interpolant based on radial basis functions is computed based on the interior and boundary data. A weighted sum of the partitioned interpolants, evaluated outside the given irregular domain, gives the smooth compactly supported function extension.

Numerical results are provided to illustrate the performance of the full method when solving the Poisson equation on irregular 2D domains, with relative errors down to fourteen digits of precision.

Function extension is an essential component in increasing the applicatility of boundary integral methods to non-homogeneous PDEs, which is needed e.g. in extension from Stokes to Navier-Stokes equations. Our method is the only general high regularity extension method that we are aware of. Due to the nature of radial basis functions, it is applicable to problems of higher dimensionality as well.

This contribution is joint work with Anna-Karin Tornberg *(KTH Royal Institute of Technology, Sweden) and* Erik Lehto *(KTH Royal Institute of Technology, Sweden).*

III. A pollution effect for BEM in acoustics

Steffen Marburg

Department of Mechanical Engineering,
Technical University of Munich,
Munich
Germany

Abstract. *The pollution effect is a well-known and well-investigated phenomenon of the finite element method for wave problems in general and for acoustic problems in particular. It is understood as the problem that a local mesh refinement cannot compensate the numerical error which is generated and accumulated in other regions of the model. This is the case for the dispersion error of the finite element method which leads to a phase lag resulting in very large numerical errors for domains with many waves in them and is of particular importance for low order elements. Former investigations of the author have shown that a pollution effect resulting from a dispersion error is unlikely for the boundary element method. However, numerical damping in the boundary element method can account for a pollution effect. A further investigation of numerical damping reveals that it has similar consequences as the dispersion error of the finite element method. One of these consequences is that the number of waves within the domain may be controlling the discretization error in addition to the size and the order of the boundary elements. This will be demonstrated in computational examples discussing traveling waves in rectangular ducts. Different lengths, cross sections, element types and mesh sizes are tested for the boundary element collocation method.*

IV. Integral potential operators for nonsmooth-coefficient Brinkman PDE system in exterior domains

Sergey E. Mikhailov

Department of Mathematics,
Brunel University London,
Uxbridge
London
UK

Abstract. *A variational approach is used to define the generalised Newtonian and layer potentials for the nonsmooth-coefficient Brinkman system (which can be considered as a modification of the Stokes system for viscous fluid flow in porous medium) in a Lipschitz exterior domain in $\mathbb{R}^3$, and prove the mapping properties of the associated operators. Some new weighted Sobolev spaces are introduced to correctly describe behaviour of the pressure field at infinity. We show that the Newtonian and layer potentials provided by the variational approach coincide with the well known Brinkman layer potentials in the integral form in the case of constant coefficient Brinkman system.*

This contribution is joint work with Mirela Kohr *(Babeş-Bolyai University, Romania).*

V. The use of the boundary element method in structural topology optimisation: Two and three-dimensional algorithms

Baseer Ullah

Centres of Excellence in Science and Applied Technologies (CESAT),
Islamabad
Pakistan

Abstract. *A level set based structural topology optimization method is presented in this study. Initially, a two-dimensional algorithm is proposed for linear elastic problems. The structural boundary is implicitly represented through the level set method, which evolves an initial geometry towards an optimal design using the bi-directional evolutionary structural optimization approach. At each optimization step only the structural boundary is discritised and the structural response is evaluated using the boundary integral equations. In comparison with the finite element method the boundary element method is attractive because it requires discretisation only at the design boundary. This reduction of problem dimensionality considerably simplifies the re-meshing task (especially in three-dimensions), which can be performed efficiently and robustly. Thus, its rapid and robust re-meshing and accurate boundary solutions make the boundary element method a natural choice for the solution of level set based topology optimization problems. In two-dimensions the classical level set method is not capable to nucleate holes, hence, a hole insertion mechanism has been proposed in this study to overcome this deficiency. However, in three-dimensions the level set method allows nucleation of new holes through the intersection of two approaching surfaces. This suggests that perturbing only the boundary can give rise to changes not only in shape, but also in topology. Complete algorithms are presented and tested for both two and three-dimensional problems and the optimal geometries generated are in close agreement with those available in the literature of structural topology optimisation.*

This contribution is joint work with John Trevelyan *(Durham University, UK),* Muhammad Rehan *(CESAT, Pakistan) and* Himayat Ullah *(CESAT, Pakistan).*

Chapter 2

DRBEM formulation for convection-diffusion-reaction problems with variable velocity

Salam A. Al-Bayati[1] **and Luiz C. Wrobel**[2]

[1] Department of Mathematics,
Brunel University London
Uxbridge UK
UB8 3PH,

[2] Department of Mechanical Engineering,
Brunel University London
Uxbridge UK
UB8 3PH,

Abstract. *A dual reciprocity boundary element method (DRBEM) formulation for the solution of steady-state convection-diffusion-reaction problems with variable velocity is developed in this paper. This scheme is based on utilising the fundamental solution of the convection-diffusion-reaction equation with constant coefficients. In this case, we decompose the velocity field into an average and a perturbation part, with the latter being treated using a dual reciprocity approximation to convert the domain integrals arising in the boundary element formulation into equivalent boundary integrals. Two different approaches were implemented to treat the convective terms with variable velocity. The first expands the concentration as a series of functions, while the other expands the concentration gradient instead. Numerical applications are included for two simple problems for which analytical solutions are available, to establish the validity of the approach and to demonstrate the efficiency of the proposed method.*

2.1 Introduction

The boundary element method (BEM) has been applied to steady-state convection-diffusion-reaction problems with variable velocity by various researchers [1, 2, 3, 4, 5, 6, 7, 8]. However, the solution of this problem is still considered a big challenge, particularly for variable and high velocities. The BEM does have an inherent advantage for the solution of convection-diffusion-reaction problems with constant velocity as the existing fundamental solution of the problem introduces the exact amount of upwind, contrary to finite element or finite-difference methods where the upwind is numerical [7]. The solution of problems involving variable coefficients is

more difficult to achieve with the BEM as fundamental solutions are only available for a small number of cases, for coefficients with very simple variations in space. The approach adopted in this paper is to split the velocity field into an average and a perturbation; the average velocity (constant) is included in the fundamental solution, while the perturbation generates a domain integral which is treated with the DRBEM. A new particular solution has been used with corresponding dual reciprocity expressions. Two different approaches were implemented to treat the convective terms with variable velocity. The first expands the concentration as a series of functions, while the other expands the concentration gradient instead. Results of two simple tests are presented and compared to analytical solutions. They show that the boundary element formulation developed in this work produces accurate results for diffusion-dominated problems with low velocity values.

2.2 Boundary Element Formulation

The two-dimensional governing equation for the steady-state convection-diffusion-reaction problem may be expressed as

$$D\nabla^2\phi - v_x\frac{\partial\phi}{\partial x} - v_y\frac{\partial\phi}{\partial y} - k\phi = 0, \tag{2.1}$$

where $v_x = v_x(x,y)$ and $v_y = v_y(x,y)$ are the components of the velocity vector v, D is the diffusivity coefficient (assuming the medium is homogeneous and isotropic) and k represents the reaction coefficient. The variable ϕ can be interpreted as temperature for heat transfer problems, concentration for dispersion problems, etc, and will be herein referred to as a potential. The mathematical description of the problem is complemented by boundary conditions of the Dirichlet, Neumann or Robin (mixed) types. For the sake of obtaining an integral equation equivalent to the above partial differential equation, a fundamental solution of equation (2.1) is necessary. However, fundamental solutions are only available for the case of constant velocity fields. Thus, the variable velocity components $v_x = v_x(x,y)$ and $v_y = v_y(x,y)$ are decomposed into average (constant) terms $\bar{v}_x$ and $\bar{v}_y$, and perturbations $P_x = P_x(x,y)$ and $P_y = P_y(x,y)$, such that

$$\begin{aligned} v_x(x,y) &= \bar{v}_x + P_x(x,y), \\ v_y(x,y) &= \bar{v}_y + P_y(x,y). \end{aligned} \tag{2.2}$$

This permits rewriting equation (2.1) as

$$D\nabla^2\phi - \bar{v}_x\frac{\partial\phi}{\partial x} - \bar{v}_y\frac{\partial\phi}{\partial y} - k\phi = P_x\frac{\partial\phi}{\partial x} + P_y\frac{\partial\phi}{\partial y}. \tag{2.3}$$

The above differential equation can now be transformed into the following equivalent integral equation

$$\phi(\xi) - D\int_\Gamma \phi^*\frac{\partial\phi}{\partial n}\,d\Gamma + D\int_\Gamma \phi\frac{\partial\phi^*}{\partial n}d\Gamma + \int_\Gamma \phi\phi^*\bar{v}_n\,d\Gamma = -\int_\Omega\left(P_x\frac{\partial\phi}{\partial x} + P_y\frac{\partial\phi}{\partial y}\right)\phi^* d\Omega, \tag{2.4}$$

where $\bar{v}_n = \bar{v}\cdot n$, n is the unit outward normal vector and the dot stands for the scalar product. In the above equation, ϕ^* is the fundamental solution of the convection-diffusion-reaction equation with constant coefficients. For two-dimensional problems, ϕ^* is of the form

$$\phi^*(\xi,\chi) = \frac{1}{2\pi D}\,e^{-\left(\frac{\bar{v}\cdot r}{2D}\right)}K_0(\mu r), \tag{2.5}$$

where

$$\mu = \left[\left(\frac{\bar{v}}{2D}\right)^2 + \frac{k}{D}\right]^{\frac{1}{2}}, \tag{2.6}$$

and in which ξ and χ are the source and field points, respectively, and r is the modulus of $\mathbf{r}$, the distance vector between the source and field points. The derivative of the fundamental solution with respect to the outward normal direction is given by

$$\frac{\partial \phi^*}{\partial n} = \frac{1}{2\pi D} e^{-\left(\frac{\bar{v}.r}{2D}\right)} \left[-\mu K_1(\mu r) \frac{\partial r}{\partial n} - \frac{\bar{v}_n}{2D} K_0(\mu r) \right]. \tag{2.7}$$

In the above, K_0 and K_1 are Bessel functions of second kind, of orders zero and one, respectively. The exponential term is responsible for the inclusion of the correct amount of upwind into the formulation [7]. Equation (2.4) is valid for source points ξ inside the domain Ω. A similar expression can be obtained, by a limit analysis, for source points ξ on the boundary Γ, in the form

$$c(\xi)\phi(\xi) - D\int_\Gamma \phi^* \frac{\partial \phi}{\partial n} d\Gamma + D\int_\Gamma \phi \frac{\partial \phi^*}{\partial n} d\Gamma + \int_\Gamma \phi \phi^* \bar{v}_n d\Gamma = -\int_\Omega \left(P_x \frac{\partial \phi}{\partial x} + P_y \frac{\partial \phi}{\partial y} \right) \phi^* d\Omega, \tag{2.8}$$

in which $c(\xi)$ is a function of the internal angle the boundary Γ makes at point ξ.

2.3 DRM Formulation for Convection-Diffusion-Reaction Problem

In the present formulation, we concentrate on the implementation of the dual reciprocity formulation DRM based on the fundamental solution to the steady-state convection-diffusion-reaction equation, where the convective velocity is assumed to be variable and is split into two parts, constant and perturbation, respectively. The basic idea is to expand the non-homogenous perturbation term on the right-hand side of equation (2.3) in the form

$$P_x \frac{\partial \phi}{\partial x} + P_y \frac{\partial \phi}{\partial y} = \sum_{k=1}^{M} f_\alpha \alpha_k. \tag{2.9}$$

This series contains a sequence of known functions $f_k = f_k(x, y)$ which are dependent only on geometry, and a set of unknown coefficients α_k. Using this approximation, the domain integral in equation (2.8) can be approximated in the form

$$\int_\Omega \left(P_x \frac{\partial \phi}{\partial x} + P_y \frac{\partial \phi}{\partial y} \right) \phi^* d\Omega = \sum_{k=1}^{M} \alpha_k \int_\Omega f_k \phi^* d\Omega. \tag{2.10}$$

The next step is to consider that, for each function f_k, there exists a related function ψ_k which is a particular solution of the equation

$$D\nabla^2 \psi - \bar{v}_x \frac{\partial \psi}{\partial x} - \bar{v}_y \frac{\partial \psi}{\partial y} - k\psi = f. \tag{2.11}$$

Thus, the domain integral can be recast in the form

$$\int_\Omega \left(P_x \frac{\partial \phi}{\partial x} + P_y \frac{\partial \phi}{\partial y} \right) \phi^* d\Omega = \sum_{k=1}^{M} \alpha_k \int_\Omega \left(D\nabla^2 \psi_k - \bar{v}_x \frac{\partial \psi_k}{\partial x} - \bar{v}_y \frac{\partial \psi_k}{\partial y} - k\psi_k \right) \phi^* d\Omega. \tag{2.12}$$

Substituting equation (2.12) into (2.8), and utilising integration by parts in the domain integral of the resulting equation, we finally obtain a boundary integral equation of the form

$$c(\xi)\phi(\xi) - D\int_\Gamma \phi^* \frac{\partial \phi}{\partial n} d\Gamma + D\int_\Gamma \phi \frac{\partial \phi^*}{\partial n} d\Gamma + \int_\Gamma \phi \phi^* \bar{v}_n d\Gamma \tag{2.13}$$

$$= \sum_{k=1}^{M} \alpha_k \left[c\left(\xi\right) \psi_k\left(\xi\right) - D \int_{\Gamma} \phi^* \frac{\partial \psi_k}{\partial n} d\Gamma + D \int_{\Gamma} \psi_k \frac{\partial \phi^*}{\partial n} d\Gamma + \int_{\Gamma} \psi_k \phi^* \bar{v}_n d\Gamma \right].$$

2.4 Discretisation

Equation (2.13) can now be re-written in discretised form in which the integrals over the boundary are approximated by a summation of integrals over individual boundary elements, i.e.

$$c_i \, \phi_i - \sum_{j=1}^{N} D \int_{\Gamma_j} \phi^* \, \frac{\partial \phi}{\partial n} \, d\Gamma \, + \, \sum_{j=1}^{N} \int_{\Gamma_j} \left(\frac{\partial \phi^*}{\partial n} + \frac{\bar{v}_n}{D} \, \phi^* \right) \, \phi \, d\Gamma \tag{2.14}$$

$$= \sum_{k=1}^{M} \alpha_k \left[c_i \, \psi_{ik}\left(\xi\right) - D \sum_{j=1}^{N} \int_{\Gamma_j} \phi^* \frac{\partial \psi_k}{\partial n} \, d\Gamma \, + \sum_{j=1}^{N} \int_{\Gamma_j} \left(\frac{\partial \phi^*}{\partial n} \, + \frac{\bar{v}_n}{D} \, \phi^* \right) \psi_k d\Gamma \right],$$

where the index i means the values at the source point ξ and N elements have been employed. The functions $\phi, q = \partial\phi/\partial n, \psi$ and $\eta = \partial\psi/\partial n$ within each boundary element are approximated in this study using constant elements. It should be remarked that functions ψ and η need not be approximated as they are known functions for a specified set f. However, doing so will greatly improve the computer efficiency of the technique with only a minor sacrifice in accuracy. Applying equation (2.14) to all boundary nodes using a collocation technique results in the following system of equations

$$H\phi - Gq = \left(H\psi - G\eta\right) \alpha. \tag{2.15}$$

As shown in the above system, the same matrices H and G are used on both sides. Both ψ and η are also geometry-dependent square matrices (assuming, for simplicity, that the number of terms in expression (2.10) is equal to the number of boundary nodes), and ϕ, q and α are vectors of nodal values. The next step in the formulation is to find an expression for the unknown vector α. Applying equation (2.10) to all M nodes, it is possible to write the resulting set of equations in the following matrix form

$$P_x \, \frac{\partial \phi}{\partial x} \, + \, P_y \, \frac{\partial \phi}{\partial y} = \, F \, \alpha, \tag{2.16}$$

where P_x and P_y can be understood as two diagonal matrices with components $P_x\left(x_i, y_i\right)$ and $P_y\left(x_i, y_i\right)$, respectively, while $\frac{\partial \phi}{\partial x}$ and $\frac{\partial \phi}{\partial y}$ are column vectors. Inverting expression (2.16), one arrives at

$$\alpha = \, F^{-1} \, \left(P_x \, \frac{\partial \phi}{\partial x} \, + \, P_y \, \frac{\partial \phi}{\partial y} \right). \tag{2.17}$$

Substituting into equation (2.15),

$$H\phi - Gq = \left(H\psi - G\eta\right) \, F^{-1} \, \left(P_x \, \frac{\partial \phi}{\partial x} \, + \, P_y \, \frac{\partial \phi}{\partial y} \right). \tag{2.18}$$

Defining a matrix S in the form

$$S = \left(H\psi - G\eta\right) \, F^{-1} \tag{2.19}$$

one can write equation (2.18) as

$$H\phi - Gq = S \, \left(P_x \, \frac{\partial \phi}{\partial x} + P_y \frac{\partial \phi}{\partial y} \right). \tag{2.20}$$

Once functions f_k are defined, matrix S can be established as this matrix depends on geometry only. Furthermore, the coefficients of matrices P_x and P_y are also known. Therefore, there remains to be found an expression relating the derivatives of ϕ to reduce equation (2.20) to a standard BEM form.

2.5 Convective Term

In this section, emphasis will be placed on convective terms. A mechanism must be established to relate the nodal values of ϕ to the nodal values of its derivatives. Two approaches will be discussed in the next subsections.

2.5.1 The Gradient-Expansion Approach

In this approach, each of the derivatives is independently expanded using again an expansion like that of expression (2.10), generating the expressions

$$\frac{\partial \phi}{\partial x} = \sum_{k=1}^{M} \Psi_k^x \, \beta_k \quad \text{and} \quad \frac{\partial \phi}{\partial y} = \sum_{k=1}^{M} \Psi_k^y \, \beta_k, \tag{2.21}$$

where β_k are constants, different from the α_k in equation (2.10). This will imply finding the values of ϕ by integrating equation (2.21). Assuming then that the function ϕ can be represented by

$$\phi = \sum_{k=1}^{M} \Im_k \, \beta_k, \tag{2.22}$$

where $\Im_k$ is the result of integrating the functions Ψ_k^x and Ψ_k^y, we shall have in matrix form, collecting together the approximations at all points, that

$$\beta \; = \Im^{-1} \, \phi. \tag{2.23}$$

Consequently, equation (2.21) will produce

$$\frac{\partial \phi}{\partial x} = \Psi^x \, \Im^{-1} \, \phi \quad \text{and} \quad \frac{\partial \phi}{\partial y} = \Psi^y \, \Im^{-1} \, \phi. \tag{2.24}$$

Now, we can re-write equation (2.20) in the form

$$(H - P) \; \phi = Gq$$

where

$$P = S \; [P_x \, \Psi^x \; + \; P_y \, \Psi^y] \; \Im^{-1}. \tag{2.25}$$

2.5.2 The Function-Expansion Approach

We now start by expanding the values of ϕ at an internal point by using expression (2.23). Differentiating it with respect to x and y produces

$$\frac{\partial \phi}{\partial x} = \sum_{k=1}^{M} \frac{\partial \Im_k}{\partial x} \, \beta \quad \text{and} \quad \frac{\partial \phi}{\partial y} = \sum_{k=1}^{M} \frac{\partial \Im_k}{\partial y} \, \beta_k. \tag{2.26}$$

Applying equation (2.22) at all M nodes, a set of equations is produced that can be represented in matrix form by

$$\phi = \Im \; \beta \tag{2.27}$$

with corresponding matrix equations for expressions (2.26) and (2.27) given as

$$\frac{\partial \phi}{\partial x} = \frac{\partial \Im}{\partial x} \, \Im^{-1} \, \phi \quad \text{and} \quad \frac{\partial \phi}{\partial y} = \frac{\partial \Im}{\partial y} \, \Im^{-1} \, \phi. \tag{2.28}$$

Equation (2.20) then takes the form

$$(H - P)\ \phi = Gq, \tag{2.29}$$

where

$$P = S \left(P_x \frac{\partial \Im}{\partial x} \ + \ P_y \frac{\partial \Im}{\partial y} \right) \Im^{-1}. \tag{2.30}$$

The coefficients of the perturbation matrix P are all geometry-dependent only. Thus, boundary conditions can be applied to equation (2.30) and the resulting system of algebraic equations solved by a direct or iterative scheme.

2.6 Choice of Radial Basis Function

This study focuses on DRBEM approximations with Radial Basis Functions (RBF). Partridge and Brebbia [3] have shown that a variety of functions can in principle be used as global interpolation functions f_k. The approach used by Wrobel and DeFigueiredo [4] was based on practical experience rather than formal mathematical analyses and motivated by a previous successful experience with axisymmetric diffusion problems in which a similar approach was used [9]. In the present work, it was decided to start with a simple form of the particular solution ψ and find the related expression for function f by substitution into equation (2.11). The resulting expressions are

$$\psi = r^3,$$

$$\eta = 3\ r\ \left[(x - x_k)\ n_x \ + (y - y_k)\ n_y \right],$$

$$f = 9\, D\, r \ - \ 3\, r\ \left[(x - x_k)\ v_x \ + (y - y_k)\ v_y \right] - k\, r^3,$$

in which (x_k, y_k) and (x,y) are the coordinates of the k-th boundary or internal point and a general point, respectively. It is important to notice that the set of function f produced depends not only on the distance r but also on the diffusivity D, velocity components v_x and v_y as well as the reaction rate k, therefore, it will behave differently when diffusion or convection is the dominating process.

2.7 Test Cases

The present section is concerned with the application of the DRBEM for the solution of steady-state convection-diffusion-reaction problems with variable velocity. We shall examine some test examples to assess the performance of the proposed formulations.

2.7.1 Test case I

This example, although one-dimensional, is treated here as a two-dimensional convection-diffusion-reaction problem with a variable velocity field in the x-direction. The velocity v_x is a linear function of x expressed as

$$v_x\,(x) = k\, x + c_1,$$

where

$$c_1 = \ln \left(\frac{\phi_1}{\phi_0} \right) - \frac{k}{2}.$$

The problem geometry, discretisation and boundary conditions are schematically described in Figure 2.1. The problem is modelled as square-shaped body with side length $1m$ and mixed boundary conditions (Neumann-Dirichlet). There is no flux in the y-direction and the values

$\phi_0 = 300$ and $\phi_1 = 10$ are specified at the faces $x = 0$ and $x = 1$, respectively, and the diffusivity coefficient takes the value $D = 1$. The problem is discretised with 120 constant elements, 30 on each face, and 8 internal points. The exact solution of the problem is given by $\phi = 300\ e^{\left(\frac{k}{2}\right) x^2 + c_1\, x}$.

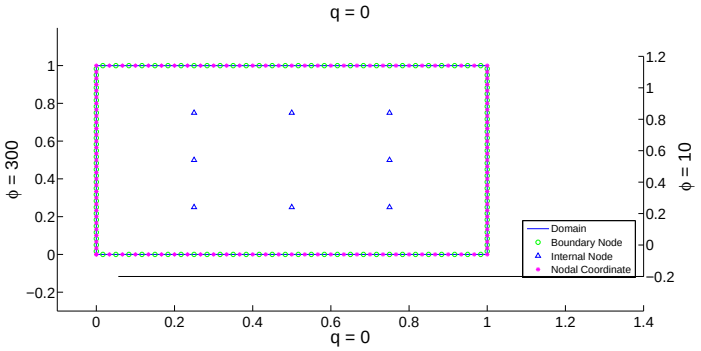

Figure 2.1: Geometry, discretisation, boundary condition and internal points with side lenght 1m

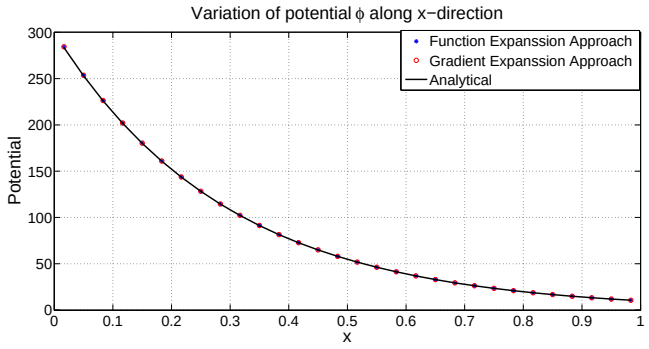

Figure 2.2: Variation of potential ϕ along face $y = 0$, with $k = 0$

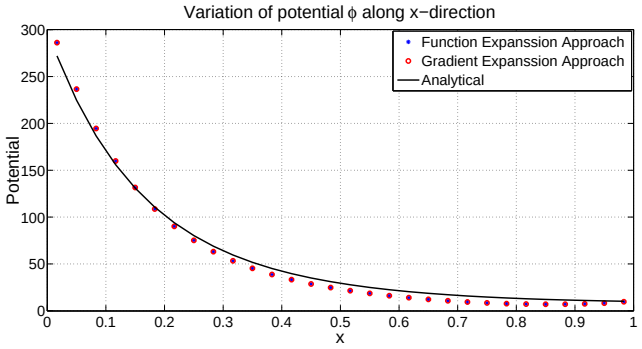

Figure 2.3: Variation of potential ϕ along face $y = 0$, with $k = 5$

A plot of the variation of the potential ϕ along the x-direction is presented in Figure 2.2 for $k = 0$, representing a case with constant velocity. It can be noticed that the agreement with the analytical solution is very good. Figures 2.3 to 2.4 present the cases $k = 5$, $(v_x = -3.401 \pm 2.5)$ and $k = 10$, $(v_x = -3.401 \pm 5)$. It is obvious that, as the velocity increases, the potential distribution becomes steeper and more difficult to reproduce with numerical models. However, all BEM solutions are still in good agreement with the corresponding analytical solutions.

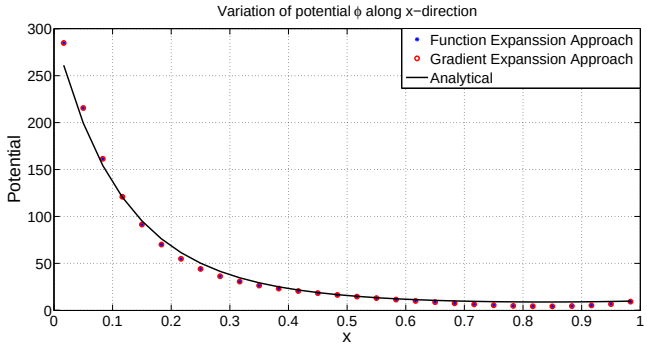

Figure 2.4: Variation of potential ϕ along face $y = 0$, with $k = 10$

2.7.2 Test case II

This test considers a two-dimensional convection-diffusion-reaction problem over a square channel $\Omega = (0,1) \times (0,1)$ as described in Figure 2.5. In the present example, a uni-directional velocity field in the x-direction depending on the coordinate y was defined by the expression

$$v_x(y) = A\,(y - B)^2.$$

The velocity field is now a second-order function of the y-coordinate, with A and B defined as constants; the values of the other coefficients are $D = 1$ and $k = 0$. The constant B defines the symmetry of the velocity field with respect to the coordinate y. If $B = 0.5$, the velocity and the potential profiles are both symmetric. The analytical solution to this problem is given by

$$\phi = \bar{\phi} e^{A^{1/3}\left(A^{1/3}\, y\left(B - \frac{y}{2}\right) + x\right)},$$

with $\bar{\phi} = 300$. The mixed boundary conditions (Neumann-Dirichlet) corresponding to the problems are defined as

$$\frac{\partial \phi}{\partial n} = q = -300\; A^{\frac{2}{3}}\, B\; e^{\left(A^{\frac{1}{3}}\right) x},\; y = 0\,;\, 0 \le x \le 1,$$

$$\phi = 300\, e^{A^{\frac{1}{3}}\left(A^{\frac{1}{3}}\, y\left(B - \frac{y}{2}\right) + 1\right)},\; x = 1;\, 0 \le y \le 1,$$

$$\frac{\partial \phi}{\partial n} = q = 300\, A^{\frac{2}{3}}\,(B-1)\; e^{A^{\frac{1}{3}}\left(A^{\frac{1}{3}}\,\left(B - \frac{1}{2}\right) + x\right)},\; y = 1\,;\, 0 \le x \le 1,$$

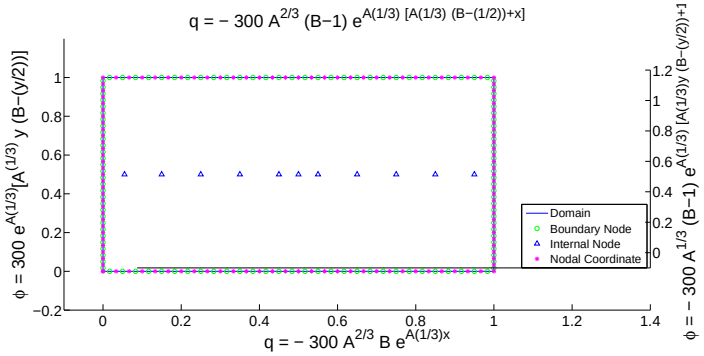

Figure 2.5: Geometry, discretisation and boundary conditions for two-dimensional problem with uni-directional velocity $v_x(y)$ and side lenght $1m$

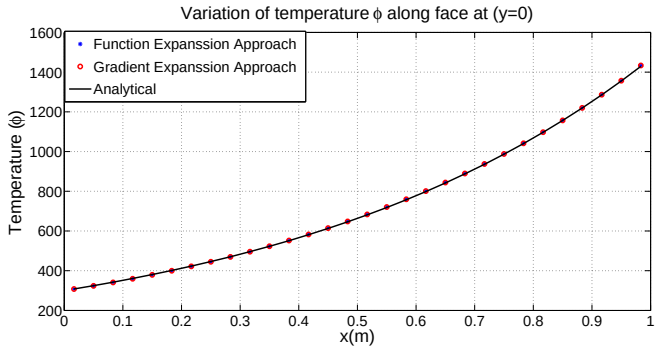

Figure 2.6: Variation of potential along face $y = 0$ with $A = 4$ and $B = 0.5$

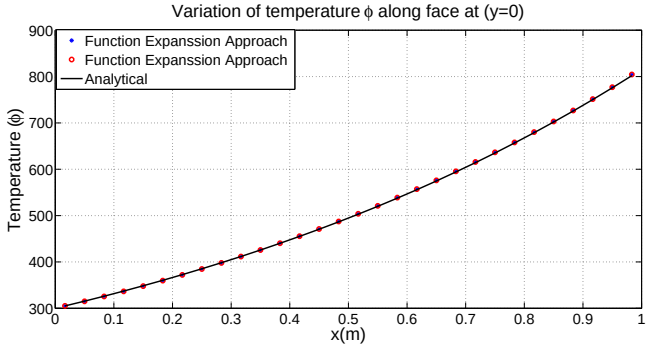

Figure 2.7: Variation of potential along face $y = 0m$ for $A = 1$, $B = 1$

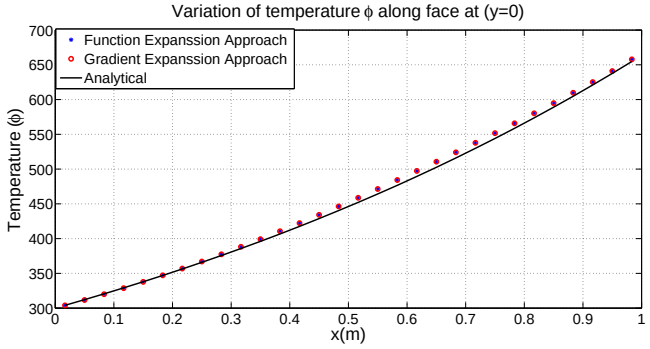

Figure 2.8: Variation of potential along face $y = 0$ with $A = 0.5$ and $B = 2$

$$\phi = \ 300e^{A^{\frac{1}{3}}\left(A^{\frac{1}{3}}\, y\left(B-\frac{y}{2}\right)\right)},\ x = 0\,; 0 \leq y \leq 1,$$

The boundary is discretised with 120 constant elements, 30 on each face, and 11 internal points adopted. Figure 2.6 shows the variation of the potential along the horizontal faces for the case $B = 0.5$, compared to the analytical solution, as the results are symmetric in this case. Figure 2.7 shows the BEM results for the potential ϕ along the face $y = 0$ for the case $B = 1$, $A = 1$. In this case, the quadratic velocity field has a minimum at the extreme $y = 0$. Next, the value of B is considered as $B = 2$ to make the velocity profile significantly non-symmetric. Figure 2.8 compares the BEM and analytical solutions for this case. Once again, the results show very good agreement.

2.8 Conclusions

In this paper, a BEM formulation for two-dimensional steady-state convection-diffusion-reaction problems with variable velocity fields is presented, employing the fundamental solution of the corresponding equation with constant coefficients and a dual reciprocity approximation of the perturbation velocity. The DRBEM is used to transform the domain integrals appearing in the BEM formulations into equivalent boundary integrals, thus retaining the boundary-only character of the standard BEM. Two proposed approaches were implemented to treat the convective terms with variable velocity. The first expands the concentration as a series of functions, while the other expands the concentration gradient instead. Both are shown to produce similar results. Such formulations are expected to be stable at low Péclet numbers (i.e. diffusion-dominated problems). Numerical applications are included to demonstrate the validity of the proposed technique, and its accuracy was evaluated by applying it to two simple tests with different velocity fields.

References

[1] Y. Tanaka, T. Honma and I. Kaji, *Mixed boundary element solution for three-dimensional convection-diffusion problem with a velocity field*, Appl Math. Modelling, 11 (1987), 402-410.

[2] D.B. Defigueiredo and L.C. Wrobel, *A boundary element analysis of convective heat diffusion problems*, in Advanced Computational Methods in Heat Transfer, Computational Mechanics Publications, Southampton and Springer-Verlag, Berlin, 1 (1990).

[3] P.W. Partridge and C.A. Brebbia, *Computer implementation of the BEM dual reciprocity method for the solution of general field equations*, Comm. Appl. Num. Meth., 6 (1990), 83-92.

[4] L.C. Wrobel and D.B. Defigueiredo, *A dual reciprocity boundary element formulation for convection-diffusion problems with variable velocity fields*, Eng. Anal. Bound. Elem., 8 (1991), 312-319.

[5] Z.H. Qiu, L.C. Wrobel and H. Power, *An evaluation of boundary element schemes for convection-diffusion problems*, Transactions on Modelling and Simulation, WIT Press, UK, 1993.

[6] Z.H. Qiu, L.C. Wrobel and H. Power, *Numerical solution of convection-diffusion problems at high Péclet numbers using boundary elements*, Int. J. Numer. Meth. Eng., 41 (1998), 899-914.

[7] J. Ravnik and L. Skerget, *A gradient free integral equation for diffusion-convection equation with variable coefficient and velocity*, Eng. Anal. Bound. Elem., 37 (2013) 683-690.

[8] A. Shiva and H. Adibi, *A numerical solution for advection-diffusion equation using dual reciprocity method*, Numer. Methods Partial Differ. Equ., 29 (2013), 843856.

[9] J.C.F. Telles, L.C. Wrobel and C.A. Brebbia, *A dual reciprocity boundary element formulation for axisymmetric diffusion problems*, Boundary Element VII, Computational Mechanics Publications, UK, 1986.

Chapter 3

Accurate quadrature methods with application to Stokes flow with particles in confined geometries

Joar Bagge and Anna-Karin Tornberg

KTH Mathematics, Linné FLOW Centre/Swedish e-Science Research Centre,
Royal Institute of Technology
100 44 Stockholm, Sweden

Abstract. *Boundary integral methods are attractive for simulating Stokes flow with particles or droplets due to the reduction in dimensionality and natural handling of the geometry. In many problems walls are present, and it becomes necessary to evaluate singular or nearly singular layer potentials over the wall. In this paper we show how this can be done using quadrature by expansion (QBX), a relatively new method based on local expansions of the layer potential. We present results for the Laplace single layer potential and the Stokes double layer potential. QBX can be used to evaluate the potentials to high accuracy arbitrarily close to the wall and on the wall. We also discuss how some quantities can be precomputed and how geometric symmetries can be used to reduce precomputation and storage.*

3.1 Introduction

3.1.1 Singular and nearly singular integrals

The motivation for this work is to study microscale flows with solid particles or droplets immersed in a fluid. In such flows, inertial effects are often negligible, and they can therefore be modelled as Stokes flow. The flow in each fluid domain $D_\mathrm{f} \subseteq \mathbb{R}^3$ is then governed by the Stokes equations

$$\begin{cases} \nabla P = \mu \nabla^2 \boldsymbol{u}, \\ \nabla \cdot \boldsymbol{u} = 0, \end{cases} \qquad \boldsymbol{x} \in D_\mathrm{f} \tag{3.1}$$

with appropriate boundary conditions on each particle surface or drop interface. Here, P is the pressure, μ is the viscosity and $\boldsymbol{u}$ is the velocity. Since (3.1) are linear equations, they can be solved using boundary integral methods, which are attractive since they reduce the dimensionality of the problem and provide a natural way of handling the moving geometry.

In a boundary integral method, the velocity in the fluid domain is expressed using a single layer potential, a double layer potential, or a combination thereof (see e.g. [6]). The Stokes

single layer potential is given by[1]

$$\mathcal{S}_i[\boldsymbol{\sigma}](\boldsymbol{x}) = \int_\Gamma S_{ij}(\boldsymbol{x},\boldsymbol{y})\sigma_j(\boldsymbol{y})\,\mathrm{d}S_{\boldsymbol{y}}, \qquad S_{ij}(\boldsymbol{x},\boldsymbol{y}) = \frac{\delta_{ij}}{r} + \frac{r_i r_j}{r^3}, \qquad \boldsymbol{x},\boldsymbol{y}\in\mathbb{R}^3 \tag{3.2}$$

with $\boldsymbol{r} = \boldsymbol{x} - \boldsymbol{y}$ and $r = \|\boldsymbol{r}\|$. Here, Γ is the boundary of the fluid domain, and the vector field $\boldsymbol{\sigma}$ defined on Γ is called the Stokes single layer density and determines the flow. The Stokes double layer potential is given by

$$\mathcal{D}_i[\boldsymbol{q}](\boldsymbol{x}) = \int_\Gamma T_{ijk}(\boldsymbol{x},\boldsymbol{y})q_j(\boldsymbol{y})n_k(\boldsymbol{y})\,\mathrm{d}S_{\boldsymbol{y}}, \qquad T_{ijk}(\boldsymbol{x},\boldsymbol{y}) = -6\frac{r_i r_j r_k}{r^5}, \qquad \boldsymbol{x},\boldsymbol{y}\in\mathbb{R}^3, \tag{3.3}$$

where $\boldsymbol{n}$ is a unit normal of Γ. The vector field $\boldsymbol{q}$ is called the Stokes double layer density and plays the same role as $\boldsymbol{\sigma}$. The tensors S_{ij} and T_{ijk} appearing in (3.2) and (3.3) are called the stokeslet and the stresslet, and they are the free-space Green's functions for velocity and stress, respectively.

To determine the density $\boldsymbol{\sigma}$ or $\boldsymbol{q}$ in (3.2) or (3.3), one lets $\boldsymbol{x}$ approach Γ and uses boundary conditions, which leads to an integral equation for the density. To solve it, one must be able to evaluate the potential $\boldsymbol{\mathcal{S}}$ or $\boldsymbol{\mathcal{D}}$ for $\boldsymbol{x}\in\Gamma$, which amounts to computing an integral with a singular integrand since the kernel S_{ij} or T_{ijk} is singular for $\boldsymbol{x} = \boldsymbol{y}$. We refer to the case $\boldsymbol{x}\in\Gamma$ as the *singular case*. Applying a standard quadrature rule designed for smooth integrands to this case would yield inaccurate results. Another problematic case is when $\boldsymbol{x}$ is inside the fluid domain but close to Γ, which happens e.g. if one part of the boundary (such as a particle) is close to another part, or if the velocity close to the boundary is computed during postprocessing. As $\boldsymbol{x}$ and $\boldsymbol{y}$ get close, the integral kernel becomes sharply peaked and hard to resolve. We refer to this case as the *nearly singular case*. As illustrated in Fig. 3.1, the error of a standard quadrature rule grows exponentially as $\boldsymbol{x}$ approaches the boundary Γ, which in this example is a flat wall. Increasing the grid resolution will move the problematic region closer to the wall, but it will not remove it.

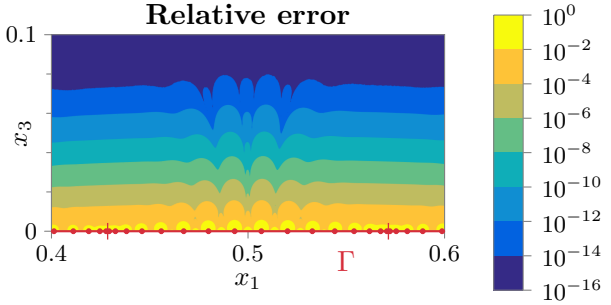

Figure 3.1: The error of a standard quadrature rule grows exponentially as the evaluation point approaches the boundary Γ. In this example, Γ is a wall in the x_1x_2-plane (seen from the side), and the quadrature rule is the one described in Section 3.2. The potential here is the Laplace single layer potential (3.5) with density given by (3.20), but the same behaviour is seen in the Stokes layer potentials as well. The setup is the same as in Section 3.5.1.

Many different techniques have been proposed to overcome these challenging cases. In two dimensions excellent methods exist, but in three dimensions this is still a very active research topic. For an overview, see [5] and the references therein.

In this paper we treat both the singular and nearly singular case using a relatively new method called quadrature by expansion (QBX), which is based on computing local expansions

[1] Throughout this paper we use Einstein's summation convention, with all indices ranging over the set $\{1,2,3\}$. δ_{ij} denotes the Kronecker delta.

of the layer potentials. The method was first introduced by Klöckner et al. for the Helmholtz equation in two dimensions [5], and has subsequently been implemented for rigid spheroidal particles in three-dimensional Stokes flow by af Klinteberg and Tornberg [1], yielding highly accurate results also for tightly packed particles in unbounded flows and periodic flows. Computing the local expansions is expensive, but most of the work can be done as a precomputation. The same precomputed data can be used for all particles of the same shape, and geometric symmetries of the spheroids such as axisymmetry and mirror symmetry greatly reduces the amount of storage needed for the precomputed data, which renders the method highly efficient.

3.1.2 Walls

In many problems, we are interested in the interaction between particles or droplets and the fixed surrounding geometry, for example in the form of walls. While unbounded flow problems are easy to treat using boundary integral methods, walls require more effort. For a single flat wall, it is possible to use the method of images (see e.g. [4]), which avoids the need to discretize the wall itself. This does not work in the case of several walls, or walls of more general shapes, which requires the walls to be discretized as a part of the external boundary. In this paper, we deal with the implementation of QBX for a rectangular flat wall. The techniques described here can be extended also to pipes and to boundaries of more general shapes, although complicated shapes would limit precomputation due to lack of symmetries.

The wall is discretized by dividing it into patches, which makes adaptivity possible. In the final flow problem, periodic boundary conditions would be imposed along the sides of the wall as shown in Fig. 3.2, but we will not discuss the solution to such a problem in this paper. Instead, we focus on the evaluation of the Stokes double layer potential over the wall, i.e. (3.3) with Γ taken as a rectangular wall, for evaluation points $\boldsymbol{x}$ on the wall or close to it. We consider here the double layer density $\boldsymbol{q}$ as a given function with compact support on the wall. The treatment of the singular and nearly singular case would be the same in the full periodic problem.

The layer potentials (3.2) and (3.3) for Stokes flow can be related to the corresponding single and double layer potentials for Laplace's equation. Considering the Laplace single layer potential for a particular but nontrivial choice of density, we can derive an analytical expression for the potential for $\boldsymbol{x}$ on the wall, and a semianalytical solution for $\boldsymbol{x}$ outside the wall. This allows us to carefully measure the accuracy of our numerical evaluation both in the singular and nearly singular case.

The paper is structured as follows: In Section 3.2 we introduce the discretization of the wall and the basic quadrature associated with it. In Section 3.3 we describe QBX which is used to handle the singular and nearly singular case, which cannot be done using the basic quadrature. We discuss precomputation in Section 3.4, and then present some numerical results for the Laplace single layer potential and the Stokes double layer potential in Section 3.5.

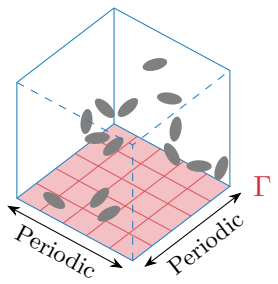

Figure 3.2: The type of flow problem serving as motivation for this paper: several particles in Stokes flow bounded by a flat wall (Γ). The problem is periodic along the sides of the wall.

3.2 Discretization and direct quadrature

Let Γ be a rectangular wall of size $L_1 \times L_2$, discretized into M patches P_α of size $a_1 \times a_2$ so that $\Gamma = \cup_{\alpha=1}^{M} P_\alpha$. On each patch, we apply a tensor product Gauss–Legendre quadrature rule with $n \times n$ points, shown in Fig. 3.3. In general the size of the patches could vary over Γ to allow for adaptivity, but we will not consider such cases here. For simplicity, we will furthermore assume that $L_1 = L_2 = L$ and $a_1 = a_2 = a$. An integral over Γ can then be approximated as

$$\int_\Gamma f(\boldsymbol{y})\,\mathrm{d}S_{\boldsymbol{y}} = \sum_{\alpha=1}^{M} \int_{P_\alpha} f(\boldsymbol{y})\,\mathrm{d}S_{\boldsymbol{y}} \approx \sum_{\alpha=1}^{M} \sum_{j=1}^{N} f(\boldsymbol{y}_{\alpha,j}) w_j, \tag{3.4}$$

where $\boldsymbol{y}_{\alpha,j}$ are the $N = n^2$ grid points of patch P_α and w_j are the weights of the tensor product Gauss–Legendre quadrature. We will call this quadrature rule the *direct quadrature* associated with the wall. The direct quadrature works well for smooth integrands and can be used for evaluating the layer potentials (3.2) and (3.3) over those patches that are sufficiently far away from the evaluation point, but it cannot handle the singular or nearly singular case. Therefore, the specialized quadrature method described in the next section must be used on those patches that are too close to the evaluation point, as indicated by Fig. 3.3.

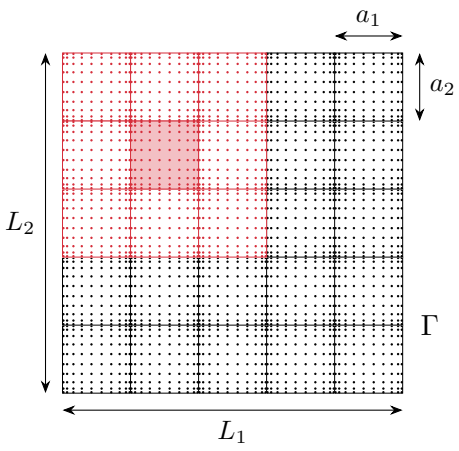

Figure 3.3: The wall Γ discretized into 25 patches, each with $n \times n$ Gauss–Legendre points. If the evaluation point is on the red shaded patch or sufficiently close to it, QBX will be used to evaluate the contribution to the layer potential from that patch and its eight neighbours (red), while direct quadrature is used on the other patches further away (black).

3.3 Quadrature by expansion

Quadrature by expansion (QBX) is based on the observation that the layer potential (3.2) or (3.3) that we want to evaluate is a smooth function in the fluid domain D_f, and therefore it can be written as a local series expansion around some point in this domain. This expansion is valid inside a ball which touches the boundary at exactly one point, and can therefore be used to evaluate the potential in both the singular and nearly singular case [3]. The coefficients of the expansion can be computed accurately using the direct quadrature as long as the expansion centre is sufficiently far away from the wall.

The expansion depends on the integral kernel of the layer potential that we want to evaluate. In the following we first introduce QBX for the Laplace single layer potential, which is a simple example that still lets us describe all the ideas in the method. Then we outline QBX for the Laplace double layer potential and the Stokes double layer potential.

3.3.1 Laplace single layer potential

The Laplace single layer potential is given by

$$\mathcal{G}[\gamma](\boldsymbol{x}) = \sum_{\alpha=1}^{M} \int_{P_\alpha} G(\boldsymbol{x},\boldsymbol{y})\gamma(\boldsymbol{y})\,\mathrm{d}S_{\boldsymbol{y}} =: \sum_{\alpha=1}^{M} \mathcal{G}_\alpha[\gamma](\boldsymbol{x}), \qquad G(\boldsymbol{x},\boldsymbol{y}) = \frac{1}{\|\boldsymbol{x}-\boldsymbol{y}\|}, \tag{3.5}$$

where γ is a scalar density defined on Γ. For example, if γ is a charge density, $\mathcal{G}$ is the electrostatic potential. We consider $\mathcal{G}_\alpha$, which is the contribution to the potential from patch P_α. To expand $\mathcal{G}_\alpha$ we begin by expanding the kernel G. This can be done using the so-called Laplace expansion, given by

$$\frac{1}{\|\boldsymbol{x}-\boldsymbol{y}\|} = \sum_{l=0}^{\infty} \frac{4\pi}{2l+1} \sum_{m=-l}^{l} r_x^l Y_l^{-m}(\theta_x,\varphi_x) \frac{1}{r_y^{l+1}} Y_l^m(\theta_y,\varphi_y). \tag{3.6}$$

The centre of this expansion is denoted by $\boldsymbol{c}$, and (r_x,θ_x,φ_x) and (r_y,θ_y,φ_y) are spherical coordinates of $\boldsymbol{x}$ and $\boldsymbol{y}$ with respect to $\boldsymbol{c}$. It is assumed that $r_x = \|\boldsymbol{x}-\boldsymbol{c}\|$ is smaller than or equal to $r_y = \|\boldsymbol{y}-\boldsymbol{c}\|$, as shown in Fig. 3.4. The spherical harmonics functions Y_l^m are given by

$$Y_l^m(\theta,\varphi) = \sqrt{\frac{2l+1}{4\pi}\frac{(l-|m|)!}{(l+|m|)!}} P_l^{|m|}(\cos\theta)\mathrm{e}^{\mathrm{i}m\varphi}, \tag{3.7}$$

where $P_l^{|m|}$ is the associated Legendre polynomial of degree l and order $|m|$.

Plugging (3.6) into (3.5) and moving terms related to $\boldsymbol{x}$ out of the integration leads to the expansion

$$\mathcal{G}_\alpha[\gamma](\boldsymbol{x}) = \sum_{l=0}^{\infty} \sum_{m=-l}^{l} d_{\alpha,lm}[\gamma] r_x^l Y_l^{-m}(\theta_x,\varphi_x) \tag{3.8}$$

with complex-valued coefficients

$$d_{\alpha,lm}[\gamma] = \frac{4\pi}{2l+1} \int_{P_\alpha} \frac{1}{r_y^{l+1}} Y_l^m(\theta_y,\varphi_y)\gamma(\boldsymbol{y})\,\mathrm{d}S_{\boldsymbol{y}}. \tag{3.9}$$

We assume that $\min_{\boldsymbol{y}\in\Gamma} r_y =: r > 0$ so that the integral in (3.9) is not singular; r is the distance from the expansion centre $\boldsymbol{c}$ to the wall. Note that this expansion is based on a separation of source $\boldsymbol{y}$ and target $\boldsymbol{x}$; the contribution from all sources are stored in the coefficients $d_{\alpha,lm}$, which once computed can be used to evaluate the potential for any target within the ball of convergence using (3.8).

The expansion given by (3.8)–(3.9) is an exact representation of the potential $\mathcal{G}_\alpha$. However, in order to use it numerically, we must introduce two approximations. First, we must truncate the infinite series in (3.8) at some $l_{\max} = p$. This introduces an error which we call the *truncation*

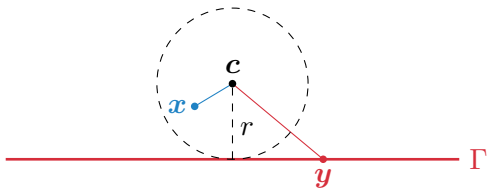

Figure 3.4: The distance $\|\boldsymbol{x}-\boldsymbol{c}\|$ must be smaller than or equal to $\|\boldsymbol{y}-\boldsymbol{c}\|$ for the Laplace expansion (3.6) to be valid. This means that the expansion (3.8) is valid inside a ball of radius $r = \min_{\boldsymbol{y}\in\Gamma} \|\boldsymbol{y}-\boldsymbol{c}\|$.

error. Second, the coefficients $d_{\alpha,lm}$ must be computed using some quadrature rule, which introduces an error that we refer to as the *coefficient error*. An estimate for the truncation error is given in [3] and for the coefficient error in [2].

We use the direct quadrature (3.4) to compute the coefficients (3.9), and in doing so we *upsample* the density γ by a factor κ. This means that the density is interpolated onto a refined Gauss–Legendre patch with $\kappa n \times \kappa n$ grid points, which is needed to properly resolve the $Y_l^m(\theta_y, \varphi_y)/r_y^{l+1}$ part of the integrand, which becomes more oscillatory and peaked as l increases.

To summarize, QBX has three parameters: r, p and κ. The expansion radius r is the distance from the expansion centre to the wall, and also the radius of the ball of convergence; the expansion degree p is the maximum l included in the expansion; the upsampling factor κ controls how much the original grid is refined. To this list we can add the side length a and number of points $N = n^2$ of the patch, which control the grid resolution of the direct quadrature. A discussion of the QBX parameters and how to choose them can be found in [1].

The QBX approximation of $\mathcal{G}_\alpha$ is denoted by $\mathcal{G}_\alpha^{(r,p,\kappa)}$ and given by

$$\mathcal{G}_\alpha^{(r,p,\kappa)}[\gamma](\boldsymbol{x}) = \sum_{l=0}^{p} \sum_{m=-l}^{l} d_{\alpha,lm}^{(r,\kappa)}[\gamma] r_x^l Y_l^{-m}(\theta_x, \varphi_x), \tag{3.10}$$

with coefficients

$$d_{\alpha,lm}^{(r,\kappa)}[\gamma] = \frac{4\pi}{2l+1} \sum_{j=1}^{(\kappa n)^2} \frac{1}{r_j^{l+1}} Y_l^m(\theta_j, \varphi_j) (\boldsymbol{U}\boldsymbol{\gamma}_\alpha)_j w_j, \tag{3.11}$$

where j enumerates all $\kappa^2 n^2$ grid points on the refined version of P_α, $(r_j, \theta_j, \varphi_j)$ are spherical coordinates of the jth grid point with respect to $\boldsymbol{c}$, and w_j are the quadrature weights. The vector $\boldsymbol{\gamma}_\alpha \in \mathbb{R}^{n^2}$ contains the value of γ at every grid point on P_α, and the matrix $\boldsymbol{U} \in \mathbb{R}^{(\kappa n)^2 \times n^2}$ upsamples this onto the refined patch. Note that the coefficients from all neighbouring patches (red in Fig. 3.3) can be added before computing the QBX potential using (3.10).

Fig. 3.5 shows how the error of the QBX approximation from a single expansion centre decreases when p is increased. Note that to cover all grid points on the wall and most of its neighbourhood, one expansion centre per grid point is needed. This may seem expensive, but most of the work can be done as a precomputation, as explained in Section 3.4.

3.3.2 Laplace double layer potential

The Laplace double layer potential is given by

$$\mathcal{F}[\boldsymbol{\rho}](\boldsymbol{x}) = \sum_{\alpha=1}^{M} \int_{P_\alpha} F_j(\boldsymbol{x}, \boldsymbol{y}) \rho_j(\boldsymbol{y}) \, \mathrm{d}S_{\boldsymbol{y}} =: \sum_{\alpha=1}^{M} \mathcal{F}_\alpha[\boldsymbol{\rho}](\boldsymbol{x}), \qquad F_j(\boldsymbol{x}, \boldsymbol{y}) = \frac{\partial}{\partial y_j} \frac{1}{r} = \frac{r_j}{r^3}, \tag{3.12}$$

with $\boldsymbol{r} = \boldsymbol{x} - \boldsymbol{y}$ and $r = \|\boldsymbol{r}\|$. The vector density $\boldsymbol{\rho}$ can be interpreted as a density of electric dipoles on Γ. Note that the integral kernel F_j is the gradient of the single layer kernel G from (3.5). We can therefore use the Laplace expansion (3.6) again, and in the same way as in Section 3.3.1 we arrive at the expansion

$$\mathcal{F}_\alpha[\boldsymbol{\rho}](\boldsymbol{x}) = \sum_{l=0}^{\infty} \sum_{m=-l}^{l} z_{\alpha,lm}[\boldsymbol{\rho}] r_x^l Y_l^{-m}(\theta_x, \varphi_x) \tag{3.13}$$

with coefficients

$$z_{\alpha,lm}[\boldsymbol{\rho}] = \frac{4\pi}{2l+1} \int_{P_\alpha} \boldsymbol{\rho}(\boldsymbol{y}) \cdot \nabla_{\boldsymbol{y}} \left(\frac{1}{r_y^{l+1}} Y_l^m(\theta_y, \varphi_y) \right) \mathrm{d}S_{\boldsymbol{y}}. \tag{3.14}$$

These coefficients can be computed up to some $l_{\max} = p$ using the direct quadrature with upsampling as in Section 3.3.1.

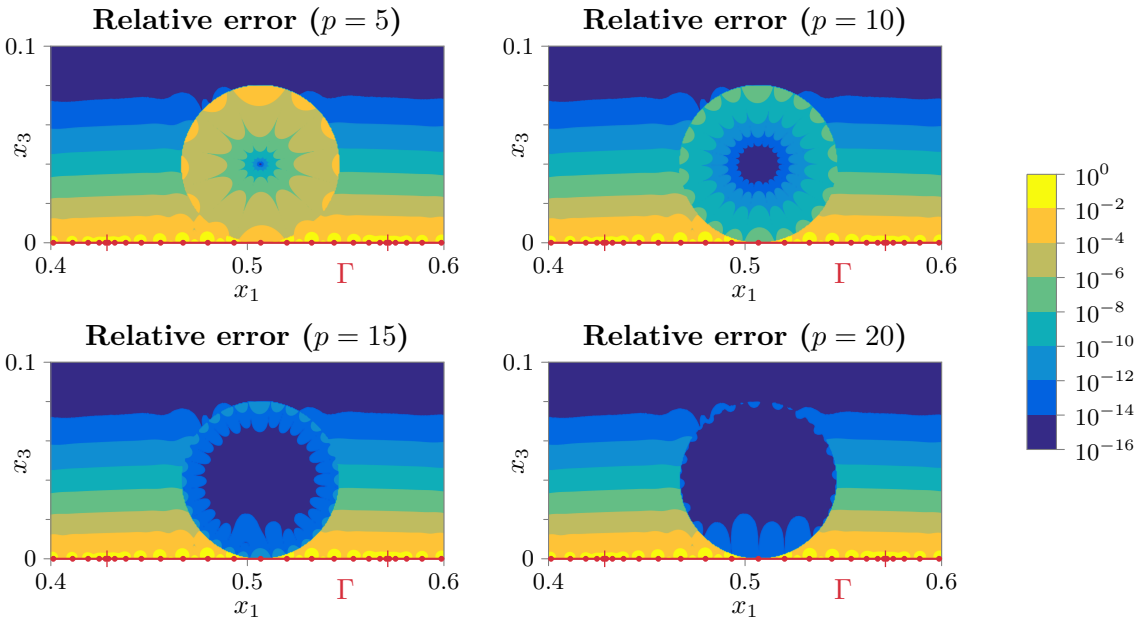

Figure 3.5: The error when QBX is used in a ball of radius $r = 0.04$, with increasing expansion degree p and upsampling factor $\kappa = 4$. The direct quadrature is shown for comparison outside the ball of convergence. The grid and density are the same as in Fig. 3.1 and Section 3.5.1.

3.3.3 Stokes double layer potential

To apply QBX to the Stokes double layer potential (3.3) we need an expansion that separates source and target, like the ones provided by the Laplace expansion in the preceding sections. To find such an expansion, we use a result by Tornberg and Greengard [7] that expresses the kernel of the Stokes double layer potential in terms of the Laplace double layer kernel F_j, namely

$$T_{ijk}(\boldsymbol{x},\boldsymbol{y})n_k = \left((x_j - y_j)\frac{\partial}{\partial x_i} - \delta_{ij}\right)F_k(\boldsymbol{x},\boldsymbol{y})n_k + \left((x_k - y_k)\frac{\partial}{\partial x_i} - \delta_{ik}\right)F_j(\boldsymbol{x},\boldsymbol{y})n_k. \tag{3.15}$$

Multiplying this relation by q_j and rearranging terms, we find that the integrand of (3.3) can be written as

$$T_{ijk}(\boldsymbol{x},\boldsymbol{y})q_j n_k = \left(x_j\frac{\partial}{\partial x_i} - \delta_{ij}\right)F_k(\boldsymbol{x},\boldsymbol{y})(q_j n_k + n_j q_k) - \frac{\partial}{\partial x_i}F_j(\boldsymbol{x},\boldsymbol{y})(y_k q_k n_j + y_k n_k q_j). \tag{3.16}$$

Thus the contribution from patch P_α to the Stokes double layer potential can be written as

$$\mathcal{D}_{\alpha,i}[\boldsymbol{q}](\boldsymbol{x}) = \left(x_j\frac{\partial}{\partial x_i} - \delta_{ij}\right)\mathcal{F}_\alpha[q_j\boldsymbol{n} + n_j\boldsymbol{q}](\boldsymbol{x}) - \frac{\partial}{\partial x_i}\mathcal{F}_\alpha[y_k q_k\boldsymbol{n} + y_k n_k\boldsymbol{q}](\boldsymbol{x}), \tag{3.17}$$

where $\mathcal{F}_\alpha$ is the Laplace double layer potential given by (3.12). In order to evaluate (3.17), we must compute four expansions (3.13) of $\mathcal{F}_\alpha$ associated with the densities $\boldsymbol{\rho}^{(j)} = q_j\boldsymbol{n} + n_j\boldsymbol{q}$, $j = 1, 2, 3$, and $\boldsymbol{\rho}^{(4)} = y_k q_k\boldsymbol{n} + y_k n_k\boldsymbol{q}$. The four sets of expansion coefficients are given by (3.14) as

$$z_{\alpha,lm}[\boldsymbol{\rho}^{(j)}] = \frac{4\pi}{2l+1}\int_{P_\alpha}(q_j\boldsymbol{n} + n_j\boldsymbol{q})\cdot\nabla_{\boldsymbol{y}}\left(\frac{1}{r_y^{l+1}}Y_l^m(\theta_y,\varphi_y)\right)\mathrm{d}S_{\boldsymbol{y}}, \qquad j = 1, 2, 3, \tag{3.18}$$

$$z_{\alpha,lm}[\boldsymbol{\rho}^{(4)}] = \frac{4\pi}{2l+1}\int_{P_\alpha}(y_k q_k\boldsymbol{n} + y_k n_k\boldsymbol{q})\cdot\nabla_{\boldsymbol{y}}\left(\frac{1}{r_y^{l+1}}Y_l^m(\theta_y,\varphi_y)\right)\mathrm{d}S_{\boldsymbol{y}}. \tag{3.19}$$

These coefficients are computed up to $l_{\max} = p$ using the direct quadrature as before.

3.4 Precomputation

In this section we briefly describe the precomputation scheme for the Laplace single layer potential. The same basic principles apply also to the other layer potentials, but we do not have room to discuss them here.

First note that since the spherical harmonics given by (3.7) are conjugate symmetric in m, i.e. $Y_l^{-m}(\theta,\varphi) = Y_l^m(\theta,\varphi)^*$, the same conjugate symmetry holds also for the expansion coefficients given by (3.9), i.e. $d_{\alpha,l,-m}[\gamma] = d_{\alpha,lm}[\gamma]^*$. It is therefore enough to compute $d_{\alpha,lm}$ for $0 \le m \le l$, meaning that $N_p = (p+1)(p+2)/2$ coefficients must be computed per expansion centre. One can view (3.11) as a matrix $\boldsymbol{M}_\alpha^{(r,\kappa)} \in \mathbb{C}^{N_p \times N}$ multiplying the vector $\boldsymbol{\gamma}_\alpha \in \mathbb{R}^N$ to yield the N_p coefficients. This matrix contains only geometric quantities and can therefore be precomputed and later applied to any density.

In principle, one $\boldsymbol{M}_\alpha^{(r,\kappa)}$ matrix is needed for every expansion centre, but once the matrices have been computed for one patch they can be reused, with appropriate scaling factors, for all patches of the same aspect ratio. Furthermore, the four mirror symmetries of a square can be used to reduce the precomputation needed. By performing the necessary reflections, one can get the coefficients for all expansion centres based only on the $\boldsymbol{M}_\alpha^{(r,\kappa)}$ matrices for the points in the shaded eighth in Fig. 3.6, thus reducing the required storage space and precomputation time by approximately a factor 1/8. (If the patch is rectangular there are only two mirror symmetries and the factor is 1/4.)

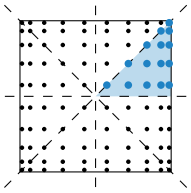

Figure 3.6: Symmetries of a patch that can be used to reduce precomputation.

One can also view (3.10) as a matrix $\boldsymbol{\Theta}_{\boldsymbol{x}} \in \mathbb{C}^{1\times N_p}$ multiplying the vector of coefficients. This matrix depends on the target $\boldsymbol{x}$, but it can be precomputed for a given target (e.g. the grid point where the ball of convergence touches Γ). This way a matrix $\boldsymbol{H}_{\alpha,j}^{(r,\kappa)} = \boldsymbol{\Theta}_{\boldsymbol{y}_{\alpha,j}} \boldsymbol{M}_\alpha^{(r,\kappa)} \in \mathbb{R}^{1\times N}$ can be precomputed for each grid point $\boldsymbol{y}_{\alpha,j}$ in the shaded eighth in Fig. 3.6, and used in the singular case for computing the potential at that grid point from the density vector $\boldsymbol{\gamma}_\alpha$.

3.5 Results

3.5.1 Laplace single layer potential

As a test case, we take the wall Γ as the unit square in the x_1x_2-plane and let the Laplace single layer density be given by a Gaussian

$$\gamma(\boldsymbol{x}) = \mathrm{e}^{-\beta\|\boldsymbol{x}-\boldsymbol{x}_*\|^2}, \qquad \boldsymbol{x} \in \Gamma, \tag{3.20}$$

where $\boldsymbol{x}_* \in \Gamma$ is the centre of the Gaussian and $\beta > 0$ controls its width. Provided that γ has compact support on Γ (up to some tolerance), the single layer potential can be shown to be

$$\mathcal{G}[\gamma](\boldsymbol{x}) = 2\pi\mathrm{e}^{-\beta R_*^2} \int_0^\infty \frac{R\mathrm{e}^{-\beta R^2}}{\sqrt{R^2+x_3^2}}\, I_0(2\beta R R_*)\,\mathrm{d}R, \qquad \boldsymbol{x} \in \mathbb{R}^3, \tag{3.21}$$

where x_3 is the distance to Γ from $\boldsymbol{x}$, $R_* = \|\boldsymbol{x}_* - \hat{\boldsymbol{x}}\|$ with $\hat{\boldsymbol{x}} = \mathrm{proj}_\Gamma \boldsymbol{x}$, and I_0 is a modified Bessel function of the first kind. The integral in (3.21) can be evaluated accurately e.g. using

MATLAB's `integral` function. For $\boldsymbol{x} \in \Gamma$ we have $x_3 = 0$ and (3.21) simplifies to

$$\mathcal{G}[\gamma](\boldsymbol{x}) = \sqrt{\frac{\pi^3}{\beta}} \mathrm{e}^{-\beta R_*^2/2} I_0(\beta R_*^2/2), \qquad \boldsymbol{x} \in \Gamma. \tag{3.22}$$

In this example we choose $\boldsymbol{x}_* = (0.51, 0.498, 0)$ and $\beta = -\log(10^{-14})/0.49^2 \approx 134.26$.

We discretize Γ into 7×7 patches of equal size with 16×16 Gauss–Legendre points on each patch. We place an expansion centre a distance $r = 0.04$ above the grid point $(0.5068, 0.5068, 0)$ and evaluate the potential directly above the grid point using QBX with $\kappa = 4$ and varying p, both near the wall and on it. As Fig. 3.7 shows, QBX permits evaluation of the potential to very high accuracy arbitrarily close to the wall. Note that simply using upsampling together with the direct quadrature is not sufficient very close to the wall, but it works well further away. In this case, one could for example use QBX for $x_3 < 0.04$ and direct quadrature with upsampling for $0.04 \leq x_3 < 0.08$.

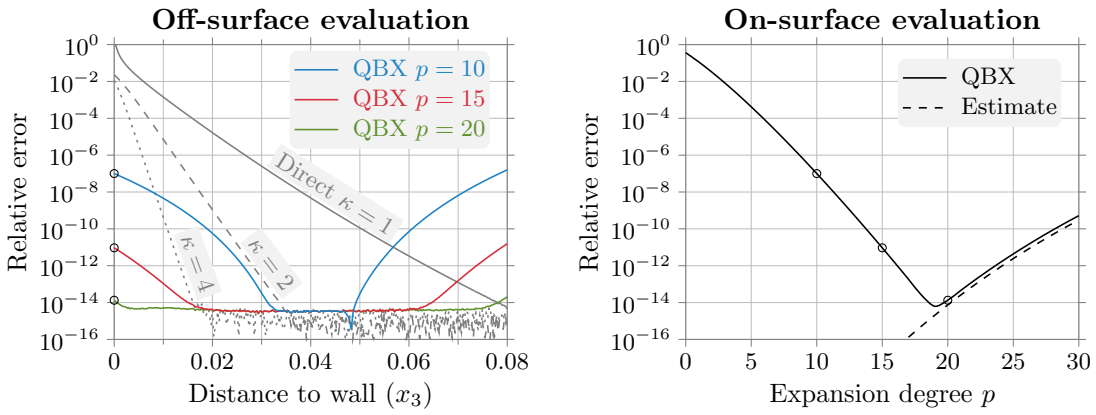

Figure 3.7: Evaluation of the Laplace single layer potential using QBX with different p. Left: off-surface evaluation (cf. Fig. 3.5). For comparison, the direct quadrature with different upsampling factors κ is also shown in grey. Right: Evaluation at the grid point on Γ. The dominating error is the truncation error for $p < 19$ and the coefficient error for $p > 19$. An estimate for the coefficient error given by [2] is also shown.

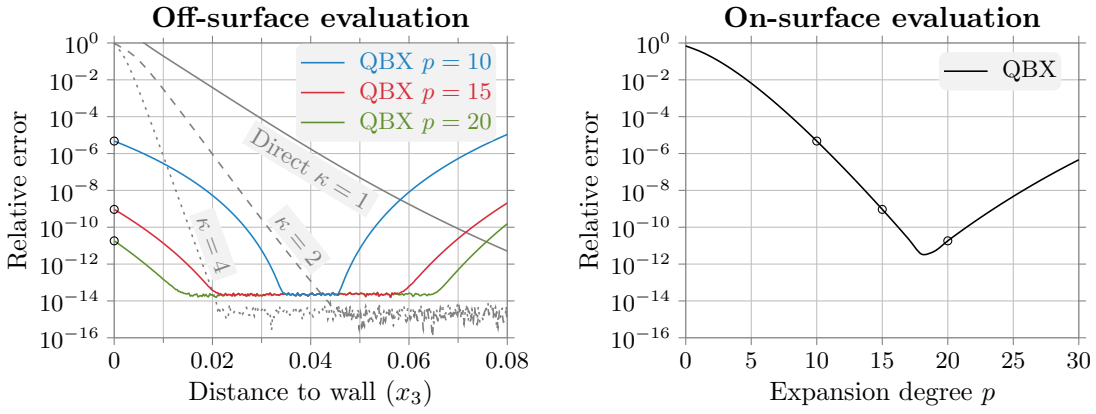

Figure 3.8: Evaluation of the Stokes double layer potential using QBX with different p, in the fluid domain (left) and on the wall (right). Compare with Fig. 3.7.

3.5.2 Stokes double layer potential

We take all parameters as in Section 3.5.1 and the Stokes double layer density

$$q_i(\boldsymbol{x}) = \mathrm{e}^{-\beta\|\boldsymbol{x}-\boldsymbol{x}_*\|^2}, \quad i = 1, 2, 3, \qquad \boldsymbol{x} \in \Gamma, \tag{3.23}$$

with β and $\boldsymbol{x}_*$ as before. In this case we have no exact solution, so we compare with a reference solution with upsampling $\kappa = 5$ and degree $p = 25$. Fig. 3.8 shows that the errors achieved by QBX are about two orders of magnitude larger than for the Laplace single layer potential.

3.6 Conclusions

In this paper we have shown how QBX can be used to evaluate singular and nearly singular layer potentials over a flat wall. The method can achieve high accuracy arbitrarily close to the wall, which we demonstrated in two test cases: one for the Laplace single layer potential in a case where a semianalytic solution is available, and one for the Stokes double layer potential with a numeric reference solution. We have also explained how certain quantities can be precomputed and how geometric symmetries can be used to reduce the amount of storage and time needed for precomputation.

Acknowledgement

We are grateful to Dr. Ludvig af Klinteberg for providing us with the QBX implementation for spheroidal particles, parts of which were reused in this work.

This work has been supported by the Göran Gustafsson Foundation for Research in Natural Sciences and by the Swedish Research Council under grant no. 2015-04998. The authors gratefully acknowledge this support.

References

[1] L. af Klinteberg and A.-K. Tornberg, *A fast integral equation method for solid particles in viscous flow using quadrature by expansion*, J. Comp. Phys., 326 (2016), 420–445.

[2] L. af Klinteberg and A.-K. Tornberg, *Error estimation for quadrature by expansion in layer potential evaluation*, Adv. Comput. Math., 43 (2017), 195–234.

[3] C. L. Epstein, L. Greengard and A. Klöckner, *On the convergence of local expansions of layer potentials*, SIAM J. Numer. Anal., 51(5) (2013), 2660–2679.

[4] Z. Gimbutas, L. Greengard and S. Veerapaneni, *Simple and efficient representations for the fundamental solutions of Stokes flow in a half-space*, J. Fluid Mech., 776 (2015), R1.

[5] A. Klöckner, A. Barnett, L. Greengard and M. O'Neil, *Quadrature by expansion: A new method for the evaluation of layer potentials*, J. Comp. Phys., 252 (2013), 332–349.

[6] C. Pozrikidis, *Boundary integral and singularity methods for linearized viscous flow*, Cambridge University Press, Cambridge, UK, 1992.

[7] A.-K. Tornberg and L. Greengard, *A fast multipole method for the three-dimensional Stokes equations*, J. Comp. Phys., 227 (2008), 1613–1619.

Chapter 4

On discretisation schemes for a boundary integral model of stochastic ray propagation

Janis Bajars and David J. Chappell

School of Science & Technology,
Nottingham Trent University
Nottingham
UK

Abstract. *A boundary integral operator method for stochastic ray tracing in billiards was recently proposed in [1]. In particular, a phase-space boundary integral model for propagating uncertain ray or particle flows was described and shown to interpolate between deterministic and random models of the flow propagation. In this work we describe discretisation schemes for this class of boundary integral operators using piecewise constant collocation in the spatial variable and either the Nyström method or the collocation method in the momentum variable. The simplicity of the spatial basis means that the corresponding spatial integration can be performed analytically. Convergence properties of the discretisation schemes and strategies for numerical implementation are presented and discussed.*

4.1 Introduction

Boundary integral formulations for propagating particle or ray densities along ray trajectories in computer graphics applications are often termed the rendering equation [2]. This equation therefore lies at the heart of a wide variety of algorithms, both for applications in computer graphics [2] and beyond [3, 4, 5]. The point of departure for this study stems from the observation that the rendering equation may be formulated using deterministic transfer operators of Frobenius-Perron (FP) type [5, 6]. Replacing the deterministic transfer operator with a stochastic one results in a boundary integral formulation for stochastic propagation of ray densities. The simplest implementation of a stochastic treatment is to assume that rays propagate uniformly with equal probability of all admissible propagated ray vectors. This formulation is known as the radiosity method (with Lambertian reflection) in the room acoustics community [3, 4]. A more widely applicable implementation arises if one assumes that the mapped ray vector is normally distributed, with mean given by the associated deterministic dynamics. The resulting stochastic evolution operator will be of Fokker-Planck type as discussed in [7, 8]. The choice of variance in this approach allows the model to be tuned to the level of uncertainty prescribed by

the application. Example applications arise in fluid dynamics [9], weather forecasting [10], linear wave dynamics or in general in describing the evolution of phase-space densities of a dynamical system.

In this work, we discuss two possible discretisation schemes for a family of boundary integral operators for stochastic ray propagation. Our discretisation strategy is based on a piecewise constant collocation method in the spatial variable, together with an exact integration procedure for the corresponding spatial integral. For the momentum variable we apply the Nyström method, which takes care of the integral over the momentum variable within the discretisation approach, or the collocation method, which separates dependence of the integral over the momentum variable from the discretisation approach. We then discuss the implementation strategies and convergence properties of the discretisation schemes.

4.2 Boundary integral operator model for the stochastic propagation of phase-space densities

Consider phase-space in two-dimensions with position vector $\mathbf{r} \in \mathbb{R}^2$ and momentum (or slowness) vector $\mathbf{p} \in \mathbb{R}^2$. Let Ω denote a finite two-dimensional domain with an associated speed of propagation c. The Hamiltonian $\hat{H} = c|\mathbf{p}| = 1$ describes the ray trajectories within Ω between reflections at the boundary $\Gamma = \partial\Omega$. We write the phase-space coordinates on the boundary of Ω as $X = (s, p)$, where s is an arc-length parametrisation of Γ and $p = c^{-1}\sin(\theta)$ is the tangential component of the momentum vector $\mathbf{p}$ at the point s, where $\theta \in (-\pi/2, \pi/2)$ is the angle between the trajectory leaving the boundary at s and the normal vector to Γ (also at s).

The stochastic propagation of a density ρ through phase-space is described by an operator of the form [1]

$$\mathcal{L}_{\boldsymbol{\sigma}}\rho(X) = \int_Q f_{\boldsymbol{\sigma}}(X - \varphi(X'))\rho(X')\,\mathrm{d}X'. \tag{4.1}$$

Here $Q = \Gamma \times (-c^{-1}, c^{-1})$ denotes the phase-space on the boundary and $\varphi : Q \to Q$ defines the boundary flow map, which maps a vector in Q to another vector in a subset of Q, leading to a deterministic evolution of the form $\varphi(X') = X$, where $X' = (s',\, p')$ and $X = (s, p)$. Geometrically, φ corresponds to the composition of a translation (from s' to s) and a rotation to the direction corresponding to a specular reflection. The kernel of the boundary integral operator (4.1) is given by a probability density function (PDF) $f_{\boldsymbol{\sigma}}$ such that

$$\int_Q f_{\boldsymbol{\sigma}}(X)\,\mathrm{d}X = 1, \tag{4.2}$$

and $\boldsymbol{\sigma}$ is a parameter set controlling its shape.

With reference to applications in vibro-acoustics, this probabilistic behaviour could be attributed to, for example, uncertain fluctuations in the wave speed c, roughness of the reflecting surface or uncertainties in the boundary conditions/source terms. In all cases we assume that the total energy $\hat{H} = c|\mathbf{p}| = 1$ remains fixed and that the total probability is conserved, that is, condition (4.2) holds throughout. Note that in contrast to the models considered in [7, 8], the range of integration in the domains considered here is in general bounded, which has implications for the choice of suitable PDFs $f_{\boldsymbol{\sigma}}$. The simplest case is to take $f_{\boldsymbol{\sigma}} = const$, upon which one arrives at a model describing propagation to all admissible positions and directions with equal probability. The system is thus by definition ergodic and independent of the underlying classical dynamics. In general, we would like to arrive at a stochastic operator which includes both deterministic propagation and the random propagation model described above as limiting cases [1]. In addition, the PDF $f_{\boldsymbol{\sigma}}$ needs to obey conditions on the sampling ranges due to the

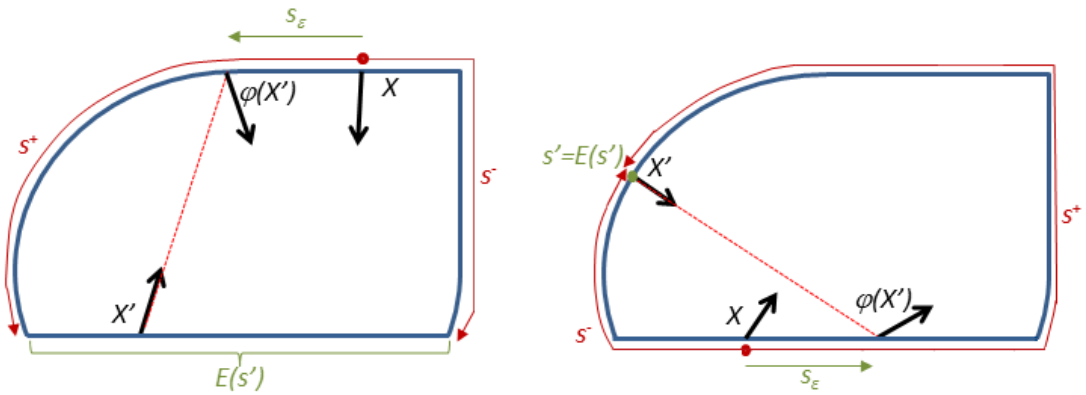

Figure 4.1: Source: Ref. [1]. Tracking ray trajectories via a noisy boundary map and truncation limits $s^\pm$ for the random variable s_ε.

limited range of the boundary map φ. For simplicity, we will restrict to convex domains Ω to avoid additional complications due to incorporating visibility functions.

For an initial boundary distribution ρ_0 on Q, the final equilibrium distribution (including contributions from arbitrarily many reflections) may be computed using the following boundary integral equation (see for example [1] and [5]):

$$(I - \mathcal{L}_{\boldsymbol{\sigma}})\rho = \rho_0. \tag{4.3}$$

Note that for the solution ρ to converge, energy losses must be introduced into the system, which could take place at the boundaries themselves, or along the trajectories. In general, a weight factor w will be added inside the integral in the definition of $\mathcal{L}_{\boldsymbol{\sigma}}$ which contains a dissipative term, and for the extension to multiple domains connected at interfaces w will also contain reflection/transmission probabilities at these interfaces.

We may interpret the evolution given by the operator in Eq. (4.1) as originating from a stochastic boundary map $\varphi_{\boldsymbol{\sigma}}$ with added noise, that is,

$$\begin{aligned} \varphi_{\boldsymbol{\sigma}}(X') &= X \\ &= \varphi(X') + X_\varepsilon, \end{aligned} \tag{4.4}$$

where $X_\varepsilon = (s_\varepsilon, p_\varepsilon)$ are random variables drawn from the PDF $f_{\boldsymbol{\sigma}}$. Note that s_ε is understood as a shift in (anti-clockwise) direction. For $X \in Q$ given, we have to ensure that $\varphi(X') = X - X_\varepsilon$ is in the range of the deterministic map φ; this yields restrictions on the possible values of X_ε and thus on the domain of $f_{\boldsymbol{\sigma}}$.

We express $\varphi = (\varphi_s, \varphi_p)$ in terms of its position and momentum components and again write the initial coordinate as $X' = (s', p')$. The range of admissible values for $\varphi_s(X')$ is $[0, L) \setminus E(s')$, where $E(s')$ is the (closed) set of all points on the same straight edge as s', see Fig. 4.1. Note that for curved edges we set $E(s') = s'$ as shown in the right plot of Fig. 4.1. Furthermore, we have that $\varphi_p(X') \in (-c^{-1}, c^{-1})$. It is therefore necessary to truncate the ranges from which X_ε are sampled to the ranges where for fixed X, $\varphi(X') \in ([0, L) \setminus E(s')) \times (-c^{-1}, c^{-1})$ in Eq. (4.4). Denoting these truncated ranges by (X^-, X^+) where $X^\pm = (s^\pm, p^\pm)$, the PDF $f_{\boldsymbol{\sigma}}$ will have support on $X_\varepsilon \in (X^-, X^+)$ only. A cut-off function $\chi(X_\varepsilon; X^-, X^+)$ for restricting the support of $f_{\boldsymbol{\sigma}}$ to (X^-, X^+) can be defined in the usual way using Heaviside step functions. Having obtained the domain of the PDF, we can now derive a PDF from an uncorrelated bivariate Gaussian distribution with mean $\mathbf{0} = (0, 0)$ and standard deviation $\boldsymbol{\sigma} = (\sigma_1, \sigma_2)$. A scaled PDF

is obtained by setting

$$f_{\boldsymbol{\sigma}}(X_\varepsilon; X^-, X^+) = \frac{\chi(X_\varepsilon; X^-, X^+) \exp\left(-\frac{s_\varepsilon^2}{2\sigma_1^2}\right) \exp\left(-\frac{p_\varepsilon^2}{2\sigma_2^2}\right)}{2\pi\sigma_1\sigma_2\psi_{\sigma_1}(s^-, s^+)\psi_{\sigma_2}(p^-, p^+)}, \tag{4.5}$$

where the scaling defined through ψ_{σ_1} and ψ_{σ_2} is given as

$$\psi_{\sigma_1}(s^-, s^+) = \frac{1}{2}\left(\operatorname{erf}\left(\frac{s^+}{\sqrt{2}\sigma_1}\right) - \operatorname{erf}\left(\frac{s^-}{\sqrt{2}\sigma_1}\right)\right), \tag{4.6}$$

and ψ_{σ_2} is defined analogously. The scaling ensures that the PDF satisfies condition (4.2) for the truncated sampling ranges specified through χ. Note that the mean and variance of $f_{\boldsymbol{\sigma}}$ differs in general from that of the underlying Gaussian distribution, but can be computed from the PDF (4.5) using standard formulae.

Taking the limit of (4.5) as $\boldsymbol{\sigma} \to \mathbf{0}$ then the distribution becomes increasingly sharp and the bivariate Gaussian tends to a two-dimensional delta distribution localised around $X_\varepsilon = X - \varphi(X') = \mathbf{0}$, which leads to a deterministic model. Taking the limit as σ_1, and σ_2 go to ∞ and using the leading order asymptotic expansion of the error function about 0 returns a uniform distribution for $s_\varepsilon \in (s^-, s^+)$ and $p_\varepsilon \in (p^-, p^+)$, leading to the fully stochastic regime described above. See [1] for a more complete discussion of the behaviour of $f_{\boldsymbol{\sigma}}$ in the limit of small and large $\boldsymbol{\sigma}$.

4.3 Discretisation of the boundary integral operator

In this section we detail the approximation of the boundary integral operator (4.1) and the energy density $\rho(X)$, where $X = (s, p)$ as before. We begin our presentation with the discretisation using a piecewise constant collocation method in the spatial variable s and a Nyström method for the momentum variable p. Consider an N-sided closed convex polygon with boundary Γ and a local subdivision of each edge into a number of boundary elements. Then the approximation of the energy density $\rho(X)$ on the boundary Γ may be written

$$\rho(X) = \sum_{j=1}^{n} b_j(s)\rho_j(p), \tag{4.7}$$

where $n \geq N$ is the total number of boundary elements, $\rho_j(p)$ are a set of directionally dependent expansion functions to be determined and $b_j(s)$ are piecewise constant spatial basis functions, i.e. $b_j(s) = 1$ if s lies on the jth element and zero elsewhere.

Substituting (4.7) into (4.1) we obtain

$$\begin{aligned} \mathcal{L}_{\boldsymbol{\sigma}}\rho(X) &= \sum_{j=1}^{n} \int_Q f_{\boldsymbol{\sigma}}(X - \varphi(X'))\rho_j(p')b_j(s')\,\mathrm{d}X' \\ &= \sum_{j=1}^{n} \int_{-c^{-1}}^{c^{-1}} \rho_j(p') \left[\int_{e_j} f_{\boldsymbol{\sigma}}(X - \varphi(X'))\,\mathrm{d}s'\right] \mathrm{d}p', \end{aligned} \tag{4.8}$$

where e_j denotes integration over the jth boundary element. Note that the spatial integral with respect to s' appearing in (4.8) can be solved analytically in terms of the error function erf; this remains tractable if we include an additional damping factor of the form $\exp(-\mu d(s, s'))$, where $\mu \geqslant 0$ is a (viscous) damping parameter and $d(s, s')$ denotes the Euclidean distance between the boundary points s' and s. In what follows, we denote this spatial integral as S_μ, where

$$S_0(s, p') = -\frac{\chi_{s'}}{2\psi_{\sigma_1}} \operatorname{erf}\left(\frac{s - s'}{\sqrt{2}\sigma_1}\right)\Bigg|_{s'=S'_{\min}(p')}^{s'=S'_{max}(p')} \tag{4.9}$$

for the undamped case when $\mu = 0$.

We now change the variable in the momentum integration from $p = c^{-1}\sin(\theta)$ to the direction angle θ and define collocation points s_i, $i = 1, ..., n$, where s_i is chosen as the centroid of the ith boundary element. First, note that the PDF $f_{\boldsymbol{\sigma}}$ defined in Eq. (4.5) can be separated into spatially dependent and directionally dependent components of the form

$$f_{\boldsymbol{\sigma}}(s_\epsilon, p_\epsilon) = \left(\chi_s \frac{\exp\left(-\frac{s_\epsilon^2}{2\sigma_1^2}\right)}{\sqrt{2\pi}\sigma_1\psi_{\sigma_1}}\right)\left(\chi_p \frac{\exp\left(-\frac{p_\epsilon^2}{2\sigma_2^2}\right)}{\sqrt{2\pi}\sigma_2\psi_{\sigma_2}}\right) = f_{\sigma_1}(s_\varepsilon) f_{\sigma_2}(p_\varepsilon).$$

Applying a numerical integration rule such as trapezoidal, Gaussian or Clenshaw-Curtis quadrature with nodes p_k and weights w_k, for $k = 0, ..., K$, then the combined collocation and Nyström method discretisation of equation (4.1) is given by

$$(\mathcal{L}_{\boldsymbol{\sigma}}\rho)(s_i, p_\kappa) = c^{-1} \sum_{j=1, j\neq i}^{n} \sum_{k=0}^{K} w_k \rho_j(\theta_k') f_{\sigma_2}(p_\varepsilon(\theta_k, \theta_k')) S_\mu(s_i, c^{-1}\sin(\theta_k'))\cos(\theta_k'), \tag{4.10}$$

where $i = 1, ..., n$ and $\kappa = 0, ..., K$. The discretisation (4.10) reduces the operator equation (4.3) to a linear system. The solution of this linear system then leads to an approximation for the final equilibrium density distribution ρ given by (4.7), at a set of momenta p_κ, $\kappa = 0, ..., K$.

Notice that the specific set of direction values p_κ in (4.10) are defined by the choice of the numerical quadrature method. In addition, the size of the transfer matrix grows with the number of quadrature nodes. In the small $\boldsymbol{\sigma}$ limit, that is, close to the deterministic dynamics, special numerical quadrature methods could be employed to more efficiently handle the singular perturbation in the PDF as $\sigma_2 \to 0$. In this case, it would be desirable to remove the dependence of the quadrature scheme (for approximating the integral over the momentum variable) from the momentum space discretisation, and hence from the size of the transfer matrix. This is directly achievable by replacing the Nyström method with collocation method in the momentum variable p.

To apply the collocation method in p we consider a finite basis approximation of the directionally dependent functions $\rho_j(p)$ in (4.7)

$$\rho_j(p) = \boldsymbol{\phi}^T(p)\boldsymbol{\rho}_j, \tag{4.11}$$

where $\boldsymbol{\phi}(p) \in \mathbb{R}^{N_p}$ is an N_p dimensional vector of basis functions and $\boldsymbol{\rho}_j \in \mathbb{R}^{N_p}$ are unknown expansion coefficients to be determined for each $j = 1, ..., n$.

Substituting (4.7) together with (4.11) into (4.1) we obtain

$$\mathcal{L}_{\boldsymbol{\sigma}}\rho(X) \;=\; \sum_{j=1}^{n}\left[\int_{-c^{-1}}^{c^{-1}} \boldsymbol{\phi}^T(p') f_{\sigma_2}(p_\varepsilon) S_\mu(s, p')\,\mathrm{d}p'\right]\boldsymbol{\rho}_j.$$

As above we consider spatial collocation points s_i, $i = 1, ..., n$, taken as the centroids of the corresponding boundary elements and introduce directional collocation points p_κ for $\kappa = 1, ..., N_p$. The combined collocation method discretisation of equation (4.1) may therefore be written in the form

$$\begin{aligned}(\mathcal{L}_{\boldsymbol{\sigma}}\rho)(s_i, p_\kappa) &= c^{-1}\sum_{j=1}^{n}\left[\int_{-\pi/2}^{\pi/2} \boldsymbol{\phi}^T(\theta') f_{\sigma_2}(p_\varepsilon(p_\kappa, \theta')) S_\mu(s_i, c^{-1}\sin(\theta'))\cos(\theta')\,d\theta'\right]\boldsymbol{\rho}_j \\ &= \mathbf{v}^T(s_i, p_\kappa)\boldsymbol{\rho}_j \end{aligned} \tag{4.12}$$

with $p_\varepsilon(p_\kappa, \theta') = p_\kappa - c^{-1}\sin(\theta')$ for all $i = 1, ..., n$ and $\kappa = 1, ..., N_p$. In compact matrix notation we may write

$$\Phi\boldsymbol{\rho}_i = V(s_i)\boldsymbol{\rho}_j, \qquad \forall\, i = 1, ..., n,$$

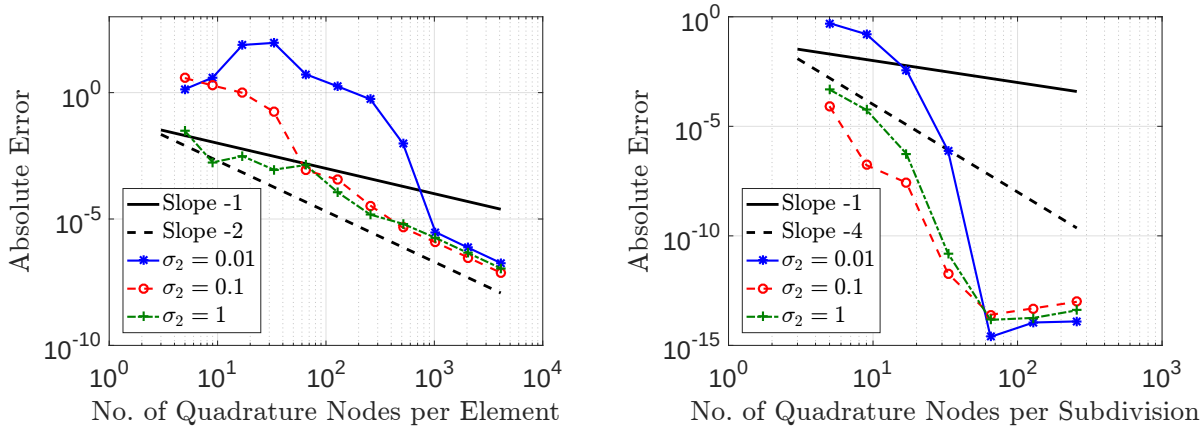

Figure 4.2: Convergence of the integral of the final stationary boundary density along the left hand edge at $x = 0$ for different values of σ_2. Left: using a direct approximation of the integrals over the momentum variable p. Right: using a subdivision strategy for the integral over the momentum variable p. Parameter values: $\sigma_1 = 0$, $c = 1$, $\mu = \pi$ and $n = 8$.

where Φ is a collocation/interpolation matrix with rows $\Phi_\kappa = \boldsymbol{\phi}^T(p_\kappa)$ and $V(s_i)$ is a matrix of integral values with rows given by $V(s_i)_\kappa = \mathbf{v}^T(s_i, p_\kappa)$.

Integrals over the direction angle θ' in (4.12) can be approximated numerically by any desirable quadrature method. Alternatively, special quadrature strategies may be considered for simulations with small σ_2 values due to the singular perturbation as $\sigma_2 \to 0$. In addition, notice that the total size of the transfer matrix compared to the Nyström method above has been changed from $n(K+1) \times n(K+1)$ to $nN_p \times nN_p$. In the next section we discuss and compare different implementation strategies of (4.10) and (4.12) leading to different convergence properties for smooth densities ρ.

4.4 Implementation strategies and convergence properties

In this section, we consider a rectangular domain $(x, y) \in (0, l) \times (0, 0.25)$ where $l = 0.75$, and apply uncertain boundary source term of the form

$$\rho_0(s, p) = \frac{\exp\left(-p^2/(2\sigma_2^2)\right)}{\sqrt{2\pi\sigma_2^2}\,\mathrm{erf}\left(1/(\sqrt{2}\sigma_2 c)\right)} \tag{4.13}$$

along the left hand edge at $x = 0$. A source term (4.13) arising from an uncertain boundary condition was originally proposed in [1]. For small σ_2, this corresponds to a unit boundary density propagating (on average) in the direction $p = 0$, perpendicular to the boundary. For large σ_2 it corresponds to randomly directed propagation from the boundary. Such a condition may be applied for all $s \in \Gamma$, or on a subset of Γ as in [1]. As $\sigma_2 \to 0$, this rectangular domain problem has an analytical ray tracing solution for the stationary interior density $\rho_\Omega(x)$ as detailed in Ref. [11].

In Fig. 4.2 we study the convergence of the integral

$$\mathrm{I} = \int_{-c^{-1}}^{c^{-1}} \rho_j(p)\,\mathrm{d}p = c^{-1} \int_{-\pi/2}^{\pi/2} \rho_j(\theta)\cos(\theta)\,\mathrm{d}\theta = c^{-1} \sum_{k=0}^{K} w_k \rho_j(\theta_k)\cos(\theta_k), \tag{4.14}$$

where $\rho_j(p)$ is the directionally dependent expansion function in (4.7), which we compute along the left hand edge at $x = 0$. The integral is approximated with the same quadrature rule used

in (4.10). We fix the boundary element mesh size taking $n = 8$ elements in total and take parameter values $c = 1$, $\mu = \pi$ and $\sigma_1 = 0$. Note that due to the nature of the exact solution, the spatial dependence of the solution along each edge of the rectangular domain is only slowly varying when σ_1 and σ_2 are relatively small and so a relatively coarse boundary element mesh suffices. The number of quadrature nodes is given by $K_m = 2^m + 1$, where $m = 1, ..., 12$ in the left plot of Fig. 4.2 and $m = 1, ..., 8$ in the right plot of Fig. 4.2. In both plots we plot the absolute error between the integral (4.14) values computed with K_m and K_{m+1} quadrature nodes. The plots show the absolute errors corresponding to the K_{m+1} node number values per element in the left plot and node number values per subdivision in the right plot, respectively.

Note that due to the polygonal nature of the domain and the discontinuous spatial collocation scheme, the direction dependent function S_μ is not continuous over the whole interval, but is at least piecewise smooth. In order to achieve spectral convergence for smooth density solutions in the discretisation schemes presented above, we must subdivide the momentum coordinate integral in (4.8). The left plot of Fig. 4.2 shows the convergence results for different values of σ_2 for a direct approximation of the integral over direction using the Nyström method (4.10) with Gaussian quadrature. This direct approximation of the directional integral leads to the loss of the spectral convergence, and one only obtains second order convergence for a sufficiently large number of quadrature nodes. The right plot shows the convergence results when subdividing the integral over direction and approximating each sub-integral separately via Gaussian quadrature. In this case we do indeed obtain spectral convergence. Equivalent results can also be obtained using the collocation method (4.12).

4.5 Conclusions

We have described a boundary integral model for uncertain high-frequency wave problems and detailed two discretisation schemes for the approximation of the wave energy density. We have discussed implementation strategies to preserve the spectral convergence properties of high order approximation schemes. However, the number of integration subdivisions grows with the number of spatial collocation points and this quadrature data must be saved or constantly recomputed. Furthermore, in the singularly perturbed case $\sigma_2 \to 0$, it would be beneficial to be able to adaptively refine the quadrature to resolve the increasingly sharp peak in the Gaussian PDF. Again, the implementation of such an adaptive scheme in the Nyström method would require a new set of fixed quadrature points for each element. These issues can be directly addressed by instead using a (spectral) collocation method in the momentum variable, which allows for a greater flexibility to tailor the quadrature scheme. Hence, the results presented here serve as motivation to further develop collocation methods for the discretisation in the momentum variable in future.

Acknowledgement

Support from the EPSRC (grant no. EP/M027201/1) and the EU (FP7-PEOPLE-2013-IAPP grant no. 612237 (MHiVec)) is gratefully acknowledged.

References

[1] D. J. Chappell and G. Tanner, *A boundary integral formalism for stochastic ray tracing in billiards*, Chaos, 24(4) (2014), 043147.

[2] J. T. Kayija, The rendering equation. In *Proceedings of SIGGRAPH 1986: 143*, DOI:10.1145/15922.15902.

[3] A. Le Bot, *Energy exchange in uncorrelated ray fields of vibroacoustics*, J. Acoust. Soc. Amer., 120(3) (2006), 1194–1208.

[4] S. Siltanen, T. Lokki, S. Kiminki and L. Savioja, *The room acoustic rendering equation*, J. Acoust. Soc. Amer., 122 (2007), 1624–1635.

[5] G. Tanner, *Dynamical energy analysis - Determining wave energy distributions in vibro-acoustical structures in the high-frequency regime*, J. Sound. Vib., 320 (2009), 1023–1038.

[6] G. Tanner, D. J. Chappell, D. Löchel and N. Søndergaard, *Discrete Flow Mapping: a mesh based simulation tool for mid-to-high frequency vibro-acoustic excitation of complex automotive structures*, SAE Int. J. Passeng. Cars - Mech. Syst., 7(3) (2014), 2014-01-2079.

[7] P. Cvitanović, C. Dettmann, R. Mainieri and G. Vattay, *Trace formulas for stochastic evolution operators: weak noise perturbation theory*, J. Stat. Phys., 93 (1998), 981–999.

[8] D. Lippolis and P. Cvitanović, *How well can one resolve the state space of a chaotic map?*, Phys. Rev. Lett., 104 (2010), 014101.

[9] A. Celani, M. Cencini, A. Mazzino and M. Vergassola, *Active and passive fields face to face*, New Journal of Physics, 6 (2004), 72.

[10] M. Sommer and S. Reich, *Phase-space volume conservation under space and time discretization schemes for the shallow-water equations*, Monthly Weather Review, 138 (2010), 4229–4236.

[11] J. Bajars, D. J. Chappell, N. Søndergaard and G. Tanner, *Transport of phase space densities through tetrahedral meshes using discrete flow mapping*, J. Comp. Phys., 328 (2017), 95–108.

[12] D. J. Chappell and G. Tanner, *Solving the stationary Liouville Equation via a boundary element method*, J. Comp. Phys., 234 (2013), 487–498.

Chapter 5

Algebraic preconditioners for the Fast Multipole Method: trends and problems

Bruno Carpentieri

Faculty of Computer Science,
Free University of Bozen-Bolzano,
Dominikanerplatz 3 - piazza Domenicani, 3
39100 Bozen-Bolzano
Italy

Abstract. *We discuss algebraic preconditioning strategies for solving electromagnetic scattering problems expresed in an integral formulation. The proposed preconditioners are based on multilevel incomplete factorization and approximate inverse methods. They are computed using only information contained in the coefficient matrix of the linear system, and can be applied to different operators and to changes in the geometry by tuning a few parameters.*

5.1 The problem

In the past few decades, thanks to the rapid advances in computer technology and the introduction of innovative algorithms with reduced computational and memory complexity, a rigorous numerical solution of the Maxwell's equations has become feasible for many practical applications. Integral equation methods can be an interesting alternative to differential equation methods for solving large electromagnetic (EM) scattering applications as they reduce a three-dimensional (3D) volume problem to a two-dimensional (2D) surface problem, simplifying considerably the mesh generation especially in the case of moving objects. In variational form, we can formulate the standard EM scattering problem as the following integral equation model:

Find the surface current $\vec{j}$ such that for all tangential test functions $\vec{j}^t$, we have

$$\int_\Gamma \int_\Gamma G(|y-x|) \left(\vec{j}(x) \cdot \vec{j}^t(y) - \frac{1}{k^2} \mathrm{div}_\Gamma \vec{j}(x) \cdot \mathrm{div}_\Gamma \vec{j}^t(y) \right) dxdy = \frac{i}{kZ_0} \int_\Gamma \vec{E}_{inc}(x) \cdot \vec{j}^t(x) dx. \quad (5.1)$$

Eqn. (5.1) is called the Electric Field Integral Equation (EFIE); we denote by $G(|y-x|) = \frac{e^{ik|y-x|}}{4\pi|y-x|}$ the Green's function, Γ is the boundary of the object, k is the wave number and $Z_0 = \sqrt{\mu_0/\varepsilon_0}$ the characteristic impedance of vacuum (ϵ is the electric permittivity and μ the

magnetic permeability). The EFIE formulation can be applied to arbitrary geometries including those with cavities, disconnected parts, breaks on the surface; hence, it is very popular in industrial modelling.

By using a Galerkin discretization over a mesh containing n edges, the surface current $\vec{j}$ is expanded into the set of so-called Rao-Wilton-Glisson basis functions $\{\vec{\varphi}_i\}_{1\leq i\leq n}$ [12], then Eqn. (5.1) is applied to each basis function $\vec{\varphi}_i$. Finally, we are led to solving the following linear system

$$\sum_{1\leq i\leq n} \lambda_i \left[\int_\Gamma \int_\Gamma G\left(|y-x|\right) \left(\vec{\varphi}_i(x)\cdot\vec{\varphi}_j(x) - \frac{1}{k^2} div_\Gamma \vec{\varphi}_i(x) \cdot div_\Gamma \vec{\varphi}_j(y) \right) dxdy \right] = \\ = \frac{i}{kZ_0} \int_\Gamma \vec{E}_{inc}(x)\cdot\vec{\varphi}_j(x)dx, \quad (5.2)$$

in the unknowns λ_i for $1 \leq i \leq n$, each λ_i being associated with the vectorial flux across an edge in the mesh. The set of equations (5.2) can be recast in matrix form as

$$A\lambda = b, \quad (5.3)$$

where $A = [A_{ij}]$ and $b = [b_i]$ have elements

$$\begin{aligned} A_{ij} &= \int_\Gamma \int_\Gamma G\left(|y-x|\right) \left(\vec{\varphi}_i(x)\cdot\vec{\varphi}_j(y) - \frac{1}{k^2} div_\Gamma \vec{\varphi}_i(x) \cdot div_\Gamma \vec{\varphi}_j(y) \right) dxdy, \\ b_j &= \frac{i}{kZ_0} \int_\Gamma \vec{E}_{inc}(x)\cdot\vec{\varphi}_j(y)dx. \end{aligned}$$

Note that the coefficient matrix A is dense complex symmetric, and the right-hand side varies with the frequency and the direction of the illuminating wave.

Linear systems arising from boundary element discretizations can be extremely large in applications as the number of unknowns grows linearly with the size of the scatterer and quadratically with the frequency of the incoming radiation. The scattering of a plane wave by a perfectly electrically conducting (PEC) sphere with a diameter of 1800λ would give rise to a matrix with more than three billion unknowns [11]. Clearly, direct methods based on both in-core and out-of-core variants of Gaussian elimination are not affordable to solve problems of this size even on modern parallel computers, due to the large memory requirements. Iterative Krylov methods can solve the problems of space of direct methods as they are based on matrix-vector (M-V) multiplications. By combining Krylov subspace solvers with the Multilevel Fast Multipole Algorithm (MLFMA) [10], it is possible to solve an $n \times n$ matrix problem in $\alpha \cdot N_{iter} \cdot \mathcal{O}(n \log n)$ arithmetic operations, where the constant α depends on the implementation of the specific iterative algorithm and N_{iter} is the number of iterations required to achieve a certain accuracy.

Briefly, multipole techniques exploit the rapid decay of the Green's function by computing interactions of degrees of freedom in the mesh at different levels of accuracy depending on their physical distance. Upon partitioning the 3D mesh of the object into boxes of roughly equal size recursively, until their size is a fraction of the wavelength, multipole coefficients are computed for all boxes starting from the smallest ones and then recursively for each parent cube by summing together multipole coefficients of the children. Interactions of degrees of freedom within an observation box and its nearby boxes are computed exactly by using the Method of Moments; interactions between boxes that are not neighbours each other but whose parents are neighbours are computed by using the FMM algorithm. All other interactions are approximated depending on their mutual distance in the mesh.

In the last twenty years, significant research efforts have been devoted to implement multiple techniques efficiently on distributed memory parallel computers to speedup M-V multiplications

involving dense boundary element matrices from $\mathcal{O}(n^2)$ down to $\mathcal{O}(n \log n)$ complexity, resulting in competitive application codes provably scalable to several million discretization points [14, 15, 9, 11]. In this paper we address the other critical component of the iterative solution in this context, that is the design of effective preconditioners to accelerate the convergence of MLFMA.

5.2 Preconditioning the FMM

The convergence of Krylov methods can be accelerated by transforming the original linear system into an equivalent one having better spectral properties, i.e. with most of the eigenvalues clustered close to one. This pre-processing stage is called *preconditioning*. The transformed system has typically the form $M^{-1}Ax = M^{-1}b$, or $AM^{-1}y = b$ with $x = M^{-1}y$, depending if one preconditions from the left or from the right; the matrix M is called *the preconditioner*. Preconditioning is critical for the EFIE as the iteration number tends to grow as $\mathcal{O}(n^{0.5})$ when n is related to the wavenumber [14]. Although some optimal operator-dependent preconditioners have been proposed for the EFIE, see e.g. [7, 2], they often lack the necessary robustness and are not simple to parallelize. In this paper, the preconditioner is computed by using only information contained in the coefficient matrix of the linear system. Far from optimal for any specific problem, fully algebraic matrix solvers can be applied successfully to different operators and geometries only by tuning a few parameters. They can maintain the $\mathcal{O}(n \log n)$ complexity of MLFMA and may integrate easily with the data structure of multipole codes.

Most algebraic preconditioning techniques for dense matrices proposed in the literature are computed by decomposing the linear system in the form

$$(S + B)x = b, \tag{5.4}$$

where S is a sparse matrix retaining the most relevant contributions to the singular integrals and is easy to invert or factorize, while B can be dense. For boundary integral equations of Fredholm type, if the continuous operator $\mathcal{S}$ underlying S is bounded and the operator $\mathcal{B}$ underlying B is compact, then $\mathcal{S}^{-1}\mathcal{B}$ is compact and

$$\mathcal{S}^{-1}(\mathcal{S} + \mathcal{B}) = \mathcal{I} + \mathcal{S}^{-1}\mathcal{B}$$

so that we may expect that the preconditioned system $\left(I + S^{-1}B\right)x = S^{-1}b$ has a good clusterization of eigenvalues close to one, see e.g. [6, pp. 182-185]. Multipole algorithms yield a matrix decomposition of the form

$$A = A_{diag} + A_{near} + A_{far}, \tag{5.5}$$

where A_{diag} is the block diagonal part of A associated with interactions of basis functions belonging to the same box, A_{near} is the block near-diagonal part of A associated with interactions within one level of neighbouring boxes (they are 8 in 2D and 26 in 3D), and A_{far} is the far-field part of A. In a multipole setting, an appropriate choice for the local matrix can be $S = A_{diag} + A_{near}$. Two approaches to precondition matrix S are considered in the next two sections.

5.2.1 Sparse approximate inverse preconditioners

Boundary element discretizations introduce a strong local coupling between the edges in the underlying mesh. Each edge is strongly connected to only a few neighbours. Far-away connections, although not null, are much weaker suggesting that a very sparse matrix can still retain most of the relevant contributions to the singular integrals. We can see in Figure 5.2 that the inverse of A exhibits a very similar structure to A and a good pattern for the approximate inverse is likely to be the nonzero pattern of a sparse approximation to A, computed by dropping

all the entries lower than a prescribed global threshold. In a multipole context, the pattern can be computed in advance from the nonzero structure of the near-field multipole matrix S. The actual entries of M may be obtained by minimizing the error matrix $\|I - SM\|_F$ for right preconditioning ($\|I-MS\|_F$ resp. left preconditioning). The Frobenius-norm allows to decouple the constrained minimization problem into n independent linear least-squares problems, one for each column (resp. row) of M when preconditioning from the right (resp. from the left). Hence the construction is inherently parallel. The independence of the least-squares problems follows from the identity

$$\|I - SM\|_F^2 = \sum_{j=1}^{n} \|e_j - Sm_{\bullet j}\|_2^2, \tag{5.6}$$

where e_j is the jth canonical unit vector and $m_{\bullet j}$ is the column vector representing the jth column of M. In the case of right preconditioning, the analogous relation

$$\|I - MS\|_F^2 = \|I - S^T M^T\|_F^2 = \sum_{j=1}^{n} \|e_j - S^T m_{j\bullet}\|_2^2 \tag{5.7}$$

holds, where $m_{j\bullet}$ is the column vector representing the jth row of M. Usually problems (5.6-5.7) can be efficiently solved by a dense QR factorization. The columns of M associated to the edges within the same box have the same structure; therefore their entries can be computed simultaneously by carrying out only one block dense QR factorization, and the overall setup cost is reduced to $\mathcal{O}(n)$ arithmetic operations [5]. We refer to this preconditioner as SPAI (SParse Approximate Inverse).

In Table 5.1 we illustrate the numerical behavior of the Frobenius-norm minimization method combined with parallel MLFMA for solving realistic RCS calculations in industry. The geometries are presented in Figure 5.1. The value of the frequency is in the range between 12 and 42 GHz for the Cetaf problem (i.e. $24 - 84\lambda$ of physical size) and between 2.3 and 11.4 GHz for the aircraft problem ($14 - 73\lambda$). The experiments are run in single precision complex arithmetic on eight processors of a Compaq Alpha server which is a cluster of Symmetric Multi-Processors. In Table 5.1 we report on the number of M-V products and solution time for GMRES; "d" means day, "h" hour and "m" minute. The tolerance for GMRES is fixed equal to 10^{-3} on the normwise backward error $\frac{||r||}{||b||}$, where r denotes the residual and b is the right-hand side of the linear system. This order of accuracy matches the relative error of the M-V product operation in our multipole code, and is accurate enough to enable the correct reconstruction of the RCS of the object. The SPAI preconditioner enables us to solve fairly large problems but it does not scale very well with the number of unknowns. The increase in the iteration count is less significant for GMRES(∞), even though convergence cannot be obtained on the largest systems because we either exceed the memory limits or the time limit allocated to a single run. On the Cetaf geometry, the solution time for the GMRES method increases superlinearly for small and medium problems, but nearly quadratically for large problems. On the largest test case, discretized with one million unknowns, unrestarted GMRES does not converge after 750 iterations requiring more than nine hours of computation on 32 processors. The Airbus aircraft is very difficult to solve because the mesh has many surface details and the discretization matrices become ill-conditioned. On small and medium problems, the number of GMRES iterations increases with the problem size, and the solution time increases superlinearly. On the largest test case, discretized with one million unknowns, full GMRES exceeds the memory limit on 64 processors. In this case, the use of large restarts (120 in this table) does not enable convergence within 2000 iterations except on a small mesh of size 94704. In Table 5.2 we observe the very good parallel scalability of the construction and of the application of the approximate inverse, that makes it a very suitable candidate for massively parallel implementation. Problems of increasing size are solved on a larger number of processors, while keeping constant the number of unknowns per processor.

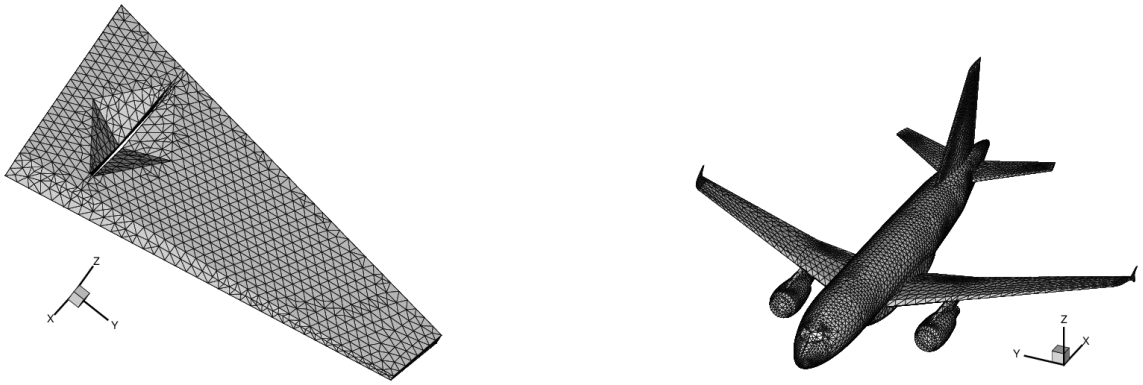

(a) (b)

Figure 5.1: Geometries considered for the numerical experiments, courtesy of EADS-CCR Toulouse. (a) The Cetaf problem. The geometry represents a wing with a slit. The physical size is 50 cm × 30 cm × 5 cm. (b) The aircraft problem. The physical size is 1.8 m × 1.9 m × 0.65 m.

Cetaf				
Size	Density SPAI	Time SPAI	GMRES(∞)	GMRES(120)
			Iter / Time	Iter / Time
86256	0.18	4m	656 / 1h 25m	1546 / 1h 44m
134775	0.11	6m	618 / 1h 45m	1125 / 1h 55m
264156	0.06	13m	710 / 9h	1373 / 4h 46m
531900	0.03	20m	844 / 1d 18m	1717 / 14h 8m
1056636	0.01	37m	T.L.E. / >9h$^{(32)}$	- / > 1d
Aircraft				
Size	Density SPAI	Time SPAI	GMRES(∞)	GMRES(120)
			Iter / Time	Iter / Time
94704	0.28	11m	746 / 2h 9m	1956 / 3h 13m
213084	0.13	31m	973 / 7h 19m	- / 7h 56m
591900	0.09	1h 30m	1461 / 16h 42m$^{(64)}$	- / 1d 57m
1160124	0.02	3h 24m	M.L.E.$^{(64)}$ / N.A.	- / > 4d

Table 5.1: Number of matrix-vector products and elapsed time required to converge on two problems on 8 processors of the Compaq machine, except those marked with $^{(k)}$, that were run on k processors. Tolerance for the iterative solution was 10^{-3}. The symbol '-' means that no convergence was achieved in 2000 iterations. Acronyms: N.A. ≡ not available. M.L.E. ≡ memory limits exceeded, T.L.E. ≡ CPU time limits exceeded.

5.2.2 Inverse-based multilevel ILU factorization preconditioner

A different preconditioning approach would factorize S instead of explicitly inverting it. In this section we use a symmetric inverse-based multilevel preconditioner based on an incomplete LDL^T factorization to precondition system (5.1). We first rescale $A = S$ by a symmetric maximum weight matching [8] such that $\widetilde{A} = DAD$ has entries $|\widetilde{a}_{ij}| \leq 1$ whilst $|\widetilde{a}_{i,\pi_i}| = |\widetilde{a}_{\pi_i,i}| = 1$ for a suitable permutation π. Afterwards, we construct a permutation matrix P_0 such that the entries $\widetilde{a}_{i,\pi_i}$, $\widetilde{a}_{\pi_i,i}$ are at least located in the tridiagonal part of $P_0^T\ DAD\ P_0$ having many 2×2 blocks

$$\begin{pmatrix} a_{i,i} & a_{i,i+1} \\ a_{i+1,i} & a_{i+1,i+1} \end{pmatrix}$$

Parallel scalability results				
Problem size	Nb procs	Construction time (sec)	Elapsed time precond (sec)	Elapsed time mat-vec (sec)
112908	8	513	0.39	1.77
221952	16	497	0.43	2.15
342732	24	523	0.47	3.10
451632	32	509	0.48	2.80
900912	64	514	0.60	3.80

Table 5.2: Parallel scalability of the implementation on the aircraft problem.

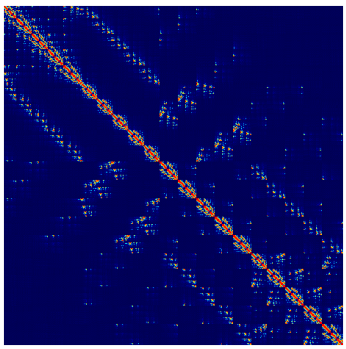

(a) Pattern of the large entries of A

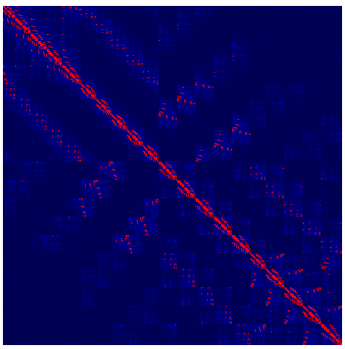

(b) Pattern of the large entries of A^{-1}

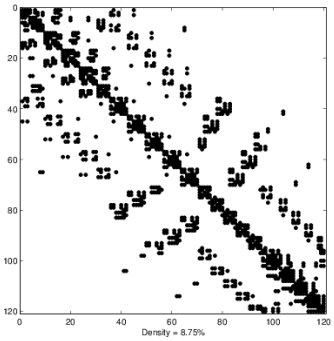

(c) Sparsity pattern of *sparsified*(A^{-1})

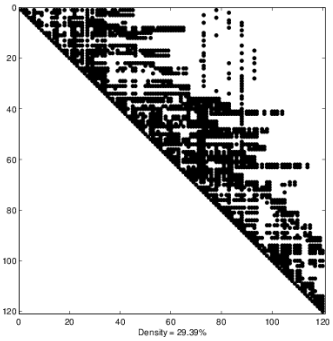

(d) Sparsity pattern of *sparsified*(L^{-1})

Figure 5.2: Typical decay of the discrete Green's function for surface integral equations. The test problem is a small sphere. Large to small magnitude entries are depicted in different colours, from red to green, yellow and blue. We used a threshold 5.0×10^{-2} to drop the smallest entries of a A^{-1} and of L^{-1} in relative magnitude.

such that $|a_{i,i+1}|=|a_{i+1,i}| = 1$, 1×1 blocks $a_{i,i}$ such that $|a_{i,i}| = 1$, while in exceptional cases also 1×1 blocks with $a_{i,i} = 0$ may occur. This preprocessing step can improve the diagonal dominance significantly. Then a symmetric reordering is applied to reduce the fill-in bandwidth. The symmetric reordering is applied to the compressed graph of $P_0^T DADP_0$, i.e., block rows and block columns associated with a 2×2 block are replaced by a single row and column having the union of the block column/row pattern as nonzero pattern. This leads to a block-structure-preserving permutation P_1 and the total reordered system is $P^T DADP$, where $P = P_0 P_1$. We point out that these scalings and reorderings maintain the symmetry of A. Next, an inverse-based ILU with static block diagonal pivoting is computed where the block diagonal pivots are

either 1×1 or 2×2 pivots depending on which of the two choices yields more block diagonal dominance. More precisely, during the approximate incomplete factorization $\hat{A} \approx LDL^T$ such that L is unit lower triangular and D is block diagonal, the norm $\|L^{-1}\|$ is estimated and if at factorization step l a prescribed bound is exceeded, the current row l and column l are permuted to the lower right end of the matrix. Otherwise the approximate factorization is continued. One single pass leads to an approximate partial factorization

$$\Pi^T \hat{A} \Pi = \begin{pmatrix} B & E^T \\ E & C \end{pmatrix} \approx \begin{pmatrix} L_B & 0 \\ L_E & I \end{pmatrix} \begin{pmatrix} D_B & 0 \\ 0 & S_C \end{pmatrix} \begin{pmatrix} L_B^T & L_E^T \\ 0 & I \end{pmatrix} \equiv L_1 D_1 L_1^T, \tag{5.8}$$

with a suitable leading block B and a suitable permutation matrix, where $\|L^{-1}\| \leq \kappa$. The remaining system S_C approximates $C - EB^{-1}E^T$ and from the relations

$$\left\{ \begin{array}{rcl} B\hat{x}_1 + E^T\hat{x}_2 & = & \hat{b}_1 \\ E\hat{x}_1 + C\hat{x}_2 & = & \hat{b}_2 \end{array} \right. \Rightarrow \left\{ \begin{array}{rcl} \hat{x}_1 & = & B^{-1}(\hat{b}_1 - E^T\hat{x}_2) \\ (C - EB^{-1}E^T)\hat{x}_2 & = & \hat{b}_2 - EB^{-1}\hat{b}_1 \end{array} \right. ,$$

at each step of an iterative solver we need to store and invert only blocks with B and $S_C \approx C - EB^{-1}E^T$ while for reasons of memory efficiency, L_E is discarded and implicitly represented via $L_E \approx EU_B^{-1}D_B^{-1}$. When the scaling, preordering and the factorization is successively applied to S_C, a multilevel variant of (5.8) is computed. The multilevel algorithm ends at some step m when either S_C is factored completely or it becomes considerably dense and switches to a dense LAPACK solver. Intermediate Schur complements S_C are discarded as soon as the Schur complement matrix S_{22} of the next level is computed. After computing an m-step ILU decomposition, for preconditioning we have to apply $L_m^{-1}AL_m^{-T}$. From the error equation $E_m = A - L_m D_m L_m^T$, we see that $\|L_m^{-1}\|$ contributes to the inverse error $L_m^{-1}E_m L_m^{-T}$. Monitoring the growth of this quantity during the partial factorization is essential to preserve the numerical stability of the solver. Furthermore, at least for real symmetric matrices, eigenvalue inclusion bounds for the eigenvalues near the origin of S_C and A can be shown [3].

Some preliminary experiments on selected linear systems arising from RCS calculation of realistic targets modelled using the EFIE formulation (5.1) are presented in Table 5.3. Although the problems are not very large in absolute sense, their solution demanded considerable resources. For example, storing the coefficient matrix for the Airbus A318 problem required 18 Gb of RAM. The solution of larger problems would clearly necessitate to use MLFMA for the M-V products and a parallel implementation of the multilevel ILU algorithm, which is still under development. In our experiments we used the LAPACK library [1] to carry out the dense M-V products. Convergence was achieved if the initial residual was reduced by 12 orders of magnitude within 3000 iterations. All the runs were carried out on one node of the Millipede cluster facility located at the University of Groningen. Each node features 12 Opteron 2.6 GHz cores and 24 GB of physical RAM.

The factorization was computed from a sparse approximation S to the dense matrix A, extracted by selecting the p largest entries in each row of A. We chose a value of p giving a number of nonzeros in S approximately equal to the expected density of the multipole operator for the same problem. We used four level of recursive factorization, prescribing bounds $\|L_1^{-1}\| \leq 100$, $\|U_1^{-1}\| \leq 100$ for the inverse factors, and set the threshold parameter $t = 1.e-2$ for dropping the small entries in the triangular factors. However, on the tough aircraft problem, we had to use $t = 1.e-3$ to achieve convergence. The results of Table 5.3 show that the proposed preconditioner can be very effective to reduce the number of Krylov iterations. The results on the Airbus aircraft is remarkable: the solver converged in less than one hundred iterations and the computation of a moderately sparse factorization took around ten minutes on one core. We were not able to achieve a comparable result with any other algebraic preconditioner that we tested [4].

Sphere - density(S) = 0.65% - 535 MHz - $\kappa_1(A) = \mathcal{O}(1)$				
prec	mem	time	GMRES(50)	
			its	time
none	-	-	+3000	+4891.44
MILUT($1e-2$)	5.2	64.12	274	461.49
Airbus A318 - density(S) = 2.73% - 800 MHz - $\kappa_1(A) = \mathcal{O}(10^7)$				
prec	mem	time	GMRES(50)	
			its	time
none	-	-	+3000	+15278.08
MILUT($1e-3$)	6.8	753.50	98	906.59

Table 5.3: Experiments with inverse-based multilevel ILU preconditioner

5.3 MLFMA as a preconditioner

In the experiments reported in Table 5.1, the solution time for GMRES increases nearly quadratically with the frequency of the problem. At high frequency the preconditioner is very sparse if the size of the smallest boxes arising from the object partitioning is related to the wavelength, as in our code. When S is very sparse, each degree of freedom is coupled to a very few neighbours. In this case, the far-field information may be totally lost. FMM approximations of an integral operator compute the near-field interactions exactly and they approximate the far-field by low-rank matrices. It is natural to incorporate these far-field approximations in the preconditioner to improve its robustness. We implement the preconditioning operation by carrying out a few steps of an inner Krylov method with a low accuracy multipole matrix. The outer iterative solver must allow to use variable preconditioning [5], for instance FGMRES [13] may be used. Iterations are stopped after a fixed number of steps. A sketch of the overall iterative algorithm is presented in Figure 5.3. Note that the matrix-vector products in the inner and outer solvers are carried out using MLFMA with different levels of accuracy. Highly accurate MLFMA is applied in the outer iterations which govern the final accuracy; less accurate MLFMA is applied in the inner iterations that only attempt to give a rough approximation of the solution. Different accuracy for the M-V calculation can be implemented by tuning various parameters in MLFMA such as the size of the smallest box, the number of multipole levels and of integration points. Note also that we precondition the inner solver (by SPAI) to decrease rapidly the residual within a few number of steps.

Outer solver $\longrightarrow$ FGMRES, GMRES$\star$
Do k $= 1, 2, \ldots$
- Matrix-vector product: FMM with high accuracy
- Preconditioning: **Inner solver** (GMRES, TFQMR, $\ldots$)

  Do i $= 1, 2, \ldots, MAX\_INNER\_ITER$
  - Matrix-vector product: FMM with low accuracy
  - Preconditioning: $SPAI$

  End Do

End Do

Figure 5.3: Inner-outer solution schemes in the FMM context. Sketch of the algorithm. Iterations are stopped after a fixed number of step (denoted by MAX_INNER_ITER).

Cetaf								
Size	GMRES(∞)		FGMRES(∞,60)		GMRES(120)		FGMRES(30,60)	
	Iter	Time	Iter	Time	Iter	Time	Iter	Time
86256	656	1h 25m	17+ 960	55m	1546	1h 44m	17+ 960	55m
134775	618	1h 45m	15+ 840	1h 19m	1125	1h 55m	15+ 840	1h 19m
264156	710	9h	17+ 960	2h 22m	1373	4h 46m	17+ 960	2h 22m
531900	844	1d 18m	19+1080	6h	1717	14h 8m	19+1080	6h
1056636	T.L.E.	$> 9h^{(32)}$	22+1260	14h	-	$>$ 1d	22+1260	14h
Aircraft								
Size	GMRES(∞)		FGMRES(∞,60)		GMRES(120)		FGMRES(30,60)	
	Iter	Time	Iter	Time	Iter	Time	Iter	Time
94704	746	2h 9m	23+1320	2h 30m	1956	3h 13m	27+1560	2h 14m
213084	973	7h 19m	30+1740	6h 11m	-	7h 56m	34+1920	5h
591900	1461	16h 42m$^{(64)}$	43+2520	12h$^{(32)}$	-	1d 57m	57+3300	1d 9h 45m
1160124	M.L.E.$^{(64)}$	$>$ 1d	43+2520	14 h 28m$^{(64)}$	-	$>$ 4d	51+2940	16h 41m$^{(64)}$

Table 5.4: Number of matrix-vector products and elapsed time required to converge on eight processors of the Compaq machine, except those marked with $^{(k)}$, that were run on k processors. The values of m and n in the symbol FGMRES(m,n) refer to the restart of the outer and of the inner solver, respectively. For FGMRES we give the number of inner plus total outer iterations needed to achieve convergence. The tolerance for the iterative solution was 10^{-3}. Acronyms: M.L.E. $\equiv$ memory limits exceeded, T.L.E. $\equiv$ CPU time limits exceeded.

We report some results to show the added value of scalability of the two-level scheme in Tables 5.4. On the geometries considered in the Section 5.2.1, we apply FGMRES as the outer solver and a SPAI-preconditioned GMRES for the inner iteration. We show the number of inner and total outer M-V products and the elapsed time needed to achieve convergence using a tolerance of 10^{-3} on eight processors of the Compaq machine. The comparison with the results reported in Table 5.1 is fair as GMRES has exactly the same storage requirements as the combination FGMRES/GMRES. For the same restart value, the storage requirement for the FGMRES algorithm is twice as large as for standard GMRES because it requires also to store the preconditioned vectors of the Krylov basis. We observe that the increase in the number of outer iterations is fairly modest. The scheme enables to solve the largest and difficult aircraft test cases whereas GMRES failes. On the aircraft problem discretized with 213084 unknowns, FGMRES is about 2 hours faster than standard GMRES; up to 973 basis vectors are to orthogonalize while in the inner-outer scheme only a basis up to 60, leading to a significant saving in the orthogonalization procedure that is extremely time consuming. Similarly, on the Cetaf discretized with one million points FGMRES(30,60) converges in 22 outer iterations whereas GMRES(120) does not converge in 2000 iterations. The savings in time is also noticeable, with a gain ranging from two to four depending on the geometry.

We recently solved a large rectangular ($30\lambda \times 30\lambda \times 300\lambda$) cavity problem with 12,697,120 unknowns by FGMRES(5,15,30) in 58 minutes and 2 outermost steps. The setup of SPAI costed 30 minutes on 36 processors, with 96GB memory in total. On 120 cores we solved a Cobra geometry with 21,682,980 unknowns in 38 minutes and a tank with 10,768,581 unknowns FGMRES in 12 minutes.

5.4 Conclusions

Large-scale scattering simulations demand scalable preconditioners combined with fast solvers like MLFMA to make boundary element techniques attractive to use in realistic applications.

We have presented solution approaches based on sparse approximate inverses and multilevel incomplete factorization methods. Thanks to the use of iterative methods and suitable preconditioners, fast integral solvers involving tens of million unknowns are nowadays feasible and can be integrated in the design processes where the bottleneck moves from the simulation to the pre- and postprocessing of the results, as the tools are not yet available to easily manipulate meshes with several millions of degrees of freedom. Further investigation is necessary to identify the best class of method for the given problem and the selected computer hardware.

References

[1] E. Anderson, Z. Bai, C. Bischof, S. Blackford, J. Demmel, J. J. Dongarra, J. D. Croz, A. Greenbaum, S. Hammarling, A. McKenney, and D. Sorensen, *LAPACK Users' Guide*. Society for Industrial and Applied Mathematics, Philadelphia, PA, third edition, 1999.

[2] F.P. Andriulli, K. Cools, F. Olyslager, A. Buffa, S. Christiansen, and E. Michielssen, A multiplicative caldern preconditioner for the electric field integral equation. 56(8) (2008), 2398–2412.

[3] M. Bollhöfer, M. J. Grote, and O. Schenk, Algebraic Multilevel Preconditioner for the Helmholtz Equation in Heterogeneous Media. *SIAM J. Scientific Computing*, 31(5) (2009), 3781–3805.

[4] B. Carpentieri and M. Bollhöfer, Symmetric inverse-based multilevel ILU preconditioning for solving dense complex non-hermitian systems in electromagnetics. *Progress In Electromagnetics Research*, 128 (2012), 55–74.

[5] B. Carpentieri, I.S. Duff, L. Giraud, and G. Sylvand, Combining fast multipole techniques and an approximate inverse preconditioner for large electromagnetism calculations. *SIAM J. Scientific Computing*, 27(3) (2005), 774–792.

[6] K. Chen, *Matrix Preconditioning Techniques and Applications*. Cambridge University Press, 2005.

[7] S. H. Christiansen and J.-C. Nédélec, A preconditioner for the electric field integral equation based on Calderon formulas. *SIAM J. Numer. Anal.*, 40(3) (2001), 1100–1135.

[8] I. S. Duff and S. Pralet, Strategies for scaling and pivoting for sparse symmetric indefinite problems. *SIAM J. Matrix Analysis and Applications*, 27(2) (2005), 313–340.

[9] Ö. Ergül and L. Gürel, Efficient parallelization of the multilevel fast multipole algorithm for the solution of large-scale scattering problems. *IEEE Transactions on Antennas and Propagation*, 56(8) (2008), 2335–2345.

[10] L. Greengard and V. Rokhlin, A fast algorithm for particle simulations. *Journal of Computational Physics*, 73 (1987), 325–348.

[11] B. Michiels, J. Fostier, I. Bogaert, and D. De Zutter, Full-wave simulations of electromagnetic scattering problems with billions of unknowns. *IEEE Trans. Antennas Propagat.*, 63(2) (2015), 796–799.

[12] S. M. Rao, D. R. Wilton, and A. W. Glisson, Electromagnetic scattering by surfaces of arbitrary shape. *IEEE Trans. Antennas Propagat.*, AP-30 (1982), 409–418.

[13] Y. Saad, A flexible inner-outer preconditioned GMRES algorithm. *SIAM J. Scientific and Statistical Computing*, 14 (1993), 461–469.

[14] J. M. Song and W. C. Chew, The Fast Illinois Solver Code: Requirements and scaling properties. *IEEE Computational Science and Engineering*, 5(3) (1998), 19–23.

[15] G. Sylvand, Complex industrial computations in electromagnetism using the fast multipole method. In G.C. Cohen, E. Heikkola, P. Joly, and P. Neittaanmdki, editors, *Mathematical and Numerical Aspects of Wave Propagation*, pages 657–662, Springer, 2003.

Chapter 6

Solving the inverse three-dimensional continuous model of electrical resistance tomography using the method of fundamental solutions and the Markov chain Monte Carlo approach

Taysir E. Dyhoum[1,2], **Robert G. Aykroyd**[2] **and Daniel Lesnic**[1]

[1] Department of Applied Mathematics,
University of Leeds
Leeds, LS2 9JT, UK

[2] Department of Statistics,
University of Leeds
Leeds, LS2 9JT, UK

Abstract. *This paper discusses the three-dimensional continuous model of electrical resistance tomography for detecting rigid inclusions embedded in a bounded background medium. The mathematical model is governed by Laplace's equation subject to a homogeneous Dirichlet boundary condition on the unknown rigid inclusion and Cauchy data on the outer boundary. The forward solver uses the meshless method of fundamental solutions, which is a discrete variant of the single layer potential in the direct form of the boundary element method for harmonic functions, but with source points shifted outside the solution domain such that singularities in the fundamental solution are avoided. The inverse solution is based on the Bayesian approach and Markov chain Monte Carlo (MCMC) estimation technique. The MCMC is used not only for estimating the desirable model parameters, but also for uncertainty and reliability assessment. Numerical examples are investigated to demonstrate the effectiveness and the accuracy of the proposed approach.*

6.1 Introduction

The paper extends the previous two-dimensional computations of direct and inverse problems [1] to three dimensions. As a remarkable step towards solving the direct and the inverse complete-electrode model of ERT in three-dimensions, we will consider first the continuous model.

Prior to this study, three-dimensional rigid inclusions have been reconstructed in [2, 6, 7] by standard regularization schemes, where the method of fundamental solutions (MFS) was used to produce the direct solution and a constrained optimization procedure was employed to determine the boundary of a three-dimensional star-shaped rigid inclusion. In this paper, we use the Bayesian statistical approach, instead of the gradient-based minimization of [2].

6.2 Main problems

We consider Laplace's equation

$$\triangle u = 0 \qquad \text{in } \Omega, \tag{6.1}$$

in various geometries $\Omega \subset \mathbb{R}^3$.
Problem 1: We consider an annular domain $\Omega = \Omega_{Outer} \backslash \overline{\Omega}_{Inner}$ with a rigid inclusion

(a)

$$\Omega_{Inner} = \left\{(x, y, z) \in \mathbb{R}^3 |\ x^2 + y^2 + z^2 < (0.5)^2\right\} \quad \text{(a sphere)} \tag{6.2}$$

or

(b)

$$\Omega_{Inner} = \left\{ (x, y, z) \in \mathbb{R}^3 \,\middle|\, \frac{x^2}{(0.5)^2} + \frac{y^2}{(0.5)^2} + \frac{z^2}{(0.4)^2} < 1 \right\} \quad \text{(an ellipsoid)} \tag{6.3}$$

inside the unit sphere $\Omega_{Outer} = \left\{(x, y, z) \in \mathbb{R}^3 | x^2 + y^2 + z^2 < 1\right\}$. Equation (6.1) is solved subject to the Dirichlet boundary conditions

$$u = f \qquad \text{on } \partial\Omega_{Outer} \tag{6.4}$$

and

$$u = 0 \qquad \text{on } \partial\Omega_{Inner}. \tag{6.5}$$

On the other hand, in the inverse formulation, since the concern is not only to find the potential u but also to reconstruct the rigid inclusion Ω_{Inner}, the following Neumann current flux measurement is required to compensate for the unknown geometry:

$$\frac{\partial u}{\partial n} = g \qquad \text{on } \partial\Omega_{Outer}. \tag{6.6}$$

As a result, the inverse problem of the continuous model of ERT is given by equations (6.1) and (6.4)-(6.6). Uniqueness of this problem when $f \not\equiv 0$ and Ω is connected is provided in [5].

Problem 2: We consider the domain $\Omega = \Omega_{Outer} \backslash (\overline{\Omega}_{Inner1} \cup \overline{\Omega}_{Inner1})$ with two disjoint rigid inclusions, which need to be detected when the inverse problem is solved, given by

$$\begin{aligned} \Omega_{Inner1} &= \left\{(x, y, z) \in \mathbb{R}^3 |\ x^2 + (y - 0.5)^2 + z^2 < (0.4)^2\right\}, \\ \Omega_{Inner2} &= \left\{(x, y, z) \in \mathbb{R}^3 |\ x^2 + (y + 0.5)^2 + z^2 < (0.4)^2\right\}. \end{aligned} \tag{6.7}$$

These are located inside the unit sphere. Then, (6.1) is solved subject to (6.4), (6.6) and

$$u = 0 \qquad \text{on } \partial\Omega_{Inner1} \cup \partial\Omega_{Inner2}. \tag{6.8}$$

6.3 The MFS for the direct problem

6.3.1 Mathematical formulation

The MFS seeks an approximation to the solution of (6.1) in a bounded domain with a rigid inclusion inside, as in (a) or (b), as a linear combination of fundamental solutions in the form

$$u(\underline{p}) = \sum_{k=1}^{2(N-1)} \sum_{l=1}^{N} c_{k,l} G(\underline{\xi}_{k,l}, \underline{p}), \quad \underline{p} \in \overline{\Omega}, \tag{6.9}$$

where $\underline{\xi}_{k,l}$ are source points located outside $\overline{\Omega}$ and G is the fundamental solution of the three-dimensional Laplace equation given by

$$G(\underline{\xi}, \underline{p}) = \frac{1}{4\pi|\underline{\xi} - \underline{p}|}. \tag{6.10}$$

The expression (6.9) results from the discretisation of a single-layer boundary integral representation of the harmonic function u with sources located outside the surface $\partial\Omega$.

The internal source points are located inside the inner domain Ω_{Inner}, and are defined, for Problem $1(a)$, by

$$\underline{\xi}_{k,l} = 0.5\ \eta_I \left(\sin\tilde{\theta}_k \cos\tilde{\phi}_l, \sin\tilde{\theta}_k \sin\tilde{\phi}_l, \cos\tilde{\theta}_k\right), \quad k = \overline{1,(N-1)}, \quad l = \overline{1,N}, \tag{6.11}$$

where $0 < \eta_I < 1$ (η_I is a contraction parameter), and, for Problem $1(b)$, by

$$\underline{\xi}_{k,l} = \eta_I \left(0.5\sin\tilde{\theta}_k \cos\tilde{\phi}_l, 0.5\sin\tilde{\theta}_k \sin\tilde{\phi}_l, 0.4\cos\tilde{\theta}_k\right), \quad k = \overline{1,(N-1)}, \quad l = \overline{1,N}, \tag{6.12}$$

$$\tilde{\theta}_k = \frac{\pi k}{N}, \quad k = \overline{1,(N-1)}, \quad \tilde{\phi}_l = \frac{2\pi(l-1)}{N}, \quad l = \overline{1,N}.$$

The external source points are located outside the outer domain Ω_{Outer}, and are defined (for both Problems $1(a)$ and $1(b)$) by

$$\underline{\xi}_{k,l} = R \left(\sin\tilde{\theta}_{k-N+1} \cos\tilde{\phi}_l, \sin\tilde{\theta}_{k-N+1} \sin\tilde{\phi}_l, \cos\tilde{\theta}_{k-N+1}\right), \quad k = \overline{N,2(N-1)}, \quad l = \overline{1,N}, \tag{6.13}$$

where $1 < R < \infty$. Similarly, the internal boundary collocation points are located on $\partial\Omega_{Inner}$, and are defined, for Problem $1(a)$, by

$$\underline{x}_{i,j} = 0.5\left(\sin\theta_i \cos\phi_j, \sin\theta_i \sin\phi_j, \cos\theta_i\right), \quad i = \overline{1,(M-1)}, \quad j = \overline{1,M}, \tag{6.14}$$

and, for Problem $1(b)$, by

$$\underline{x}_{i,j} = \left(0.5\sin\theta_i \cos\phi_j, 0.5\sin\theta_i \sin\phi_j, 0.4\cos\theta_i\right), \quad i = \overline{1,(M-1)}, \quad j = \overline{1,M}, \tag{6.15}$$

where

$$\theta_i = \frac{\pi i}{M}, \quad i = \overline{1,(M-1)}, \quad \phi_j = \frac{2\pi(j-1)}{M}, \quad j = \overline{1,M}.$$

The external boundary collocation points are located on $\partial\Omega_{Outer}$, and are defined (for both Problems $1(a)$ and $1(b)$) by

$$\underline{x}_{i,j} = \left(\sin\theta_{i-M+1} \cos\phi_j, \sin\theta_{i-M+1} \sin\phi_j, \cos\theta_{i-M+1}\right), \quad i = \overline{M,2(M-1)}, \quad j = \overline{1,M}. \tag{6.16}$$

In order to obtain the coefficient $\underline{c} = (c_{k,l})_{k=\overline{1,2(N-1)},\, l=\overline{1,N}}$, (6.9) is substituted into the boundary conditions (6.4) and (6.5). This results in

$$\sum_{k=1}^{2(N-1)} \sum_{l=1}^{N} G_{i,j,k,l} c_{k,l} = f_{i,j}, \quad i = \overline{1, 2(M-1)}, \quad j = \overline{1, M}, \tag{6.17}$$

where $f_{i,j} = f(\underline{x}_{i,j})$ and $G_{ijkl} = \frac{1}{4\pi|\underline{\xi}_{k,l} - \underline{x}_{i,j}|}$ for $i = \overline{1, 2(M-1)}$, $j = \overline{1, M}$, $k = \overline{1, 2(N-1)}$ and $l = \overline{1, N}$. Note that from (6.5), $f_{i,j} = 0$ for $i = \overline{1, (M-1)}, j = \overline{1, M}$. The linear system of algebraic equations (6.17) consists of $2(M-1) \times M$ equations with $2(N-1) \times N$ unknowns. If $M = N$, we can apply the Gaussian elimination method to obtain the MFS coefficients $\underline{c}$. If $M > N$ the least-squares method is used to solve the over-determined system of equations (6.17). Once the coefficient vector $\underline{c}$ has been obtained accurately, equation (6.9) provides explicitly the solution for the potential u inside the domain Ω and, by differentiation, the current flux $\partial u/\partial n$ on the boundary $\partial\Omega$.

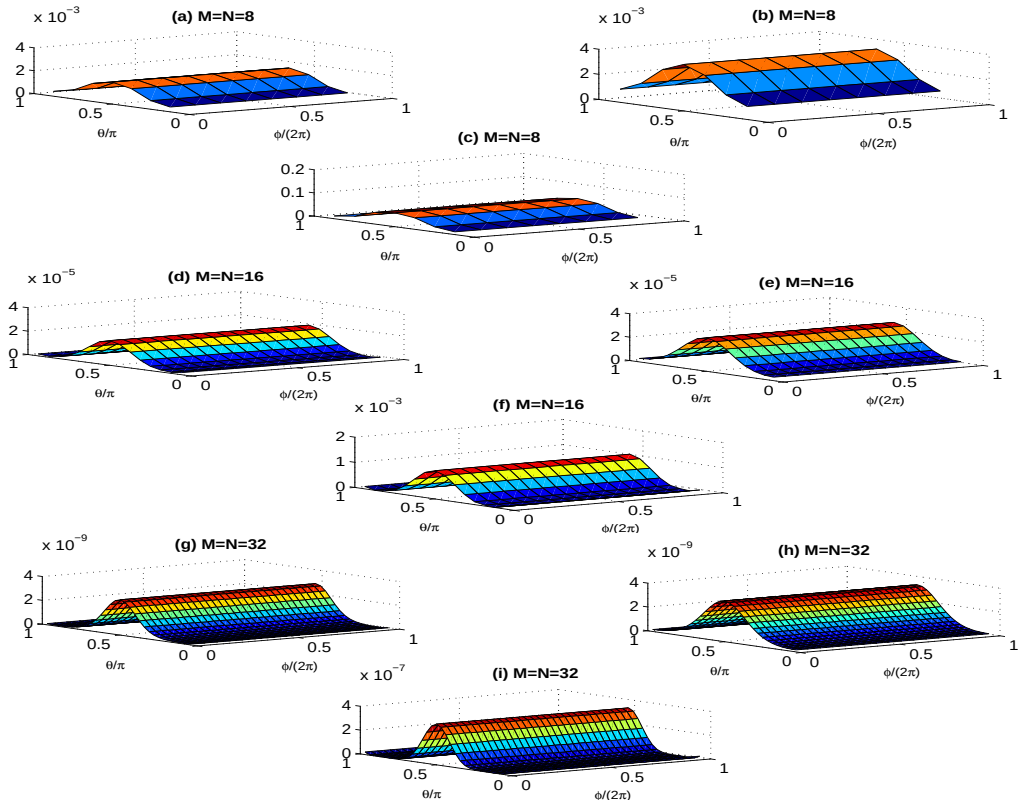

Figure 6.1: (a, d, g) The absolute errors between the MFS and exact interior solutions $u^{MFS}(0.6, \theta, \phi)$ and $u^{Exact}(0.6, \theta, \phi)$, (b, e, h) the absolute errors between the MFS and exact outer derivative $(\partial u/\partial n^{MFS})(1, \theta, \phi)$ and $(\partial u/\partial n^{Exact})(1, \theta, \phi)$, and (c, f, i) the absolute errors between the MFS and exact inner derivative $(\partial u/\partial n^{MFS})(0.5, \theta, \phi)$ and $(\partial u/\partial n^{Exact})(0.5, \theta, \phi)$, for $M = N = \{8, 16, 32\}$, as functions of $\phi/(2\pi)$ and θ/π.

6.3.2 Numerical results

Example 1: Solve, using the MFS, the direct problem $1(a)$ given by (6.1), (6.4) with $f = -1$, and (6.5) which has the analytical solution given by

$$u(x,y,z) = \frac{1}{\sqrt{x^2+y^2+z^2}} - \frac{1}{0.5}, \quad (x,y,z) \in \Omega. \tag{6.18}$$

Solution: Choosing $M = N = 16$ results in $30 \times 16 = 480$ boundary collocation points and 480 source points. We also take $R = 5$ and $\eta_I = 0.6$.

Figure 6.1 illustrates the absolute errors between the exact and the numerical MFS solutions for various values of $M = N \in \{8, 16, 32\}$. From this figure, it can be seen that as $M = N$ increases, the accuracy of MFS solution increases.

Example 2: Consider the numerical solution of the direct problem 2 given by (6.1), (6.4), (6.7) and (6.8) using the MFS when

$$f(x,y,z) = x^2 + y^2 - 2z^2, \quad (x,y,z) \in \partial\Omega_{Outer}. \tag{6.19}$$

Note that in this case an analytical solution is not available. The MFS implementation requires some changes when the two inclusions (6.7) are present but these are straight forward.

Solution: Choosing $M = N = 16$ results in $45 \times 16 = 720$ collocation points and 720 source points. We also take $R = 5$ and η_I=0.6.

Figure 6.2 illustrates the rapid convergence of the MFS numerical normal derivative on the external boundary $\partial\Omega_{Outer}$ for various $M = N = \{8, 16, 32, 64\}$. It is also obvious that the two peaks are caused by the existence of the two inner rigid inclusions (6.7).

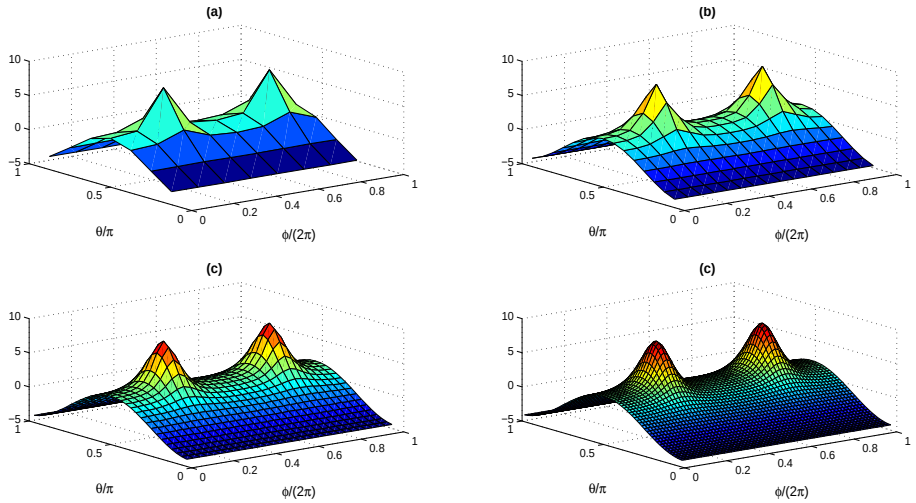

Figure 6.2: The MFS outer derivative $(\partial u/\partial n)^{MFS}_{Outer}(1,\theta,\phi)$, as a function of $\phi/(2\pi)$ and θ/π, for (a) $M = N = 8$, (b) $M = N = 16$, (c) $M = N = 32$, (d) $M = N = 64$, when $R = 5$ and $\eta_I = 0.6$.

6.4 The inverse solution in three dimensions

6.4.1 One rigid inclusion (inverse problems $1(a)$ and $1(b)$)

Consider a three-dimensional star-shaped object Ω_{Inner} centered at the origin in the unit sphere Ω_{Outer} and parametrised by

$$r_{i,j} = r(\tilde{\theta}_i, \tilde{\phi}_j), \quad i = \overline{1,(N-1)},\ j = \overline{1,N}, \tag{6.20}$$

using the spherical coordinates representation

$$\Omega_{Inner} = \{r(\theta,\phi)\,(\sin\theta\cos\phi, \sin\theta\sin\phi, \cos\theta) \mid \phi \in [0, 2\pi), \theta \in (0,\pi)\}. \tag{6.21}$$

The boundary potential u is specified as in (6.4) and the current flux $\partial u/\partial n$ is obtained numerically by solving the direct problem in order to provide the current flux data (6.6). Afterwards, the potential and current flux values are corrupted with noise as

$$w_{i,j} = f(x_{i,j}) + \eta_{i,j}, \quad v_{i,j} = g(x_{i,j}) + \zeta_{i,j}, \quad i = \overline{M, 2(M-1)}, \quad j = \overline{1, M}, \tag{6.22}$$

where the additive noise variables $\eta_{i,j}$ and $\zeta_{i,j}$ follow independent Gaussian distributions with zero means and variances σ_w^2 and σ_v^2, respectively.

Based on (6.9), (6.20) and (6.21), the rigid-inclusion condition (6.5) is imposed as

$$\sum_{k=1}^{2(N-1)} \sum_{l=1}^{N} c_{k,l} G\left(\underline{\xi}_{k,l}, r_{i,j}(\sin\tilde{\theta}_i\cos\tilde{\phi}_j, \sin\tilde{\theta}_i\sin\tilde{\phi}_j, \cos\tilde{\theta}_i)\right) = 0, \quad i = \overline{1, (N-1)},\ j = \overline{1, N}. \tag{6.23}$$

Also, (6.4) and (6.6) yield

$$\sum_{k=1}^{2(N-1)} \sum_{l=1}^{N} c_{k,l} G(\underline{\xi}_{k,l}, \underline{x}_{i,j}) = w_{i,j}, \quad i = \overline{M, 2(M-1)},\ j = \overline{1, M}, \tag{6.24}$$

$$\sum_{k=1}^{2(N-1)} \sum_{l=1}^{N} c_{k,l} \frac{\partial G}{\partial n}(\underline{\xi}_{k,l}, \underline{x}_{i,j}) = v_{i,j}, \quad i = \overline{M, 2(M-1)},\ j = \overline{1, M}. \tag{6.25}$$

Equations (6.23)-(6.25) create a nonlinear system of $(N-1)\times N + 2(M-1)\times M$ equations with $3(N-1)\times N$ unknowns given by the radii $\underline{r} = (r_{i,j})$ for $i = \overline{1, (M-1)}$, $j = \overline{1, N}$ and the MFS coefficients $\underline{c} = (c_{k,l})$ for $k = \overline{1, 2(M-1)}$, $l = \overline{1, N}$. Although the linearity in $\underline{c}$ is obvious in equations (6.24) and (6.25), equation (6.23) clearly shows the nonlinearity between $\underline{r}$ and $\underline{c}$.

The constraint $0 < r_{ij} < 1$ for $i = \overline{1, (N-1)}$, $j = \overline{1, N}$ is imposed to ensure that the inner star-shaped object remains within the unit sphere during the reconstruction process.

6.4.2 Two rigid inclusions (inverse problem 2)

Now consider two three-dimensional star-shaped objects Ω_{Inner1} and Ω_{Inner2} centered at given points say, (X_0, Y_0, Z_0) and (X_1, Y_1, Z_1) in the unit sphere Ω_{Outer} and represented by $\underline{r}_1 = (r^1_{i,j})_{i=\overline{1,(N-1)},\, j=\overline{1,N}}$ and $\underline{r}_2 = (r^2_{i,j})_{i=\overline{1,(N-1)},\, j=\overline{1,N}}$, respectively, defined as in (6.20).

Conditions (6.8), (6.4) and (6.6) are

$$\sum_{k=1}^{3(N-1)} \sum_{l=1}^{N} c_{k,l} G\left(\underline{\xi}_{k,l}, r_{i,j}(\sin\tilde{\theta}_i\cos\tilde{\phi}_j, \sin\tilde{\theta}_i\sin\tilde{\phi}_j, \cos\tilde{\theta}_i)\right) = 0, \quad i = \overline{1, 2(N-1)},\ j = \overline{1, N}. \tag{6.26}$$

$$\sum_{k=1}^{3(N-1)} \sum_{l=1}^{N} c_{k,l} G(\underline{\xi}_{k,l}, \underline{x}_{i,j}) = w_{i,j}, \quad i = \overline{(2(M-1)+1), 3(M-1)},\ j = \overline{1, M}, \tag{6.27}$$

$$\sum_{k=1}^{3(N-1)} \sum_{l=1}^{N} c_{k,l} \frac{\partial G}{\partial n}(\underline{\xi}_{k,l}, \underline{x}_{i,j}) = v_{i,j}, \quad i = \overline{(2(M-1)+1), 2(M-1)},\ j = \overline{1, M}. \tag{6.28}$$

Equations (6.26)-(6.28) create a nonlinear system of $2(N-1) \times N + 2(M-1) \times M$ equations with $5(N-1) \times N$ unknowns. We also need to take into account that the distance between the centres is greater than the sum of the diameters, namely,

$$S = \sqrt{(X_0 - X_1)^2 + (Y_0 - Y_1)^2 + (Z_0 - Z_1)^2} > \text{diam}(\Omega_{Inner_1}) + \text{diam}(\Omega_{Inner_2}), \tag{6.29}$$

where the diameters of Ω_{Inner_1} and Ω_{Inner_2} are defined as

$$\text{diam}(\Omega_{Inner_i}) = \max_{\underline{x}, \underline{y} \in \partial\Omega_{Inner_i}} |\underline{x} - \underline{y}|, \quad i = 1, 2. \tag{6.30}$$

6.4.3 Statistical approach

The solution of the inverse problem (6.23)-(6.25) or (6.26)-(6.28) is obtained using the MCMC, as described in [1, 4]. Due to the ill-posedness and non-linearity of the ERT inverse problem, we consider the Bayesian approach which is linked to Markov chain Monte Carlo (MCMC) algorithms to work as a regularization scheme interpreted in terms of prior information. Modelling the prior information is a very important process in order to obtain reliable conclusions about the solution.

The main ingredients in the Bayesian statistical framework are the likelihood function and a prior distribution which describes the model parameters before the data is considered. The product of the likelihood function and the prior distribution, an application of Bayes theorem, leads to the posterior distribution (the solution of the inverse problem), see [4] for more details. In the inverse problem, the model parameters which must be estimated using the potential and current flux data, are the MFS coefficients $\underline{c}$ and the radii $\underline{r}$. These are high-dimensional parameters, for both inverse problems considered in this paper, which make the posterior distribution complicated to solve numerically using standard methods. This is why the MCMC technique is used in this paper to estimate the shape and the size of the inner rigid inclusions. Another advantage of using MCMC is that it also allows deeper understanding of the posterior distribution in terms of accuracy and reliability, foe example by calculation of credible intervals of the unknown parameters, [1, 4].

Although the MCMC offers a flexible tool to fully investigate the reliability and quantify uncertainty of the posterior distribution, it makes intensive use of the forward solver which can be a drawback especially when three-dimensional ERT problems are being solved. Hence, using a meshless method, such as the MFS described in the previous subsections, is more advantageous than using domain or boundary discretisation methods.

The type of MCMC technique which is used here is the Metropolis-Hastings algorithm where the initial guess of the radii is selected by finding a well-fitting circle for the inner inclusion and the initial values for the MFS coefficients are chosen to be zero. For more details of similar use of MCMC see [1, 3, 4].

6.4.4 Numerical results and discussion

Experiment 1. Find the inverse solution of Problem $1(a)$ satisfying (6.1) and (6.4), with $f = -1$, and (6.5) by fitting a star-shaped object model using the data (6.6) from a spherical inclusion (a) of radius 0.5 centred at $(0, 0, 0)$.

First of all, the current flux $\partial u/\partial u$ on the external boundary $\partial\Omega_{Outer}$, is calculated numerically by solving the forward Dirichlet problem (6.1), (6.4) and (6.5) using the MFS with

$(N-1)N = 35 \times 36 = 1260$. Then, (6.22) is considered on a set of equally-spaced collocation points, with $(M-1)M = 13 \times 14 = 182$, on the external fixed boundary $\partial\Omega_{Outer}$. We add noise to those boundary measurements with a standard deviation $\sigma_w = \sigma_v = 0.01$.

We take $(N-1)N = 14 \times 15 = 210$ which makes the discretised problem (that defined in (6.23)-(6.25)) under-determined, since it consists of $(N-1)N+2(M-1)M = 210+2\times182 = 574$ equations with $3(N-1)N = 3 \times 210 = 630$ unknowns. We take $\eta_I = 0.6$ and $R = 5$.

Secondly, the hierarchical structure of the statistical model in [1] is considered. The values of the hyper-prior parameters of the internal and external MFS coefficients are fixed at $\alpha_{C_I} = 0.0116$ and $\alpha_{C_E} = 0.2457$, respectively, as well as the hyper-prior parameter value for the radius at $\alpha_r = 0.1$ (based on previous work [1, 3]).

It can be seen from Table 6.1 that as the number K of MCMC iterations increases, the three-dimensional reconstruction for the star-shaped model (6.20) become better. This is due to the average of corresponding estimated radii becoming closer to the true value which is 0.5 and its standard deviation (given in brackets) is much smaller.

Experiment 2. Find the inverse solution of Problem 1(b) by fitting a star-shaped object

K	The estimated radius	The standard deviation
5	0.4895	0.0153
10	0.4888	0.0103
20	0.4926	0.0178
40	0.4968	0.0094

Table 6.1: The average of the estimated radii with the corresponding standard deviations, for Experiment 1, for various iterations $K \in \{5, 10, 20, 40\}$.

model using the data from an ellipsoid inclusion of radius given by

$$r(\theta,\phi) = \sqrt{(0.5\sin\theta\cos\phi)^2 + (0.5\sin\theta\sin\phi)^2 + (0.4\cos\theta)^2}, \quad \theta \in (0,\pi),\ \phi \in [0,2\pi). \tag{6.31}$$

The Dirichlet data (6.4) on $\partial\Omega_{Outer}$ is taken as

$$u(x,y,z) = f(x,y,z) = e^{x+y}, \quad (x,y,z) \in \partial\Omega_{Outer}. \tag{6.32}$$

Figure 6.3 shows an excellent three-dimensional reconstruction for the ellipsoid (6.31). The MCMC algorithm converges to the exact ellipsoid within just a few iterations with a run time, for $K = 80$, of about three hours. One way to illustrate that the MCMC works well is to

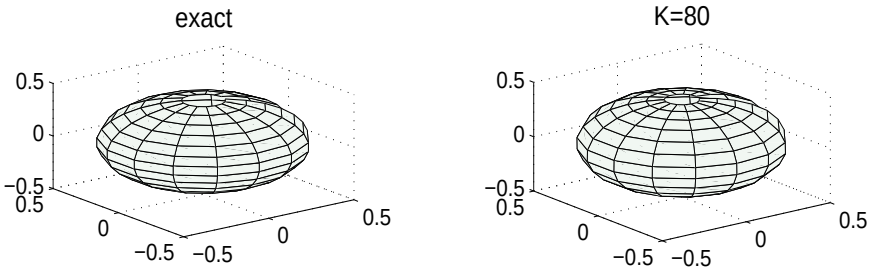

Figure 6.3: Star-shaped model reconstruction: The exact inner ellipsoid and the fitted ellipsoids after $K = 80$ iterations.

consider the 2-norm values of $(r_{i,j}^{MFS} - r_{i,j}^{exact})$, $i = \overline{1,14}$, $j = \overline{1,15}$, as well as the maximum absolute error values for $K \in \{5, 10, 20, 40, 80\}$, see Table 6.2. The random fluctuations suggest

K	$\|\|r_{i,j}^{MFS} - r_{i,j}^{exact}\|\|$	$\max \|r_{i,j}^{MFS} - r_{i,j}^{exact}\|$
5	0.0068	0.0063
10	0.0053	0.0036
20	0.0066	0.0036
40	0.0086	0.0052
80	0.0084	0.0031
160	0.0102	0.0028
320	0.0168	0.0047

Table 6.2: The 2-norm of $(r_{i,j}^{MFS} - r_{i,j}^{exact})$, $i = \overline{1,14}$, $j = \overline{1,15}$, and the maximum absolute error, for Experiment 2, for various $K \in \{5, 10, 20, 40, 80, 160, 320\}$.

that the MCMC algorithm is in equilibrium and mixing well.

A better way to illustrate the reliability of the MCMC algorithm is to plot, see Figure 6.4, the object boundary credible intervals for some cross-sections in the xy-plane of the three-dimensional reconstruction. From this figure, it can be seen that the width of the credible intervals is very narrow near the top and the bottom of the reconstructed ellipsoid compared to the ones at the middle due to the data distribution.

Experiment 3. Find the inverse solution of Problem 2 satisfying (6.1), (6.4) with f given by

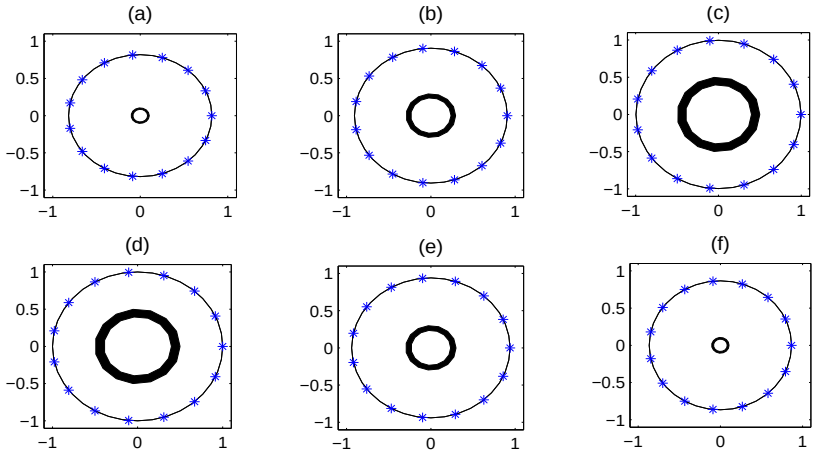

Figure 6.4: Credible intervals for various cross-sections (a) $\theta = \frac{\pi}{14}$, (b) $\theta = \frac{3\pi}{14}$, (c) $\theta = \frac{6\pi}{14}$, (d) $\theta = \frac{8\pi}{14}$, (e) $\theta = \frac{11\pi}{14}$, and (f) $\theta = \frac{13\pi}{14}$ and $(\phi)_{j=\overline{1,15}} \in [0, 2\pi)$, for Experiment 2.

(6.32) and (6.8) by fitting a star-shaped object model using the data (6.6) from two spherical inclusions (6.7) of radii 0.4 centred at $(0, 0.5, 0)$ and $(0, -0.5, 0)$.

Firstly, the current flux $\partial u/\partial u$ is calculated numerically on the external boundary $\partial\Omega_{Outer}$ by solving the forward Dirichlet problem (6.1), (6.4), (6.7) and (6.8) using the MFS with the same inputs as in Experiment 1. Note that in the inverse problem, by extending the number of rigid inclusions to two leads to a greater number of equations, $2(N-1)N + 2(M-1)M = 2 \times 210 + 2 \times 210 = 840$ equations with $5(N-1)N = 5 \times 210 = 1050$ unknowns.

Figure 6.5 shows the credible intervals over some selected cross-sections of the three-dimensional reconstructions confirming the solution's reliability.

6.5 Conclusion

The MFS has been successfully employed in combination with the MCMC to solve the three-dimensional inverse problem in the continuous model of ERT. The combined method has successfully detected three-dimensional star-shaped rigid inclusions (single sphere and ellipsoid, and two spheres). This was further justified by producing and interpreting cross-sections of credible intervals for the inner radii. Further work will consider reconstructing rigid inclusions from voltage measurements resulted from the three-dimensional complete-electrode model of ERT.

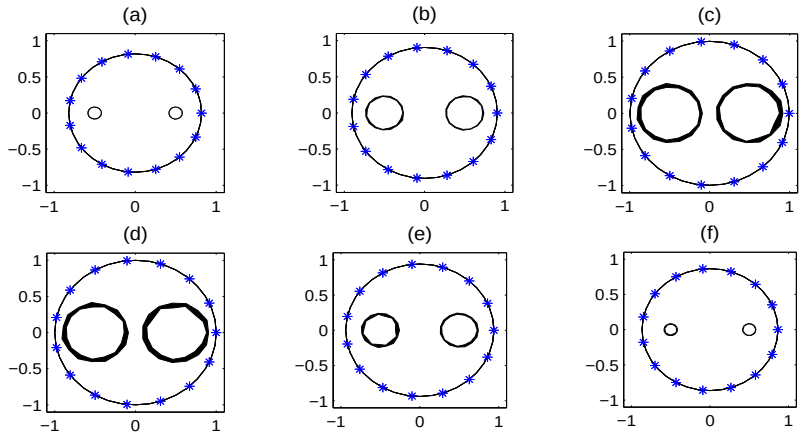

Figure 6.5: Credible intervals for various cross-sections (a) $\theta = \frac{\pi}{14}$, (b) $\theta = \frac{3\pi}{14}$, (c) $\theta = \frac{6\pi}{14}$, (d) $\theta = \frac{8\pi}{14}$, (e) $\theta = \frac{11\pi}{14}$, and (f) $\theta = \frac{13\pi}{14}$ and $(\phi)_{j=\overline{1,15}} \in [0, 2\pi)$, for Experiment 3.

References

[1] R. G. Aykroyd, D. Lesnic and A. Karageorghis, *A fully Bayesian approach to shape estimation of objects from tomography data using MFS forward solutions*, Int. J. Tomography Simul., **28** (2015), 1-21.

[2] D. J. Borman, D. B. Ingham, B. T. Johansson and D. Lesnic, *The method of fundamental solutions for detection of cavities in EIT*, J. Integral Equations Appl., **21** (2009), 381-404.

[3] T. E. Dyhoum, D. Lesnic and R. G. Aykroyd, *Solving the complete-electrode direct model of ERT using the boundary element method and the method of fundamental solutions*, Electronic J. of Boundary Elements, **12** (2014), 26-71.

[4] T. E. Dyhoum, R. G. Aykroyd and D. Lesnic, Reconstructing rigid inclusions in the complete-electrode model of ERT. In: *Inverse Problems and Computational Mechanics*, Chapter 4, (eds. L. Marin, L. Munteanu and V. Chiroiu), 75-104, 2016.

[5] H. Haddar and R. Kress, *Conformal mappings and inverse boundary value problems*, Inverse Problems, **21** (2005), 935-953.

[6] A. Karageorghis, D. Lesnic and L. Marin, *A moving pseudo-boundary MFS for three-dimensional void detection*, Adv. Appl. Math. Mech., **5** (2013), 510-527.

[7] P. Serranho, *A hybrid method for inverse scattering for sound-soft obstacles in* $\mathbb{R}^3$, Inverse Problems Imaging, **1** (2007), 691-712.

Chapter 7

An exponentially convergent Volterra-Fredholm method for integro-differential equations

Abigail I. Fairbairn and Mark A. Kelmanson

Department of Applied Mathematics
University of Leeds
Leeds
LS2 9JT

Abstract. *Extending the authors' recent work [15] on the explicit computation of error bounds for Nyström solvers applied to one-dimensional Fredholm integro-differential equations (FIDEs), presented herein is a study of the errors incurred by first transforming (as in, e.g., [21]) the FIDE into a hybrid Volterra-Fredholm integral equation (VFIE). The VFIE is solved via a novel approach that utilises N-node Gauss-Legendre interpolation and quadrature for its Volterra and Fredholm components respectively: this results in numerical solutions whose error converges to zero exponentially with N, the rate of convergence being confirmed via large-N asymptotics. Not only is the exponential rate inherently far superior to the algebraic rate achieved in [21], but also it is demonstrated, via diverse test problems, to improve dramatically on even the exponential rate achieved in [15] via direct Nyström discretisation of the original FIDE; this improvement is confirmed theoretically.*

7.1 Introduction

Although there is a substantial body of literature devoted to the development of methods for approximating the numerical solution of one-dimensional Fredholm integro-differential equations (FIDEs), corresponding error analyses, an aspect considered to be a default element in the exposition of new numerical methods, are relatively scarce. For example, though the independent studies (in chronological order) [27, 4, 28, 20, 5, 11, 25, 29, 6, 22, 2, 1, 16, 26] present diverse FIDE-solution techniques of varying degrees of efficiency and (disparate) accuracy, only [20, 29, 22, 1] include a discussion of errors and, in even these cases, error analyses are limited (see summary in [15, §1]) to estimates of convergence rates: that is, the direct computation of theoretically predicted error bounds is absent.

The present work is therefore motivated on two fronts: to develop not only a novel numerical method that converges exponentially in the dimension N of the discrete numerical method, but also an explicit error analysis that is implementable and yields errors in terms of only the computed numerical solution. In [15], the authors develop a novel approach for achieving these

two goals, but the method developed therein—based on a combination of numerical quadrature and numerical differentiation—has a global error dictated by the latter process, which is considerably less accurate than the former. Accordingly, an approach independent of [15] is presently pursued in which the need for numerical differentiation is circumvented by first transforming the FIDE (as in, e.g., [21]) into a Volterra-Fredholm integal equation (VFIE); though the solution of this can be approximated in a number of ways (see, e.g., [18, 12, 10, 7, 24]), a novel approach is adopted herein.

The remainder of this paper is structured as follows. In §7.2 is presented an FIDE-to-VFIE conversion approach from [21], in which the VFIE is solved to (only; see below) *quadratic* order in the number N of Simpson's-rule panels used. In §7.3 the VFIE is solved numerically to *spectral* order in N, the degree of the highest-order orthogonal polynomial used in the approximation of the VFIE solution. This approach obviates the need for the numerical differentiation matrices used in a related paper [15]. In §7.4 is presented a novel error analysis, for the VFIE numerical solution procedure, whose distinctive aspect is computation of the error in the numerical solution of the original FIDE *explicitly* in terms of the numerical approximation of the derivate that results from the VFIE reformulation. In §7.5 numerical results of test problems, some challenging, are presented that validate to spectral accuracy both the implementation outlined in §7.3 and the error analysis of §7.4. Brief conclusions are presented in §7.6.

7.2 Conversion from FIDE to VFIE

The canonical form on the normalised interval $[-1, 1]$ of the first-order one-dimensional Fredholm integro-differential equation (FIDE) for the unknown function $u(x)$ is

$$u(x) - \mu(x)\,\frac{du}{dx}(x) - \lambda \int_{-1}^{1} K(x, y)\,u(y)\,dy = f(x)\,, \quad x \in [-1, 1]\,, \tag{7.1}$$

in which the source function $f : [-1, 1] \to \mathbb{R}$, the kernel $K : [-1, 1] \times [-1, 1] \to \mathbb{R}$ and coefficient function $\mu : [-1, 1] \to \mathbb{R}$ are prescribed functions of $x, y \in [-1, 1]$ and the parameter $\lambda \in \mathbb{R}$ is a constant. By hypothesis, (7.1) is solvable and so $u(x)$ exists. In symbolic form, (7.1) is

$$u - \mu\,\mathcal{D}\,u - \lambda\,\mathcal{K}\,u = f\,, \tag{7.2}$$

where $u,\ f \in \mathcal{C} \equiv C[-1, 1]$, the Banach space with supremum norm $\|\cdot\|$ on which the action of the differential operator $\mathcal{D}$ on u is defined by

$$\mathcal{D}\,u = (\mathcal{D}\,u)(x) \equiv u'(x)\,,$$

wherein a prime denotes differentiation with respect to x. The action in (7.2) of the compact integral operator $\mathcal{K}$ on u is defined by

$$\mathcal{K}\,u = (\mathcal{K}\,u)(x) \equiv \int_{-1}^{1} K(x, y)\,u(y)\,dy\,.$$

The FIDE (7.1) is augmented by the boundary condition (BC)

$$u(\xi) = \zeta, \quad \xi \in [-1, 1]\,, \tag{7.3}$$

i.e. ζ is a prescribed real constant in the interval containing all Legendre nodes. When the BC is given for the end-points $\xi = \pm 1$, the FIDE can be converted into a Volterra-Fredholm integral equation (VFIE) following the approach in, e.g., [21]; the details of this conversion for $\xi = -1$ are as follows. Define the function $v(x)$ by

$$v(x) \equiv u'(x)\,, \tag{7.4}$$

integration of which, upon using (7.3), yields

$$u(x) = \zeta + \int_{-1}^{x} v(y)\,dy\,, \tag{7.5}$$

whence the FIDE (7.1) becomes

$$\zeta + \int_{-1}^{x} v(y)\,dy - \mu(x)\,v(x) - \lambda \int_{-1}^{1} K(x,y)\,\left(\zeta + \int_{-1}^{y} v(z)\,dz\right)\,dy = f(x)\,. \tag{7.6}$$

By the existence of $u(x)$ and (7.5), $v(x)$ is integrable, hence the order of double integration in the final term on the right-hand side of (7.6) can be exchanged, thereby rendering (7.6) as the VFIE

$$v(x) = g(x) + \frac{1}{\mu(x)} \int_{-1}^{x} v(y)\,dy - \lambda \int_{-1}^{1} k(x,y)\,v(y)\,dy\,, \tag{7.7}$$

in which the modified source function $g(x)$ is given by

$$g(x) = \frac{1}{\mu(x)}\left(\zeta - \lambda\,\zeta\,\int_{-1}^{1} K(x,y)\,dy - f(x)\right)\,,$$

and the modified kernel $k(x,y)$ by

$$k(x,y) = \frac{1}{\mu(x)}\,\int_{y}^{1} K(x,z)\,dz\,. \tag{7.8}$$

By defining the action of the (Volterra) integral operator $\mathcal{V}$ on $v \in \mathcal{C}$ by

$$\mathcal{V}\,v = (\mathcal{V}\,v)(x) \equiv \int_{-1}^{x} v(y)\,dy\,, \tag{7.9}$$

and that of the (Fredholm) integral operator $\mathcal{F}$ on $v \in \mathcal{C}$ by

$$\mathcal{F}\,v = (\mathcal{F}\,v)(x) \equiv \int_{-1}^{1} k(x,y)\,v(y)\,dy\,, \tag{7.10}$$

the symbolic form of the VFIE (7.7) corresponding to FIDE (7.2) is

$$v = g + \frac{\mathcal{V}\,v}{\mu} - \lambda\,\mathcal{F}\,v\,. \tag{7.11}$$

The FIDE-to-VFIE conversion for the case when the BC is at $x = 1$ follows analogously by replacing integrals $\int_{-1}^{x}$ with $\int_{x}^{1}$ in (7.5), (7.6), (7.7) and (7.9) and replacing $\int_{y}^{1}$ with $\int_{-1}^{y}$ in (7.8).

The original FIDE (7.2) can now be solved via (7.5) and (7.7) without the need for numerical differentiation. The symbolic equation (7.11) will form the basis of the error analysis in section §7.4.

7.3 Numerical Solution of the VFIE

Let $y_{j,N},\ j = 1(1)N$ be a set of N distinct nodes in $[-1,1]$ ordered so that $-1 \le y_{1,N} < y_{2,N} < \ldots < y_{N-1,N} < y_{N,N} \le 1$, using which the action of the N-node Lagrange-interpolation operator $\mathcal{L}_N$ on $v \in \mathcal{C}$ is defined as

$$\mathcal{L}_N\,v = (\mathcal{L}_N\,v)(x) \equiv \sum_{j=1}^{N} L_{j,N}(x)\,v(y_{j,N})\,, \tag{7.12}$$

wherein the Lagrange basis functions are given by

$$L_{j,N}(x) = \prod_{\substack{l=1 \\ l\neq j}}^{N} \frac{x - y_{l,N}}{y_{j,N} - y_{l,N}}, \quad j = 1(1)N\,. \tag{7.13}$$

To approximate the Volterra term in (7.11), define the (Volterra-Lagrange) operator $\mathcal{V}_N \equiv \mathcal{L}_N\,\mathcal{V}$. Application of the operator $\mathcal{V}$ to both sides of the approximate Lagrange interpolation $v \approx \mathcal{L}_N\,v$ then yields

$$\mathcal{V}\,v \approx \mathcal{V}_N\,v = (\mathcal{V}_N\,v)(x) \equiv \sum_{j=1}^{N} \tau_{j,N}(x)\,v(y_{j,N})\,, \tag{7.14}$$

in which

$$\tau_{j,N}(x) = \mathcal{V}\,L_{j,N}(x)\,, \quad j = 1(1)N\,.$$

To approximate the Fredholm term in (7.11), define the (Fredholm-Gauss) operator $\mathcal{F}_N$ that approximates the action of $\mathcal{F}$ by the Nyström quadrature

$$\mathcal{F}\,v \approx \mathcal{F}_N\,v = (\mathcal{F}_N\,v)(x) \equiv \sum_{j=1}^{N} w_{j,N}\,k(x, y_{j,N})\,v(y_{j,N})\,, \tag{7.15}$$

in which $w_{j,N}$ and $y_{j,N}$ are respectively the weights and abscissae of the Gaussian integration rule. As the weight function in the integral (7.10) for $\mathcal{F}\,v$ is unity, the nodes $y_{j,N}$ can be chosen as Gauss-Legendre, Legendre-Gauss-Radau or Legendre-Gauss-Lobatto distributions. Via (7.14) and (7.15), the discrete approximation of VFIE (7.7) is obtained as

$$v_N(x) = g(x) + \sum_{j=1}^{N} \left\{ \frac{\tau_{j,N}(x)}{\mu(x)} - \lambda\,w_{j,N}\,k(x, y_{j,N}) \right\} v_N(y_{j,N}) \tag{7.16}$$

which, when collocated at nodes $x = y_{i,N},\ i = 1(1)N$, yields the $N \times N$ linear system

$$(\mathbf{I}_N - \mathbf{M}_N)\,\mathbf{v}_N = \mathbf{g}_N\,. \tag{7.17}$$

The matrix and vector entries in (7.17) are given by, for $i, j = 1(1)N$,

$$\begin{gathered} \{\mathbf{I}_N\}_{i,j} = \delta_{ij}\,, \quad \{\mathbf{M}_N\}_{i,j} = \frac{\tau_{j,N}(y_{i,N})}{\mu(y_{i,N})} - \lambda\,w_{j,N}\,k(y_{i,N}, y_{j,N})\,, \\ \{\mathbf{v}_N\}_i = v_N(y_{i,N}) \quad \text{and} \quad \{\mathbf{g}_N\}_i = g(y_{i,N})\,, \end{gathered} \tag{7.18}$$

wherein δ_{ij} is the Kronecker delta. Inversion of (7.17) yields the N nodal values $v_N(y_{i,N})$ which, when substituted into the inversion formula (7.16), give the approximate solution $v_N(x)$ of (7.7), which in symbolic form is

$$v_N = g + \frac{\mathcal{V}_N v_N}{\mu} - \lambda\,\mathcal{F}_N v_N. \tag{7.19}$$

Note that computing $v_N(x)$ directly via the inversion formula (7.16) is more accurate [13] than using Lagrange interpolation (7.12). By (7.5), the exact solutions v and u, of the VFIE and FIDE respectively, satisfy the symbolic equation

$$u = \zeta + \mathcal{V}\,v\,, \tag{7.20}$$

to which application of $\mathcal{D}$ to both sides yields $\mathcal{D}\,u = \mathcal{D}\,\mathcal{V}\,v$, i.e. $v = \mathcal{D}\,\mathcal{V}\,v$, so that $(\mathcal{D})^{-1} = \mathcal{V}$. Additionally, (7.20) implies that there are two cases to consider when recovering the numerical

solution u_N from its derivative v_N computed via (7.17)–(7.19). First, if $v_N(x)$ is exactly integrable (case 1) then the approximate numerical solution u_N of (7.2) can be computed from v_N as

$$\widetilde{u}_N = \zeta + \mathcal{V}\, v_N\,. \tag{7.21}$$

Second, if functions $\mu(x)$, $K(x,y)$ and $f(x)$ in IDE (7.1) are such that (7.19) is not exactly integrable (case 2) then the approximate numerical solution u_N of (7.2) must in this case be computed from v_N as

$$\widehat{u}_N = \zeta + \mathcal{V}_N\, v_N, \tag{7.22}$$

which yields $\widehat{u}_N(x)$ as a polynomial of degree N in x. Note that this method requires only (7.17)–(7.18), as $v_N(x)$ does not need to be computed via (7.19) since only its nodal values, given by the solution vector $\mathbf{v}_N$ of (7.17), are present in the last term in (7.22).

7.4 Error Analysis

A theoretical analysis of the error incurred in computing u_N is now presented. Though a basic consideration of errors appears in the VFIE approach in [21], it not only computes the Volterra component of the VFIE crudely using Simpson's rule, but also concerns only convergence rates of $\|v - v_N\|$ (NB and not $\|u - u_N\|$) using a known exact solution. By contrast, the present work computes both Volterra and Fredholm components of the VFIE to spectral accuracy and, moreover, determines explicit error bounds for $\|u - u_N\|$ using only the approximate derivative v_N of the numerical solution u_N. The error analysis is now presented for cases 1 and 2 given in (7.21) and (7.22) respectively.

Case 1

Defining the linear operators $\mathcal{S}$ and $\mathcal{S}_N$ as

$$\mathcal{S} \equiv \frac{\mathcal{V}}{\mu} - \lambda\,\mathcal{F} \quad \text{and} \quad \mathcal{S}_N \equiv \frac{\mathcal{V}_N}{\mu} - \lambda\,\mathcal{F}_N\,, \tag{7.23}$$

the exact solution (7.11) of VFIE (7.7) can be written as

$$v = g + \mathcal{S}\, v \tag{7.24}$$

and the numerical solution (7.19) of (7.11) can be written as

$$v_N = g + \mathcal{S}_N\, v_N\,. \tag{7.25}$$

Subtraction of (7.25) from (7.24) yields

$$v - v_N = \mathcal{S}\, v - \mathcal{S}_N\, v_N = \mathcal{S}\,(v - v_N) + (\mathcal{S} - \mathcal{S}_N)\, v_N\,. \tag{7.26}$$

Since $v = \mathcal{D}\, u$ and $v_N = \mathcal{D}\, \widetilde{u}_N$, (7.26) can be rearranged to yield

$$(\mathcal{I} - \mathcal{S})\,\mathcal{D}\,(u - \widetilde{u}_N) = (\mathcal{S} - \mathcal{S}_N)\, v_N\,,$$

giving an explicit error formula for the exact solution u of the FIDE (7.1) as

$$u - \widetilde{u}_N = (\mathcal{D} - \mathcal{S}\,\mathcal{D})^{-1}\big((\mathcal{S} - \mathcal{S}_N)\, v_N\big)\,,$$

yielding the error bound

$$\|u - \widetilde{u}_N\| \le C\,\sigma_N\,, \tag{7.27}$$

where

$$C = \left\| (\mathcal{D} - \mathcal{S}\,\mathcal{D})^{-1} \right\| \quad \text{and} \quad \sigma_N = \left\| (\mathcal{S} - \mathcal{S}_N)\, v_N \right\| . \tag{7.28}$$

The term σ_N can be expressed via (7.25) as

$$\sigma_N = \left\| \mathcal{S}\, v_N - v_N + g \right\| , \tag{7.29}$$

which demonstrates that the error is proportional to the residual obtained when the numerical solution $v_N(x)$ is inserted into the exact VFIE (7.7). Alternatively, via (7.23), a bound on σ_N can be obtained as

$$\sigma_N \leq \frac{\left\| (\mathcal{V} - \mathcal{V}_N)\, v_N \right\|}{\|\mu\|} + |\lambda| \left\| (\mathcal{F} - \mathcal{F}_N)\, v_N \right\| , \tag{7.30}$$

in which $\left\| (\mathcal{V} - \mathcal{V}_N)\, v_N \right\|$ is obtained from the definition of $\mathcal{V}_N$, which gives

$$(\mathcal{V} - \mathcal{V}_N)\, v_N(x) = \mathcal{V}\,(\mathcal{I} - \mathcal{L}_N)\, v_N(x) = \frac{\mathcal{V}\, p_N(x)}{N!}\, v_N^{(N)}(\eta) , \quad \eta \in (-1, 1) , \tag{7.31}$$

wherein $p_N(x)$ is the monic polynomial whose roots are the N nodes $y_{i,N}$, i.e.

$$p_N(x) = \prod_{i=1}^{N} (x - y_{i,N}) . \tag{7.32}$$

Therefore, in (7.31), there results

$$\left\| (\mathcal{V} - \mathcal{V}_N)\, v_N \right\| \leq Q_N \left\| v_N^{(N)} \right\| = Q_N \left\| \widetilde{u}_N^{(N\,+\,1)} \right\| , \tag{7.33}$$

in which

$$Q_N \equiv \frac{\left\| \mathcal{V}\, p_N(x) \right\|}{N!} ; \tag{7.34}$$

moreover, by standard Gaussian quadrature results [19],

$$\left\| (\mathcal{F} - \mathcal{F}_N)\, v_N \right\| \leq \psi_N^{(\nu)}\, \mathbb{F}_{2N\,-\,\nu} , \tag{7.35}$$

in which [15]

$$\psi_N^{(\nu)} \sim \frac{2^{2\nu\,-\,1}\sqrt{\pi}}{N^{(1\,-\,2\nu)/2}} \left(\frac{\mathrm{e}}{4N} \right)^{2N} , \; N \to \infty \quad \text{and} \quad \mathbb{F}_M = \max_{x,y \in [-1,1]} \left| \frac{\partial^M}{\partial y^M} \big(k(x,y)\, v_N(y) \big) \right| , \tag{7.36}$$

in which ν corresponds to the number of endpoints included in the distribution, i.e. $\nu = 0,\ 1$ and 2 for Legendre, Radau and Lobatto nodes respectively. Combining (7.30), (7.33) and (7.35) yields

$$\sigma_N \leq \frac{Q_N \left\| v_N^{(N)} \right\|}{\|\mu\|} + |\lambda|\, \psi_N^{(\nu)}\, \mathbb{F}_{2N\,-\,\nu}. \tag{7.37}$$

With σ_N in (7.27) bounded by (7.37), the constant C given by (7.28) can be bounded via

$$C = \left\| \big((\mathcal{I} - \mathcal{S})\, \mathcal{D} \big)^{-1} \right\| = \left\| \mathcal{D}^{-1}\, (\mathcal{I} - \mathcal{S})^{-1} \right\| = \left\| \mathcal{V}\, (\mathcal{I} - \mathcal{S})^{-1} \right\| \leq \|\mathcal{V}\| \left\| (\mathcal{I} - \mathcal{S})^{-1} \right\| , \tag{7.38}$$

in which, adopting the approach of Atkinson [3, Eqns. (4.1.13)–(4.1.17)], $\|\mathcal{V}\|$ is computed as

$$\|\mathcal{V}\| = \|\mathcal{V}\, 1\| = \max_{x \in [-1,1]} |x + 1| = 2 .$$

By (7.23), operators $\mathcal{S}$ and $\mathcal{S}_N$ are linear combinations of $\mathcal{V}$, $\mathcal{F}$, $\mathcal{V}_N$ and $\mathcal{F}_N$, for which, by the definitions of Lagrangian interpolation and Gaussian quadrature respectively, $(\mathcal{V} - \mathcal{V}_N)\, v(x) \to 0$ and $(\mathcal{F} - \mathcal{F}_N)\, v(x) \to 0$ as $N \to \infty$ for all $v \in \mathcal{C}$ and $x \in [-1, 1]$. That is, $\mathcal{S}_N\, v$ is pointwise

uniformly convergent to $\mathcal{S}\,v$ as $N \to \infty$ for all $v \in \mathcal{C}$ and $x \in [-1, 1]$, and hence, by [3, Thm 4.1.2] and [17, Eq. (4.7.17b)], $(\mathcal{I} - \mathcal{S})^{-1}$ in (7.38) exists and is uniformly bounded by

$$\left\|(\mathcal{I} - \mathcal{S})^{-1}\right\| \leq \frac{1 + \left\|(\mathcal{I} - \mathcal{S}_N)^{-1}\right\| \|\mathcal{S}\|}{1 - \|(\mathcal{I} - \mathcal{S}_N)^{-1}\| \, \|(\mathcal{S} - \mathcal{S}_N)\, \mathcal{S}\|}\,, \tag{7.39}$$

the denominator of which is positive by construction. The sub-elements on the right-hand side of (7.39) are computed using the approach in Atkinson [3, Eqns. (4.1.13)–(4.1.17)], which gives $\|\mathcal{S}\|$ as

$$\|\mathcal{S}\| = \|\mathcal{S}\,1\| \equiv \|s\|\,,$$

say, in which $s(x)$ is given by (7.9), (7.10) and (7.23) as

$$s(x) = \frac{x+1}{\mu(x)} - \lambda \int_{-1}^{1} k(x, y)\, dy\,. \tag{7.40}$$

Similarly, $\|(\mathcal{S} - \mathcal{S}_N)\, \mathcal{S}\|$ in (7.39) is computed as

$$\|(\mathcal{S} - \mathcal{S}_N)\, \mathcal{S}\| = \|(\mathcal{S} - \mathcal{S}_N)\, \mathcal{S}\, 1\| = \|(\mathcal{S} - \mathcal{S}_N)\, s\|$$

and $\|(\mathcal{I} - \mathcal{S}_N)^{-1}\|$ as

$$\|(\mathcal{I} - \mathcal{S}_N)^{-1}\| = \|(\mathcal{I} - \mathcal{S}_N)^{-1}\, 1\| \equiv \|r_N\|\,,$$

say, in which $r_N(x)$ is the solution of

$$r_N - \mathcal{S}_N\, r_N = 1\,,$$

whose left-hand side is of the same form as VFIE (7.25). Consequently, nodal values of $r_N(x)$ are found by solving a linear system with the same matrix as in (7.17), i.e.

$$(\mathbf{I}_N - \mathbf{M}_N)\, \mathbf{r}_N = \mathbf{1}\,, \tag{7.41}$$

in which $\mathbf{I}_N$ and $\mathbf{M}_N$ are as given in (7.18) and the entries of the vectors $\mathbf{r}_N$ and $\mathbf{1}$ are given by

$$\{\mathbf{r}_N\}_i = r_N(y_{i,N}) \quad \text{and} \quad \{\mathbf{1}\}_i = 1\,, \quad i = 1(1)N\,.$$

It is noted that, for the purposes of efficiency, (7.17) and (7.41) can be solved in the partitioned form

$$(\mathbf{I}_N - \mathbf{M}_N)\, (\mathbf{v}_N | \mathbf{r}_N) = (\mathbf{g}_N | \mathbf{1})\,.$$

Solving (7.41) gives the nodal vector $\mathbf{r}_N$, the elements of which are used in the Nyström inversion formula

$$r_N(x) = 1 + \sum_{j=1}^{N} \left\{ \frac{\tau_{j,N}(x)}{\mu(x)} - \lambda\, w_{j,N}\, k(x, y_{j,N}) \right\} r_N(y_{j,N})\,,$$

from which $\|r_N\|$ can be computed directly; similarly, $\|s\|$ can be computed directly from (7.40). Finally, (7.27), (7.29) and (7.38) give the case-1 theoretical bound

$$\|u - \widetilde{u}_N\| \leq \frac{2\,(1 + \|r_N\|\,\|s\|)}{1 - \|r_N\|\,\|(\mathcal{S} - \mathcal{S}_N)\, s\|}\, \|\mathcal{S}\, v_N - v_N + g\| \tag{7.42}$$

on the (case-1) error $u - \widetilde{u}_N$ that is explicitly computable in terms of only the derivative v_N of the case-1 numerical solution $\widetilde{u}_N$.

Case 2

Subtraction of (7.22) from (7.21) and addition of $u - u = 0$ to the resulting left-hand side gives a bound on the case-2 error as

$$\widetilde{u}_N - u + u - \widehat{u}_N = (\mathcal{V} - \mathcal{V}_N)v_N \Rightarrow \|u - \widehat{u}_N\| \leq \|u - \widetilde{u}_N\| + \|(\mathcal{V} - \mathcal{V}_N)\, v_N\|$$

which, by (7.33) and (7.42), yields

$$\|u - \widehat{u}_N\| \leq \frac{2\ (1 + \|r_N\|\,\|s\|)}{1 - \|r_N\|\,\|(\mathcal{S} - \mathcal{S}_N)s\|}\, \|\mathcal{S}\, v_N - v_N + g\| + Q_N \big\|v_N^{(N)}\big\|\,. \tag{7.43}$$

As the case-2 solution arises when $v_N(x)$ is not integrable, the bound (7.43) is not computable as the operator $\mathcal{S}$ contains the Volterra operator $\mathcal{V}$ via (7.23). Therefore, the term $\|\mathcal{S}\, v_N - v_N + g\|$ in (7.43)—defined as σ_N in (7.29)—must be bounded using (7.37). Similarly, as $\mathcal{S}\, s$ will in general be uncomputable, a bound (analogous to (7.37)) on $\|(\mathcal{S} - \mathcal{S}_N)\, s\|$ can be found as

$$\|(\mathcal{S} - \mathcal{S}_N)\, s\| \leq \frac{Q_N \|s^{(N)}\|}{\|\mu\|} + |\lambda|\ \psi_N^{(\nu)}\, \mathbb{S}_{2N\,-\,\nu}\,,$$

in which

$$\mathbb{S}_M = \max_{x,y\in[-1,1]} \left| \frac{\partial^M}{\partial y^M} \big(k(x,y)\, s(y)\big) \right|\,.$$

Collecting results, the computable case-2 error bound is given by

$$\|u - \widehat{u}_N\| \leq \frac{2\ (1 + \|r_N\|\,\|s\|)\ \big(Q_N \big\|v_N^{(N)}\big\| + |\lambda| \|\mu\|\, \psi_N^{(\nu)}\, \mathbb{F}_{2N\,-\,\nu}\big)}{\|\mu\| - \|r_N\|\ \big(Q_N \|s^{(N)}\| + |\lambda| \|\mu\|\, \psi_N^{(\nu)}\, \mathbb{S}_{2N\,-\,\nu}\big)} + Q_N \left\|v_N^{(N)}\right\|\,. \tag{7.44}$$

Computable error bounds (7.42) and (7.44) have now been derived for the general FIDE (7.2).

Asymptotic large-N approximations for Q_N were obtained in terms of N and ν; the details are cumbersome and omitted for reasons of space. These approximations explicitly reveal that the present VFIE approach is of order $O(N^{(\nu^2\,-\,\nu\,-\,7)/2})$ times more accurate than the direct FIDE approach, henceforth denoted as "case 0", used in [15].

7.5 Numerical Results

Using the algebraic manipulator `Maple`, the methods and bounds derived above were respectively implemented and validated on four test problems, each with known solutions, chosen to demonstrate the accuracy of the theory on potentially challenging problems. The components of each test problem are shown in Table 7.1. As the results were qualitatively similar for each nodal distribution, only the results for the Legendre distribution, for which $\nu = 0$, are presented.

Problem	Type	Solution $u(x)$	$\mu(x)$	Kernel $K(x,y)$	λ
1	Smooth	$\sin x + x^2$	$\sec x$	$(x^3 - 1)\, y \cos y$	$\frac{1}{3}$
2	Runge	$\frac{1}{1+25x^2}$	$\frac{1}{x-2}$	$(x+1)(y^2 - 5)$	$-\frac{1}{2}$
3	Steep	e^{15x}	e^{x}	e^{x+y}	1
4	Oscillatory	$\cos 12x$	$\frac{1}{x^5-3x+1}$	$\sin x\, y^3$	2

Table 7.1: Test problems with solutions of four qualitatively distinct forms. The Runge phenomenon [8, 9], extreme gradient and high-frequency oscillations, in the solutions of problems 2, 3 and 4 respectively, offer well-documented challenges to approximation methods.

Figure 7.1 shows that, for each test problem, the case-1 errors are lower than the case-2 errors and so, as expected, it is more accurate to integrate the numerical VFIE solution exactly to obtain the FIDE solution rather than to integrate its Lagrange interpolant. Additionally, as predicted at the end of Section 7.4, the new case-1 and case-2 errors are smaller in magnitude than the case-0 errors incurred in [15], confirming that bypassing the need for numerical differentiation by converting from FIDE to VFIE form yields a more accurate numerical solution.

Figure 7.1 also reveals that the case-1 error bound is more accurate (by comparison with the actual computed errors) than the case-2 error bound, particularly for problem 2 in which the case-2 error bound diverges whilst the true errors converge with increasing N: this divergence, and the large discrepancy between true case-2 errors and error bounds for the other problems, is due to the terms $\left\|v_N^{(N)}\right\|$ and $\mathbb{F}_{2N-\nu}$ in the error bound (7.44). Via the mean-value theorem used to derive (7.31), the truncation parameter $\eta \in (-1, 1)$ that yields the true error $(\mathcal{V} - \mathcal{V}_N)\, v_N$ is unknown, so $v_N^{(N)}(\eta)$ must be replaced by $\left\|v_N^{(N)}\right\|$, the latter of which may be much greater than the former. The same argument applies to the Gaussian-quadrature error term (7.35), which includes the unknown values of x and y in (7.36); as these are unknown, $\mathbb{F}_{2N-\nu}$ must be computed by maximising over $x, y \in [-1, 1]$, and so the quadrature error may also be over-estimated.

7.6 Conclusions

A novel method for the accurate numerical solution of one-dimensional, first-order Fredholm integro-differential equations has been developed by first converting the problem into a Volterra-Fredholm integral equation. The technique has been validated on diverse and challenging test problems. A novel error analysis has been conducted and validated to yield explicitly computable (using only the numerical solution) error bounds that predict true computational errors to spectral accuracy. Two independent sub-approaches have been analysed depending upon whether or not intermediate stages of the novel process admit exact integration. For both cases, errors are shown theoretically and numerically to be smaller in magnitude than the errors incurred by a previous approach [15].

References

[1] O. A. Arqub, M. Al-Smadi and N. Shawagfeh, *Solving Fredholm integro–differential equations using reproducing kernel Hilbert space method*, Appl. Math. Comput., 219 (2013), 8938–8948.

[2] E. Aruchunan and J. Sulaiman, *Quarter-sweep Gauss-Seidel method for solving first order linear Fredholm integro-differential equations*, Matematika, 27 (2011), 199–208.

[3] K. E. Atkinson, *The Numerical Solution of Integral Equations of the Second Kind*, Cambridge University Press, Cambridge, UK, 1997.

[4] E. Babolian and L. M. Delves,*A fast Galerkin scheme for linear integro-differential equations*, IMA J. Numer. Anal., 1 (1981), 193–213.

[5] E. Babolian, M. T. Kajani and M. Ghasemi,*Numerical solution of linear integro-differential equation by using sine–cosine wavelets*, Appl. Math. Comput., 180 (2006), 569–574.

[6] N. Bildik, A. Konuralp and S. Yalçinbaş, *Comparison of Legendre polynomial approximation and variational iteration method for the solutions of general linear Fredholm integro-differential equations*, Comput. Math. Appl., 59 (2010), 1909–1917.

[7] A. H. Borzabadi and M. Heidari, *A successive numerical scheme for some classes of Volterra-Fredholm integral equations*, Iranian Journal of Mathematical Sciences and Informatics, 10 (2015), 1–10.

[8] J. P. Boyd, *Defeating the Runge Phenomenon for equispaced polynomial interpolation via Tikhonov regularization*, Appl. Math. Lett., 5 (1992), 57–59.

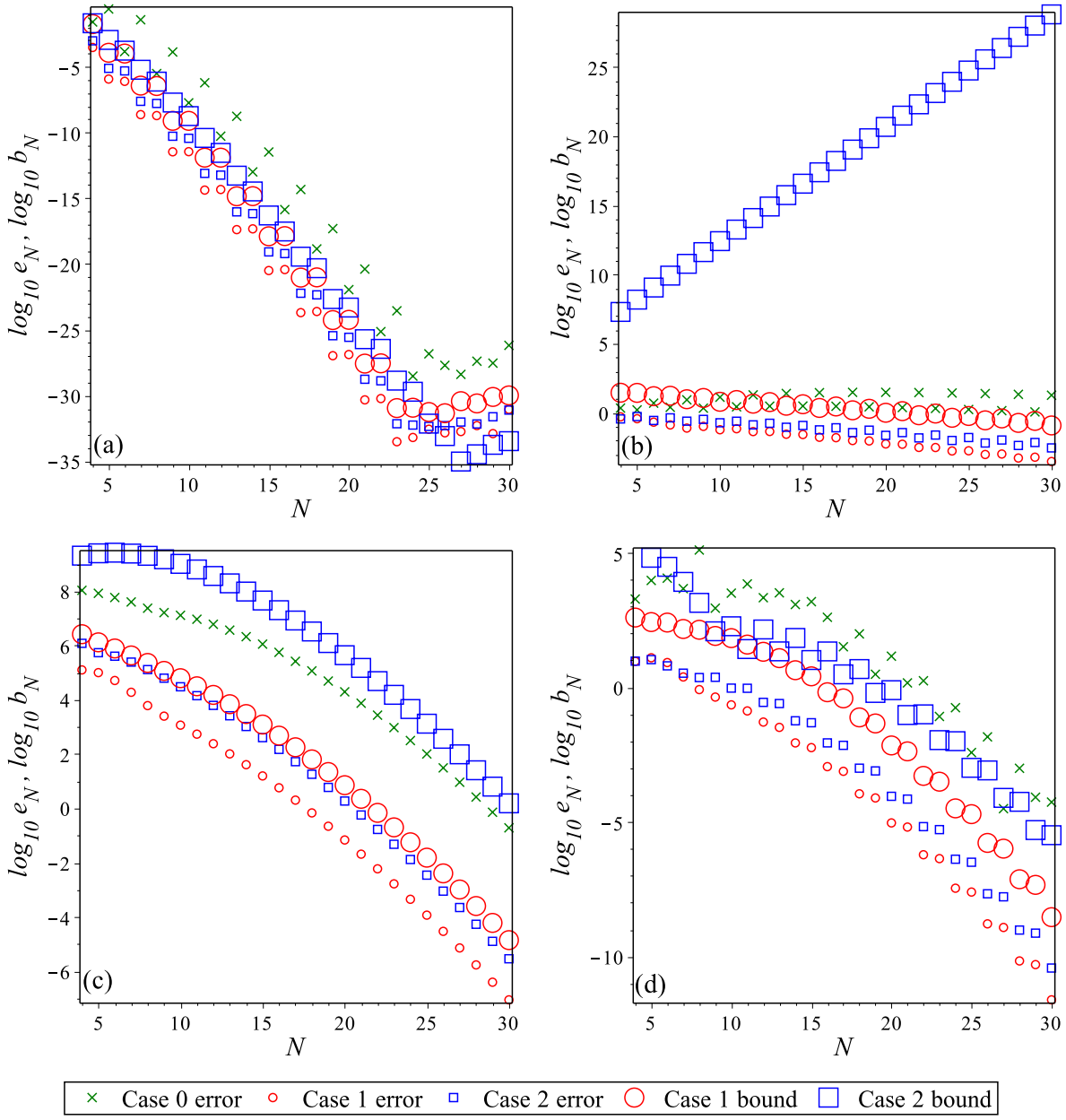

Figure 7.1: Logarithmic plots showing convergence or divergence with N of error $e_N = ||u - u_N||$ and bound b_N given by (7.42) and (7.44), for cases 0, 1 and 2 for each of problems (a) 1 "smooth", (b) 2 "Runge", (c) 3 "steep" and (d) 4 "oscillatory". All computations are conducted on Legendre nodes, i.e. $\nu = 0$. Note the divergence of the case-2 bound for the Runge problem, as discussed in the text. In all four problems, the new case-1 and case-2 errors are smaller than those incurred in [15].

[9] J. P. Boyd, *Exponentially accurate Runge-free approximation of non-periodic functions from samples on an evenly spaced grid*, Appl. Math. Lett., 20 (2007), 971–975.

[10] Z. Chen and W. Jiang, *An approximate solution for a mixed linear VolterraFredholm integral equation*, Appl. Math. Lett., 25 (2012), 1131–1134.

[11] P. Darania and A. Ebadian, *A method for the numerical solution of the integro-differential equations*, Appl. Math. Comput., 188 (2007), 657–668.

[12] H. Laeli Dastjerdi and F. M. Maalek Ghaini, *Numerical solution of Volterra–Fredholm integral equations by moving least square method and Chebyshev polynomials*, Appl. Math. Model., 36 (2012), 3283–3288.

[13] A. I. Fairbairn and M. A. Kelmanson, Computable theoretical error bounds for Nyström methods for Fredholm integral equations of the second kind. In *Proc. 10th UK Conf. on Boundary Integral Methods*, 85–94, 2015.

[14] A. I. Fairbairn and M. A. Kelmanson, *Spectrally accurate Nyström-solver error bounds for 1-D Fredholm integral equations of the second kind*, submitted to Appl. Math. Comput., June 29 2016, 20pp.

[15] A. I. Fairbairn and M. A. Kelmanson, *Computable a priori error bounds for Nyström methods applied to 1-D integro-differential Fredholm equations*, submitted to IMA J. Num. Anal., February 15 2017, 19pp.

[16] M. Fathy, M. El-Gamel and M. S. El-Azab, *Legendre-Galerkin method for the linear Fredholm integro-differential equations*, Appl. Math. Comput., 243 (2014), 789–800.

[17] W. Hackbusch, *Integral Equations: Theory and Numerical Treatment*, Birkhäuser Verlag, Basel, Switzerland, 1995.

[18] F. A. Hendi and A. M. Albugami, *Numerical solution for Fredholm–Volterra integral equation of the second kind by using collocation and Galerkin methods*, Journal of King Saud University - Science, 22 (2010), 37–40.

[19] F. B. Hildebrand, *Introduction to Numerical Analysis*, McGraw-Hill, New York, 1974.

[20] S. M. Hosseini and S. Shahmorad, *Tau numerical solution of Fredholm integro-differential equations with arbitrary polynomial bases*, Appl. Math. Model., 27 (2003),145–154.

[21] P. Linz, *A method for the approximate solution of linear integro-differential equations*, SIAM J. Numer. Anal., 11 (1974), 137–144.

[22] K. Maleknejad and M. Attary, *An efficient numerical approximation for the linear class of Fredholm integro-differential equations based on Cattani's method*, Commun. Nonlinear Sci. Numer. Simulat., 16 (2011), 2672–2679.

[23] M. M. Mustafa and I. N. Ghanim, *Numerical solution of linear Volterra-Fredholm integral equations using Lagrange polynomials*, Mathematical Theory and Modeling, 4 (2014), 137–146.

[24] S. Nemati, *Numerical solution of Volterra–Fredholm integral equations using Legendre collocation method*, J. Comput. Appl. Math., 278 (2015), 29–36.

[25] J. Rashidinia and M. Zarebnia, *The numerical solution of integro-differential equation by means of the Sinc method*, Appl. Math. Comput., 118 (2007), 1124–1130.

[26] P. K. Sahu and S. Ray, *Legendre spectral collocation method for Fredholm integro-differential equation with variable coefficients and mixed conditions*, Appl. Math. Comput., 268 (2015), 575–580.

[27] M. A. Wolfe, *The numerical solution of non-singular integral and integro-differential equations by iteration with Chebyshev series*, Comput. J., 12 (1969), 193–196.

[28] S. Yalçinbaş and M. Sezer, *The approximate solution of high-order linear volterra-fredholm integro-differential equations in terms of taylor polynomials*, Appl. Math. Comput., 112 (2000), 291–308.

[29] S. Yalçinbaş, M. Sezer and H. H. Sorkun, *Legendre polynomial solutions of high-order linear Fredholm integro-differential equations*, Appl. Math. Comput., 210 (2009), 334–349.

Chapter 8

Application of the Gauss-Chebyshev quadrature for planar rectangular cracks

Alexander N. Galybin

The Schmidt Institute of Physics of the Earth
B.Gruzinskaya 10-1, Moscow, Russia

Abstract. *This paper presents a modified form of the integral equation in the theory of planar cracks in space. This form is obtained from the standard form of the integro-differential equation that is not appropriate for the application of the quadratures of highest order often used in 2D crack problems. In this study we transform the integro-differential equation to the singular integral equation over a rectangular domain to unable one to use the Gauss-Chebyshev quadratures for the discretisation of the integral equation. This is accomplished by integration by parts, which eliminates the Laplace operator in the integro-differential equation and produces the Cauchy type kernel in the integrand of the modified equation. As a consequence one can directly take into account the square root singularity in the sought density of the displacement discontinuity function and to obtain a two dimensional quadrature formula rule as the Cartesian product of one-dimensional Gauss-Chebyshev rules. Therefore the numerical algorithm for the one-dimensional SIE is extended for the two dimensional SIE without any essential modification of the quadrature formulas. The paper examines the efficiency of the proposed algorithm by calculation the mode I stress intensity factor along the crack front for the rectangular cracks and the profiles of crack opening.*

8.1 Introduction

Stress intensity factors, SIF, for planar cracks of different shapes can be found in handbooks [1], [2], where one can also find many references on the original works. It is understood, e.g. [3], that for the case of arbitrary loads, analytical solutions are available only for penny-shaped cracks and for elliptical cracks subjected to polynomial loads. Recently Potapenko et al [4] have reported an effective semi-analytical approach for elliptical cracks under arbitrary loading. However extension of this technique to the planar crack of a general shape is questionable. Moreover, the existing approaches are aimed at the calculation of SIF only and do not provide effective approaches for calculation of crack opening displacements, COD. The latter, however, is important in some applications, in particular, for studying hydrofracture propagation, which is a coupled problem of fracture mechanics and fluid dynamics. Although obtaining numerical solutions do not present essential difficulties, it could be a time-consuming task as in the case

of hydrofractures. Indeed, in this case the pressure acting inside the crack depends on the crack opening, therefore modelling of hydrofracture growth requires recalculations of the profiles of fluid pressures and COD which involves iterations on every time step. Thus, there is a strong demand to develop fast and accurate numerical methods for finding SIF and COD for arbitrary loads acting inside the crack of arbitrary shape.

The integro-differential equation for a mode I planar crack can be written in the form [4]

$$\Delta_{xy} \int\limits_{\Omega} \int \frac{w(x',y')dx'dy'}{\rho(x-x',y-y',0)} = -\frac{4\pi(1-\nu^2)}{E} p(x,y), \quad (x,y) \in \Omega \tag{8.1}$$

Here it is assumed that the planar crack Ω is located on the plane $z = 0$, the unknown function $w(x,y)$ presents the displacements parallel to the z-axis (note that COD $= 2w$), $p(x,y)$ is the normal pressure acting on the crack surfaces, E is the Young's modulus and ν is the Poison's ratio and the following notations are used

$$\rho(x,y,z) = \sqrt{x^2+y^2+z^2} \tag{8.2}$$

$$\Delta_{xy} = \frac{\partial^2}{\partial x^2} + \frac{\partial^2}{\partial y^2} \tag{8.3}$$

Leonov [5] showed that the two-dimensional Laplace operator can be transferred under the integral sign, which leads to the following 2D singular integral equation

$$\int\limits_{\Omega} \int \frac{\tilde{w}(x',y')dx'dy'}{\rho(x-x',y-y',0)} = -\frac{4\pi(1-\nu^2)}{E} p(x,y), \quad (x,y) \in \Omega \tag{8.4}$$

for the determination of the new unknown function

$$\tilde{w}(x,y) = \Delta_{xy} w(x,y) \tag{8.5}$$

The aim of this study is to obtain another singular integral equation, SIE, of the form suitable for application of the Gauss-Chebyshev quadratures [6] that take into account the square root singularity of the unknown function near the crack front and, therefore, provide the best possible accuracy when diverting the integral into the discrete form.

For simplicity we further consider rectangular cracks. It can be mentioned that the hydrofracture is often considered as the union of rectangular planar cracks [7], thus the case considered further on has direct application to hydrofracture design provided that certain continuity conditions are introduced for the adjacent rectangles.

8.2 Problem formulation and singular integral equation

Let us consider the configuration depicted in Fig. 8.1 where the domain Ω is rectangular and its long side is parallel to the x-axis, i.e.

$$\Omega = \{(x,y) : |x| < a, |y| < b\}, \quad 0 < b \le a \tag{8.6}$$

The crack is loaded by normal load $P(x,y)$ that can be considered as a superposition of internal and external loads. In this problem the stresses at infinity vanish.

Let us derive a SIE from integro-differential equation (8.1) by using the following relationship

$$\Delta_{xy} \rho(x,y,z) = \rho^{-3}(x,y,z) - 3z\rho^{-5}(x,y,z) \tag{8.7}$$

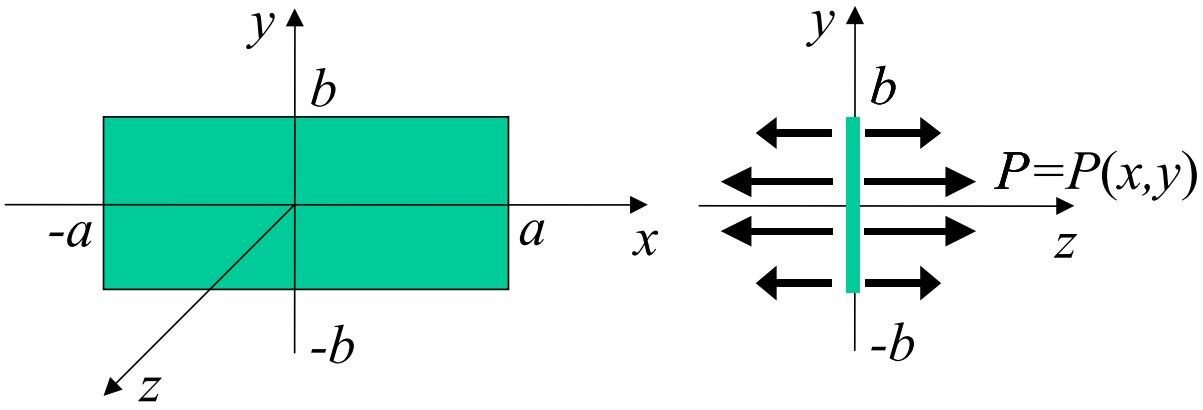

Figure 8.1: Geometry and loads

On the plane $z = 0$ the latter term in the right hand side of (8.7) vanishes and (8.1) takes the following form

$$\int_{-b}^{b}\int_{-a}^{a} \frac{w(x',y')\,dx'dy'}{\rho^3(x-x',y-y',0)} = -\frac{4\pi(1-\nu^2)}{E}p(x,y), \quad (x,y)\in\Omega \tag{8.8}$$

Taking into account that $w(\pm a,y) = w(x,\pm b) = 0$ and the fact that the crack surface near the crack front is of ellipsoidal shape one can present the unknown function $w(x,y)$ in the form

$$w(x,y) = \sqrt{a^2-x^2}\sqrt{b^2-y^2}\frac{w_0x,y)}{\sqrt{ab}}, \quad |x|<a, \quad |y|<b \tag{8.9}$$

where $w_0(x,y)$ is a new unknown dimensionless function continuous in the closed domain.

Evaluating the internal integral in (2.8) by using integration by parts one obtains

$$\int_{-a}^{a} \frac{w(x',y')\,dx'}{\rho^3(x-x',y-y',0)} = \int_{-a}^{a} \frac{(y-y')w'_{x'}(x',y')\,dx'}{(x-x')^2\rho(x-x',y-y',0)} \tag{8.10}$$

Here the non-integral term has vanished due to (8.9). Substitution of (8.10) into (8.8) followed by changing the order of integration and using integration by parts (taking again (8.9) into account) results in the following SIE

$$\int_{-b}^{b}\int_{-a}^{a} \frac{\rho(x-x',y-y',0)\tilde{w}_{x'y'}(x',y')\,dx'dy'}{(x-x')(y-y')} = \frac{4\pi(1-\nu^2)}{E}p(x,y), \quad (x,y)\in\Omega \tag{8.11}$$

It follows from (8.11) that the new unknown function has square root singularity near the crack front. On the other hand the kernel of SIE (8.11) has the form of the singular double integral of the Cauchy type. This fact allows one to use the quadrature formulas of the Gauss-Chebyshev type for the discretisation of SIE (8.11).

Firstly, let us transform (8.11) to the square domain by introducing dimensionless variables as follows

$$x = a\varphi, \quad y = b\psi, \quad x' = a\varphi', \quad y' = b\psi', \qquad |\varphi|<1, \quad |\psi|<1 \tag{8.12}$$

Then

$$\rho(x-x',y-y',0)=a\sqrt{(\varphi-\varphi')^2+\beta^2(\psi-\psi')^2} \tag{8.13}$$

where $\beta=\frac{b}{a}$ is the aspect ratio. The surface displacement function (8.9) takes the form

$$w(a\varphi,b\psi)=\sqrt{ab}\sqrt{1-\varphi^2}\sqrt{1-\psi^2}w_0(\varphi,\psi) \tag{8.14}$$

Secondly, let us seek the unknown function in SIE (8.11) in the form

$$\tilde{w}_{xy}(a\varphi,b\psi)=\frac{\omega_0(\varphi,\psi)}{\sqrt{ab}\sqrt{1-\varphi^2}\sqrt{1-\psi^2}} \tag{8.15}$$

Hereafter we consider $\omega_0(\varphi,\psi)$ as a dimensionless polynomial of the degree n-1 with respect to both variables.

Now one can present the dimensionless form of SIE (8.11) as follows

$$\frac{1}{\pi\sqrt{\beta}}\int\limits_{-1}^{1}\int\limits_{-1}^{1}\frac{\sqrt{(\varphi-\varphi')^2+\beta^2(\psi-\psi')^2}\,\omega_0(\varphi',\psi')d\varphi'd\psi'}{\sqrt{1-\varphi'^2}\sqrt{1-\psi'^2}(\varphi-\varphi')(\psi-\psi')}=\sigma(\varphi,\psi),\quad |\varphi|<1,\quad |\psi|<1 \tag{8.16}$$

Here the right had side of (8.11) has been denoted as

$$\sigma(\varphi,\psi)=\frac{4(1-\nu^2)}{E}P(a\varphi,b\psi) \tag{8.17}$$

It follows from (8.9) that SIEs (8.11) and (8.16) should be complemented by the conditions that express the absence of normal displacements along the crack front. These can be imposed on the functions $w_0(x,y)$ or $\omega_0(\varphi,\psi)$. For the latter these conditions assume the following form

$$\int\limits_{-1}^{1}\frac{\omega_0(\varphi',\psi')d\varphi'}{\sqrt{1-\varphi'^2}}=\int\limits_{-1}^{1}\frac{\omega_0(\varphi',\psi')d\psi'}{\sqrt{1-\psi'^2}}=0 \tag{8.18}$$

We further deal with the formulation given by formulas (8.16) and (8.18).

8.3 Numerical approach

8.3.1 System discretisation and its solution

For numerical solution of the system (8.16)-(8.18) we use the Cartesian product of one- dimensional Gauss-Chebyshev quadrature rules. Therefore the numerical algorithm for the one-dimensional SIE is extended to the two-dimensional SIE without any essential modification of the quadrature formulas. These have the standard form [6] and assume introduction of nodes, ξ_k, and collocation points η_j, on (-1,1) as follows

$$\xi_k=\cos\left(\frac{2k-1}{2n}\pi\right),\quad \eta_j=\cos\left(\frac{j}{n}\pi\right),\quad k=1\ldots n,\quad j=1\ldots n-1 \tag{8.19}$$

Application of the Gauss-Chebyshev rule to SIE (8.16) results in

$$\frac{\pi}{n^2\sqrt{\beta}}\sum_{k=1}^{n}\sum_{j=1}^{n}\frac{\sqrt{(\xi_j-\eta_i)^2+\beta^2(\xi_k-\eta_m)^2}}{(\xi_j-\eta_i)(\xi_k-\eta_m)}X_{j,k}=\sigma(\eta_i,\eta_m),\quad i,m=1\ldots n-1 \tag{8.20}$$

Here the unknowns $X_{j,k}$ have been introduced as the values of the sought function at the nodes

$$X_{j,k} = \omega_0(\xi_j, \xi_k), \quad j,k = 1 \dots n \tag{8.21}$$

The system in (8.20) consists of $(n-1)^2$ equations while the number of unknowns is n^2. In order to make it consistent one should complement (8.20) by $(2n-1)$ homogeneous equations obtained by discretisation of the conditions in (8.18) of the form

$$\sum_{k=1}^{n} X_{k,j} = 0, \quad j = 1 \dots n; \quad \sum_{k=1}^{n} X_{l,k} = 0, \quad l = 1 \dots n-1 \tag{8.22}$$

The system (8.20)-(8.22) has dimension $n^2 \times n^2$, it is solved by a standard procedure built in MathCAD package.

8.3.2 Calculation of COD

Calculation of COD requires integration of the obtained numerical solution, which can be time consuming. Therefore we use the following procedure.

Let us seek the unknown function w_0 as a polynomial with unknown coefficients $c_{m,k}$

$$w_0(\varphi, \psi) = \sum_{m=0}^{n-1} \sum_{k=0}^{n-1} c_{m,k} \varphi^k \psi^m \tag{8.23}$$

Then by substitution of (8.23) into (8.14) followed by differentiation and substitution in (8.15) one finds the following expression for the sought function $\omega_0(\varphi, \psi)$

$$\omega_0(\varphi, \psi) = \sum_{m=0}^{n-1} \sum_{k=0}^{n-1} c_{m,k} [k\varphi^{k-1} - (k+1)\varphi^{k+1}][m\psi^{m-1} - (m+1)\psi^{m+1}] \tag{8.24}$$

As long as the solution for $\omega_0(\varphi, \psi)$ is known, this makes it possible to find the unknown coefficients. This can be accomplished by introducing the matrices $\mathbf{X}=\{X_{j,k}\}$,$\mathbf{C}=\{c_{j,k}\}$ and $\mathbf{M}(\varphi)$ with the coefficients as follows

$$M(\varphi)_{j,k+1} = k\varphi_k^{k-1} - (k+1)\varphi_k^{k+1}, \quad k = 0 \dots n-2, \quad M(\varphi)_{j,n} = k\varphi_k^{n-2}, \quad j = 1 \dots n \tag{8.25}$$

Then the solution of (8.25) can be written in the following matrix form

$$\mathbf{C} = \mathbf{M}^{-1}(\xi) \left[\mathbf{M}^{-1}(\xi)\mathbf{X}\right]^T, \quad \xi = (\xi_1, \dots \xi_n) \tag{8.26}$$

The coefficients of the matrix $\mathbf{C}$ being substituted into (8.23) determine the profile of normal displacements of the crack surfaces. The displacements normalised by the length of the sort side b can be found from (8.14) and (8.23) in the form

$$\frac{w(a\varphi, b\psi)}{b} = \frac{1}{\sqrt{\beta}} \sqrt{1-\varphi^2} \sqrt{1-\psi^2} \sum_{m=0}^{n-1} \sum_{k=0}^{n-1} c_{m,k} \varphi^k \psi^m \tag{8.27}$$

The map of (8.27) is shown in Fig. 8.2 for the case $\beta = 1/3$ and unit uniform load.

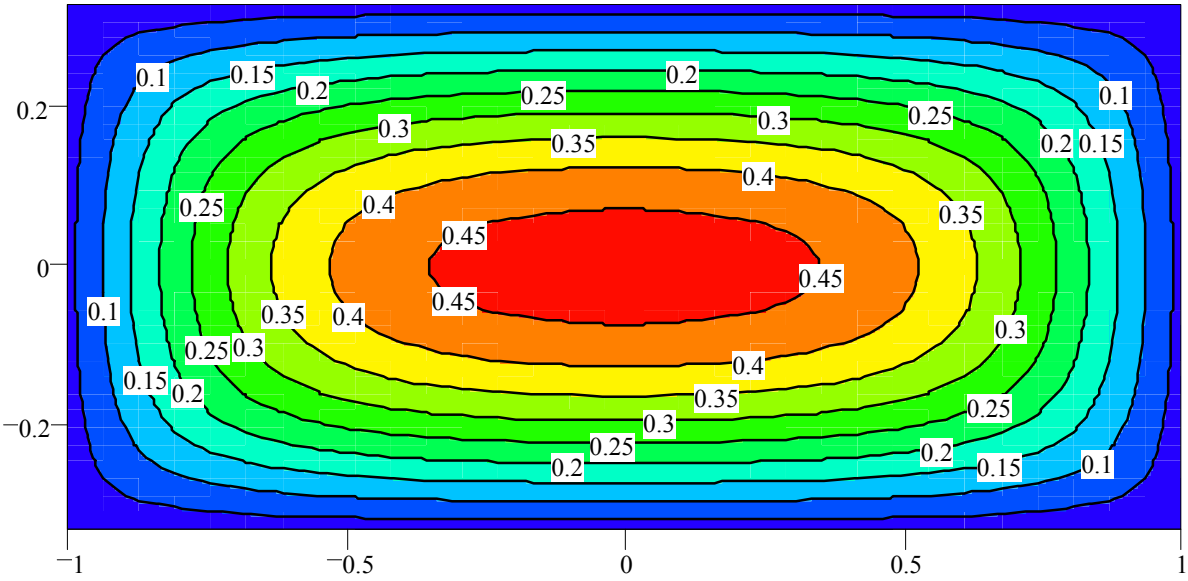

Figure 8.2: The map of crack opening displacements calculated by (8.27) for aspect ratio β=1/3.

8.3.3 Calculation of SIF

Stress intensity factors can be found from the expressions for crack opening in formulas (8.14), (8.23) or (8.28). For the sake of comparison they are normalised by the SIF for 2D crack of the half-length b under uniform load q, which has the form

$$K_I = q\sqrt{\pi b} \tag{8.28}$$

The normalised mode I SIF along the crack front is proportional to the coefficient at the leading term in expansion of COD into power series when φ or ψ tend to unity. Thus the SIFs $K_{I\varphi}$, $K_{I\psi}$ along the long side, sort side respectively are found as follow

$$\frac{K_{I\varphi}(\varphi)}{q\sqrt{\pi b}} = 2\sqrt{1-\varphi^2}w_0(\varphi,1), \quad \frac{K_{I\psi}(\psi)}{q\sqrt{\pi b}} = 2\sqrt{1-\psi^2}w_0(1,\psi) \tag{8.29}$$

The profiles of normalised SIFs are shown in Fig. 8.3 for the case of $q = 1$ and $\beta = 1/3$. It is seen from the figure that the crack profiles along the long side is closed to the value of K_I in (8.28), while the SIF along the sort side are essentially smaller then for plane cracks. The values reported here have been obtained by using 16 nodes that led to the system of 256 unknowns which solution (including of COD) required few seconds. The results for calculations have been quite close to those obtained for $n = 8$ and $n = 32$.

In order to obtain the dimensional SIFs one should multiply the normalised ones by K_I in (8.28), which results in

$$K_{I\varphi}(\varphi) = 2q\sqrt{1-\varphi^2}w_0(\varphi,1)\sqrt{\pi a}, \quad K_{I\psi}(\psi) = 2q\sqrt{1-\psi^2}w_0(1,\psi)\sqrt{\pi b} \tag{8.30}$$

Note that for arbitrary loading the stress q can be considered as a normalisation parameter.

The stress intensity factors for rectangular domains are reported in [1] for the points located at the middle of the longest side a. They vary in the range from 0.75 to 1 depending on the aspect ratio. The results of the present study agree with the results from handbook[1]. For example for the square domain both calculations produce the value for the dimensionless SIF of about 0.75 of the SIF for a planar crack of the length $2b$ loaded by the normal stress of the same

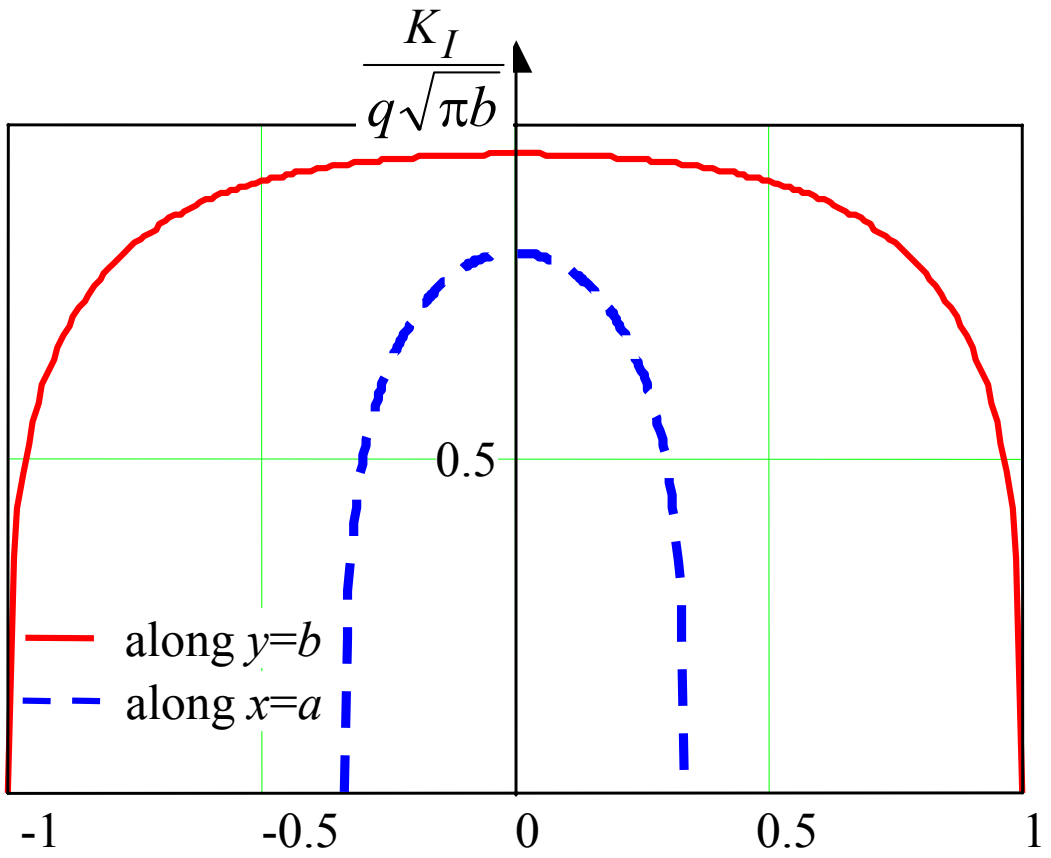

Figure 8.3: Profiles of normalised SIF along short (solid) and long (dashed) sides for aspect ratio β=1/3.

intensity. Moreover the results in [1] seems to be interpolated by using five points for ratios $b/a = 0, 0.5, 0.2, 0.1, 0$, while the present study provides the calculations of SIFs for any given ratio, which does not require much computational resources.

8.4 Discussion and Conclusions

The efficiency of the algorithm has been verified by calculation the mode I SIF along the crack front for the rectangular cracks of different aspect ratios (the ratio of the long side of the rectangular to its short side). It has been found that for uniform normal loads and for $\beta > 3$ the SIF along the long side is close to the one for 2D crack of the length equal to the short side, b. Moreover, not many nodes are required to obtain quite accurate solutions for the cracks with the aspect ratios between $1 < \beta < 10$. However for β of the order 100 and more, the number of the nodes in Gauss-Chebyshev quadratures should be increased to obtain accurate SIF along the short side of the rectangular. For example, for $\beta = 100$, eight nodes are enough to calculate SIF accurately on the long side, while 32 nodes are required to compute the SIF on the short side with the same accuracy.

It is also shown that the developed approach is capable to handle discontinuous loads, which is important in modelling of hydraulic fracture propagation.

This study has presented an effective approach for the determination of fracture characteristics and crack opening for planar rectangular cracks. The method is based on the standard integro-differential equation to derive the SIE suitable for application of the Gauss-Chebyshev quadrature rules. This allows one to apply the most effective numerical formulation for solving

2D SIE, which essentially reduces computational efforts and provides high accuracy.

Acknowledgement

The author is grateful to the RFBR for the financial support of this work.

References

[1] Y. Murakami *Stress intensity factors handbook*, Pergamon Press, 1987.

[2] G.C. Sih *Handbook of Stress Intensity Factors*, Lehigh University, 1973.

[3] M.K. Kassir, G.S. Sih *Three-dimensional crack problems*, Northrop International Publishing, Leyden, 1975.

[4] S. Potapenko E. Atroshchenko, G. Glinka, Stress intensity factors and weight functions for the elliptical and semi-elliptical cracks. In *Proceedings of 12th International Conference on Fracture*, Paper ID fin00935 (2009), 8pp.

[5] M. Ia. Leonov, *On the theory of design of elastic foundations*, PMM Journal of Applied Mathematics and Mechanics, 3(2), (1939) 53–78 (in Russian).

[6] F. Erdogan, G.D. Gupta, *On the numerical solution of singular integral equations*. Quart. Appl. Math. 29 (1972), 525–534.

[7] Meyer and Associates, Users Guide Meyer Fracturing Simulators, 9th ed, 2011.

Chapter 9

Application of Filon-type methods to highly oscillatory integrals arising from the Partition of Unity BEM for 2D wave scattering simulations

Benjamin D. Gilvey[1], Georges A. Wagner[1], Jon Trevelyan[1], Mohammed Seaïd[1] and Jing Gao[2]

[1] School of Engineering and Computing Sciences,
Durham University
South Road
Durham

[2] School of Mathematics and Statistics,
Xian Jiaotong University
Xi'an
China

Abstract. *The Partition of Unity BEM (PU-BEM) is an enriched numerical method in which the fundamental wave behaviour is included within the element formulation. With engineering accuracy in mind, PU-BEM reduces the requirement of 8-10 degrees of freedom per wavelength (when using conventional BEM) to approximately 2.5 degrees of freedom per wavelength. However, in order to take full advantage of the consequent reduction in the size of the system, it is important to develop a method of evaluating the highly oscillatory integrals that arise. Attempts to reduce this expense using numerical steepest descent and/or coordinate transformations enjoy success in some (simpler) cases, but as yet do not offer a robust procedure that can be safely used for all boundary integrals. In the current work we utilise an asymptotic expansion as opposed to the local Taylor expansions relied upon by conventional quadrature schemes. In particular, we employ the Filon scheme of Iserles and Nørsett in which we integrate the highly oscillatory component of our integrals analytically by parts and multiply the results by coefficients of an interpolating polynomial that approximates the non-oscillatory component of our integral. Initial testing on flat elements in the absence of stationary points demonstrates the ability of this method to reach the required precision using a small number of computations.*

9.1 Introduction

Wave propagation and scattering problems are a rich field of study, in which BEM perfoms particularly well when compared with FEM. This is largely due to the fact that discretisation is only required on the boundary rather than having to truncate an entire domain. In the case of an infinite domain, BEM satisfies the Sommerfield radiation condition at infinity by construction, whereas FEM requires artificial boundary conditions and domain truncation. Further improvement is achieved by using PU-BEM [2], which provides highly accurate results and requires significantly fewer degrees of freedom than conventional BEM thanks to its plane wave enrichment. However, this introduces oscillatory behaviour into the integrals which can provide a challenge for traditional quadrature schemes. This inclusion renders it necessary to investigate integration schemes developed for this specific purpose.

In order to frame this problem, we begin by presenting the time-harmonic reduction of the wave equation, the Helmholtz equation

$$\nabla^2 u + k^2 u = 0, \tag{9.1}$$

where the wavenumber $k = 2\pi/\lambda$, in which λ is the wavelength. The unknown potential is u and ∇^2 is the well-known Laplacian operator. Making use of Green's second identity as in [1] this potential can be expressed as

$$\frac{u(p)}{2} + \int_\Gamma \frac{\partial G(p,q)}{\partial \mathbf{n}} u(q) d\Gamma_q = \int_\Gamma \frac{\partial u(q)}{\partial \mathbf{n}} G(p,q) d\Gamma_q + u^i(p), \tag{9.2}$$

where the boundary Γ is assumed to be smooth, hence the first term in (9.2) is divided by 2. The points $p = (x_p, y_p)$ and $q = (x_q, y_q)$ are the so called 'source' and 'field' points respectively, both of which are located on Γ. The vector $\mathbf{n}$ is of unit value and is normal to the boundary, pointing outward. As the focus of this paper remains in two-dimensional space, the Green's function $G(p,q)$ is defined

$$G(p,q) = \frac{i}{4} H_0^{(1)}(kr), \tag{9.3}$$

where $H_0^{(1)}$ is the Hankel function of the first kind and of order zero. The argument of $H_0^{(1)}$ contains the wavenumber and r which is the distance between p and q.

At this point we make the distinction between conventional BEM and PU-BEM. In the the former, the unknown potential over each element is expressed as

$$u = \sum_{j=1}^{J} N_j(\xi) u_j, \tag{9.4}$$

in which N_j refers to the polynomial shape function (typically Lagrangian), u_j are the unknown nodal potential values and J is the number of nodes in the element. In contrast, PU-BEM includes an enrichment in the formulation, expressing the unknown potential as a linear combination of plane waves propagating in different directions, i.e.

$$u = \sum_{j=1}^{J} \sum_{m=1}^{M} N_j(\xi) A_{j,m} e^{ik\mathbf{d}_{j,m}\cdot\mathbf{q}}, \tag{9.5}$$

where $A_{j,m}$ are the unknown plane wave amplitudes, $\mathbf{d}_{j,m}$ are the direction vectors of the plane waves, $i = \sqrt{-1}$ and M is the number of planes waves included per node. We obtain the

integral under investigation by imposing the 'acoustically rigid' Neumann boundary condition in which $\partial u/\partial \mathbf{n} = 0$, discretising the boundary into elements, subsequenty parameterising each element. Hence, when considering a single element, its contribution to the second term of (9.2) in a PU-BEM setting becomes the integral

$$I_2 = -\frac{ik}{4}\int_{-1}^{1} H_1^{(1)}(kr)N_j(\xi)e^{ik\mathbf{d}\cdot\mathbf{q}}\frac{\partial r}{\partial \mathbf{n}_q}J\mathrm{d}\xi, \tag{9.6}$$

where $H_1^{(1)}$ is the Hankel function of the first kind and of order 1, $\xi \in (-1, 1)$ is the parametric coordinate of the element, and J is the Jacobian. The plane wave enrichment function direction $\mathbf{d}$ can be expressed as $(\cos\phi, \sin\phi)$. The focus of this paper is the application of a Filon-type method to the integral (9.6) for the mid-high frequency range.

9.2 Numerical integration

The most dominant method in FEM and BEM is that of Gaussian quadrature, in which the panel sizes are not equal (as in the more rudimentary composite rules). The formula for an 'n' point Gauss scheme is given by

$$\int_a^b f(x)dx \approx \frac{b-a}{2}\sum_{i=1}^{n} w_i f\left(\frac{b-a}{2}x_i + \frac{a+b}{2}\right), \tag{9.7}$$

where x_i and w_i are the abscissas and weights respectively, for $i = 1, ..., n$. The intention is to select appropriate x_i and w_i values in order to create a scheme which is exact when approximating polynomials of degree $2n-1$ or less. A common theme among traditional quadrature schemes is the requirement to increase the number of sub-intervals when the integrand becomes highly oscillatory.

There exist a number of alternatives in the field of asymptotic analysis, such as the asymptotic expansion which is obtained by repeatedly integrating by parts [5]. This expansion benefits from increased accuracy as frequency increases but suffers from a drawback that convergence is not guaranteed for fixed frequency. The method of stationary phase [8] considers the leading contribution of the integral, located in a window surrounding stationary points in the oscillating function. Another alternative is the method of steepest descent also in [8], where the path of integration is deformed into the complex plane, removing the oscillatory behaviour from the kernel. Before moving on to the focus of this paper (Filon-type methods), it is necessary to mention some more recent developments. Firstly, the numerical steepest descent in [3] which applies quadrature methods to integrals arising from the method of steepest descent, and secondly, the Levin-type methods of [9] where the integrand is reformulated in terms of derivatives, and the result is approximated. These asymptotic methods essentially suffer inverse drawbacks when compared with the traditional quadrature schemes in that they require few sample points but only converge for extremely large frequency. Hence, there is a requirement to investigate methods which retain the benefits of asymptotic methods but have a controllable error for a fixed frequency.

The origin of the Filon method [10] dates back to 1928, but is greatly elaborated on by Iserles in [6] and [7], in which the ideas of Filon are extended to integrals of the form

$$I = \int_a^b f(x)e^{ikg(x)}\mathrm{d}x, \tag{9.8}$$

where $f(x)$ and $g(x)$ are 'smooth' functions. There are a variety of Filon-type methods which have been derived from the original, but the premise remains the same in each; $f(x)$ is approximated by a polynomial and the oscillatory kernel is multiplied by the coefficients of that polynomial. This means that the integrand is approximated but then the integral is evaluated analytically. The main difference between approaches under the the umbrella term of Filon-type methods lies in the construction of the interpolating polynomial. A versatile method is that of the Filon-Clenshaw-Curtis (FCC) method [11] where polynomial weights are pre-computed using the Fast Fourier Transform and the function is sampled at the classic Chebyshev locations. A benefit of this method is that no derivative information is required and the pre-computed weights allow applicability to a variety of problems without the requirement of reformulating and solving a new matrix. In the interest of maximising efficiency, however, the authors opt for the scheme of Iserles [4], where $f(x)$ is sampled only at the end points of the interval. The degree of approximating polynomial is increased by providing derivative information rather than adding extra nodes as in the FCC method. An advantage of this method of construction is that it targets the end points which are the key locations in evaluating highly oscillatory integrals.

9.3 Application to a PU-BEM integral

In this preliminary work we consider the integration over a single, flat boundary element having end points $(0,0)$ and $(x_e,0)$, with midpoint $(x_m,0)$. In order to evaluate (9.6) using the Filon method, we must approximate the Hankel function with its asymptotic expansion [12] which is given by

$$H_v(kr) \sim \left(\frac{2}{\pi kr}\right)^{\frac{1}{2}} e^{i(kr-\frac{1}{2}v\pi-\frac{1}{4}\pi)} \sum_{s=0}^{\infty} i^s \frac{a_s(v)}{(kr)^s}, \quad \text{as } (kr)\to\infty, \tag{9.9}$$

with

$$a_s = \frac{(4v^2-1^2)(4v^2-3^2)...(4v^2-(2s-1)^2)}{s!8^s}, \quad a_0(v)=1. \tag{9.10}$$

An alternative approximation will be required for when $(kr)\to 0$, but this is not discussed in the current work. Inserting (9.9) into (9.6) produces

$$I_2 \approx -\frac{i}{4}\left(\frac{2}{\pi}\right)^{\frac{1}{2}} e^{-\frac{3i\pi}{4}} J \sum_{s=0}^{S} i^s \frac{a_s(1)}{k^{s-\frac{1}{2}}} \int_{-1}^{1} f_2(\xi,s) e^{ikg(\xi)} \mathrm{d}\xi, \tag{9.11}$$

where

$$f_2(\xi,s) = \frac{N_j(\xi)(y_q-y_p)}{r^{s+\frac{3}{2}}} \tag{9.12}$$

and

$$g(\xi) = r + \mathbf{d}\cdot\mathbf{q}(\xi) = \sqrt{(x_m(1+\xi)-x_p)^2+y_p^2} + x_m(1+\xi)\cos(\phi). \tag{9.13}$$

Transforming the coordinate of integration to g, and making use of a Hermite polynomial approximation of degree M to f_2, i.e.

$$H_s(g) = h_{s,0} + h_{s,1}g + h_{s,2}g^2 + ... + h_{s,M}g^M \approx f_s(\xi(g),s)\frac{d\xi}{dg} = F_2(g,s), \tag{9.14}$$

subject to the following interpolation conditions:

$$H_s(a) = F_2(a,s) \tag{9.15}$$

$$H_s(b) = F_2(b,s) \tag{9.16}$$

$$H_s'(a) = F_2'(a,s) \tag{9.17}$$

$$H_s'(b) = F_2'(b,s), \tag{9.18}$$

where $a = g(-1), b = g(1)$, produces the following

$$I \approx \sum_{s=0}^{S} \sum_{m=0}^{M} h_{s,m} \int_a^b g^m e^{ikg} \mathrm{d}g. \tag{9.19}$$

The integrals in (9.19) are referred to as 'Filon moments' and can be evaluated analytically by parts. Thus, we require only the solution of a small system of equations to determine the Hermite coefficients $h_{s,m}$ and compute the Filon moments for each value of s.

9.4 Acceptable regions

To achieve 'engineering accuracy' in our overall PU-BEM scheme, numerical tests suggest it is required that the integrals are evaluated to 5 digits of accuracy. Before presenting a numerical example, it is important to determine the areas in which this is obtainable using the above scheme. In particular, at certain locations the integrand in I_2 will become non-oscillatory or 'stationary'. At these stationary points, i.e. where $g'(\xi) = 0$, the overall value of the integral is largely dictated by the behaviour of the integrand in a window surrounding each point.

Setting $g'(\xi) = 0$ it is observed that where there is a stationary point $x_m(1+\xi) - x_p = -r\cos(\phi)$, which is reformulated to provide stationary point locations at $\xi = \xi^*$, where

$$\xi^* = \frac{x_p \pm |y_p \cot(\phi)|}{x_m} - 1. \tag{9.20}$$

In the current work, focus is concentrated on cases in the absence of stationary points i.e. $g'(\xi) \neq 0$ for $\xi \in (-1, 1)$, although this still requires locating stationary points in order to determine the properties of our mapping from $\xi \mapsto g$. We begin by defining x_p and y_p trigonometrically, according to Fig. 9.1.

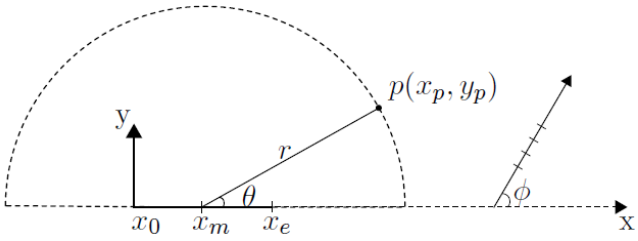

Figure 9.1: Location of source point p and plane wave w.r.t. x-axis.

It can be shown using the definition in (9.20) that when $\theta = \pm\phi$ there is a stationary point at $\xi = 0$ and that on either side of this, $g(\xi)$ is either monotonically increasing or decreasing. This is illustrated in Fig. 9.2 in which ϕ is fixed, θ is varying from $0 \to 2\pi$ and r is varying with respect to the element length x_e. The blue regions are those in which we find acceptable error, and the white regions clearly depict the zones of influence around stationary points.

The symmetry about π that is evident in the figure, combined with the monotonic behaviour of $g(\xi)$ is important as when mapping $\xi \mapsto g$ we must compute $d\xi/dg$ and $d^2\xi/dg^2$ which differ, subject to their location with respect to stationary points. The monotonic behaviour on either side of the stationary point is represented in Fig. 9.3.

A final observation involving stationary point locations is that as either r or k increase, the zone of influence decreases. This is largely due to the asymptotic approximation of (9.9) becoming

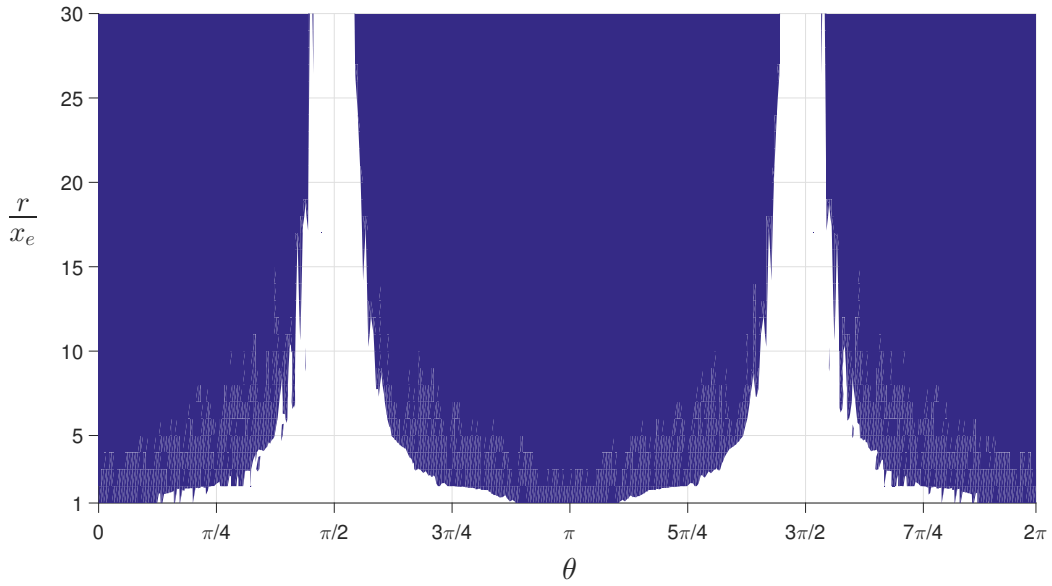

Figure 9.2: Acceptable error for the case $\phi = \pi/2$ and $k = 500$.

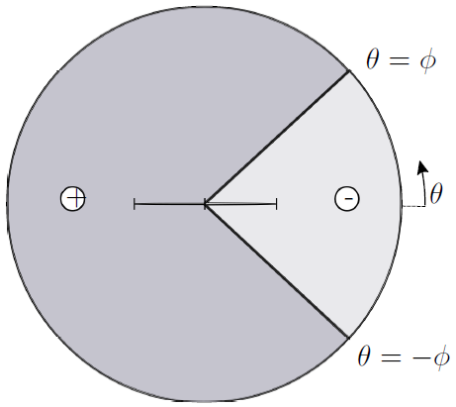

Figure 9.3: Monotonic behaviour of $g(\xi)$ for θ varying around an element with some fixed ϕ.

more valid when its argument increases. This is seen as r/x_e becomes larger in Fig. 9.2 but is also illustrated in Fig. 9.4 by increasing k and observing the narrowing of our 'unacceptable' region.

9.5 Numerical example

A simple example is presented to highlight the efficiency of the above method, taking a $3rd$ degree polynomial. Consider the case of a flat element lying in $y = 0$, setting the input variables $(x_p = -3, y_p = -3, y_q = 0, J = 2, \phi = \pi/3)$ and taking N_j to be the quadratic Lagrangian shape function

$$N(\xi) = -\frac{1}{2}\xi(1-\xi). \tag{9.21}$$

Table 9.1 compares the time taken in seconds to compute the integral using Filon with competing techniques: Gauss-Legendre and trapezium rule. Results were obtained using MATLAB on a 64-bit, core $i7$ desktop.

It is interesting to note from Table 9.1 that as k increases, the Gauss and trapezium methods

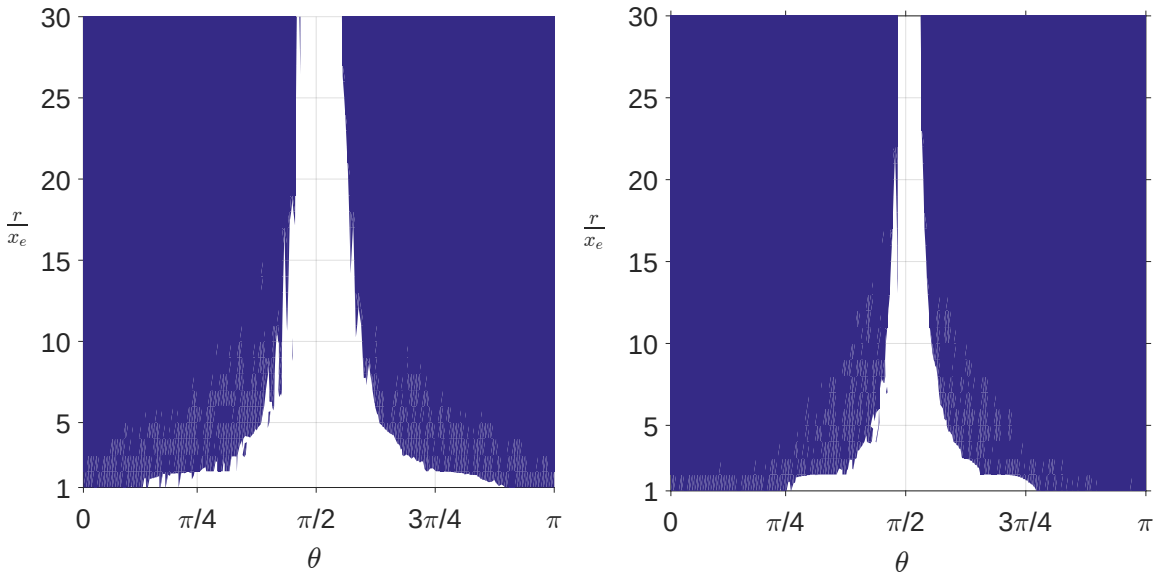

Figure 9.4: Acceptable error for the case $\phi = \pi/2$ and $k = 500$ (left), $k = 2000$ (right).

	Filon		Gauss		Trapezium	
k	time	η	time	η	time	η
500	0.032	$6.63e-07$	0.051	$1.07e-07$	0.733	$1.04e-07$
1000	0.035	$9.42e-08$	0.079	$1.08e-07$	1.412	$1.18e-06$
2000	0.034	$2.33e-08$	0.138	$1.07e-07$	2.787	$1.72e-06$
10000	0.033	$1.41e-09$	0.594	$1.07e-07$	13.792	$2.15e-06$

Table 9.1: Solution time in seconds and relative error η.

require more time to maintain their level of accuracy while the Filon approch not only maintains a shorter run-time but simultaniously increases in accuracy. This accuracy was computed by comparing with a converged Gauss-Legendre result.

9.6 Conclusions

Preliminary testing has shown the Filon method to perform highly effectively in the 'acceptable regions' which comprise the vast majority of cases, proving it to be a promising inclusion in a PU-BEM scheme. It retains the desirable properties of asymptotic methods in that the accuracy increases for higher frequencies but shares the applicability of traditional quadrature schemes. An important consideration is that when moving into three-dimensional space with curved elements, the stationary point cases will constitute a larger proportion of the integrals requiring evaluation. It is therefore necessary to adapt this method to accommodate stationary points and cases with small r in order to design a robust method.

Acknowledgements

The authors are grateful for the financial support awarded by the Royal Society and the National Science Foundation of China under their International Exchanges Scheme.

References

[1] A. A. Becker, *The boundary element method in engineering: a complete course*, McGraw-Hill, Maidenhead, 1992.

[2] E. Perry-Debain, J. Trevelyan and P. Bettess, *Wave boundary elements:a theoretical overview presenting applications in scattering of short waves*, Eng. Anal Bound. Elem., 28 (2004), 131–141.

[3] M. E. Honnor, J. Trevelyan and D. Huybrechs, *Numerical evaluation of 2D partition of unity boundary integrals for Helmholtz problems*, J. Comp. Appl. Math., 234 (2010), 1656–1662.

[4] A. Iserles and S.P. Nørsett, *On quadrature methods for highly oscillatory integrals and their implementation*, BIT, 44 (2004), 755–772.

[5] A. Iserles and S.P. Nørsett, *Efficient quadrature of highly oscillatory integrals using derivatives*, Proc. Royal Soc., 461 (2005), 1383–1399.

[6] A. Iserles, *On the numerical quadrature of highly-oscillatory integrals I: Fourier transforms*, IMA. J. Num. Anal., 24 (2004), 1110–1123.

[7] A. Iserles, *On the numerical quadrature of highly-oscillatory integrals II: Irregular oscillators*, IMA. J. Num. Anal., 25 (2004), 25–44.

[8] F. W. J. Olver, *Asymptotics and special functions*, Academic Press, Inc, New York, 1974.

[9] D. Levin, *Procedures for computing one- and two-dimensional integrals of functions with rapid irregular oscillations*, Math. Comput., 38 (1982), 531–538.

[10] L. N. G. Filon, *On a quadrature formula for trigonometric integrals*, Proc. Royal Soc., 49 (1928), 38–47.

[11] V. Dominguez, I. G. Graham, and V. P. Smyshlyaev, *Stability and error estimates for Filon-Clenshaw-Curtis rules for highly-oscillatory integrals*, IMA J. Numer. Anal., 31 (2011), 1253–1280.

[12] F. W. J. Olver, D. W. Lazier, R. F. Boisvert, C. W. Clark, *NIST Handbook of Mathematical Functions*, Cambridge University Press, New York, 2010.

Chapter 10

A mathematical model of the formation of the chemical trails behind moving cells

Paul J. Harris

School of Computing, Engineering and Mathematics,
University of Brighton
Lewes Road
Brighton

Abstract. *Chemotaxis is the biological process whereby a cell moves in the direction in which the concentration of a chemical in the fluid medium surrounding the cell is increasing. In some cases of chemotaxis, cells secrete the chemical in order to create a concentration gradient that will attract other nearby cells to form clusters. When the cell secreting the chemical is stationary the linear diffusion equation can be used to model the concentration of the chemical as it spreads out into the surrounding fluid medium. However, if the cell is moving then its motion, and the resulting motion of the surrounding fluid, needs to be taken into account in any model of how the chemical spreads out.*

This paper presents a mathematical model for simulating the concentrations of chemical secreted into the surrounding fluid medium from a moving cell. The boundary integral method is used to determine the velocity of the fluid due to the motion of the cell. The concentration of the chemical in the fluid is modelled by the convection-diffusion equation where the fluid velocity term is that given by the boundary integral equation. The resulting differential equation is then solved using the finite element method.

10.1 Introduction

In experimental work in biology it has been widely observed that cells, either singularly or in small clusters, can move in response to the gradient of chemical in the surrounding fluid medium. This process is known as chemotaxis. Whilst in some cases the chemical is simply present in the fluid, in other cases the chemical (in form of proteins) is secreted by a cell in order to signal to and attract other cells (or clusters of cells) in its immediate vicinity. The paper by Nitta et al [11], for example, reports on some typical experiments where chemotaxis has been observed due to the gradient of a chemical which is present in the surrounding fluid.

In much of the existing work, the diffusion-reaction equation has been used to model how the concentrations of a type of cell change in response to changes in the concentration of a chemical signal. Such models are often called Keller-Segel models in the literature (see [1, 5, 7, 8] for

examples of this type of model). However, most of these models only consider the concentrations of the cells and do not model the motion of the individual cells. Further, as they do not consider the motion of the individual cells, these models generally do not include the motion of the surrounding fluid, although the model proposed by [3] does include some effects of the fluid motion. Models of how an individual cell moves in response to the gradient of a chemical in the surrounding fluid have also been proposed, see [4] for example.

In the cases where the chemical is secreted by the cells, the process of how the chemical spreads out through the surrounding fluids has to be taken into account. In recent experimental work there have been observations of proteins being secreted by cells, as reported in [13, 14, 15] for example. In these cases the spread of the chemical can be modelled by the linear diffusion equations as the cells and the surrounding fluid are stationary. However, if the cell is moving the situation is not so straight-forward as both the motion of the cell and resulting motion of the surrounding fluid need to be taken into account.

It is noted here that mathematical models of the biological processes by which a cell synthesizes the chemical or protein that it is secreting have also be developed, see [12, 16] for example. However, such models have not yet been incorporated to the model presented here.

The work in this paper is concerned with modelling how a chemical secreted by a moving cell spreads into the surrounding fluid. The convection-diffusion equation will be used to model how the concentration of the chemical evolves over time. For simplicity the process by which the cell synthesizes the chemical will be modelled using the source term in the governing differential equation and more sophisticated model of how the cell synthesizes the chemical can be incorporated later if necessary. As part of the fluid motion model, the cells are assumed to be rigid bodies as there is experimental evidence that they do not change shape as they move (see the images in [11] for example). Further, it is assumed that the fluid domain is a thin layer so that the vertical motion of the fluid and the vertical variation of the concentration of the chemical can be neglected.The fluid is assumed to be inviscid and incompressible, and the flow is assumed to be irrotational, so that a potential flow model of a rigid body moving through the fluid can be used to determine the fluid velocity at any point in the fluid.

10.2 Mathematical model

The concentration c of a chemical spreading through a fluid domain which is moving with velocity $\mathbf{u}(\mathbf{x}, t)$ can be modelled using the convection-diffusion equation [10]

$$\frac{\partial c(\mathbf{x}, t)}{\partial t} = \nabla \cdot [\mu(\mathbf{x}, t) \nabla c(\mathbf{x}, t)] - \nabla \cdot [c(\mathbf{x}, t)\mathbf{u}(\mathbf{x}, t)] + f(\mathbf{x}, t) \tag{10.1}$$

where $\mu(\mathbf{x}, t)$ is the diffusion parameter and $f(\mathbf{x}, t)$ is a source term. Here the domain Ω of the differential equation is the whole of the (x, y) plane and is partitioned into two sub-domains, Ω_C which contains the cell and Ω_F which contains the fluid exterior to the cell. The values of the diffusion parameter μ and the fluid velocity term $\mathbf{u}$ will depend on which sub-domain $\mathbf{x}$ is in.

10.2.1 Calculation of the fluid velocity

Consider the problem of determining the velocity field in the fluid due to the motion of a rigid cell moving through the fluid. Let Γ denote the boundary of the cell and $\mathbf{v}$ denote the velocity of the cell. As the fluid is assume to be incompressible and inviscid and that the flow is assumed to be irrotational, the velocity $\mathbf{u}(\mathbf{x}, t)$ for any $\mathbf{x} \in \Omega_F$ can be expressed as the gradient of a scalar potential ϕ which satisfies the Laplace equation [9]

$$\nabla^2 \phi = 0.$$

Assuming that the fluid velocity field tends to zero as the distance from the cell increases, Green's theorem can be used to obtain the well known direct boundary integral representation of the fluid velocity potential [6]

$$-\frac{1}{2}\phi(\mathbf{x}) + \int_\Gamma \phi(\mathbf{y})\frac{\partial G(\mathbf{x},\mathbf{y})}{\partial \mathbf{n_y}}\,\mathrm{d}C_\mathbf{y} = \int_\Gamma G(\mathbf{x},\mathbf{y})\frac{\partial \phi(\mathbf{y})}{\partial \mathbf{n_y}}\,\mathrm{d}C_\mathbf{y} \tag{10.2}$$

where $\mathbf{n}$ denotes the unit normal to Γ directed into the fluid domain and

$$G(\mathbf{x},\mathbf{y}) = -\frac{1}{2\pi}\ln(|\mathbf{x}-\mathbf{y}|)$$

is the free-space Green's function for Laplaces equation.

Since the velocity of the cell is known, the continuity of normal velocity on the boundary of each cell gives

$$\frac{\partial \phi(\mathbf{x})}{\partial \mathbf{n}} = \mathbf{v}\cdot\mathbf{n}(\mathbf{x}) = J\mathbf{v} \qquad \mathbf{x}\in\Gamma \tag{10.3}$$

where J is the operator which computes the normal derivative of the potential on the surface of the cell from its velocity. Substituting (10.3) into (10.2) yields a second kind Fredholm equation for the velocity potential ϕ on the boundary of the cell.

Once (10.2) has been solved for the potential ϕ on the boundary of the cell the velocity at any point in the fluid can be computed using

$$\mathbf{u}(\mathbf{x}) = \nabla_\mathbf{x}\phi(\mathbf{x}) = \int_\Gamma \phi(\mathbf{y})\nabla_\mathbf{x}\left(\frac{\partial G(\mathbf{x},\mathbf{y})}{\partial \mathbf{n_y}}\right)\,\mathrm{d}C_\mathbf{y} - \int_\Gamma \nabla_\mathbf{x}\left(G(\mathbf{x},\mathbf{y})\right)\frac{\partial \phi(\mathbf{y})}{\partial \mathbf{n_y}}\,\mathrm{d}C_\mathbf{y} \tag{10.4}$$

for $\mathbf{x}\in\Omega_F$.

10.2.2 Modelling the spread of the chemical

As previously stated, the spread of the chemical through both the fluid medium and the cell can be modelled using equation (10.1). For points $\mathbf{x}$ which are in the fluid the diffusion parameter is μ_F and the velocity term $\mathbf{u}$ is given by (10.4). For points which are in the cell the diffusion parameter is μ_C and the velocity term $\mathbf{u}$ is taken to be the same as the velocity of the cell $\mathbf{v}$.

Here the finite element method will be used to solve (10.1), although this means that the infinite domain Ω of the differential equation is replaced by a finite sized approximate domain Ω_a and a suitable boundary condition has to be applied to the artificial outer boundary. However, truncating the domain should not present any major problems provided that the approximate outer boundary is chosen to be far enough away so that the chemical signal does not change significantly from its initial value for points close to the outer boundary. Here the boundary condition

$$[\mu(\mathbf{x},t)\nabla\tilde{c}(\mathbf{x},t) - \tilde{c}(\mathbf{x},t)\mathbf{u}(\mathbf{x},t)]\cdot\mathbf{n} = 0$$

has been used for simplicity as it avoids the need to calculate any additional finite element boundary terms on the external boundary.

Another potential problem is the motion of the cell. If the finite element mesh is partitioned in to separate parts for Ω_F and Ω_C, then the domain would need to be re-meshed at every time-step and the concentrations interpolated to the new nodes. The alternative is to effectively superimpose the boundary of the cell on top of the finite element mesh and simply use different parameters in the calculation of the stiffness matrix depending on whether a point is in the fluid or in the cell. However, this does mean that for some elements the diffusion parameter and velocity terms will not be continuous over the element.

If $\mathbf{c}$ is used to denote the vector of the value of the concentration at the finite element nodes, and an over-dot is used to represent differentiation with respect to time, applying the finite element method to (10.1) yields [17]

$$M\dot{\mathbf{c}} = K(t)\mathbf{c} + \mathbf{f}(t) \tag{10.5}$$

where

$$M_{ij} = \int_{\Omega_a} \psi_i(\mathbf{x})\psi_j(\mathbf{x})\,\mathrm{d}\mathbf{x}$$

$$K_{ij}(t) = -\int_{\Omega_a} [\mu(\mathbf{x},t)\nabla\psi_j(\mathbf{x}) - \psi_j(\mathbf{x})\mathbf{u}(\mathbf{x},t)] \cdot \nabla\psi_i(\mathbf{x})\,\mathrm{d}\mathbf{x}$$

$$\mathbf{f}_i(t) = \int_{\Omega_a} f(\mathbf{x},t)\psi_i(\mathbf{x})\,\mathrm{d}\mathbf{x}$$

and $\{\psi_1, \psi_2, \ldots, \psi_m\}$ are the finite element basis functions.

10.2.3 Modelling the production of the chemical by the cell

Mathematical models of how a biological cell produces chemicals and/or proteins is an active areas of research [12, 16]. The most sophisticated models simulate the processes that take place inside cells that enable them to produce the chemical signal. However, such detailed processes are not required for the work presented here and it is assumed that the production of the chemical inside the cell can be represented by the source term $f(\mathbf{x},t)$ in (10.1). In the results presented in Section 10.3 the source term function

$$f(\mathbf{x},t) = \begin{cases} \dfrac{R}{2}\left(1 - \cos\left(\dfrac{2\pi t}{T}\right)\right) & \mathbf{x} \in \Omega_C \text{ and } 0 \le t \le T \\ 0 & \text{otherwise} \end{cases}, \tag{10.6}$$

has been used, where R is the rate at which the cell is producing the chemical and T is the time interval over which it is produces the chemical.

10.2.4 Time integration scheme

Let $\mathbf{r}$ denote the position vector of a reference point for the location of the cell. In the cases considered here the reference point will be the centroid of the cell. If subscripts are used to denote the time-step at which a quantity has been calculated, the time-stepping algorithm used here is as follows:

1. Calculate the location of the cells reference point at the new time-step using

   $$\mathbf{r}_{n+1} = \mathbf{r}_n + h\mathbf{v}$$

   where h is the length of the time-step. As this is a potential flow model with just one rigid cell there are no hydrodynamic or external forces acting on the cell so its velocity does not change. However, if there is more than one cell then the hydrodynamic forces and acceleration of the cells needs to be taken into account.

2. Use the location of the reference point to determine the locations of the boundary elements and then use the boundary integral equation (10.2) with the boundary condition given by (10.3) to calculate the velocity potential. Here the Galerkin boundary element method with linear elements was used to calculate the results presented in Section 10.3.

3. Calculate K_{n+1}, the finite element stiffness matrix at the new time-step, using either (10.4) to calculate $\mathbf{u}$ for $\mathbf{x} \in \Omega_F$ or $\mathbf{u} = \mathbf{v}$ for $\mathbf{x} \in \Omega_C$. Also calculate the vector $\mathbf{f}_{n+1}$ from the source term (10.6).

4. Calculate the concentrations of the chemical at the new time-step by solving [2]

$$(2M - hK_{n+1})\,\mathbf{c}_{n+1} = (2M + hK_n)\,\mathbf{c}_n + h\,(\mathbf{f}_n + \mathbf{f}_{n+1})\,. \tag{10.7}$$

   where K_n and $\mathbf{f}_n$ from the previous time-step are reused.

5. Repeat for the next time-step.

10.3 Numerical results

The results presented in this paper were calculated using the different finite element meshes described in Table 10.1. For each mesh the approximate domain Ω_a was the square $-11 \leq x, y \leq 11$. For all of the results presented here the values $\mu_F = 0.05$ and $\mu_C = 0.1$ were used.

Mesh	Number of Nodes	Number of Elements
A	7,921	15,488
B	31,329	61,952
C	124,609	247,808
D	497,025	991,232

Table 10.1: Details of the finite element meshes used.

The first example is a circular cell of radius 1 unit moving horizontally from left to right (so $v_x = 1$ and $v_y = 0$). The values $R = 1$ and $T = 1$ were used in the source term given by (10.6) and 20 boundary elements were used to calculate the fluid velocity potential at each time-step. The maximum value of the concentration at nodes close to the outer edge of the finite element mesh was less than 6×10^{-10} which is of the order of the level of precision used in the iterative method used to solve the linear system (10.7). This demonstrates that it is reasonable to use the approximate domain Ω_a for solving this problem as by the end of the calculations the chemical has not had time to spread to the outer edge of the finite element mesh.

Figure 10.1 shows the norm of the difference in the concentrations calculated using meshes A, B and C are compared to the concentrations calculated using mesh D. The results presented in this graph show that the finite element method is converging as the mesh is refined. Figure 10.2 shows the norm of the difference in the concentrations when using different boundary element meshes to calculate the fluid velocity potential with finite element mesh B. Here the values of the concentration are compared to those where the fluid velocity potential has been calculated using an exact dipole approach. As expected, refining the boundary element mesh leads to a smaller difference between the concentrations calculated using the boundary element method and those calculated using the dipole method.

Figure 10.3 shows the chemical concentrations for the circular cell calculated using mesh D and 20 boundary elements for the fluid velocity potential, showing that the cell leaves a trail of the chemical as it moves through the fluid.

Figure 10.4 shows the chemical concentrations secreted by a moving cell which is not circular calculated using finite element mesh D. The radius of the circular end-caps of the cell were 1 unit and the length of the straight sides were also 1 unit. The velocity of this cell was $v_x = 1$ and $v_y = 0$ and the values $R = 1$ and $T = 1$ were used in the source term (10.6). The fluid velocity potential for this cell was computed using 82 boundary elements. The results again show that the cell leaves a trail of the chemical as it moves through the fluid. The concentrations in the

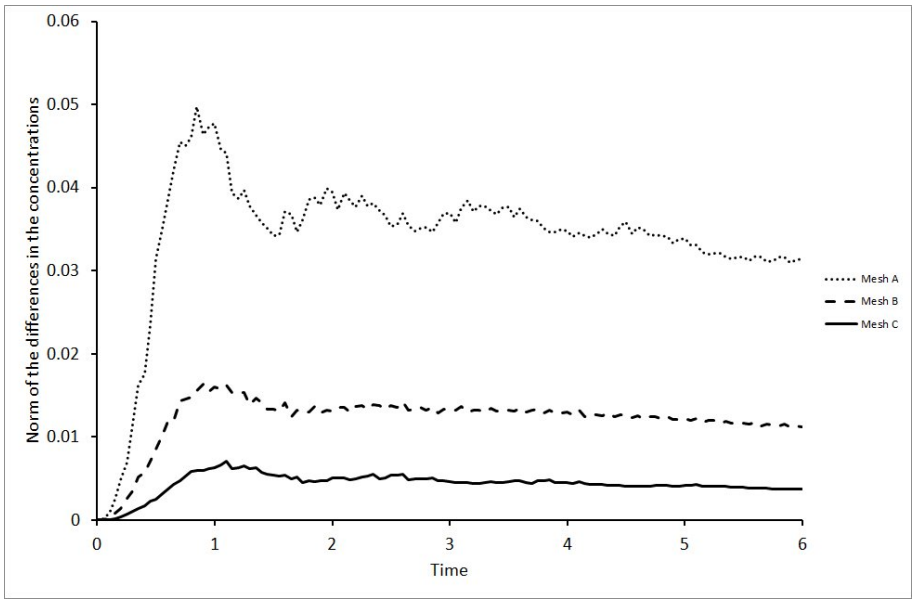

Figure 10.1: The differences in the concentrations obtained using finite element meshes A, B and C when compared to the concentrations obtained using mesh D.

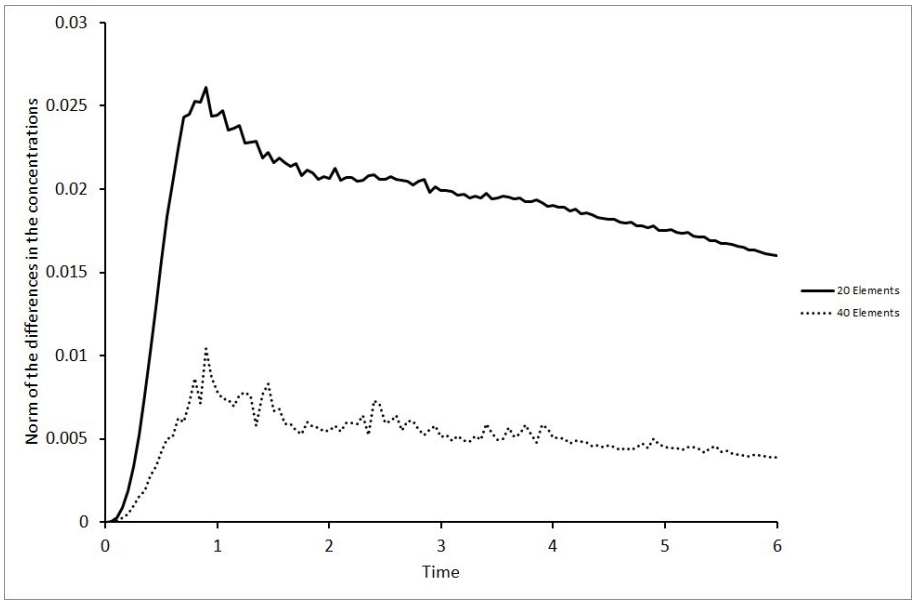

Figure 10.2: The differences in the concentrations obtained using linear boundary element meshes with 20 and 40 when compared to the concentrations obtained a dipole model of the fluid velocity potential.

trail are higher for this non-circular cell as the area of the this cell is larger than the area of the circular cell meaning that overall it synthesizes more of the chemical over the same period of time.

10.4 Conclusions

The results in this paper show that using the finite element finite method to solve convection-diffusion equation where the boundary integral method is used to determine the motion of the

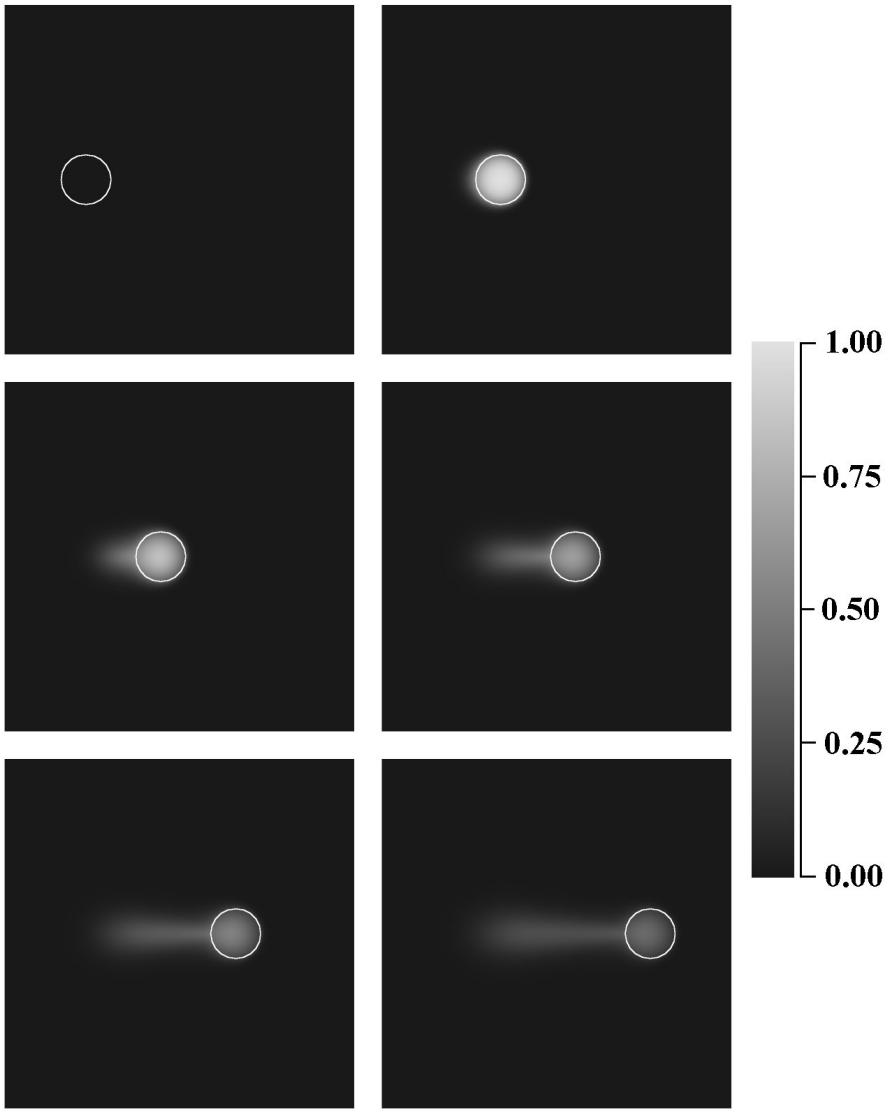

Figure 10.3: The concentrations of the a chemical secreted by moving circular cell at times $t = 0$ (top left), $t = 1$ (top right), $t = 2$ (middle left), $t = 3$ (middle right), $t = 4$ (bottom left) and $t = 5$ (bottom right).

fluid is an accurate method for modelling how a chemical secreted from a moving cell spreads out into the surrounding fluid medium. In particular, the model shows how a cell can leave a trail of the chemical in its wake as it moves through the fluid. The use of the boundary integral method for the determining the velocity of the fluid means that the model can be used to simulate the secretions from a cell which is not circular in shape.

This model is a partial development of a full simulation of how a cell, or group of cells, move due to chemotaxis where a chemical is secreted by one cell in order to signal to other nearby cells. However, an effective mathematical model of how a cell senses the chemical signal (and/or the gradient of the signal) and moves in response to that signal needs to be developed. A model, such as the one proposed by Elliott et al [4], where the cell moves by changing shape could be used. However, there is some experimental evidence that the cells essentially move a rigid bodies and it may be possible to devise a less complicated model of how a cell moves in response to the chemical signal.

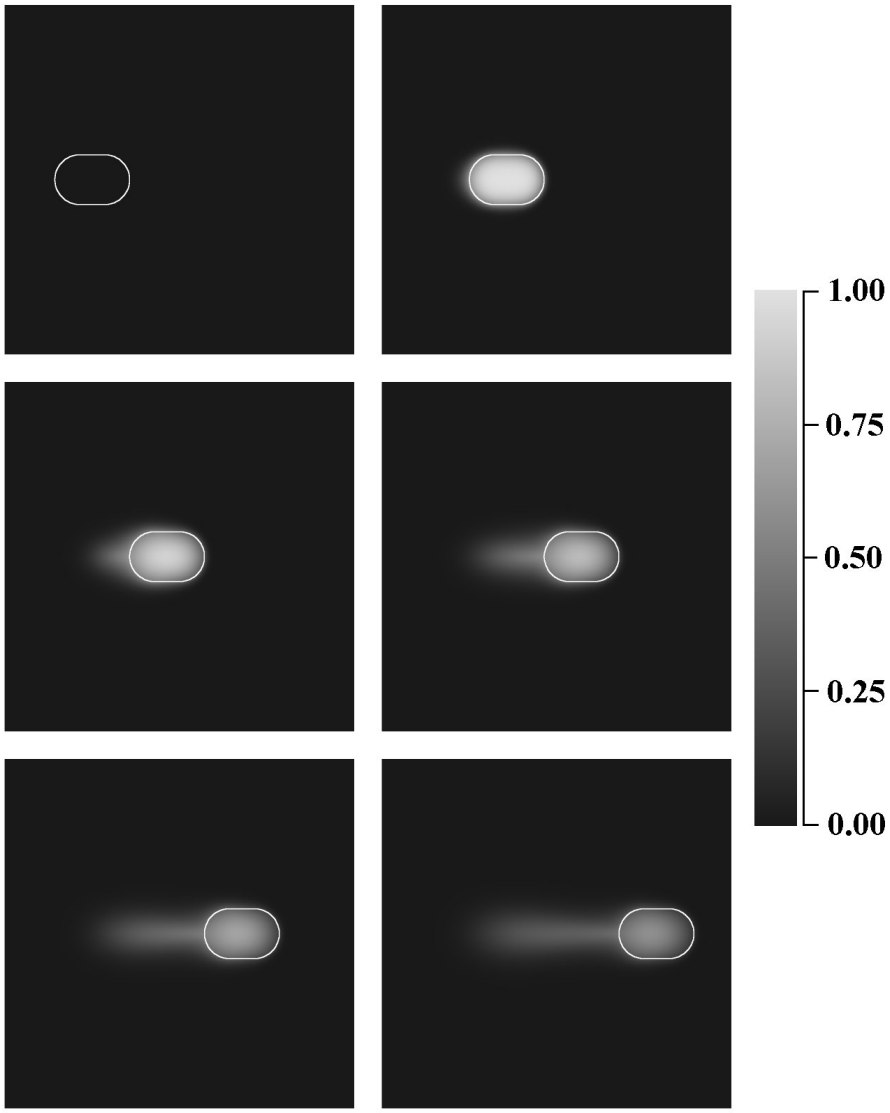

Figure 10.4: The concentrations of the a chemical secreted by moving cells at times $t = 0$ (top left), $t = 1$ (top right), $t = 2$ (middle left), $t = 3$ (middle right), $t = 4$ (bottom left) and $t = 5$ (bottom right).

The fluid mechanics model would also need to be modified for cases where there is more than one cell. For a single isolated cell moving through a fluid with a simple potential flow model, it is well known that there are no hydrodynamic forces on the cell. However, if there is more than one cell it is possible for the motion of one cell to cause a pressure force on a second cell, and vice versa.

Acknowledgement

The author would like to thank Matteo Santin and Gary Phillips from The Brighton Centre for Regenerative Medicine for their help and advice with the biological aspects of this work.

References

[1] A. Chertock, A. Kurganov, X. Wang and Y. Wu, *On a chemotaxis model with saturated chemotactic flux*, Kin. and Rel. Mod, 5(1), (2012), 51 – 95.

[2] J. Crank and P. Nicolson *A practical method for numerical evaluation of solutions of partial differential equations of the heat-conduction type* Mathematical Proceedings of the Cambridge Philosophical Society, 43(1), (1947), 50 – 67.

[3] Y. Deleuze, C. Chiang, M. Thiriet and A. W. H. Sheu *Numerical study of plume patterns in a chemotaxis-diffusion-convection coupling system*, Computers & Fluids, 126, (2016), 58 – 70.

[4] C. M. Elliott, B. Stinner, B. and C. Venkataraman *Modelling cell motility and chemotaxis with evolving surface finite elements* J. R. Soc. Interface, 9, (2012), 3027 – 3044.

[5] H. Gajewski and K. Zacharias, *Global behaviour of a reaction - diffusion system modelling chemotaxis*, Math. Nachr, 195, (1998), 77 – 114.

[6] M. A. Jaswon and G. T. Symm. *Integral equation methods in potential theory and elastostatics.* Academic Press, London, UK, 1977.

[7] E. F. Keller and L. A. Segel, *Model for chemotaxis*, J. Theor. Biol. 30, (1971) 225 – 234.

[8] I. R. Lapidus and R. Schiller, *A mathematical model for bacterial chemotaxis*, Biophys. J., 14, (1974), 825 – 834.

[9] M. J. Lighthill. *An informal introduction to theoretical fluid mechanics.* IMA Monograph Series, Oxford University press, Oxford, UK, 1986.

[10] S. E. Malawista, A. D. Chevance and L. A. Boxer The mathematics of diffusion. In *An Introduction to Mathematical Physiology and Biology*, Cambridge University Press, Cambridge, UK, 1999.

[11] N. Nitta, T. Tsuchiya, A. Yamauchi, T. Tamatani and S. Kanegasaki. *Quantitative analysis of eosinophil chemotaxis tracked using a novel optical device TAXIScan.* Journal of Immunological Methods, 320, (2007), 155 – 163.

[12] M. G. Pedersen, A. Tagliavini, G. Cortese, M. Riz and F. Montefusco *Recent advances in mathematical modeling and statistical analysis of exocytosis in endocrine cells.* Mathematical Biosciences, 283, (2017), 60 – 70.

[13] D. Raghu, J. A. Christodoulides, J. B. Delehanty, J. M. Byers and M. P. Raphael *A Label-free Technique for the Spatio-temporal Imaging of Single Cell Secretions*, JOVE-Journal Of Visualized Experiments, 105, (2015).

[14] M. P. Raphael, J. A. Christodoulides, J. B. Delehanty, J. P. Long and J. M. Byers *Quantitative Imaging of Protein Secretions from Single Cells in Real Time*, BiophysicaL Journal, 105(3), (2013), 602 – 608.

[15] Y. Shirasaki, M. Yamagishi, N. Suzuki, K. Izawa, A. Nakahara, J. Mizuno, S. Shoji, T. Heike, TY. Harada, R. Nishikomori and O. Ohara *Real-time single-cell imaging of protein secretion*, Scientific Reports, 4 (2014).

[16] T. von der Haar *Mathematical and computational modelling of ribosomal movement and protein synthesis: an overview*, Computational and Structural Biotechnology Journal, 1(1), (2012).

[17] O. C. Zienkiewicz and R. L. Taylor. *The finite element method Vols 1 and 2*, McGraw-Hill, London, UK, 1991.

Chapter 11

Nyström-type discretisations of integral equations for inverse scattering in waveguides

Rebecca K. Haunton and Simon N. Chandler-Wilde

Department of Mathematics and Statistics,
University of Reading
Berkshire
UK

Abstract. *The solution of integral equations is a necessary step in many methods for solving inverse scattering problems, not least the Point Source Method of Potthast (IMA J. Appl. Math. 61, 119-140, 1998), which has recently been modified and developed (Proceedings of IoA: Acoustics 2016. 38(1), 306-316, 2016) to apply to inverse scattering in waveguides. This involves the solution by Tikhonov regularisation of an ill-posed, first-kind Fredholm equation whose kernel is the Green's function for a uniform sound hard waveguide with no obstruction.*

For numerical implementation purposes, discretisation of this integral equation is required, and we propose and implement a Nyström-type method. We show that this can be interpreted as a semi-discrete variant of the PSM in a waveguide, and that many of the convergence theorems from the analysis of the continuous version of the PSM in a waveguide can be carried over to this semi-discrete form.

11.1 Introduction

We consider the *inverse scattering problem* of detection and characterisation of obstructions in waveguides, with the application in mind of sewer pipe inspection by acoustic means. There has been considerable recent interest [1, 7] in acoustic methods as a cost effective alternative to CCTV, the methods of [1, 7] employing clever heuristic signal processing and pattern matching techniques. A popular algorithm in inverse scattering, the so-called *Linear Sampling Method (LSM)*, has also been employed in a waveguide configuration, [2, 6] providing 3D computational experiments for acoustic detection of the position and shape of an obstacle within a waveguide. These numerical experiments are somewhat encouraging, demonstrating very accurate reconstructions of the position and shape of a number of obstacles. However, the method fails in the simplest case where there is a complete blockage of the pipe. Additionally, the number of acoustic measurements required (many microphone positions and many acoustic source positions) makes the method much less attractive than the more heuristic methods of [1, 7].

Another well-known inverse scattering algorithm, the *Point Source Method (PSM)* [8, 9] has also been adapted [3, 4] for a two-dimensional waveguide configuration, notable advantages of this method over the LSM being the reduced number of measurements required (many microphone positions but only a single source position), and the successful detection of the obstruction in the complete blockage case. In this paper we look in more detail at the PSM for a waveguide, and in particular at the ill-posed, first-kind integral equation the method requires us to solve. We consider a discrete version of the PSM with finite measurement data and show some theoretical results analogous to the analysis of the PSM at the continuous level. We also show that this can be interpreted instead as an application of the Nyström method, using the composite midpoint rule, to the original continuous integral equation. We present some results from numerical simulations, for a single time-harmonic point source and 15 remote measurements, showing accuracy of the method.

11.2 Inverse Scattering in Waveguides

Assume a time-harmonic acoustic source ($e^{-i\omega t}$ time dependence) at some point z in a two-dimensional waveguide of width $L > 0$. Assume further the waveguide contains a sound-soft scattering object Γ and let D denote the domain of propagation given that the point source is located at z, that is, D is the connected component of the waveguide exterior to Γ that contains z. We focus specifically on the case where Neumann (sound-hard) conditions hold on the walls of the waveguide $\partial D := \overline{D} \cap \{y : y_2 = 0 \text{ or } L\}$ (as usual, $\overline{D}$ denotes the closure of D).

Where c is the sound speed, let $k = \omega/c$ denote the wavenumber. The complex acoustic pressure field satisfies the Helmholtz equation

$$\Delta u + k^2 u = -\delta_z \text{ in } D, \tag{11.1}$$

where δ_z is a Dirac delta function supported at z, and the Dirichlet condition

$$u = 0 \text{ on } \Gamma.$$

Vertical propagation of the acoustic field is restricted by the walls of the waveguide, explicitly

$$\frac{\partial u}{\partial n} = 0 \quad \text{on } \partial D, \tag{11.2}$$

whereas horizontal propagation out to infinity is governed by the standard waveguide *partial radiation conditions*, the requirement that, for some constants $a_- < a_+$, it holds that

$$u(x) = \sum_{n=0}^{\infty} C_n^- e^{-\mathrm{i}\beta_n x_1} \cos(\alpha_n x_2), \quad x = (x_1, x_2) \in \bar{D},\ x_1 \le a_-, \tag{11.3}$$

$$u(x) = \sum_{n=0}^{\infty} C_n^+ e^{\mathrm{i}\beta_n x_1} \cos(\alpha_n x_2), \quad x \in \bar{D},\ x_1 \ge a_+. \tag{11.4}$$

Here

$$\alpha_n := \frac{n\pi}{L},$$

$$\beta_n := \begin{cases} \sqrt{k^2 - \alpha_n^2}, & \text{if } \alpha_n \le k, \\ \mathrm{i}\sqrt{\alpha_n^2 - k^2}, & \text{otherwise,} \end{cases}$$

and $C_n^{\pm}$ are complex constants. Throughout we impose the condition that the wavenumber k lies in the set

$$\mathbb{R}_L := \mathbb{R}^+ \setminus \left\{ \frac{n\pi}{L} : n \in \mathbb{Z} \right\}, \tag{11.5}$$

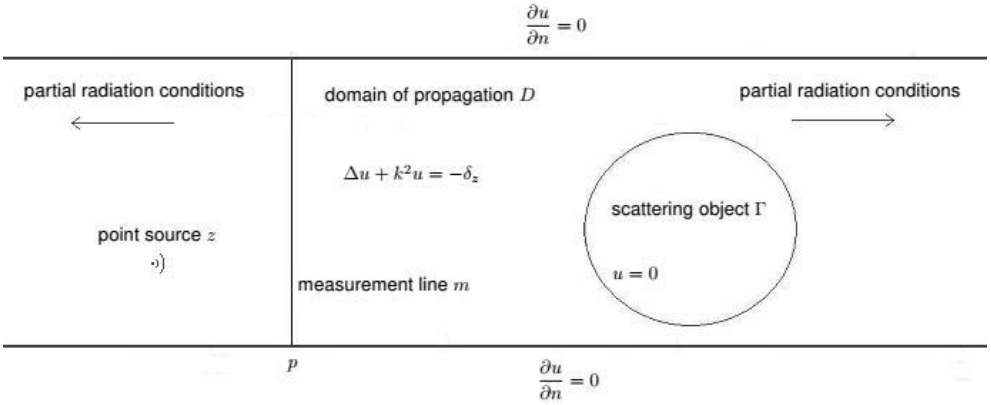

Figure 11.1: The inverse scattering problem in a two-dimensional waveguide.

since the solution to this problem, even in the absence of an obstacle, blows up as k approaches this set. Note that $k \in \mathbb{R}_L$ if and only if $\beta_n \neq 0$, for all $n \in \mathbb{Z}$.

Let Φ_k^L be defined by

$$\Phi_k^L(x,z) := \sum_{n=0}^{\infty} \frac{c_n}{\beta_n} e^{\mathrm{i}\beta_n |x_1 - z_1|} \cos(\alpha_n x_2), \tag{11.6}$$

where

$$c_0 := \frac{\mathrm{i}}{2L},\ c_n := \frac{\mathrm{i}}{L}\ \cos(\alpha_n z_2),\ n = 1, 2, ..$$

$\Phi_k^L(\cdot, z)$ is the Neumann Green's function for the waveguide, i.e. the total acoustic field due to a point source excitation at z when the waveguide contains no obstruction. We note that (11.5) ensures that (11.6) is well defined.

Let

$$\gamma := \{(p, x_2) : 0 \leq x_2 \leq L\}, \tag{11.7}$$

for some $p \in \mathbb{R}$, denote a vertical cross-section of the waveguide, along which we measure the acoustic field. We assume the measurement line γ, like the point source z, lies to the left of the scattering object Γ, as in Figure 11.1. The inverse scattering problem we then consider is the following:

Given a sound-soft bounded object or blockage $\Gamma \subset D$ and noisy measurements of the total field $G_k^{L,\delta}(x,z)$ for $x \in \gamma$, and a single source position $z \in D \setminus \gamma$, determine the location of Γ.

Here $\delta > 0$ is the noise level and it holds that the L^2 norm of the error in the measured data,

$$\left\| G_k^{L,\delta}(\cdot, z) - G_k^L(\cdot, z) \right\|_{L^2(\gamma)} \leq \delta. \tag{11.8}$$

To solve this inverse scattering problem, we employ an adaptation to waveguides [3, 4] of the *point source method* for scattering by obstacles in free space proposed by [8, 9]. This method initially reconstructs the total field $G_k^L(x^*, z)$, at locations x^* in the domain. This reconstruction is given by

$$G_k^{L,\alpha,\delta}(x^*, z) := \Phi_k^L(x^*, z) + \int_\gamma \left[G_k^{L,\delta}(y, z) - \Phi_k^L(y, z) \right] \phi_{x^*}^\alpha(y)\, ds(y), \tag{11.9}$$

where $G_k^{L,\delta}(y, z)$ for $y \in \gamma$ is the (known, noisy) measured data, and $\phi_{x^*}^\alpha$ is the solution of a first kind integral equation regularised with regularisation parameter $\alpha > 0$. It is shown in [3, 4] why

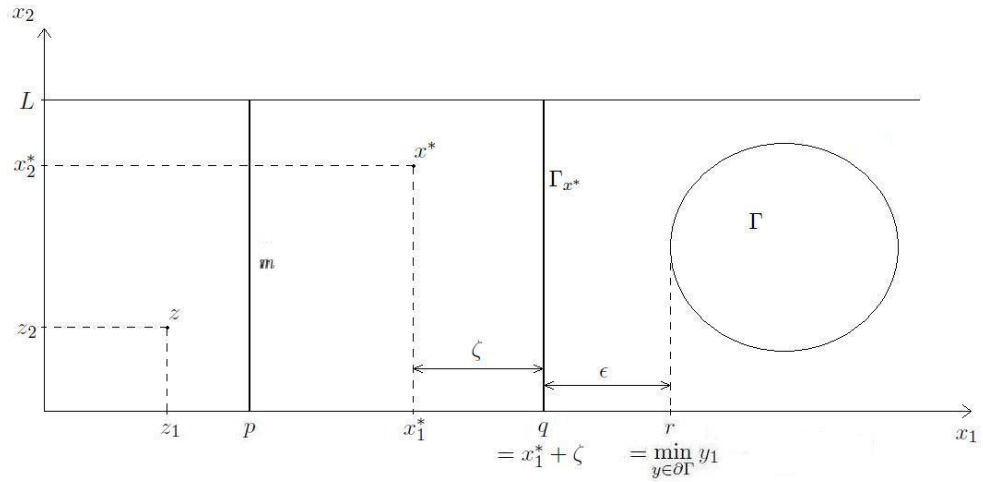

Figure 11.2: The setup required for the application of the Point Source method in a waveguide.

(11.9) is an appropriate approximation, and proven that, at least for some locations x^* in the waveguide, (11.9) converges to the true total field as $\alpha, \delta \to 0$.

For $x^* \in D$ and $\zeta > 0$, let

$$q := x_1^* + \zeta,$$

and let Γ_{x^*} denote the finite vertical line

$$\Gamma_{x^*} = \{(x_1^* + \zeta, x_2) : 0 < x_2 < L\}$$

as in figure 11.2.

The function $\phi_{x^*}^\alpha$ is defined as an approximate solution of the integral equation

$$\int_\gamma \Phi_k^L(x, y)\phi_{x*}(y)\, ds(y) = \Phi_k^L(x, x^*),\ x \in \Gamma_{x^*}. \tag{11.10}$$

In operator form (11.10) is given by

$$K\phi_{x*} = g \tag{11.11}$$

where $g(x) = \Phi_k^L(x, x^*)$ and the integral operator $K : L^2(\gamma) \to L^2(\Gamma_{x^*})$ is defined by

$$K\psi(x) = \int_\gamma \Phi_k^L(x, y)\psi(y)\, ds(y),\ x \in \Gamma_{x^*}. \tag{11.12}$$

The equation (11.11) has no exact solution, but can be solved approximately to arbitrary accuracy since the operator K has dense range [3, 4]. To do this we employ Tikhonov regularisation, calculating $\phi_{x^*}^\alpha \in L^2(\gamma)$ as the unique solution of

$$\alpha\phi_{x^*}^\alpha + K^*K\phi_{x^*}^\alpha = K^*g, \tag{11.13}$$

where K^* denotes the adjoint of K. We have shown previously the following [4, 3]

Theorem 1. *Suppose for all $y = (y_1, y_2) \in \Gamma$,*

$$y_1 > x_1^* + \zeta,$$

and let $G_k^{L,\alpha,\delta}$ be the approximation for the total field defined by (11.9)*. Then there exists a constant C, independent of δ and α, such that*

$$\left|G_k^{L,\alpha,\delta}(x^*, z) - G_k^L(x^*, z)\right| \leq C\left\|K\phi_{x^*}^\alpha - g\right\|_{L^2(\Gamma_{x^*})} + \frac{\delta}{\sqrt{\alpha}}\left\|g\right\|_{L^2(\Gamma_{x^*})}.$$

Further, if we choose $\alpha = \alpha(\delta)$ *such that*

$$\alpha(\delta) \to 0 \text{ and } \frac{\delta^2}{\alpha(\delta)} \to 0, \text{ as } \delta \to 0,$$

then

$$\left| G_k^{L,\alpha,\delta}(x^*, z) - G_k^L(x^*, z) \right| \to 0,$$

as $\delta \to 0$.

11.3 A Point Source Method with finite measurement data

In this section we discuss the main concern of this paper, namely a discrete version of the PSM in a waveguide, requiring only finite measurements. We shall see this can be interpreted as a Nyström method approximation, using the composite midpoint rule, to the integral equation (11.11). We initially consider the semi-discrete operator $K_M : \mathbb{C}^M \to L^2(\Gamma_{x^*})$ defined by

$$K_M \boldsymbol{\psi}(x) := \frac{L}{M} \sum_{j=1}^{M} \Phi_k^L(x, y_j)\psi_j, \ x \in \Gamma_{x^*}, \tag{11.14}$$

where $y_j = (p, (j - 1/2)L/M) \in \gamma, j = 1, .., M$, are discrete measurement points and $\boldsymbol{\psi} = (\psi_1, .., \psi_M)^T \in \mathbb{C}^M$. By definition, for $\psi \in L^2(\Gamma_{x^*})$, $K_M^* : L^2(\Gamma_{x^*}) \to \mathbb{C}^M$ is given by

$$(K_M^* \psi)_i = \frac{L}{M} \int_{\Gamma_{x^*}} \overline{\Phi_k^L(x, y_i)}\psi(x)ds(x), \ i = 1, .., M,$$

so $K_M^* K_M : \mathbb{C}^M \to \mathbb{C}^M$, is given by

$$\begin{aligned}(K_M^* K_M \boldsymbol{\psi})_i &= \left(\frac{L}{M}\right)^2 \sum_{j=1}^{M} \left[\int_{\Gamma_{x^*}} \overline{\Phi_k^L(x, y_i)} \Phi_k^L(x, y_j) ds(x) \right] \psi_j, \\ &= \left(\frac{L}{M}\right)^2 \sum_{j=1}^{M} a(y_i, y_j)\psi_j, \ i = 1, .., M,\end{aligned}$$

where

$$a(x, y) := \int_{\Gamma_{x^*}} \overline{\Phi_k^L(z, x)} \Phi_k^L(z, y) ds(z), \ x, y \in \bar{\gamma}.$$

Further,

$$(K_M^* g)_i = \frac{L}{M} \int_{\Gamma_{x^*}} \overline{\Phi_k^L(x, y_i)} g(x) ds(x) = \frac{L}{M} \left(K^* g\right)(y_i).$$

The discrete PSM approximation to the total field is then given by

$$\begin{aligned}G_k^{L,\alpha_1,\delta,M}(x^*, z) &:= \Phi_k^L(x^*, z) \\ &\quad + \frac{L}{M} \sum_{j=1}^{M} \left[G_k^{L,\delta}(z, y_j) - \Phi_k^L(z, y_j) \right] \left(\boldsymbol{\phi}_{x^*,M}^{\alpha_1} \right)_j,\end{aligned} \tag{11.15}$$

where $\boldsymbol{\phi}_{x^*,M}^{\alpha_1}$ is the approximate solution of $K_M \boldsymbol{\phi}_{x^*,M}^{\alpha_1} = g$. Precisely, we find $\boldsymbol{\phi}_{x^*,M}^{\alpha_1} \in \mathbb{C}^M$ as the solution of

$$\left(\alpha_1 I_M + K_M^* K_M\right) \boldsymbol{\phi}_{x^*,M}^{\alpha_1} = K_M^* g, \tag{11.16}$$

for some $\alpha_1 \geq 0$. That is, to solve the linear system

$$\alpha_1 \left(\boldsymbol{\phi}^{\alpha_1}_{x^*,M}\right)_i + \left(\frac{L}{M}\right)^2 \sum_{j=1}^{M} a(y_i, y_j) \left(\boldsymbol{\phi}^{\alpha_1}_{x^*,M}\right)_j = \frac{L}{M} \left(K^* g\right)(y_i), \ i = 1, .., M. \tag{11.17}$$

Remark 1. *We have introduced the above scheme* (11.16) *as a discrete version of the PSM in a waveguide. It does, however, have another interpretation. The linear system* (11.17) *is precisely the same linear system obtained applying the Nyström method [5] to* (11.13) *using the composite midpoint rule, provided*

$$\alpha_1 = \frac{L}{M}\alpha.$$

We claim the following regarding the semi-discrete operator K_M.

Lemma 1. *For every positive integer M, the semi-discrete operator K_M as defined by* (11.14) *is injective.*

Corollary 1. *For every positive integer M and for every $\alpha_1 \geq 0$, equation* (11.16) *has exactly one solution $\boldsymbol{\phi}^{\alpha_1}_{x^*,M} \in \mathbb{C}^M$, and this solution is the (unique) minimiser of*

$$\alpha_1^2 \left\|\boldsymbol{\phi}^{\alpha_1}_{x^*,M}\right\|_2^2 + \left\|K_M \boldsymbol{\phi}^{\alpha_1}_{x^*,M} - g\right\|^2_{L^2(\Gamma_{x^*})}$$

Unlike the continuous operator K defined by (11.12), $K_M : \mathbb{C}^M \to L^2(\Gamma_{x^*})$ does not have dense range, the range of K_M is of dimension M. It is clear, however, that

$$\min_{\boldsymbol{\phi} \in \mathbb{C}^M} \|K_M \boldsymbol{\phi} - g\|_{L^2(\Gamma_{x^*})} \to 0,$$

as $M \to \infty$. This follows from the fact that $K : L^2(\gamma) \to L^2(\Gamma_{x^*})$ has dense range, $C^\infty(\bar{\gamma})$ is dense in $L^2(\gamma)$, and that for every $\phi \in C^\infty[0, L]$,

$$\left|K\phi(x) - K_M \boldsymbol{\phi}^{(M)}(x)\right| \to 0,$$

as $M \to \infty$, uniformly for $x \in \Gamma_{x^*}$ where $\boldsymbol{\phi}^{(M)} = (\phi(y_1), .., \phi(y_M))^T$. Using these observations we can prove the following theorem analogous to Theorem 1.

Theorem 2. *Suppose for all $y = (y_1, y_2) \in \Gamma$,*

$$y_1 > x_1^* + \zeta,$$

and let $G_k^{L,\alpha_1,\delta,M}$ be the approximation for the total field defined by (11.15)*. Then there exists a constant C, independent of δ, α_1 and M, such that*

$$\left|G_k^{L,\alpha_1,\delta,M}(x^*, z) - G_k^L(x^*, z)\right| \leq C \left\|K_M \boldsymbol{\phi}^{\alpha_1}_{x^*,M} - g\right\|_{L^2(\Gamma_{x^*})} + \frac{\delta}{\sqrt{\alpha_1}} \|g\|_{L^2(\Gamma_{x^*})}.$$

Further, if we choose $\alpha_1 = \alpha_1(\delta)$ and $M = M(\delta)$ such that

$$\alpha_1(\delta) \to 0, \ M(\delta) \to \infty \text{ and } \frac{\delta^2}{\alpha_1(\delta)} \to 0, \text{ as } \delta \to 0,$$

then

$$\left|G_k^{L,\alpha_1,\delta}(x^*, z) - G_k^L(x^*, z)\right| \to 0,$$

as $\delta \to 0$.

11.4 Numerical Implementation

In this section we shall look at the numerical implementation of the method and provide results for scattering in a waveguide for a selection of scattering objects. Equation (11.16) is a discrete Nyström method approximation to (11.13) (equivalently, see Remark 1, a discrete version of the PSM in a waveguide), but arguably not fully discrete as the computation of the action of $K_M^* K_M$ requires computations of the function $a(x, y)$. To obtain a fully discrete scheme we approximate a by a_N, the composite midpoint rule approximation using N points, namely

$$a_N(x, y) := \frac{L}{N} \sum_{l=1}^{N} \overline{\Phi_k^L(z_l, x)} \Phi_k^L(z_l, y), \ x, y \in \bar{\gamma},$$

where $z_j = (x_1^* + \zeta, (j - 1/2)L/N), j = 1, .., N$. We approximate the right hand side, $K^* g$ by b_N, the (same) composite midpoint rule approximation using N points, defined by and

$$b_N(x) := \frac{L}{N} \sum_{l=1}^{N} \overline{\Phi_k^L(z_l, x)} g(z_l).$$

Putting these approximations into the linear system (11.17), we obtain an equation for a fully discrete approximation $\phi_{x^*,M,N}^{\alpha_1}$,

$$\begin{aligned} \alpha_1 \left(\boldsymbol{\phi}_{x^*,M,N}^{\alpha_1} \right)_i + \left(\frac{L}{M} \right)^2 \frac{L}{N} \sum_{j=1}^{M} \sum_{l=1}^{N} \overline{\Phi_k^L(z_l, y_i)} \Phi_k^L(z_l, y_j) \left(\boldsymbol{\phi}_{x^*,M,N}^{\alpha_1} \right)_j \\ = \frac{L}{M} \frac{L}{N} \sum_{l=1}^{N} \overline{\Phi_k^L(z_l, y_i)} g(z_l), \ i = 1, .., M. \end{aligned} \tag{11.18}$$

For the numerical results presented in this paper, $\phi_{x^*,M,N}^{\alpha_1} \in \mathbb{C}^M$ has been computed as the solution of (11.18) with

$$\alpha_1 = \frac{L^3}{M} c \delta^p,$$

where $c = 2.4 \times 10^{-6}$ and $p = 2/3$. The approximation to the total field in the waveguide is then calculated as

$$G_k^{L,\alpha,\delta,M}(x^*, z) = \Phi_k^L(x^*, z) + \frac{L}{M} \sum_{j=1}^{M} \left[G_k^{L,\delta}(z, y_j) - \Phi_k^L(z, y_j) \right] \left(\boldsymbol{\phi}_{x^*,M,N}^{\alpha_1} \right)_j .$$

The "measured (noisy) data" $G_k^{L,\delta}(z, y)$ for $y \in \gamma$, is computed as the exact solution (or an approximation using a boundary element method) of the direct scattering problem, with synthetic noise with normal distribution added independently to each measurement such that the bound (11.8) is satisfied.

The point source is taken to be located at $(z_1, 2L/3)$ with $z_1 = -10$, where the waveguide occupies the space $\mathbb{R} \times [0, L]$ with $L = 3$. The wavenumbers considered are

$$k_j := \frac{(j - 1/2)\pi}{L}, \text{ for } j = 1, 2, .., 10,$$

the geometry allowing for up to j propagating modes at wavenumber k_j. The measurement line γ is located at $z_1 + L/3$ and fifteen measurement positions are considered, specifically $(z_1 + L/3, t_j := (j - 1/2)L/M)$, where $M = 15$. The vertical line Γ_{x^*} is located at $x_1^* + \zeta$ where $\zeta = L/30$, and this is split into $N = 15$ points.

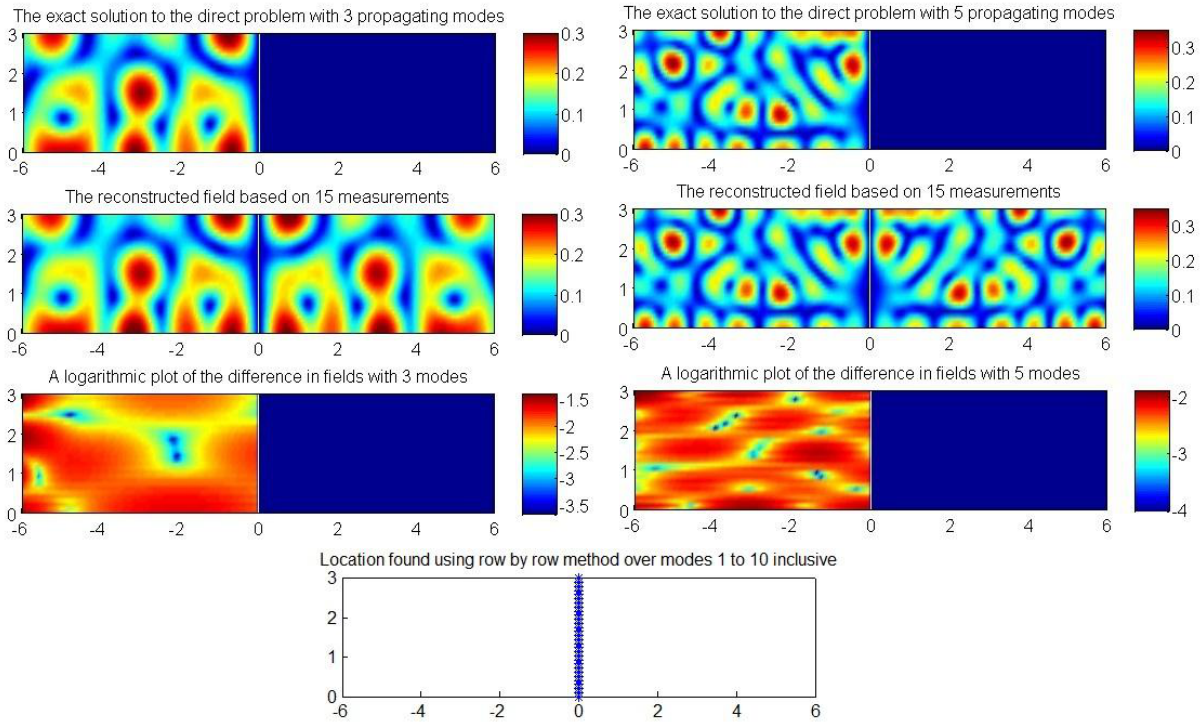

Figure 11.3: Results for a vertical screen example. The exact solution is known in this case and compared to our reconstructions. The object location is determined based on the sum of the reconstructions for 1 to 10 propagating modes.

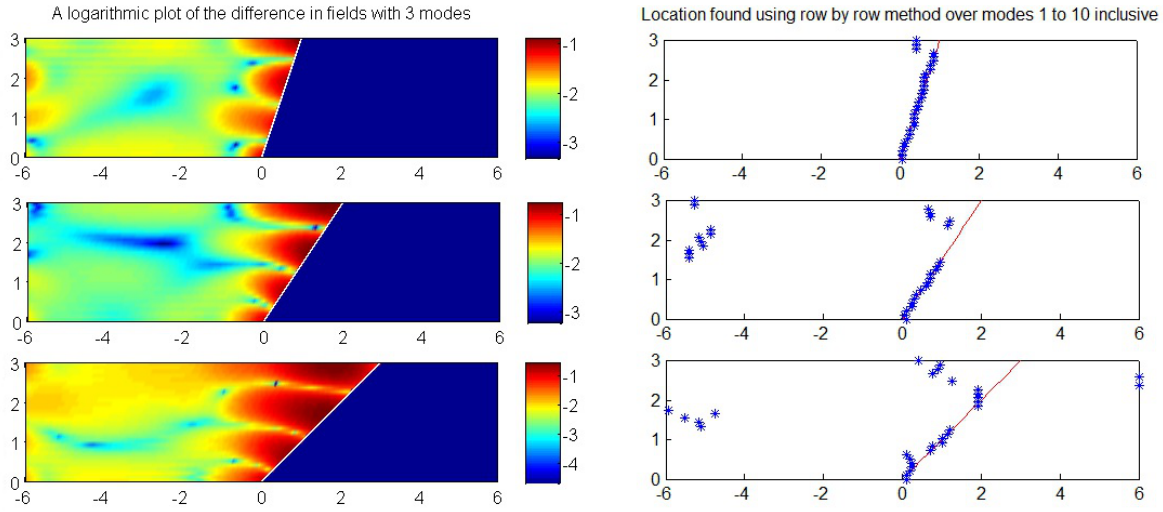

Figure 11.4: Results for 3 slanted screens. We note the inaccuracy to the right of $x_1 = -0.1$ is anticipated by the theory, since we require $y_1 > x_1^* + \zeta$ for all $y = (y_1, y_2) \in \Gamma$.

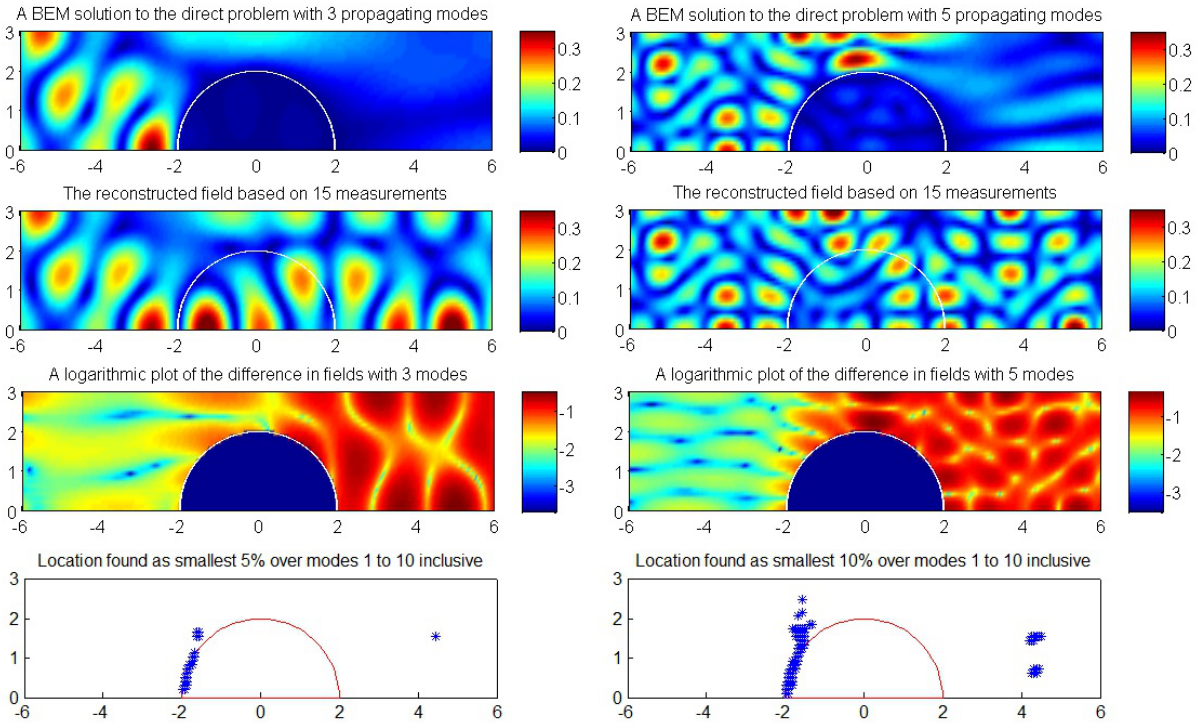

Figure 11.5: Results for a semicircle example. We see equally accurate results in this case of a bounded object contained within the waveguide as with the cases of fully blocked waveguides.

For our inital numerical simulations, we assume a vertical, flat, sound-soft screen is blocking the waveguide completely. Although arguable the simplest example, this is a setup in which the LSM mentioned previously fails. Figure 11.3 shows the exact and reconstructed values of the total field with a vertical screen at $x_1 = 0$ where the noise level $\delta = 10\%$. The difference between these fields is also shown, with results for wavenumber k_3 (up to 3 propagating modes) shown on the left, and wavenumber k_5 (up to 5 propagating modes) on the right hand side.

We also consider a slanted screen, results for a slope of $1/3, 2/3$ and 1 are presented in Figure 11.4, again with wavenumber k_3 and noise level $\delta = 10\%$. A boundary element method with 100 boundary elements has been implemented to compute an approximation to the solution of the direct problem (the "measured" values). The condition of the scattering object Γ being fully contained to the right of Γ_{x^*} is not satisfied for all locations x^* in this case, and the accuracy of the reconstruction is affected.

To determine the location of the scattering object, we compute the summation of the reconstructed fields over the ten wavenumbers $k_i, i - 1, .., 10$, and (recalling the Dirichlet boundary condition on Γ) search for locations where this summation of reconstructions is small. In Figure 11.3 and Figure 11.4 a so-called *row by row* method has been employed, plotting the location of the minimum value on each row in the waveguide.

The final set of examples presented here are for a semicircle scatterer. Here again a boundary element method with 100 boundary elements is used to solve the direct scattering problem. In Figure 11.5 synthetic noise has then been added, this time with $\delta = 20\%$. Results for wavenumber k_3 and k_5 are given, and the summation over all ten wavenumbers $k_1, .., k_{10}$ used to predict the location of the scattering object. In this case where the scattering object does not reside on every row of the waveguide, the location is computed as the positions where the reconstruction takes a value within the smallest $x\%$ of all the reconstructed values, and in Figure 11.5 we show these locations in the cases where $x = 5\%$ (on the left) and $x = 10\%$ (on the right).

11.5 Conclusions

We have considered a discrete PSM in a waveguide using finite measurement data and shown how several of the convergence theorems from the continuous level can be carried through to this discrete variant. We have also seen this gives rise to a linear system which is identical to the system obtained through application of the Nyström method, using the composite midpoint rule, to the original integral equation from the continuous PSM in a waveguide, with the regularisation parameters linked in a specific way. The theory provided shows our discrete PSM approximation to the total field tends to the actual value of the total field as the noise level decreases, provided the Tikhonov regularisation parameter is chosen in a specific way, and provided the scattering object lies to the right of the line Γ_{x^*}. The numerical results provided illustrate this, and in Figure 11.4 and Figure 11.5 we see the difficulties arising with detecting obstructions that are not completely contained to the right of Γ_{x^*}.

Further work is currently being undertaken to adapt the shape of Γ_{x^*} so that the above condition on the geometry is satisfied for more points $x^* \in D$. Adaptation to the three-dimensional case, and consideration of different boundary conditions on the scattering object, are also areas of interest to progress this method further.

References

[1] M. T. Bin Ali, K. V. Horoshenkov and S. J. Tait: *Rapid detection of sewer defects and blockages using acoustic-based instrumentation*, Water Science and Technology 64 (2011), 1700–1707.

[2] L. Bourgeois and E. Luneville: *The linear sampling method in a waveguide: a modal formulation*, Inverse Problems 24 (2008), 1–20.

[3] R. Haunton and S. N. Chandler-Wilde:, *A novel point source method for inverse scattering in waveguides*. In *Proceedings of IoA: Acoustics 2016*, 38(1) (2016), 306–316.

[4] R. Haunton and S. N. Chandler-Wilde: *Inverse scattering in waveguides: a new point source method*, in preparation.

[5] R. Kress, V. Maz'ya and V. Kozlov: *Linear integral equations*, Berlin: Springer-Verlag 1989.

[6] P. Monk and V. Selgas: *Sampling type methods for an inverse waveguide problem*, Inverse Problems and Imaging 6 (2012), 709–747.

[7] H. Plihal, F. Kretschmer, M. T. Bin Ali, C. H. See, A. Romanova, K. Horoshenkov and T. Ertl: *A novel method for rapid inspection of sewer networks: combining acoustic and optical means*, Urban Water Journal 13 (2016), 3–14.

[8] R. Potthast: *Point Sources and multipoles in Inverse Scattering Theory*, Chapman and Hall 2001.

[9] R. Potthast *A point source method for inverse acoustic and electromagnetic obstacle scattering problems*, IMA Journal of Applied Mathematics 61 (1998), 119–140.

Chapter 12

Coupling modes in high-frequency multiple scattering problems: the case of two circles

Daan Huybrechs and Peter Opsomer

Department of Computer Science,
KU Leuven,
Belgium

Abstract. *One can reformulate a high-frequency scattering problem as a boundary integral equation. In the presence of multiple scattering obstacles, the wave pattern becomes very complicated, but wavenumber-independent simulation schemes have been proposed based on ray tracing. In such schemes, one can note that the phases of the corresponding densities on each of the obstacles converges to an equilibrium after a few iterations. For the case of two circular scatterers, we will compute a Taylor approximation of this limiting phase, independently of the incident wave and with a computational complexity independent of the wavenumber.*

12.1 Introduction

Numerical simulations in acoustics are often based on a Boundary Integral equation reformulation of the Helmholtz equation, see for example [10, 21]. An incoming wave that is scattered by an obstacle with boundary Γ results in a scattered field $u^{\mathrm{s}}(\mathbf{x})$ that can be represented by the so-called *single layer potential*,

$$u^{\mathrm{s}}(\mathbf{x}) = (Sv)(\mathbf{x}) = \int_{\Gamma} K(\mathbf{x},\mathbf{y})v(\mathbf{y})ds(\mathbf{y}). \tag{12.1}$$

Here, $K(\mathbf{x},\mathbf{y})$ is the Green's function of the Helmholtz equation with wavenumber k and $v(\mathbf{y})$ is the unknown *density function*, defined on Γ. Though other representations of the scattered field exist, for the analysis in this paper, the equation above is the simplest to proceed with and sufficient to obtain the results.

So-called hybrid numerical-asymptotic methods aim to avoid refining the discretization for increasing k by incorporating information about the solution from asymptotic analysis (see the review [8] and references therein). In particular, phase-extraction methods use information about the phase g of the solution $v(\mathbf{y})$ in order to discretize only the remaining non-oscillatory part f in the following factorization:

$$v(\mathbf{y}) = f(\mathbf{y},k)e^{ikg(\mathbf{y})}. \tag{12.2}$$

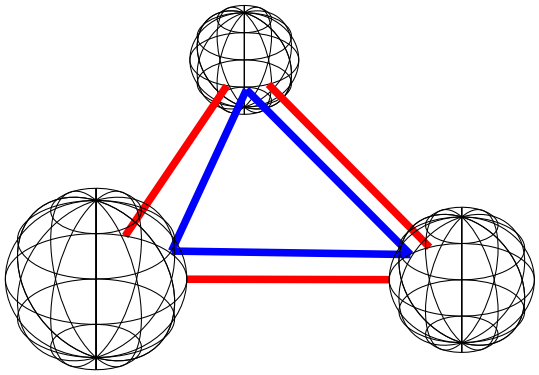

Figure 12.1: Depiction of periodic orbits between three spherical scatterers: one periodic orbit visits all three scatterers in a triangle-shaped trajectory minimizing the total path length (blue), and one periodic orbit exists between each combination of two spheres (red).

Phase extraction methods are simplest for convex obstacles, and require ray-tracing or similar techniques for more complicated domains or multiple scattering configurations [7, 12, 11, 2, 13, 9, 3, 4, 1]. For an overview, see [5, 8].

Ray tracing methods for scattering configurations with multiple obstacles at high frequencies lead to a sequence of single-scattering problems, where the phase can be extracted in each case. The first computation is the scattering of the incoming wave by just one of the obstacles. Next, the reflected field is considered as an incoming wave for another obstacle, and so on. This process is repeated and care has to be taken to include all reflections by all obstacles until convergence. It was shown by Ecevit et al. that the sequence of single-scattering problems can be organised according to certain *periodic orbits* [11, 2]. Examples of these are illustrated in Fig. 12.1. Each such orbit consists of the shortest path between a subset of obstacles, and one can intuitively understand them as follows. Rays originate in a source and reflect off obstacles in the scene. Rays that do not reflect on another obstacle leave the scene forever. For rays that do, one can repeat the reasoning on the next iteration of reflections. Fewer and fewer rays will remain, and those that do are close to the aforementioned periodic orbits. Indeed, a ray that travels exactly *on* the shortest path between a collection of obstacles remains trapped in the scene forever, while any other ray ultimately leaves the scene.

Rays that travel along a periodic orbit induce a density on each of the participating obstacles. We will call the corresponding density a 'mode', and note that it has the same structure as (12.2):

$$V_j(\tau) \sim v_{\mathrm{j,smooth}}(\tau) e^{ik\phi_j(\tau)}, \qquad j = 1, \ldots, J. \tag{12.3}$$

Here, J is the number of obstacles in the orbit. One can observe that the densities of rays travelling close to the periodic orbits converge to a limit. One can see this in for example [12, Fig. 1 & 2], although this feature was not further investigated there. We will aim to calculate the limiting phases, i.e. the functions ϕ_j in the above expression.

The modes can be seen as eigenfunctions of the multiple scattering problem. Indeed, the existence of a limit indicates that a wave with the density V_1 on the first obstacle induces a density V_2 on the second obstacle, V_3 on the third obstacle and so on, such that the last density V_J induces precisely the density V_1 again on the first obstacle, up to a constant factor. This constant factor can be seen as an eigenvalue, and the collection of densities on each of the obstacles is an eigenfunction of the sequence of single scattering problems.

In our initial study, we restrict ourselves to the case of two circles, as shown in Fig. 12.2. In this case, there is a single periodic orbit, namely the shortest path between the two circles. We analyze the limiting phase via its Taylor series around the point where the shortest path hits

the boundary. Using symmetry, it is sufficient to study a single phase function. The advantage of the Taylor series approximation is that it leads to fully explicit expressions.

Our implementation of the numerical experiments in this paper is publicly available on GitHub [18] and a copy of the code can always be obtained from the authors.

12.2 Setting and problem statement

We formulate the problem as an eigenvalue problem for an oscillatory integral operator that represents scattering by a circle. Looking for eigenfunctions of the form (12.2) leads to oscillatory integrals. In order to analyze these asymptotically for a large wavenumber k, we use the well-known method of steepest descent [20, 6]. It deforms the path of integration into the path of steepest descent $h(p)$ in the complex plane such that oscillating integrands are transformed to rapidly decaying integrands.

A similar methodology was employed in [14] to find the asymptotic expansion of the solution of a scattering problem, possibly involving multiple obstacles as well. In particular, the method of steepest descent was used in [14] to track the forward propagation of rays, given an initial incoming wave. The main difference is that in our current setting, we are concerned with an eigenvalue problem instead.

The non-overlapping circles in Fig. 12.2 are separated by a distance d and the corresponding shortest path is the periodic orbit along which rays will be trapped forever. We parametrize the circles as

$$\Gamma_1(\tau) = r[\sin(2\pi\tau), \cos(2\pi\tau)], \quad \tau \in [0,1], \tag{12.4}$$

$$\Gamma_2(\tau) = [0, d+2r] + r[\sin(2\pi\tau), -\cos(2\pi\tau)], \quad \tau \in [0,1], \tag{12.5}$$

with r and $d > 0$ such that $\tau = 0$ gives the points on the circles closest to each other. The unknown phase function for the density on Γ_1 is denoted $\phi_1(\tau)$. Due to symmetry, we have that $\phi_2(\tau) = \phi_1(\pm\tau) + \nu$, where ν is a constant phase factor. We choose $\phi_2(\tau) = \phi_1(\tau)$.

In order to formulate the eigenvalue problem, recall the single layer potential (12.1). We shall use the notation $S_{ij}v_i$ for its application on a density v_i defined on Γ_i, and with the point $\mathbf{x}$ on Γ_j. An incident wave on Γ_j is written as u_j^{inc}. Disregarding the possibility of resonances, for the time being, the single layer potential leads to coupled integral equations of the first kind for a multiple scattering sound-soft Dirichlet problem,

$$S_{11}v_1 + S_{21}v_2 = -u_1^{\text{inc}}, \tag{12.6}$$

$$S_{12}v_1 + S_{22}v_2 = -u_2^{\text{inc}}. \tag{12.7}$$

The operator under investigation in this paper is given succinctly by

$$Tv = S_{11}^{-1}S_{21}S_{22}^{-1}S_{12}v, \tag{12.8}$$

and in particular, we look for a function v_1 of the form (12.2) such that

$$Tv_1 = \lambda v_1. \tag{12.9}$$

A discretisation of the combined multiple scattering problem leads to a BEM matrix A with the following block structure form,

$$A = \begin{pmatrix} A_{11} & A_{21} \\ A_{12} & A_{22} \end{pmatrix}. \tag{12.10}$$

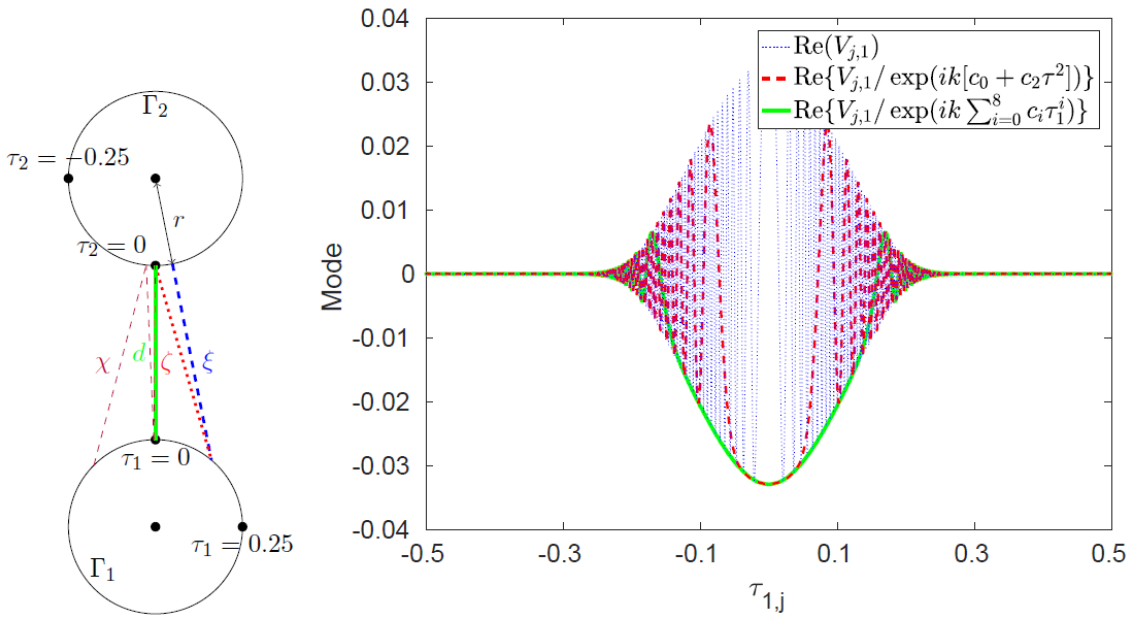

Figure 12.2: Two circles under consideration in this paper (left) and a numerical illustration of the eigenvector $V_{j,1}$ of the discrete operator M, divided by different phases (right). The parameters are $k = 2^9$, $r = \frac{1}{2}$ and $d = 1$.

Here, A_{11} and A_{22} respectively represent the self-interaction of the first and second obstacle, while A_{21} gives the action of the density on Γ_2 on the location of the first circle Γ_1. A full cycle of reflections is represented by

$$M = A_{11}^{-1} A_{21} A_{22}^{-1} A_{12} = V D V^{-1}. \tag{12.11}$$

The discrete operator M corresponds closely to T in equation (12.8).

In order to illustrate the coupling mode between two circles, we have used a collocation discretisation with piecewise linear approximation of the density function. In this case, the first eigenvector of M is the mode we are looking for, evaluated at the collocation points on Γ_1. It is shown in the right panel of Fig. 12.2. This is an oscillatory function, but factoring out the Taylor approximation of $\phi(\tau)$ (which we will compute later on) provides a much less oscillatory function. One can also note that it is supported in the region where the circles can 'see' each other. The corresponding highest eigenvalue $D_{1,1}$ equals λ, and its phase is $2d$. The latter is the twice the distance between the circles in Fig. 12.2, which is also the length of the periodic orbit studied in [11, 2] and here.

We proceed by analyzing the operator T asymptotically for large k. Due to symmetry, we only have to analyze S_{11} and S_{21}. We proceed with the latter first, since it does not appear with its inverse in (12.8).

12.3 Field scattered by the second circle onto the first circle

When we calculate the field that Γ_2 scatters onto the location Γ_1, we obtain

$$u^s(\tau_1) = S_{21} V_2 = \int_{\Gamma_2} \frac{i}{4} H_0^{(1)}(k\delta[\tau_1, \tau_2]) V_2(\tau_2) d\Gamma_2, \tag{12.12}$$

$$u^s(\tau_1) \sim \int_0^1 \frac{i}{4} (k\delta[\tau_1, \tau_2]\pi/2)^{-1/2} e^{ik\delta[\tau_1,\tau_2] - i\pi/4} v_{2,\text{smooth}}(\tau_2) e^{ik\phi_2(\tau_2)} \|\nabla\Gamma_2(\tau_2)\|_2 d\tau_2, \tag{12.13}$$

where $\delta(\tau_1, \tau_2) = \|\Gamma_1(\tau_1) - \Gamma_2(\tau_2)\|_2$ is the Euclidean distance between two points on the circles. We have replaced the Hankel function $H_0^{(1)}$ by the leading order term of its expansion for large arguments. More terms in the expansion can be found by substituting the full expansion, a process detailed in [14].

As is standard in asymptotic expansions of integrals [20, 15, 6], one notes that the only important contribution to an oscillatory integral originates in a region around the stationary point of the phase. This means finding a function $\chi(\tau)$ such that

$$\left.\frac{\partial \delta[\tau_1, \tau_2] + \phi(\tau_2)}{\partial \tau_2}\right|_{\tau_2 = \chi(\tau_1)} = 0. \tag{12.14}$$

The phase of the resulting integral (12.13) will then be $\delta[\tau_1, \chi(\tau_1)] + \phi[\chi(\tau_1)]$.

Physically, this means that the scattered field due to density V_2 on Γ_2 consists of rays, and that the ray hitting the point τ_1 on Γ_1 comes from the point $\chi(\tau_1)$ on Γ_2. In particular, we know that $\chi(0) = 0$, since that is precisely the periodic orbit, and we intend to study only local perturbations of this point.

12.4 Single scattering problem on the first circle

Next, we consider S_{11}^{-1}. A full computation of the asymptotic expansion of the solution to a single scattering problem, even with phase extraction, is rather involved. The computation is carried out in [14]. The problem of computing the phase of the solution is simpler since, in fact, it is known that the phase of the solution equals the phase of the incoming wave.

For completeness, the process of obtaining full asymptotics is as follows. Assuming a density of the form (12.3), the application of the integral operator on Γ_1 yields

$$S_{11}V_1(\tau_1) = u(\tau_1) = \int_{\Gamma_1} \frac{i}{4} H_0^{(1)}\left(k\|\Gamma_1(\tau) - \Gamma_1(\tau_1)\|_2\right) \left(v_{1,\text{smooth}}(\tau) e^{ik\phi_1(\tau)}\right) \|\nabla \Gamma_1(\tau)\|_2 d\tau. \tag{12.15}$$

A technical complication is the appearance of the logarithmically singular Hankel function, which in this case can not be replaced by its expansion for large arguments as before in (12.13), where it led to a simpler oscillatory exponential. An alternative is to substitute the Hankel function by its Mehler-Sonine integral representation [16, (10.9.10)], which has a complex exponential in the integrand. After interchanging integration variables, a regular steepest descent analysis can be applied on the resulting bivariate integral [14].

The main observation to make here is that, in the absence of multiple scattering effects, the only contribution to the singular oscillatory integral originates in the singularity at $\tau_1 = \tau$. As one can apply a path of steepest descent such that the Mehler-Sonine integral representation of $H_0^{(1)}$ does not contribute to the phase of the integrand, the phase of $S_{11}V_1$ indeed equals the phase of V_1.

In order not to change the shape of our mode (12.3) after another reflection, the phase on Γ_1 should equal the phase of the integral (12.13) up to a constant shift μ. This is expressed by the equation

$$\phi(\tau_1) + \mu = \delta[\tau_1, \chi(\tau_1)] + \phi[\chi(\tau_1)]. \tag{12.16}$$

The phase shift μ will correspond to half the phase of the eigenvalue, i.e. we have that $\lambda = ce^{2ik\mu}$. It must equal half the path length of the periodic orbit, and indeed $\mu = d$ follows from (12.16) in the special case $\tau_1 = \chi(\tau_1) = 0$ that corresponds to the shortest path.

12.5 Symbolic computation of Taylor coefficients of ϕ

The system of equations that $\phi(\tau)$ and $\chi(\tau)$ should satisfy is (12.14)–(12.16). This is a non-linear system which even in the case of two circles does not seem to allow an explicit analytic solution. We resort to series expansions that do lead to fully explicit expressions for the coefficients.

We look for a Taylor series of the form

$$\phi(\tau) \sim \sum_{i=0}^{\infty} c_i \tau^i. \tag{12.17}$$

We are free to choose the constant c_0, since it corresponds purely to a constant phase shift and eigenfunctions are only determined up to a constant factor: we set $c_0 = d$. We expand the other relevant functions into Taylor series as well:

$$\chi(\tau_1) \sim \sum_{j=0}^{\infty} a_j \tau_1^j \tag{12.18}$$

$$\phi[\chi(\tau_1)] + \delta[\tau_1, \chi(\tau_1)] - \phi(\tau_1) \sim \sum_{i=0}^{\infty} \omega_i \tau_1^i \tag{12.19}$$

$$\left.\frac{\partial \delta[\tau_1, \tau_2] + \phi(\tau_2)}{\partial \tau_2}\right|_{\tau_2 = \chi(\tau_1)} \sim \sum_{i=0}^{\infty} \psi_i \tau_1^i \tag{12.20}$$

We already know that $a_0 = 0$ since $\chi(0) = 0$. Note that the coefficients ω_i and ψ_i can be computed explicitly in terms of a_i and c_i, since we can explicitly expand the Euclidean distance function $\delta[\tau_1, \tau_2]$ as well.

The coefficient ω_0 may be nonzero because of (12.16): it is equal to $\mu = d$. All other coefficients are computed in a recursive procedure: for each index i, starting from $i = 0$, we solve $\omega_{i+1} = 0 = \psi_i$ for a_i and c_{i+1}. The newly found coefficients can be used in the next iteration.

For the case of the two circles, $\omega_1 = 0 = \psi_0$ yields

$$a_1 c_1 - c_1 = 0 = c1 \quad \Rightarrow \quad c_1 = 0, \tag{12.21}$$

which is intuitively correct due to symmetry. For $i = 1$, we obtain a system of quadratic equations

$$\begin{aligned} 0 &= \frac{3}{2}\pi^2 a_1^2 - \pi^2 a_1 + a_1^2 c_2 + 3/2\pi^2 - c_2, \\ 0 &= 3\pi^2 a_1 - \pi^2 + 2 a_1 c_2 \end{aligned} \tag{12.22}$$

from which we deduce

$$c_2 = \sqrt{2}\pi^2, \quad a_1 = 3 - 2\sqrt{2}. \tag{12.23}$$

We have discarded the other solution $a_1 = 3 + 2\sqrt{2}, c_2 = -\sqrt{2}\pi^2$ as the left side of Fig. 12.3 indicates that $c_2 > 0$ and, furthermore, $a_1 > 1$ would imply moving away from the periodic orbit shown in the left part of Fig. 12.2. For higher i, the system of equations is linear in the coefficients and the solution is unambiguous. Due to symmetry, all $a_i = 0 = c_{i+1}$ for even i.

Further computation leads to the next nonzero coefficients

$$c_4 = \frac{-11}{12}\sqrt{2}\pi^4, \qquad a_3 = -7\pi^2(17\sqrt{2} - 24) \tag{12.24}$$

and

$$c_6 = \frac{2783\sqrt{2}\pi^6}{2520}, \qquad a_5 = -\frac{\pi^4}{84}(1205811\sqrt{2} - 1705312), \tag{12.25}$$

$$c_8 = \frac{-358021}{205632}\sqrt{2}\pi^8, \qquad a_7 = \frac{-\pi^6}{128520}(289615597399\sqrt{2} - 409578202752). \tag{12.26}$$

12.6 A geometric interpretation

We can assign a geometric meaning to the stationary point function $\chi(\tau)$. Recall that $\chi(\tau_1)$ is the point on Γ_2 from which a ray hits the point $\Gamma_1(\tau_1)$. By symmetry, the converse also holds, and applying χ again yields a point back on Γ_1. In the sequence $\chi(\chi(\tau_1))$, $\chi(\tau_1)$, τ_1, it should be true that the incoming and reflected ray at the middle point $\chi(\tau_1)$ on Γ_2 are at equal angles with the normal direction. In our setting, this leads to the equation

$$\begin{aligned} 0 = 4\pi\chi(\tau_1) &+ \arctan\left(\frac{r\sin(2\pi\chi(\tau_1)) - r\sin(2\pi\chi[\chi(\tau_1)])}{d + 2r - r\cos(2\pi\chi(\tau_1)) - r\cos(2\pi\chi[\chi(\tau_1)])}\right) \\ &+ \arctan\left(\frac{r\sin(2\pi\chi(\tau_1)) - r\sin(2\pi\tau_1)}{d + 2r - r\cos(2\pi\chi(\tau_1)) - r\cos(2\pi\tau_1)}\right). \end{aligned} \tag{12.27}$$

This equation is again highly non-linear, and is hard to get a symbolic solution on account of the application of χ on itself. Therefore, one computes a Taylor series of this expression for τ_1 near zero, sets all coefficients equal to zero and this results in the same a_i as in the procedure described before.

One can numerically approximate χ using (12.27), and can then obtain the phase in a limited range of τ via (12.14):

$$\phi(\tau) = -\left(\int \frac{\partial\delta(\tau_1,\tau_2)}{\partial\tau_2}\bigg|_{\tau_2=\chi(\tau_1)} \chi'(\tau_1)\mathrm{d}\tau_1\right)\bigg|_{\tau_1=\chi^{-1}(\tau)}. \tag{12.28}$$

To obtain ϕ in a wider domain, one notes that the phase is defined in terms of itself and the distance to a stationary point on the other obstacle, as equation (12.16) expresses. It is this self-referential definition of the limiting phase that complicates an analytical expression. However, one can note that phases in high-frequency wave scattering correspond to the length of the trajectory of a ray. In a homogeneous medium, rays are straight lines and phases correspond to distances. Our rays originate in a small region around the periodic orbit and reflect outward until they leave the scene, but it is easier to think of them travelling in the opposite way. The length of such a path, followed by recursive application of χ, is infinite because of the infinite number of reflections. However, we already take into account a phase shift μ at each reflection in the eigenvalue λ. So, writing $\chi^{[r]}$ for the function χ applied r times to the identity, a geometrical interpretation of the phase is

$$\phi(\tau) = c_0 + \sum_{r=0}^{\infty}\left(\delta(\chi^{[r]}(\tau), \chi^{[r+1]}(\tau)) - \mu\right). \tag{12.29}$$

12.7 Results

We first compute χ by applying six functional Newton iterations on (12.27) with an initial guess $\chi(\tau) \approx (3 - 2\sqrt{2})\tau$ in Chebfun [19]. This satisfies (12.27) up to machine precision and its series expansion coefficients also correspond to our a_i. We have added a few iterations of χ as dashed purple lines in Fig. 12.2: the ray is nearly indistinguishable from the periodic orbit after the

second reflection. Next, we compute the phase as (12.29) where we choose $c_0 = 1$ and we end the summation after $r = 10$ reflections as the next term is near machine precision. The series expansion coefficients of this phase also converge to our c_i, and $\phi(\tau)$ is not equal to $\delta[\tau, \chi(\tau)]$.

In Fig. 12.3, one can see that this phase lies in between the two physical distances ζ and ξ shown in Fig. 12.2. These are the distances from a point on Γ_1 to the point $\Gamma_2(0)$ or to the closest point on the other circle respectively. These physical distances may be suitable starting points for an iterative procedure to solve the non-linear system of equations (12.14)–(12.16) in a more general setting. In the right part of Fig. 12.3, we also see that our Taylor expansions with coefficients c_i converge with the expected orders. The phase can indeed also be computed as (12.28), although in a smaller domain due to the inverse of χ.

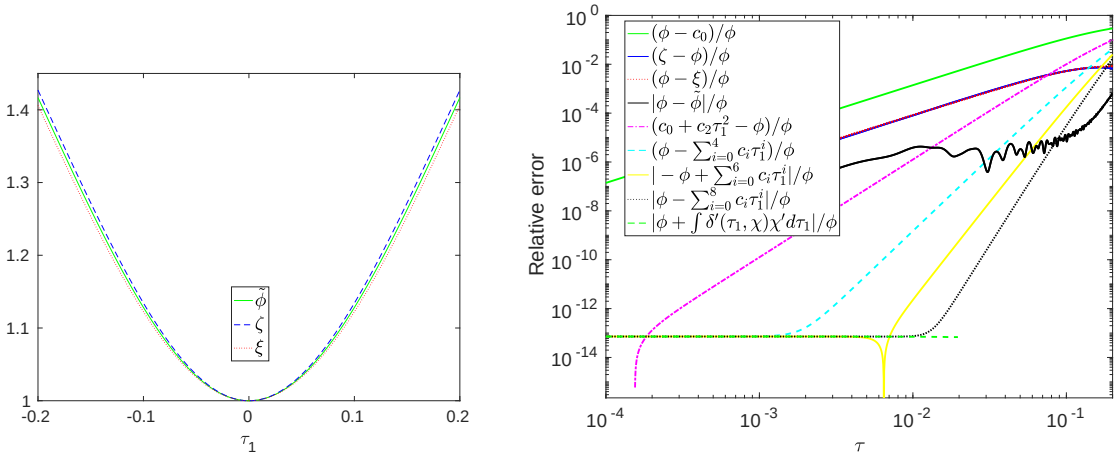

Figure 12.3: Distances and phase $\phi(\tau)$ from (12.29) (left) and relative errors with respect to the latter for the former, our symbolical series expansion, $\tilde{\phi}$ and (12.28) (right).

In order to show that these solutions are indeed related to an eigenvalue problem, we discretized the scattering problem in a classical boundary element method. The radius $r = 1/2$, the wavenumber $k = 2^9$ and the number of degrees of freedom $N = 10k$ in a collocation scheme with piecewise linears. We computed the eigenvalue decomposition of the matrix M and selected the eigenvector $V_{j,1}$ corresponding to the largest eigenvalue, see Fig. 12.2.

From this vector, we compute an approximate phase $\tilde{\phi(\tau)}$ as follows. We have chosen $\phi(0) = d$, half the length of the periodic orbit. Assuming that the argument of $v_{\text{smooth}}(\tau)$ varies much more slowly than $\text{Arg}(\exp[ik\phi(\tau)])$, the estimated reference phase $\tilde{\phi}$ at other collocation points $\tau_{1,j}$ is:

$$\tilde{\phi}\,(\tau_{1,j}) = \tilde{\phi}\,(\tau_{1,j\mp1}) + \frac{\text{Arg}(V_{j,1}) - \text{Arg}(V_{j\mp1,1})}{k} - \frac{2\pi}{k}\left\lfloor \frac{\text{Arg}(V_{j,1}) - \text{Arg}(V_{j\mp1,1})}{2\pi} \right\rfloor. \tag{12.30}$$

In the right part of Fig. 12.3, the error of $\tilde{\phi}$ is about 10^{-6} due to the accuracy of $V_{j,1}$ with respect to the continuous problem and because we compute its angles. We have also been able to verify that the coefficients of polynomial approximations of $\tilde{\phi}(\tau_1)$ converge to the respective c_i.

12.8 Conclusions

At high frequencies, standard boundary element methods become computationally too expensive, while the cost of hybrid numerical-asymptotic methods can be frequency-independent.

However, these require a priori information on the phase of the solution, for example via ray tracing. We note that this phase converges to some equilibrium after a number of reflections in a multiple scattering scene, and it is given by the phase of the eigenfunction of the operator representing a full cycle of reflections.

For the case of two circles, we can find all coefficients in the Taylor expansion of the phase $\phi(\tau_1)$ via a simple and recursive scheme. This phase is given by the distance to the periodic orbit via an infinite number of reflections, where one subtracts the distance between the circles at each reflection.

The scheme to compute the Taylor coefficients is not dependent on the wavenumber nor on the incident wave, an advantage when computing the 'Radar cross section' for example. In the future, we intend to find a series expansion of $v_{\text{smooth}}(\tau)$ as well. Though the computations in this paper were specific to the case of two circles, we also expect a similar methodology to work for arbitrary collections of more general objects.

Acknowledgments

The authors would like to thank Samuel Groth and Marcus Webb for interesting and useful discussions on topics related to this paper. The authors were supported by FWO Flanders [projects G.0617.10, G.0641.11 and G.A004.14].

References

[1] T. Abboud, J.-C. Nédélec, and B. Zhou, *Méthode des équations intégrales pour les hautes fréquences*, CR Acad. Sci. I Math., 318 (1994), 165–170.

[2] A. Anand, Y. Boubendir, F. Ecevit, and F. Reitich, Analysis of multiple scattering iterations for high-frequency scattering problems. II: The three-dimensional scalar case. *Numer. Math.*, 114 (2010), 373–427.

[3] A. Asheim and D. Huybrechs, Local solutions to high-frequency 2D scattering problems, *J. Comput. Phys.*, 229 (2010), 5357–5372.

[4] A. Asheim and D. Huybrechs, Extraction of uniformly accurate phase functions across smooth shadow boundaries in high frequency scattering problems, *SIAM J. Appl. Math.*, 74(2) (2014), 454–476.

[5] V. M. Babich and V. S. Buldyrev, *Short-wavelength diffraction theory*, Springer-Verlag, Berlin, 1991.

[6] N. Bleistein and R. A. Handelsman, *Asymptotic expansions of integrals*, Dover Publications Inc., Mineola, NY, 1986.

[7] O. Bruno, C. Geuzaine, J. J. Monro, and F. Reitich, Prescribed error tolerances within fixed computational times for scattering problems of arbitrarily high frequency: the convex case, *Phil. Trans. R. Soc. Lond. A*, 362 (2004), 629–645.

[8] Chandler-Wilde, I. S., Graham, S. Langdon, and E. Spence, Numerical-asymptotic boundary integral methods in high-frequency acoustic scattering, *Acta Numer.* (2012), 89–305.

[9] S. N. Chandler-Wilde, D. P. Hewett, S. Langdon, and A. Twigger, A high frequency boundary element method for scattering by a class of nonconvex obstacles, *Numerische Mathematik*, 129(4) (2015), 647–689.

[10] D. L. Colton and R. Kress, *Integral equation methods in scattering theory*, John Wiley & Sons, New York, 1983.

[11] F. Ecevit and F. Reitich, Analysis of multiple scattering iterations for high-frequency scattering problems. I: The two-dimensional case, *Numer. Math.*, 114 (2009), 271–354.

[12] C. Geuzaine, O. Bruno, and F. Reitich, On the O(1) solution of multiple-scattering problems, *IEEE Trans. Magn.*, 41(5) (2005), 1488–1491.

[13] S. P. Groth, D. P. Hewett, and S. Langdon, Hybrid numerical-asymptotic approximation for high-frequency scattering by penetrable convex polygons, *IMA J. Appl. Math.*, 80 (2015), 324–353.

[14] S. P. Groth, D. Huybrechs and P. Opsomer, High-order terms in the ray expansion for high-frequency scattering by single and multiple obstacles, (2017), in preparation.

[15] D. Huybrechs and S. Vandewalle, On the evaluation of highy oscillatory integrals by analytic continuation, *SIAM J. Numer. Anal.*, 44(3) (2006), 1026–1048.

[16] NIST, NIST Digital Library of Mathematical Functions, `//dlmf.nist.gov/`, 2016. Online companion to [17].

[17] F. W. J. Olver and D. W. Lozier and R. F. Boisvert and C. W. Clark, *NIST Handbook of Mathematical Functions*, Cambridge University Press, New York, 2010. Print companion to [16].

[18] P. Opsomer, `https://github.com/popsomer/asyBEM/releases`, March 2017. Release 1: Coupling modes in two circles.

[19] The University of Oxford & the Chebfun Developers, Chebfun, `www.chebfun.org`, 2017.

[20] R. S. Wong, *Asymptotic approximations of integrals*, SIAM, Philadelphia, 19104-2688, USA, 2001.

[21] T. Wu., *Boundary element acoustics*, WIT Press, 2005.

Chapter 13

Towards Isogeometric Boundary Element Method Based on Adaptive Hierarchical Refinement of NURBS for 3D Geometries

Hamed Khaki, Jon Trevelyan and Gabriel Hattori

School of Engineering and Computing Sciences,
Durham University
South Road, Durham, UK
DH1 3LE

Abstract. *The considerable potential of isogeometric methods from the promise of cost and run-time saving to more efficient and accurate results, continuity level, convergence and refinement properties attracted numerous computational and numerical researchers in engineering and mathematics to work on different aspects of these methods. The core idea of Isogeometric Analysis (IGA) is to make a shortcut between computer-aided modelling and analysis by describing precise geometries and using them directly in analysis. The direction of this research is to study direct design to analysis by Isogeometric Boundary Element Method (IGABEM) for 3D models by making adaptive refinements to provide reliable solutions even starting from a coarse CAD description. Emphasis will be on the automotive industry. A key aspect of this work is the development of an effective set of algorithms allowing adaptive refinement of Non-Uniform Rational B-Spline (NURBS) surfaces. This work started with IGABEM -NURBS for simple 3D models under simple boundary conditions and the plan is to develop the method for more complex geometries, more boundary conditions, more accurate and fast results by local refinement of NURBS using an adaptive hierarchical scheme.*

13.1 Introduction

Isogeometric Analysis (IGA) was first introduced by Hughes et al in 2005 [1]. The main idea of IGA is to use the same basis functions for representing the geometry in CAD and approximating the solution fields in analysis; therefore, there is no need to do mesh generation which can considerably reduce the time required for the analysis of complex engineering designs. To understand the importance of IGA, should have a look at current engineering design and analysis processes and find the bottlenecks which lead to delays in engineering projects. Analysis in IGA can also be done by a suitable numerical method such as Finite Element Method (IGAFEM)

or the Boundary Element Method (IGABEM). In comparison to FEM approaches, BEM needs only the boundary of geometries to be meshed which is even more appealing in combination with IGA since splines used in CAD geometries only describe the boundary of objects to be modelled. Hence, the need to generate 3D solid analysis models as required in IGAFEM, being one of the issues in IGA, is omitted. Existing CAD models, especially those typically used in automotive industry, are most often NURBS-based. NURBS does not provide a natural possibility for local mesh refinement. Due to its rigid tensor product structure, refinement of NURBS is a global process that propagates throughout the domain. Perhaps one of the most significant developments to solve this problem is the introduction of T-splines [2] and later PHT-splines[3] that produce watertight geometries and can be locally refined. However, as NURBS has its own prospectives and popularities in car manufacturing industry, we aim to use it in our IGA framework and try to develop a refinement scheme to overcome the deficiencies of NURBS to produce *watertight* geometries and allow local refinement. In refinement of NURBS, it is a vital that the chosen scheme can handle the degree of continuity, singularity, smoothness while adding knots and on the other hand allow local editing. Forsey and Bartels [4] introduced hierarchical B-splines as an accumulation of tensor-product splines with nested knot vectors. More precisely, the method is based on modifying existing surfaces by locally adding patches representing finer details. So, this research works on isogeometric boundary analysis using adaptive hierarchical refinement of NURBS for 3D geometries.

13.2 Isogeometric Boundary Element Method (IGABEM)

13.2.1 Boundary Integral Equations (BIE) for 3D Linear Elastostatic Problem

We solve the problem of elasticity in 3D solids. In absence of body forces we have the well-known boundary integral equation as:

$$C_{ij}\left(sp\right)u_i\left(sp\right)+\int_S T_{ij}\left(sp,fp\right)u_j\left(fp\right)dS\left(fp\right)=\int_S U_{ij}\left(sp,fp\right)t_j\left(fp\right)dS\left(fp\right), \tag{13.1}$$

where C_{ij} is the jump term that arises from the strongly singular integral, and depends on the geometry of boundaries, S is the domain boundary $S=S_u\cup S_t$, T_{ij} is the traction kernel, U_{ij} is the displacement kernel, $u_i\left(sp\right)$ is the displacement at a boundary (source) point sp, and $u_j\left(fp\right)$ and $t_j\left(fp\right)$ are the displacement and traction components at fp.

13.2.2 IGABEM Discretization of BIE 3D

To solve equation (1.1) numerically, the boundary S must first be discretized into a series of elements. In this work we use a NURBS description of the solution variables so the discretized BIE becomes:

$$\begin{aligned}C_{ij}\left(sp\right)u_i\left(sp\right)+\sum_{s=1}^{n}\sum_{t=1}^{m}\int_{-1}^{+1}\int_{-1}^{+1}T_{ij}\left(sp,fp\right)R_{s,t}\left(u,v\right)J\left(u,v\right)dudvA_{s,t}=\\ \sum_{s=1}^{n}\sum_{t=1}^{m}\int_{-1}^{+1}\int_{-1}^{+1}U_{ij}\left(sp,fp\right)R_{s,t}\left(u,v\right)J\left(u,v\right)dudvB_{s,t},\end{aligned} \tag{13.2}$$

where $R_{s,t}$ is the NURBS basis function for the control point (s,t). U_{ij} and T_{ij} in equation

(1.2) are functions of $1/r$ and $1/r^2$ respectively, rendering them weakly and strongly singular. The weakly singular U_{ij} kernel does not generally present a problem and can be easily solved by Telles Transformation [6]. However, the T_{ij} kernel must be integrated in specific method suitable for IGABEM to cancel the singularity. A regularization method was used in this work. The approach is to appropriate manipulation of the BIE identities to reduce the strength of singularity to at most, weakly singular integrals. Further details of the idea are shown in [7] with a full implementation.

When collocated at a sufficient number of points, p, the integral equation (1.2) yields the matrix form:

$$\mathbf{Hu} = \mathbf{Gt}, \tag{13.3}$$

where $\mathbf{H}$ is a square matrix containing a combination of the integrals of the traction kernel and the jump terms, $\mathbf{G}$ is a rectangular matrix of displacement kernel integrals, $\mathbf{u}$ and $\mathbf{t}$ are a mix of unknown values and the values prescribed by boundary conditions. By swapping unknowns and knowns the equation (1.3) can be rewritten as:

$$\mathbf{Ax} = \mathbf{b}, \tag{13.4}$$

where $\mathbf{A}$ is a fully populated and non-symmetric matrix of coefficients, the vector $\mathbf{x}$ contains coefficients $A_{s,t}$, $B_{s,t}$ from which displacement and traction components can be recovered from the NURBS expansion and the vector $\mathbf{b}$ arises from known boundary conditions and corresponding boundary integrals. The equation (1.4) is a linear system which can be simply solved to obtain the coefficients $A_{s,t}$, $B_{s,t}$, from which values of the unknown displacement and tractions can be recovered.

13.3 B-Spline, NURBS Curve and NURBS Surface

In order to develop an understanding of B-splines, it is important to start with some key definitions. A knot vector is a non-decreasing set of coordinates, written $\Xi = [\zeta_1, \zeta_2, ..., \zeta_{n+p+1}]$, where ζ_i is the ith knot, p is the degree or polynomial order, and n is the number of basis functions. The basis function $N_{i,p}$ could be defined using the Cox-de Boor [8] recursion formula:

$$N_{i,0}(u) = \begin{cases} 1 & \text{if } \zeta_i \leq u < \zeta_{i+1}, \\ 0 & \text{otherwise} \end{cases} \tag{13.5}$$

$$N_{i,p}(u) = \frac{u - \zeta_i}{\zeta_{i+p} - \zeta_i} N_{i,p-1}(u) + \frac{\zeta_{i+p+1} - u}{\zeta_{i+p+1} - \zeta_{i+1}} N_{i+1,p-1}(u). \tag{13.6}$$

B-splines are combined in a linear approach to generate a curve or surface in the following manner:

$$C(u) = \sum_{i=1}^{n} N_{i,p}(u) B_i, \tag{13.7}$$

$$C(u,v) = \sum_{i=1}^{n} \sum_{j=1}^{m} N_{i,p}(u,v) M_{j,q}(u,v) B_{i,j}, \tag{13.8}$$

where $C(u)$ and $C(u,v)$ are the location of the physical curve and surface, B_i and $B_{i,j}$ are control point coordinates in 2D and 3D, u and v are the spatial coordinate in parameter space, p and q are the degree of spline and n and m are the number of control points.

13.3.1 Rational B-spline Curves and Surfaces

A rational B-Spline is a type of B-spline with weighted control points, and is formulated as:

$$R_{i,p}(u) = \frac{\omega_i B_i N_{i,p}(u)}{\sum_{i=1}^{n} \omega_i N_{i,p}(u)}, \tag{13.9}$$

$$R_{i,p}(u,v) = \frac{\omega_{i,j} B_{i,j} N_{i,p}(u,v) M_{j,q}(u,v)}{\sum_{i=1}^{n}\sum_{j=1}^{n} w_{i,j} N_{i,p}(u,v) M_{j,q}(u,v)}, \tag{13.10}$$

where ω_i and $\omega_{i,j}$ are the weights of control points. The rational B-spline curves and surfaces are given by:

$$C(u) = \sum_{i=1}^{n} R_{i,p}(u) B_i, \tag{13.11}$$

$$C(u,v) = \sum_{i=1}^{n}\sum_{j=1}^{m} R_{ij,pq}(u,v) B_{i,j}. \tag{13.12}$$

13.4 Location of collocation points

Contrary to the traditional BEM, the control points in IGABEM may lie off the physical problem boundary. This requires an additional step to compute feasible locations for the collocation points. Using the Greville Abscissae method [9] we have:

$$\overline{\zeta}_a = \frac{\zeta_{a+1} + \zeta_{a+2} + ... + \zeta_{a+p}}{p} \qquad a = 1, 2, ., n, \tag{13.13}$$

where n is the number of control points, p is the order, $\overline{\zeta}_a$ are collocation points and ζ_{a+i} are knot values. The first and last knots in the knot vector are excluded when applying equation(1.13).

13.5 Numerical Examples

Simple examples are studied with degree of p=2, knot vector $\Xi = [0\ 0\ 0\ 1\ 1\ 1]$ in u and v direction, and all weights are defined to be 1 . Simple geometries like a cube and a quarter cylinder were created by NURBS starting with 3×3 control points in each patch (Figure 1.1) and the geometry basis functions were used for analysis under different boundary conditions (Figure 1.2).

A uniform vertical compression of 1MPa was applied over the top patch of the cube and three patches were constrained by roller supports (Figure 1.2.a). An internal pressure of 1MPa was considered at the inner radius of the quarter cylinder and rollers were again applied as

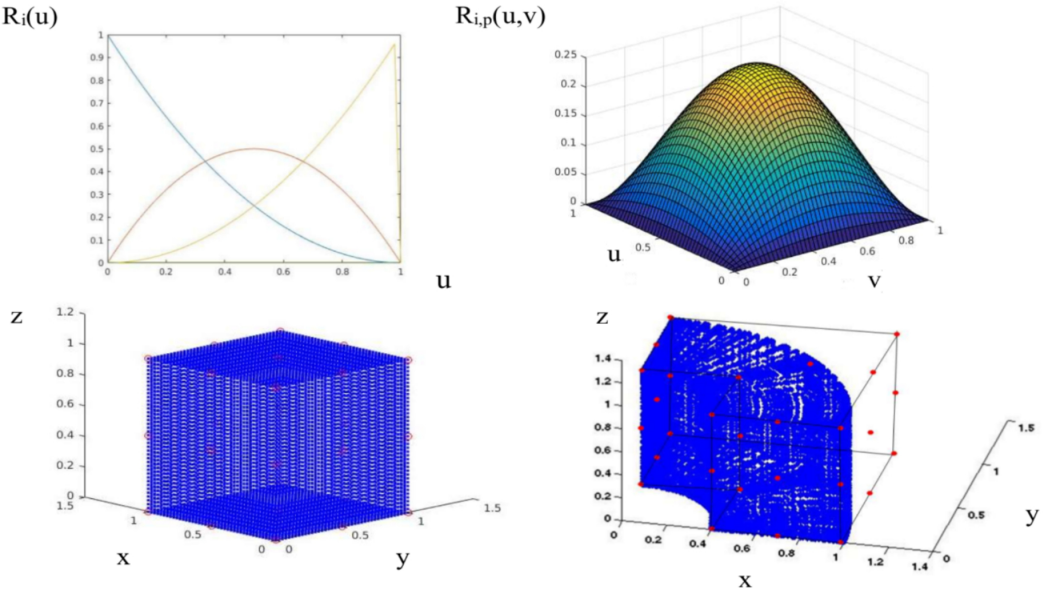

Figure 13.1: Top left: NURBS curve, Top right: NURBS surface, Bottom left: Unit cube and Bottom right: Quarter cylinder with knot vector $\Xi = [0\ 0\ 0\ 1\ 1\ 1]$.

displacement constraints (Figure 1.2.b). The cube is a unit cube and the inner radius of the quarter cylinder is 0.4m, outer radius is 1m, height is 1m, and the material for both is of steel with Young's Modules of 200GPa and Poisson's ratio of 0.3.

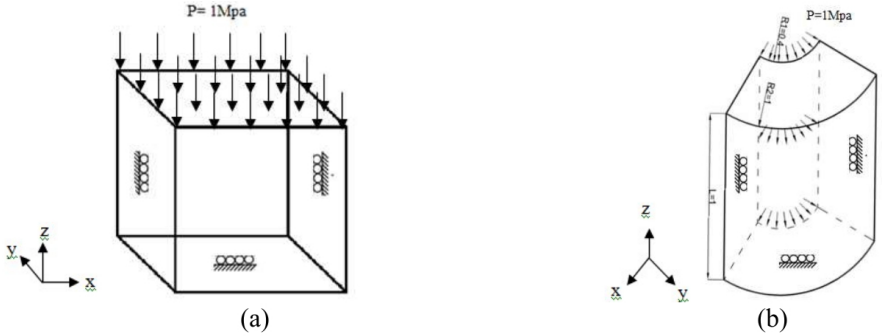

Figure 13.2: Boundary Conditions

13.6 Results

Convergence of the IGABEM algorithm was studied. Knot insertion was used to provide h-refinement, and the effect of the order of Gauss Legendre quadrature also investigated. Figure 1.3 shows the convergence of the scheme to the analytical displacement of $5 \times 10^{-6} m$ at the top surface for the cube problem.

An IGABEM analysis was used to obtain the distribution of hoop stress of the top patch of a quarter cylinder and the results by changing the number of Gauss points and the number of control points are shown in Figure 1.4.

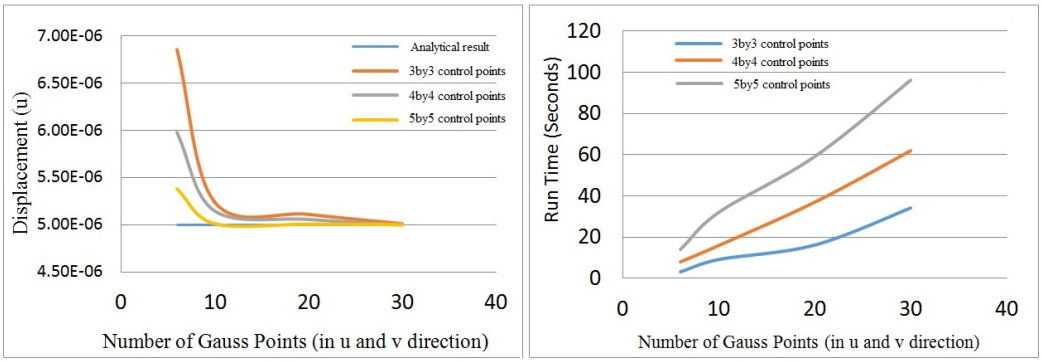

(a) (b)

Figure 13.3: (a): The trend of IGABEM result for cube by increasing number of control points and number of Gauss points (b): The trend of Matlab run-time by increasing number of knots and number of Gauss points

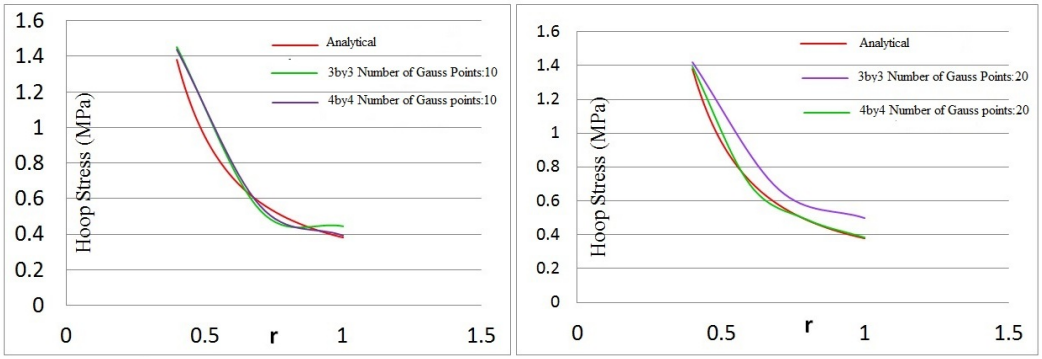

Figure 13.4: Hoop Stress calculated by IGABEM and Analytical result for different number of control points and Gauss points in a quarter cylinder

13.7 Adaptive Hierarchical Refinement of NURBS

Local refinement of NURBS is a key issue as already discussed in introduction. Due to the tensor-product structure of NURBS, it is difficult to be locally refined and obtain finer grids without propagation of the refinement. Consequently, for a general local refinement approach it is vital that it can handle and inherit any given degree of continuity. Hierarchical schemes are able to meet this requirement. On the other hand, the usage of multiple knots that lead to a decrease of smoothness is also possible. The hierarchical model allows complete local control of the refinement by using a spline hierarchy whose levels identify subsequent levels of refinement for the underlying geometric representation. It looks like a grid which divides the element into sub-elements and can focus and work on desired ones like on-off system.

It is also necessary to discuss the issue of error estimation for the purpose of adaptivity. We can classify the existing studies on error estimation into residual type, interpolation error type, boundary integral equation error type, nodal design sensitivity type and solution difference type. -**Residual type**: This method is very easy to calculate (L1 Norm, H0(L2) Norm, H1/2(norm), H2(Norm)), suitable for FEM and Galerkin BEM but it has uncertainty on Collocation BEM. The accuracy of the result is strongly dependent on the boundary situation (smooth or non-smooth). A posteriori residual error estimation type has been developed [11] to solve the problem of uncertainty for collocation BEM.

-**Interpolation error type**: The method is relatively straightforward to implement and it is widely used in FEM and BEM. The exact solution is approximated by higher order interpolation functions than the initial analysis and then, the difference between the numerical and predicted exact solutions is estimated as the error. The problem with this method is that computational accuracy of the predicted solutions is not guaranteed.
-**Integral equation type**: The method is suitable for BEM collocation Method. The residual is estimated using the boundary integral equation and the accuracy can be increased by changing the position of collocation points. The difficulty of this method in BEM collocation method is that the residual always disappears on the initial collocation points, special techniques are necessary for this purpose. In a collocation BEM scheme the residual is by definition of zero at the collocation points, so residuals need to be calculated at a different set of points.
-**Nodal design sensitivity type**: Accounted to be a sophisticated scheme since the original integral equation has the singular property.
-**Solution difference type**: In this method the solution error is defined as the difference between the solutions of the initial BEM analysis and some other (usually more refined) simulation. The method is very simple but has been shown to offer lower accuracy than schemes based on residual error indicators.[11]

An adaptive scheme proceeds by refining the model in some way (traditionally usually h, p or hp) in a way informed by the error indicator. In the proposed framework, we will adopt hierarchical B-splines [4] as a technology that allows local refinement within an isogeometric analysis code. We note that other solutions are available, notably T-splines, where useful properties like hanging nodes are permitted.

13.8 Conclusions

The basic Isogeometric Analysis Boundary Element Method (IGABEM) has been presented, and shown to converge for simple problems in linear elasticity. Results are shown that demonstrate the convergence for simple models with the number of control points and order of Gauss-Legendre quadrature. We note that the Gauss order shown considers the integration over an entire boundary patch, and not over an individual knot-span. For this reason, the number of Gauss points shown appears large compared with conventional BEM schemes. In spite of this consideration, the results suggest the required Gauss order is likely to be higher than that normally used for conventional BEM implementations. In this article we have also discussed different methods for error estimation. By considering the computational accuracy, cost and being suitable for collocation IGABEM, *a posteriori error estimation* [11] based on weighted residual error estimation is a great choice for the purpose of adaptive hierarchical refinement. In future work, we aim to develop an adaptive algorithm through the use of hierarchical NURBS for 3D geometries and to test its performance for a range of typical solid components found in the automotive industry by isogeometric boundary element method.

References

[1] T. J. R. Hughes, J. A. Cottrell and Y. Bazilevs, *CAD, finite elements, NURBS, exact geometry and mesh refinement.*, Computer Methods in Applied Mechanics and Engineering, 194(39) (2005), 4135–4195.

[2] P. Wang, J. Xu, J. Deng, *Isogeometric analysis using T-splines.*, Computer Methods in Applied Mechanics and Engineering, 199(58) (2010), 229-263.

[3] N. Nguyen-Thanh, J. Kiendl, H. Nguyen-Xuan, R. Wchner, K.U. Bletzinger, Y. Bazilevs, T. Rabczuk, *Rotation free isogeometric thin shell analysis using PHT-splines.*, Computer Methods in Applied Mechanics and Engineering, 200(4748) (2011), 3410-3424.

[4] D. R. Forsey, R. H. Bartels, *Hierarchical B-Spline Refinement.*, SIGGRAPH, 22(4) (1988), 205–212.

[5] D.J Benson, Y. Wang and A. P Nagy, *A multi-patch nonsingular isogeometric boundary element method using trimmed elements.*, Computational Mechanics, 56(1) (2015), 1–19.

[6] B.I. Yun, *A generalized transformation for evaluating singular integrals.*, Journal of Numerical Methods in Engineering 65 (2006), 1947–969.

[7] R.N. Simpson, M.A. Scott , M. Taus, D.C. Thomas, H. Lian, *Acoustic isogeometric boundary element analysis.*, Comput. Methods Appl. Mech. Engrg. 269 (2014), 265-290.

[8] A.A. Becker, *The boundary element method in engineering.*, a complete course. McGraw-Hill Companies, 1992.

[9] R.W. Johnston, *Higher order b-spline collocation at the greville abscissae.*, Applied Numerical Mathematics, 52(1) (2005), 63–75.

[10] A.-V. Vuong, C. Giannelli,B. J. uttler and B. Simeon , *A Hierarchical Approach to Adaptive Local Refinement in Isogeometric Analysis.*, Computational Methods in Applied Mechanical Engineering, 200(49-52) (2011,) 3554–3567.

[11] M. Feischl, G. Gantner, A. Haberl , D. Praetorius, *Adaptive 2D IGA boundary element methods.*, Engineering Analysis with Boundary Elements 62 (2016), 141-153.

Chapter 14

Can linear collocation ever beat quadratic?

Rebecca Martin, David J. Chappell, Nadia Chuzhanova and Jonathan J. Crofts

Department of Mathematics and Physics,
Nottingham Trent University
Nottingham
UK

Abstract. *Computational approaches are becoming increasingly important in neuroscience, where complex, nonlinear systems modelling neural activity across multiple spatial and temporal scales are the norm. This paper considers collocation techniques for solving neural field models, which typically take the form of a partial integro-differential equation. In particular, we investigate and compare the convergence properties of linear and quadratic collocation on both regular grids and more general meshes not fixed to the regular Cartesian grid points. For regular grids we perform a comparative analysis against more standard techniques, in which the convolution integral is computed either by using Fourier based methods or via the trapezoidal rule. Perhaps surprisingly, we find that on regular, periodic meshes, linear collocation displays better convergence properties than quadratic collocation, and is in fact comparable with the spectral convergence displayed by both the Fourier based and trapezoidal techniques. However, for more general meshes we obtain superior convergence of the convolution integral using higher order methods, as expected.*

14.1 Introduction

Neural field theory employs a continuum approach to model the activity of large populations of neurons in the cortex [1]. Such models are of great interest, not only from a mathematical point of view, but also from an experimental neuroscience point of view, since they are capable of replicating experimentally observed patterns of brain activity [2, 3]. Typically, such models take the form of a non-linear partial integro-differential equation such as

$$\frac{\partial}{\partial t}u(\mathbf{x},t) = -u(\mathbf{x},t) + \int_{\Omega} w(\mathbf{x}-\mathbf{x}')S(u(\mathbf{x}'))d\mathbf{x}'. \tag{14.1}$$

Here $u(\mathbf{x},t)$ describes the average activity of the neuronal population at position $\mathbf{x} \in \Omega$ at time t, while the nonlinear function S represents the mean firing rate, and typically takes the form of a sigmoid function. The connectivity kernel, w, describes how neurons positioned at $\mathbf{x}$ and $\mathbf{x}'$ interact [4]. Note that for special choices of the integral kernel, the neural field model (NFM) in (14.1) can be reduced to a partial differential equation (PDE), and the theory and tools of

PDEs can be deployed to investigate its solutions [5]. However, when considering more general, physiologically realistic kernels, the determination of solutions and their subsequent analysis requires numerical techniques.

In this work, we consider a two-dimensional NFM of the form (14.1) adapted so as to include a recovery variable, which acts to repolarise neuronal activity via negative feedback, as in [6]. Thus, we consider the following coupled system of equations

$$\begin{aligned}\frac{\partial u(x,y,t)}{\partial t} &= A\int_{-L}^{L}\int_{-L}^{L} w(x-x',y-y')S(u(x',y',t)-h)\mathrm{d}x'\mathrm{d}y' \\ &\quad - u(x,y,t) - a(x,y,t), \\ \tau\frac{\partial a(x,y,t)}{\partial t} &= Bu(x,y,t) - a(x,y,t).\end{aligned} \tag{14.2}$$

Here, $u(x,y,t)$ denotes population activity and $a(x,y,t)$ the recovery variable, at position (x,y) and time t. The parameters A, B, h and τ are related to the sensitivities and time-scale of the problem [6], and we set $\Omega = [-L,L]^2$ and impose periodic boundary conditions in both x and y for all of our experiments.

The role of S is to convert population activity into firing frequency, and it does this at a rate governed by the steepness parameter β [1]. Explicitly, S takes the form of a sigmoid with "steepness" parameter β as follows

$$S(u) = \frac{1}{1+e^{-\beta u}}.$$

The integral kernel $w(x-x',y-y')$ describes interactions between neighbouring neurons, as described earlier, and in our work is set to be a Mexican-hat type function

$$w(x,y) = e^{-(x^2+y^2)} - 0.17e^{-0.2(x^2+y^2)}.$$

The main source of error in the numerical approximation of Equation (14.2) is the convolution integral and so here we propose collocation techniques as a method for evaluating this integral. The main advantage of such a choice is that it can be directly generalised to the more general, typically asymmetric domains that result from modern neuroimaging studies. For completeness, we compare our results against standard techniques that typically use either Fourier based methods or the trapezoidal rule to compute the convolution integral in (14.2) when simple rectangular geometries are considered.

The paper is organised as follows. In §14.2 we employ the collocation technique to obtain a set of equations that can be solved to approximate the NFM in Equation (14.2). Then in §14.3, we consider the effect of mesh regularity on the accuracy of our solutions, and perform a comparative analysis against more standard techniques, deploying either trapezoidal rule or Fourier based techniques to compute the convolution integral in (14.2), in the case of a regular grid. We finish in §14.4 by giving an overview of the work as well as explaining its possible implications, before outlining a number of possibilities for future work.

14.2 The collocation method

Collocation is an example of a projection method that approximates an infinite dimensional problem, such as (14.2), by a finite dimensional one via a suitably defined projection operator $\mathcal{P}_n$. In what follows we provide brief details of the method as applied to Equation (14.2) (further details can be found in [7]).

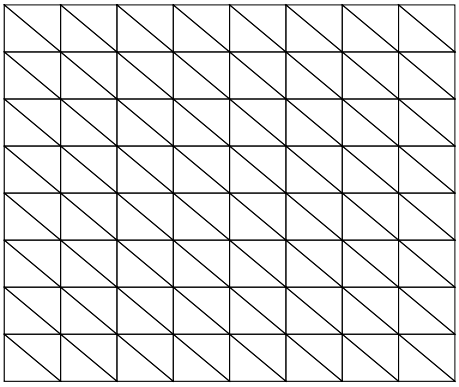

Figure 14.1: Illustration of a domain that uses Cartesian grid points as triangle vertices.

Consider the following triangulation $\mathcal{T}_n = \{\triangle_1, ..., \triangle_n\}$ of the square $[-L, L]^2$ and suppose that on each triangle $\triangle_k$ we employ a piecewise polynomial approximation of the unknown functions $u(x, y, t)$ and $a(x, y, t)$. In this case the projection operator takes the form

$$\begin{aligned} \mathcal{P}_n u(x,y,t) &= u_n(x,y,t) \\ &= \sum_{j=1}^{d} u(v_{k,j},t) l_j(x,y), \quad \text{for } (x,y) \in \Delta_k,\ k = 1,2,...,n. \end{aligned}$$

Here, $v_{k,j}$ denotes the (x, y) coordinates of the j^{th} interpolation point of the k^{th} triangle, the l_j are the corresponding Lagrange basis functions, and d denotes the number of interpolation nodes. In this study we take $d = 3$ or 6 depending upon whether linear or quadratic interpolation is applied, respectively.

The above allows us to formulate the following approximation to (14.2):

$$\begin{aligned} \frac{\partial u_n(x,y,t)}{\partial t} &= A\mathcal{P}_n \left\{ \int_{-L}^{L} \int_{-L}^{L} w(x-x', y-y') S(u-h) \mathrm{d}x' \mathrm{d}y' \right\} \\ &- u_n(x,y,t) - a_n(x,y,t), \\ \tau \frac{\partial a_n(x,y,t)}{\partial t} &= B u_n(x,y,t) - a_n(x,y,t). \end{aligned} \tag{14.3}$$

Assuming this expression holds exactly at the node values $v_1, v_2, ..., v_{n_v}$, where n_v refers to the total number of globally indexed node points $v_{k,j}$, we obtain a collocation scheme for (14.2).

To make the above collocation scheme more tractable we perform the integration in (14.3) by applying a quadrature rule over each triangle and summing the result. More specifically, we employ the transformation $T_k : \sigma \to \triangle_k$, given by

$$(x, y) = T_k(r, s) = (1 - r - s)v_{k,1} + sv_{k,2} + rv_{k,3}, \tag{14.4}$$

which maps the unit simplex σ on to each triangle $\triangle_k$. This enables us to integrate an arbitrary function, g say, over the triangle $\triangle_k$ as follows

$$\int_{\triangle_k} g(x, y) \mathrm{d}x \mathrm{d}y = 2\text{Area}(\triangle_k) \int_{\sigma} g(T_k(r, s)) \mathrm{d}r \mathrm{d}s.$$

Substituting this expression into (14.3) gives

$$\begin{aligned}\frac{\mathrm{d}u_n(v_i)}{\mathrm{d}t} &= 2A\sum_{k=1}^{n_t}\mathrm{Area}(\triangle_k)\int_\sigma w(v_i - T_k(r,s))S\left(\sum_{j=1}^{d}u(v_{k,j})l_j(r,s) - h\right)\mathrm{d}r\mathrm{d}s \\ &- u_n(v_i) - a_n(v_i), \\ \tau\frac{\mathrm{d}a_n(v_i)}{\mathrm{d}t} &= Bu_n(v_i) - a_n(v_i),\end{aligned} \tag{14.5}$$

for $i = 1, ..., n_v$ which is a system of $2n_v$ ordinary differential equations that can be solved to determine approximate solutions to (14.2).

14.3 Error analysis

When considering the numerical solution of Equation (14.2) the main source of error is the convolution integral and so we shall focus our analysis on the accurate representation of the integral

$$I = \int_{-L}^{L}\int_{-L}^{L} w(x - x', y - y')S(u(x', y') - h)dx'dy', \tag{14.6}$$

in the remainder of the paper.

We compare the accuracy of both linear and quadratic collocation against fast Fourier transform (FFT) techniques together with the convolution theorem, and the trapezoidal method, both of which require a regular spatial discretisation such as the one displayed in Figure 14.1. To probe grid convergence, we consider a sequence of refinements of an initial, regular grid consisting of $N_0 = 81$ nodes, such that at the mth stage of refinement, the number of nodes is given by $N_m = (2^m \cdot 8 + 1)^2$ for $m = 1, 2, \ldots, 7$. If we then denote by I_m the numerical approximation of (14.6) on the grid of size N_m, we can approximate the order of convergence of the respective discretisation schemes by considering a log-log plot of the absolute error between consecutive grids $|I_m - I_{m+1}|$ versus grid size N_{m+1}. Here we consider point-wise convergence and so all results shown are for a representative grid point. Note that we have repeated the analysis for other grid points and observed almost identical behaviour (experiments not shown).

Our results are displayed in figures 14.2 and 14.3. In particular, from Figure 14.2 we see that both trapezoidal rule and FFTs display geometric convergence, as expected (see [8] for a discussion of the convergence properties of the trapezoidal rule on a periodic domain); however, we find, perhaps somewhat surprisingly, that linear collocation also exhibits geometric convergence. This is in contrast to quadratic collocation, which converges quadratically. To understand the above result, we consider the collocation technique as applied to (14.6) in more detail below.

Firstly, note that employing linear collocation alongside the three point quadrature rule

$$\int_\sigma G(r,s)\mathrm{d}r\mathrm{d}s = \frac{1}{6}[G(0,0) + G(0,1) + G(1,0)],$$

with $G(r,s) = g(T_k(r,s))$, as defined in §14.2, enables us to construct the following approxima-

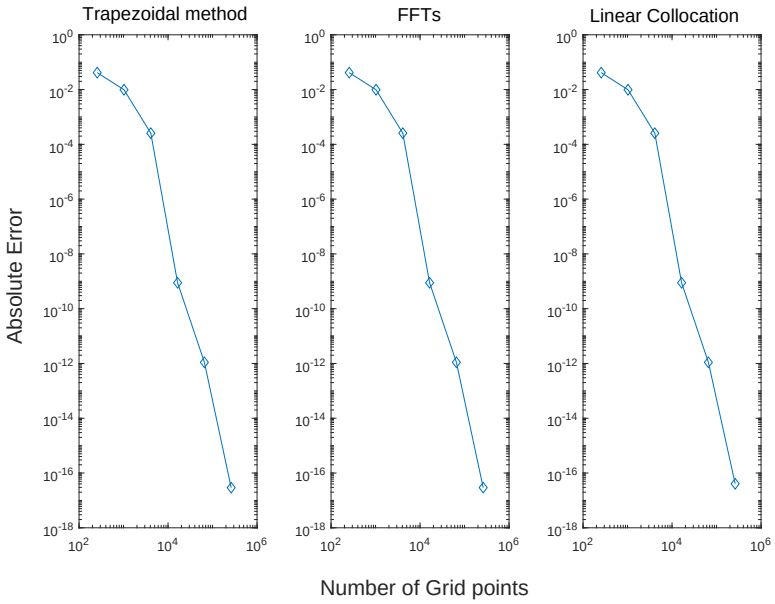

Figure 14.2: The error $|I_m - I_{m+1}|$ plotted against grid size N_{m+1} reveals geometric convergence rates for trapezoidal rule, FFTs and linear collocation when computing the integral in (14.6).

tion to (14.6):

$$I \approx \frac{1}{3}\sum_{k=1}^{n} \text{Area}\,(\Delta_k) \left[w(v - T_k(0,0))S\left(\sum_{j=1}^{3} u(v_{k,j}) l_j(0,0) - h\right) + \right.$$
$$w(v - T_k(0,1))S\left(\sum_{j=1}^{3} u(v_{k,j}) l_j(0,1) - h\right) + \tag{14.7}$$
$$\left. w(v - T_k(1,0))S\left(\sum_{j=1}^{3} u(v_{k,j}) l_j(1,0) - h\right) \right].$$

We can further simplify the above by noting that since we are solving on a uniform Cartesian domain, $\text{Area}\,(\Delta_k) = \Delta x^2/2$ for all triangles, where here, Δx $(= \Delta y)$ is the local mesh spacing. Substituting this into (14.7) and evaluating the Lagrange basis functions at the node points gives

$$\frac{\Delta x^2}{6}\sum_{k=1}^{n} \left[w(v - T_k(0,0))S(u(v_{k,1}) - h) + w(v - T_k(0,1))S(u(v_{k,2}) - h) \right.$$
$$\left. + w(v - T_k(1,0))S(u(v_{k,3}) - h) \right].$$

Recalling that $T_k(0,0)$ denotes the coordinates of the first vertex in Δ_k, $T_k(0,1)$ the second and

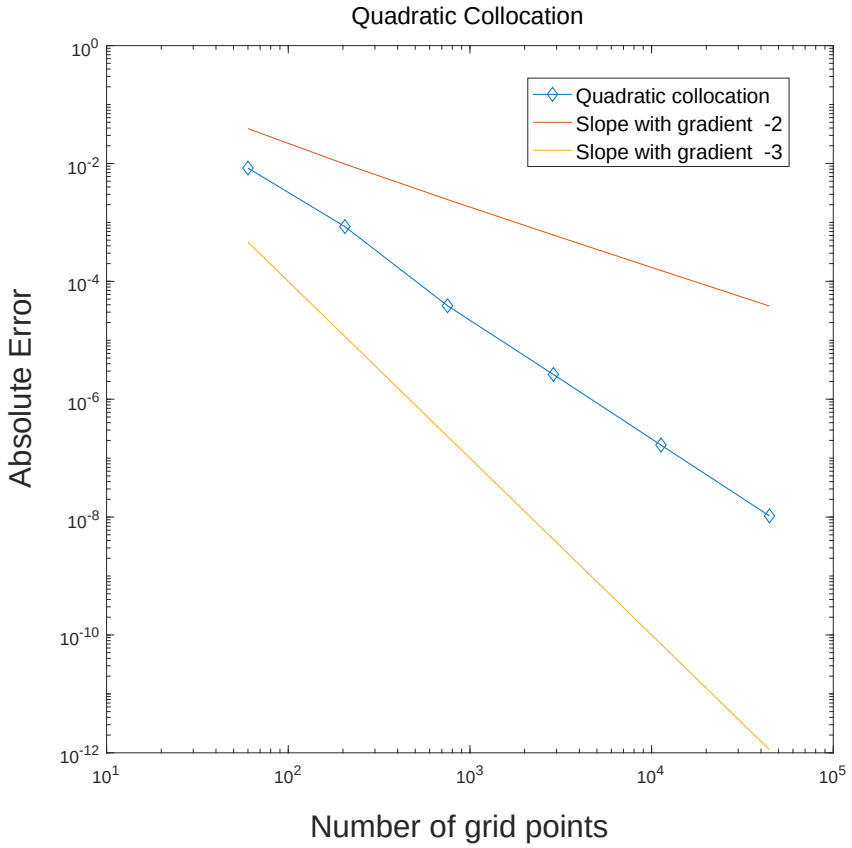

Figure 14.3: Convergence of quadratic collocation when computing the integral in (14.6) with the error $|I_m - I_{m+1}|$ plotted against grid size N_{m+1}.

$T_k(1,0)$ the third, we can rewrite the above as

$$\frac{\Delta x^2}{6}\sum_{k=1}^{n}\Big[w(v-v_{k,1})S(u(v_{k,1})-h)+w(v-v_{k,2})S(u(v_{k,2})-h) \\ +w(v-v_{k,3})S(u(v_{k,3})-h)\Big]. \tag{14.8}$$

However, for a regular grid the triangle vertices are simply the Cartesian mesh points and so Equation (14.8) is nothing other than the trapezoidal rule for solving (14.6) on a periodic two-dimensional domain. The factor of $1/6$ occurs due to the fact that each node appears six times in the sum in (14.8). Thus, we have shown that for a regular grid with periodic boundary conditions solving Equation (14.6) using linear collocation and a quadrature rule based only on the triangle vertices is equivalent to using the trapezoidal rule. This explains the spectral convergence observed in Figure 14.2.

Next we consider the effects of mesh regularity on solutions of Equation (14.6). To do this we deployed the DistMesh Matlab package [9] to generate a general mesh, that is, one in which the triangle vertices do not lie on a Cartesian grid, as in our previous investigations. As before, numerical errors were approximated by comparing the numerical solution of (14.6) at the same grid point across a range of increasingly fine meshes. A refined triangulation was created by subdividing each triangle into four similar triangles, as shown in Figure 14.4. Results for linear and quadratic collocation are displayed in Figure 14.3. Note that in contrast to earlier results,

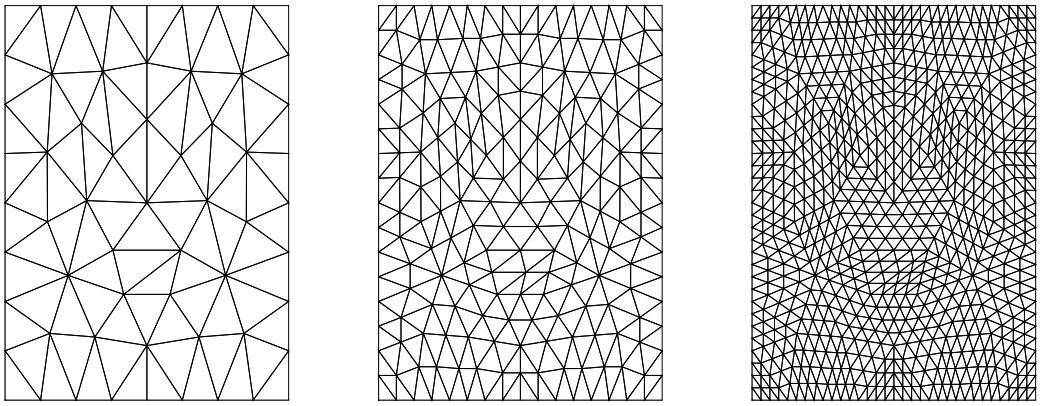

Figure 14.4: An illustration of the refinement procedure for a general triangulated domain. Meshes are generated using the DistMesh Matlab package [9].

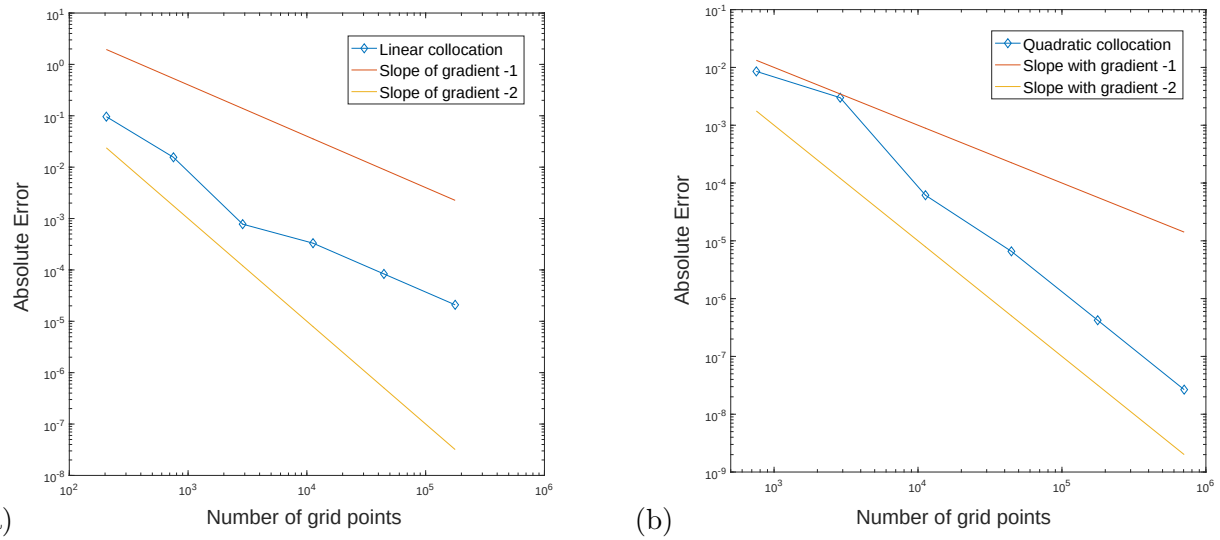

Figure 14.5: Convergence of (a) linear and (b) quadratic collocation when computing the integral in (14.6) using a general triangulation (see Figure 14.1).

superior convergence is now observed for quadratic collocation: linear and quadratic convergence is attained for linear and quadratic collocation, respectively. Thus, the geometric convergence displayed previously breaks down for more general triangulations, as expected.

14.4 Conclusions

In this work, we have employed collocation techniques to solve a two-dimensional NFM on a periodic, square domain $\Omega = [-L, L]^2$. Importantly, we found that these techniques were capable of reproducing solutions found by standard methods, which compute the convolution integral in the NFM using either Fourier based methods or the trapezoidal rule. Moreover, we found that when employing a regular triangulation based upon a Cartesian grid then, perhaps surprisingly, linear collocation out performed quadratic collocation. In fact, the linear collocation scheme was found to exhibit spectral convergence, similar to the Fourier based and trapezoidal methods. This result can be explained by noting that for a regular mesh with periodic boundary conditions, linear collocation can be shown to be equivalent to the trapezoidal rule for the particular quadrature methods employed here. For more general meshes the behaviour of lin-

ear and quadratic collocation was as expected, that is convergence was linear and quadratic, respectively. Future work shall deploy the methods discussed here, in conjunction with efficient numerical schemes for computing geodesic distances, to solve NFMs on two-dimensional curved geometries such as a sphere or torus. The overarching aim will be to extend these methods to more physiologically realistic cortical domains [10, 11, 12].

Acknowledgement

R. Martin would like to acknowledge Nottingham Trent University for an RAE funded PhD scholarship.

References

[1] P. C. Bressloff, *Spatiotemporal dynamics of continuum neural fields*, Journal of Physics A: Mathematical and Theoretical, 45(3) (2011), 033001.

[2] S. Coombes, *Large-scale neural dynamics: simple and complex*, Neuroimage, 52(3) (2010), 731–739.

[3] I. Bojak, *et al.*, *Towards a model-based integration of coregistered electroencephalography/functional magnetic resonance imaging data with realistic neural population meshes*, Phil. Trans. R. Soc. A, 369, (2011), 3785-3801.

[4] P. Sanz-Leon, *et al.*, *Mathematical framework for large-scale brain network modelling in the virtual brain*, Neuroimage, 111 (2015), 385–430.

[5] C. R. Laing, *Neural Field Theory*, Springer, Berlin, 2013.

[6] C. R. Laing, *Numerical bifurcation theory for high-dimensional neural models*, Journal of Mathematical Neuroscience, 4 (2014), 13.

[7] K. E. Atkinson, *The Numerical Solution of Integral Equations of the Second Kind*, Cambridge University Press, Cambridge, UK, 1997.

[8] L. N. Trefethen and J. A. C. Weideman, *The exponentially convergent trapezoidal rule*, SIAM Review, 56(3) (2014), 385–458.

[9] P. O. Persson and G. Strang, *A simple mesh generator in MATLAB*, SIAM Review, 46(2) (2004), 329–345.

[10] R. O'dea, *et al.*, *Spreading dynamics on spatially constrained complex brain networks*, Journal of the Royal Society Interface, 10 (2013), 20130016.

[11] J. A. Henderson and P. A. Robinson, *Relations between geometry of cortical gyrification and white matter network architecture*, Brain Connectivity, 4 (2014), 112–130.

[12] Y-P. Lo, *et al.*, *A geometric network model of intrinsic grey-matter connectivity of the human brain*, Scientific reports, 5 (2015), 15397.

Chapter 15

Rapid solution of the modified Helmholtz and heat equations

Anita A. Mayo

Department of Mathematics,
Baruch College, CUNY
One Bernard Baruch Way
NY NY 10010 USA

Abstract. *We present high order accurate methods for solving the modified Helmholtz and heat equations on general smooth regions in two dimensions. The methods use new fourth order accurate techniques we have developed for evaluating certain volume and surface integrals. These integrals are evaluated using fast finite difference methods on larger rectangular regions in which we embed the smooth integration regions, and require $O(n^2 \log n)$ operations where n is the number of mesh points in each direction in the embedding region. Computational results are provided.*

15.1 Introduction

In this paper we present new methods for solving the modified Helmholtz and heat equations on smooth two dimensional regions. The methods make use of rapid, high order accurate techniques for evaluating volume integrals whose kernels are the fundamental solution of the modified Helmholtz equation and surface integrals whose kernels are the normal derivative of the fundamental solution. The regions of integration can be any smooth curve or region, and the cost of evaluating either integral is essentially equal to the cost of inverting a discrete approximation to the modified Helmholtz operator on a rectangular two dimensional region. Thus, by using Fourier methods [7] both types of integrals can be evaluated in $O(n^2 \log n)$ operations. Our method is an extension of one we developed previously for solving Poisson's and the biharmonic equation on general regions. See, for example, [10],[11],[12],[5],[3].

The essential idea is the following. Let L denote the modified Helmholtz operator, and suppose the integral W is such that $LW = f$ in D and $LW = 0$ outside. (f can be 0 if W is a surface integral) We first embed D in a larger rectangular region R with a uniform mesh, and compute a fourth order accurate approximation to $L_h W$, the discrete modified Helmholtz operator L_h applied to W, at all the mesh points of R. Then we apply an operator that inverts L_h on R to obtain an approximation to W. It is easy to compute an such approximation at most mesh points of R. At mesh points inside D that have all their neighboring mesh points inside D we approximate $L_h W$ by f since $LW = f$ on D. Similarly, at mesh points outside D

whose neighboring mesh points are also outside D, we set $L_h W = 0$ since $LW = 0$ outside D. The difficulty arises at the other, "irregular" mesh points. Because of the discontinuities in the derivatives of W across the boundary of D the discrete modified Helmholtz operator is not well approximated by the continuous Helmholtz operator at those points. It turns out, however, that one can compute an approximation using the discontinuities in W, which depend on f and its derivatives, and information about the boundary of D.

In order to solve the modified Helmholtz equation we use an integral equation formulation that was also used by Kropinski and Quaife [9]. They solved the equation using a fast multipole method, and for the discretization they used hybrid Gauss-trapezoidal quadrature rules. We used a Nystrom method with the trapezoid rule as the quadrature method, and solved the resulting linear system of equations using a preconditioned conjugate gradient method. Our cost of solving the integral equation is therefore $O(N^2)$. Our method of evaluating integrals can and should, of course, be combined with FMM type methods for solving integral equations [13], [12]. For simplicity we also used the same discretization in time of the heat equat equation as Kropinski and Quaife, and combined it with our method of evaluating volume and surface integrals.

The most common methods for evaluating volume integrals involve direct application of a quadrature formula, and therefore $O(n^4)$ operations are needed to evaluate the integral at every point of an n by n grid, since evaluating each integral requires $O(n^2)$ operations. In contrast, our method only requires $O(n^2 \log\, n)$ operations.

Another difficulty encountered when using straightforward quadrature formulas is that fundamental solutions of the modified Helmholtz equation are discontinuous and have discontinuities in their derivatives as the point at which one is evaluating the integral nears a point of the region of integration. Therefore, it is difficult compute these integrals very accurately at points in, or near, the region of integration. The method we use does not have these problems. We note other rapid and sophisticated methods have been developed for evaluating volume integrals, but many require smooth extension of the inhomogeneous term from the irregular region to the rest of the rectangular embedding region. Our methods have no such requirement.

15.2 Evaluation of volume and surface integrals

In this section we present our method for evaluating an integral whose kernel is a fundamental solution of the modified Helmholtz equation $\Delta u - a^2 u = \delta$. Here δ is the Dirac function.

15.2.1 Evaluation of volume integrals

We start by embedding the integration region D in a larger rectangular region R with a uniform grid, say with mesh width h, which ignores the boundary of D.

Let

$$W(x,y) = \frac{1}{2\pi a^2} \int_D K_0\left(\frac{r}{a}\right) f(x',y') dV \tag{14.1}$$

where $r = \sqrt{(x-x')^2 + (y-y')^2}$, and $K_0(r)$ is the zeroth order modified Bessel function of the second kind.

We evaluate W by first approximating $L_h W$ where L_h is a discrete approximation to the modified Helmholtz operator at all the mesh points of R. Then we apply an operator, L_h^{-1} which inverts L_h on R. We note that inverting L_h on a grid with n points only requires $O(n \log n)$ operations [7].

Since

$$\Delta W - a^2 W = f \text{ in } D \text{ and } \Delta W - a^2 W = 0 \text{ outside } D, \tag{14.2}$$

at mesh points inside D, which have all their neighboring mesh points inside D we set $L_h W_h = f$, and at points outside D, with all their neighbors outside we set $L_h W = 0$.

The problem then reduces to approximating $L_h W$ at the points which are in one region, but have neighboring mesh points in the other region. It turns out that in order to approximate $L_h W$ at these points it suffices to know the discontinuities in the derivatives of W in the coordinate directions at the boundary of the region D. We now show how to find these discontinuities.

Suppose the boundary of D is given by $(x(t), y(t))$. For a function g defined on R let $[g(p)]$ denote the discontinuity in g at a point p on ∂D. An integral of the form (14.1) and it's normal derivative are continuous across ∂D. Therefore, for p in ∂D

$$[W(p)] = 0, \tag{14.3}$$

and

$$[W_n(p)] = \dot{y}(t)[W_x(p)] - \dot{x}(t)[W_y(p)] = 0. \tag{14.4}$$

Differentiating (14.3) in the tangential direction t, we see

$$[W_t(p)] = \dot{x}(t)[W_x(p)] + \dot{y}(t)[W_y(p)] = 0, \tag{14.5}$$

so $[W_x] = [W_y] = 0$.

By (14.2) the second derivatives of W are discontinuous and

$$[W_{xx}] + [W_{yy}] = f \tag{14.6}$$

Differentiating (14.4) and (14.5) in the tangential direction we have

$$\dot{x}(t)^2[W_{xx}] + \dot{y}(t)[W_{yy}] + 2\dot{x}(t)\dot{y}(t)^2[W_{xy}] = 0. \tag{14.7}$$

$$\dot{x}(t)\dot{y}(t)[W_{xx}] - \dot{x}(t)\dot{y}(t)[W_{yy}] + (\dot{y}^2(t) - \dot{x}^2(t))[W_{xy}] = 0. \tag{14.8}$$

Equations (14.6), (14.7) and (14.8) determine $[W_{xx}], [W_{yy}]$ and $[W_{xy}]$. We use similar methods in order to determine the discontinuities in third and higher order derivatives.

Next we show how to use these discontinuities to approximate $L_h W$. Let $\tilde{w}(p)$ denote the values of $W(p)$ at points p outside D, $w(p)$ denote the values of $W(p)$ at points p inside D, and let B be the set of irregular mesh points, that is the set of points which have at least one of their neighboring mesh points on the opposite side of D.

We now show how to approximate L_h at points of B. For simplicity we begin by showing how to compute a second order accurate approximation, i.e. we let

$$L_h^5 W = \left(\frac{1}{h^2} \begin{bmatrix} & 1 & \\ 1 & -4 & 1 \\ & 1 & \end{bmatrix} - a^2 \right) W.$$

Suppose a point p is in D, and the point to the right, p_E, is not. Let p^* be the point on the line between p and p_E which intersects ∂D, let h_1 be the distance between p_E and p^*, and let $h_2 = h - h_1$.

By manipulating the Taylor series centered at p and p_E and evaluated at p^* we can derive the following expression for $\tilde{w}(p_E) - w(p)$: (For details see [10])

$$\tilde{w}(p_E) - \tilde{w}(p) = [\tilde{w}(p^*) - w(p^*)] - h_1[\tilde{w}_x(p^*) - w_x(p^*)] + \frac{1}{2}h_1^2[\tilde{w}_{xx}(p^*) - w_{xx}(p^*)]$$

$$-\frac{1}{6}h_1^3[\tilde{w}_{xxx}(p^*) - w_{xxx}(p^*)] + \frac{1}{24}h_1^4[\tilde{w}_{xxxx}(p^*) - w_{xxxx}(p^*)]$$

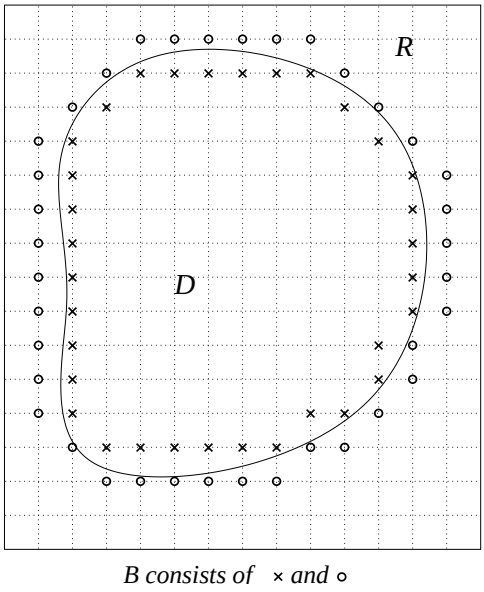

Figure 15.1: Points of the set B.

$$-h\tilde{w}_y(p) + \frac{1}{2}h^2\tilde{w}_{yy}(p) - \frac{1}{6}h^3\tilde{w}_{yyy}(p) + \frac{1}{24}h^4\tilde{w}_{yyyy}(p) + O(h^5) \tag{14.9}$$

Note the first five terms depend on the discontinuities between w and $\tilde{w}$ and in their x derivatives across ∂D. The other terms are the usual Taylor series terms. Therefore, the right hand side of (14.9) is a sum of terms we can evaluate in terms of the discontinuities between w and $\tilde{w}$ and their x derivatives, and terms we would have if the boundary of D did not pass between p and p_E.

Now let p_W, p_N, p_S be the mesh points to the left of, above, and below p. We obtain the

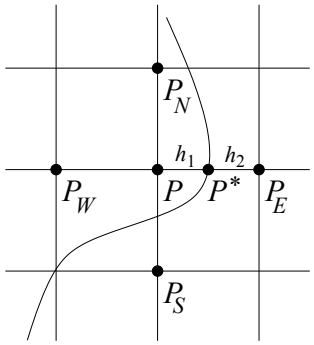

Figure 15.2: Mesh points in the vicinity of point p.

same type of expressions for the differences between the value of W at p and at its other neighbors, that is $W(p_W) - W(p), W(p_N) - W(p), W(p_S) - W(p)$, except that there will not be any boundary terms unless ∂D passes between p and that neighbor. Therefore, we can compute an approximation to $L_h^5 W$, which is just the sum of the above four differences divided by h^2 minus $a^2 W(p)$

$$L_h^5 W(p) = \frac{W(p_E) + W(p_W) + W(p_N) + W(p_S) - 4W(p)}{h^2} - a^2 W(p),$$

at the irregular points when we know the derivatives of the boundary curve and the derivatives of f.

More precisely, for points p in B we define $m(p)$ to be the extra terms in $L_h^5 W$ due to the discontinuities in W and its derivatives and W_h to be the solution of the equations:

$$L_h^5 W_h(p) = \begin{cases} f(p) & p \in D - B \\ f(p) + m(p) & p \in B \cap D \\ m(p) & p \in B \cap D^c \\ 0 & p \in R - D \cap B \end{cases}$$

$$W_h(p) = W(p) \quad p \in \partial R$$

The accuracy of $m(p)$ determines the accuracy of the solution. In particular, if $m(p)$ is first order accurate W^h will be a second order accurate approximation to W. See [2].

We can also approximate $L_h^9 W$ where L_h^9 is a fourth order accurate 9 point approximation to L. Then, by applying an operator which inverts the operator L_h^9 we can obtain a fourth order accurate solution.

Specifically, to evaluate the surface and volume integrals we use the fourth order accurate approximation to the modified Helmholtz operator :

$$L_h^9 = \left(\Delta_h^9 - \left(a^2 + \frac{a^4 h^2}{12}\right)\right) u = f + \frac{h^2}{12}\left(f + \Delta f\right)$$

where

$$\Delta_h^9 W = \frac{1}{6h^2} \begin{bmatrix} 1 & 4 & 1 \\ 4 & -20 & 4 \\ 1 & 4 & 1 \end{bmatrix} W$$

To see that this operator is fourth order accurate we note that for any smooth function u

$$\Delta_h^9 u = \Delta u + \frac{h^2}{12}\Delta\left(\Delta u\right) + O(h^4).$$

So, if $\Delta u = a^2 u + f$, then

$$\Delta_h^9 u = a^2 u + f + \frac{h^2}{12}\Delta\left(a^2 u + f\right) + O(h^4)$$

$$= a^2 u + f + \frac{h^2}{12}\left(a^2(a^2 u + f) + \Delta f\right) + O(h^4)$$

$$= \left(a^2 + \frac{a^4 h^2}{12}\right) u + f + \frac{h^2}{12}\left(f + \Delta f\right) + O(h^4).$$

To approximate $\Delta_h^9 W$ we use the fact that

$$\Delta_h^9 = \frac{2}{3}\Delta_h^5 + \frac{1}{3}\Delta_h^x$$

where

$$\Delta_h^x W = \frac{1}{2h^2} \begin{bmatrix} 1 & & 1 \\ & -4 & \\ 1 & & 1 \end{bmatrix} W.$$

In order to compute an approximation to $\Delta_h^x W$ we need the discontinuities of W in the $u = \frac{x+y}{\sqrt{2}}$ and $v = \frac{x-y}{\sqrt{2}}$ directions. The discontinuities can, of course, be computed in terms of the discontinuities in the x and y directions. For example, if p^* is on ∂D, then

$$[W_u(p^*)] = \frac{[W_x(p^*)]}{\sqrt{2}} + \frac{[W_y(p^*)]}{\sqrt{2}}.$$

Once we know these discontinuities we may, in the same way as before, use them to compute a higher order accurate approximation to $\Delta_h^x W$, and thereby $\Delta_h^9 W$ and $L_h^9 W$.

The accuracy of the resulting method is same as the accuracy to which the discrete Helmholtz operator is computed. That is, the errors in computed values of the potential W_h are bounded by a constant times the maximum truncation error of $L_h^5 W$ or $L_h^9 W$, and if the potential function which is being computed is smooth, the errors are $O(h^2)$ or $O(h^4)$.

15.2.2 Evaluation of surface integral

We use essentially the same method to compute surface integrals of the form

$$U(x,y) = \frac{1}{2\pi a^2} \int_{\partial D} \mu(s) K_0 \left(\frac{r}{a}\right) ds.$$

As when we evaluate volume integrals the problem reduces to evaluating LU in the regions inside and outside D, and evaluating the discontinuities in U and its derivatives across the boundary of D. We first note that

$$(\Delta - a^2)U = 0 \text{ inside } D, \text{ and } (\Delta - a^2)U = 0 \text{ outside } D. \tag{14.10}$$

That is, the integral satisfies the modified Helmholtz in the region inside D and in the region outside D. It is also known that such an integral is continuous in the normal direction, and has a discontinuity equal to the density in the tangential direction:

$$[U] = \mu \tag{14.11}$$

and

$$[U_n] = 0. \tag{14.12}$$

It follows that

$$[U_x] = \frac{\dot{\mu}\dot{x}}{\dot{x}^2 + \dot{y}^2} \text{ and } [U_y] = \frac{\dot{\mu}\dot{y}}{\dot{x}^2 + \dot{y}^2}.$$

To find the discontinuities in the second derivatives of U we note that by (14.10)

$$[\Delta U] = a^2 [U] = a^2 \mu$$

We also note that by (14.11) and (14.12)

$$[U_{tt}] = \ddot{\mu}$$

and

$$[U_{nt}] = 0.$$

The above three equations determine $[U_{xx}], [U_{xy}]$ and $[U_{yy}]$.

To find the discontinuities in the four third derivatives we use the following four equations:

$$[(\Delta U)_n] = a^2 [U_n] = 0,$$

$$[(\Delta U)_t] = a^2 [U_t] = a^2 \dot{\mu}$$

$$U_{ttt} = \dddot{\mu} \text{ and } U_{ntt} = 0.$$

As before, once determined we use these discontinuities in the derivatives of U to compute approximations to $L_h^5 U$ or $L_h^9 U$ at the irregular mesh points of R, and then apply a fast solver L_h^{-1} to obtain an approximation to U.

It is, of course, necessary to provide boundary conditions at the edge of the computational region R. The integral we obtain an approximation to with this method is is the one associated with the same boundary conditions as the fast Helmholtz solver we use. For example, if we use a doubly periodic Helmholtz solver, then we obtain an approximation to the integral whose kernel is the doubly periodic Green's function for the modified Helmholtz equation on R. It is also possible to obtain approximations to integrals which satisfy free space boundary conditions. In that case we can use a method originally developed by Hockney [6] and later improved by James [8].

15.3 Solution of modified Helmholtz and heat equations

15.3.1 Modified Helmholtz equation

As in [9], in order to solve the inhomogeneous equation $(\Delta - a^2)U = f$ when Dirichlet boundary conditions $U(x, y) = g(x, y)$ on ∂D are prescribed we use the representation of the solution as the sum of a volume integral and an integral of a double layer density function:

$$U(x,y) = W(x,y) + U_S(x,y) = \int_D f(x',y')K_0 dV + \int_{\partial D} \frac{\partial K_0}{\partial n}\mu(s)ds \tag{14.13}$$

We first evaluate W_h, the approximation to the volume integral W at points of R, and then we interpolate its values onto the discretization points of ∂D using the known discontinuities in its derivatives. More precisely, we use the values of W_h at points on both sides of ∂D and the discontinuities in the second and third derivatives of W to compute the extension of the inside function w to nearby points of R outside D. We then interpolate values of the extended function w onto ∂D using fourth order Lagrange interpolation.

Also, as in [9], in order to determine the density $\mu(s)$ for the surface integral U_S we solve the integral equation

$$-\frac{\mu(t)}{2a^2} + \frac{1}{2\pi a^2}\int_{\partial D} \frac{\partial}{\partial n_s} K_0\left(\frac{r}{\alpha}\right)\mu(s)ds = \omega(t) \tag{14.14}$$

where $\omega(t) = g(t) - w(t)$.

As noted, in our experiments we discretized the above equation using a Nystrom method with the trapezoid rule with equally spaced points as the quadrature formula [1]. By the Euler Maclaurin formula the trapezoid rule is highly accurate for smooth functions on periodic regions.

Once we have solved the integral equation we evaluate the surface integral U_S using the method described in the previous section.

15.3.2 Heat equation

We also used the surface and volume integrals to solve the heat equation

$$u_t(x,y,t) - \Delta u(x,y,t) = F(x,y,t), \quad 0 \le t \le t_f$$

with Dirichlet boundary conditions

$$u(x,y,t) = f(x,y,t) \quad (x,y) \in \partial D, t \in [0,t_f]$$

and initial conditions

$$u(x,y,0) = u_0(x,y)$$

prescribed where D is a general two dimensional region.

Instead of using an integral equation approach based on a fundamental solution of the heat equation we first discretized with respect to time. Specifically, as in [9] we used the implicit second order accurate extrapolated Gear method:

$$\Delta u^{N+1} - \frac{1}{\alpha^2} u^{N+1} = \frac{1}{3\alpha^2}\left(u^{N-1} - 4u^N + 4\delta t F^N - 2\delta t F^{N-1}\right) \equiv B^N \tag{14.15}$$

where δt is the time step and $\alpha^2 = \frac{2}{3}\delta t$.

At the Nth time step the approximation to the solution u^N is the sum of a volume integral W^N and a surface integral U_S^N:

$$u^N = W^N + U_S^N$$

where

$$\Delta W^N - \alpha^2 W^N = B^N, \tag{14.16}$$

and

$$\Delta U_S^N - a^2 U_S^N = 0 \quad (x,y) \in D$$
$$U^N = f(x,y,t^N) - W^N(x,y), \quad (x,y) \in \partial D.$$

Thus, at each time step we must solve one integral equation and evaluate two integrals.

We can accurately approximate B^N, the right hand side of (14.16) and it's Laplacian. However, since we cannot approximate the normal derivative of the right hand side accurately enough, we cannot accurately approximate the discontinuities in the third and higher order derivatives of W^N. Therefore the method should only be second order accurate in space. In practice, however, we have found the method to be somewhat more accurate.

15.4 Numerical Experiments

In this section we present results of some of our numerical experiments.

In the experiments we report on the irregular region D was the unit disc, and the embedding region R was a square of side 1.6. In the tables nx and ny denote the number of mesh points in the x and y directions.

In our first experiment we chose the volume integral $W(x,y)$ such that

$$\Delta W - a^2 W = 4b$$

where $b = -\frac{K_1\left(\frac{d}{a}\right)}{2da}$. When D is a disc of radius d the analytic value of the integral is known:

$$W = b(r^2 - d^2) + K_0\left(\frac{d}{a}\right) \text{ for } r \le d$$

and

$$W = K_0\left(\frac{r}{a}\right) \text{ for } r > d$$

The results in Table 1 are for $a = .45$, the errors are the maximum relative errors, and the numbers in the last column are the ratios of the consecutive errors.

Table 1

nx	ny	abs. error	rate
17	17	0.181E-03	.
33	33	0.123E-04	14.72
65	65	0.822E-06	14.96
129	129	0.557E-07	14.76
257	257	0.371E-08	15.02

These numbers confirm that our method of evaluating volume integrals is essentially fourth order accurate.

In our next experiment we tested our method for solving the integral equation and evaluating the surface integral. We chose the boundary values

$$g(x,y) = I_1(ar)\,.$$

If the region D is the disc of radius d the density function and the values of the surface integral inside are

$$\mu = (I_1(ad) - cK_1(ad))\,x/r$$

where $I_1(r)$ is the first order modified Bessel function of the first kind, and

$$U_S(r) = I_1(ar)x/r \text{ for } r \le d \text{ and } U_S(r) = cK_1(ar)x/r \text{ for } r > d.$$

In the table 2 ns is the number of discretization points on ∂D, $a = 10.0$, and $d = .5$.

Table 2

nx	ns	rel. error	rate
17	50	0.110E+00	.
33	100	0.156E-01	7.05
65	200	0.120E-02	13.40
129	400	0.809E-04	14.83
257	800	0.532E-05	15.20

In Table 3 we present our results of solving the inhomogeneous heat equation whose solution is $\sin(t)\sin(x)\sin(y)$ on the unit disc for $0 \le t \le 1$. The numbers nt are the number of time steps and the errors are the r.m.s. errors at $t = 1$.

Table 3

nx	ns	nt	error	rate
17	50	12	0.966E-03	.
33	100	12	0.160E-03	6.04
65	200	12	0.168E-04	9.52
129	400	12	0.221E-05	7.60
17	50	24	0.198E-03	.
33	100	24	0.332E-04	5.95
65	200	24	0.430E-05	7.72
129	400	24	0.581E-06	7.41

15.5 Conclusions

We have presented rapid, fourth order accurate numerical methods for evaluating volume integrals whose kernels are a fundamental solution of the modified Helmholtz equation and surface integrals whose kernels are the normal derivatives of such functions. We have also shown how these methods can be used as part of efficient numerical methods for solving both the modified Helmholtz and heat equations on general two dimensional regions in space.

Acknowledgement

The work of the author was supported by the Dean of the Weissman School Baruch College and is gratefully acknowledged.

References

[1] K. E. Atkinson, *The Numerical Solution of Integral Equations of the Second Kind*, Cambridge University Press, Cambridge, UK, 1997.

[2] T. Beale and A. Layton , *On the accuracy of finite difference methods for elliptic problems with interfaces*, Comm. Appl. Math. Comp. Sci., 1(1), (2006), 91-119.

[3] G. Biros, L. Ying, and D. Zorin, *A fast solver for the Stokes equations with distributed forces in complex geometries*, J. Comput. Phys., 193(1), (2004), 317-348.

[4] J. Bramble, and B. Hubbard, *A priori bounds on the discretization error in the numerical solution of the Dirichlet problem*, Contributions to Differential Equations, 2(4), (1963), 229-207.

[5] A. Greenbaum and A. Mayo, *Rapid parallel evaluation of three dimensional integrals in potential theory*, J. Comput. Phys., 145(2), (1998), 731-742.

[6] R. Hockney, *The potential calculation and some applications* Methods of Comput. Phys., 9(1), (1970), 135-211.

[7] R. Hockney, *Computer Simulation Using Particles*, McGraw Hill, New York, 1981.

[8] R. James, *The solution of Poisson's equation for isolated source distributions* J. Comput. Phys, 25(71) (1977), 1534-1578.

[9] M. Kropinski, and B. Quaife, *Fast integral equation methods for the modified Helmholtz Equation*, J. Comput. Phys, 230(2), (2011), 425-434.

[10] A. Mayo, *The fast solution of Poisson's and the biharmonic equations on Irregular Regions*, SIAM J. Numer. Anal., 21(2) (1984), 285-297.

[11] A. Mayo and A. Greenbaum, *Fast parallel solution of Poisson's and the biharmonic equations on irregular regions*, SIAM J. on Sci. and Stat. Comput., 13(1), (1992), 1-26.

[12] A. McKenney, L. Greengard and A. Mayo, *A fast Poisson solver for complex geometries*, J. Comput. Phys, 118(2), (1995), 348-371.

[13] V. Rokhlin, *Rapid solution of integral equations of classical potential theory*, J. Comput. Phys., 60(2), 1985, 187-207.

Chapter 16

Design of flexible composites for high-strain applications

Oleksandr Menshykov, Maryna Menshykova, Igor A. Guz and Snizhana Ross

School of Engineering,
University of Aberdeen
Aberdeen AB24 3UE
UK

Abstract. *The study is focused on stress and strain analysis of multilayered thick-walled fibre reinforced composite pipes subjected to bending loading and pressure. The problem is considered for perfectly bonded layers and stress and displacement continuity conditions imposed on interfaces. The system of integral equations obtained from the moment equilibrium relation is solved. The research provides numerical solution and study of stresses and strains distribution in the pipes with different lay-ups and reinforcement orientations.*

16.1 Introduction

Having advantages over conventional materials in weight, strength, stiffness, corrosion resistance etc. composite materials are becoming more and more attractive for structural and non-structural applications in the modern industry. However, in spite of their undoubted advantages, the main of which may be the ability to be tailored for specific purpose, their introduction in the industry is a very slow process. Lack of appropriate performance information, regulatory requirements, efficient design procedures and reparability issues are the main obstacles. High specific strength as well as overall weight-saving and resistance to a wide range of fluids (including seawater, aerated water, and hydrocarbons) makes the composite materials attractive for use offshore and onshore. One of the most successful application areas for composites is in pipework where they are used for both low- and high-pressure applications with a wide variety of fluids, including hydrocarbons.

In the current paper we investigate composite tubes under bending loading. The composite pipes subjected to pure bending were considered by a number of researchers. The formulation of the problem of anisotropic single-layer pipe subjected to bending load was given by [4]. Bending behaviour of thick-walled filament-wound sandwich pipes made of a non-reinforced core layer and alternate-ply skin layers was studied by [8]. Laminated plate theory and Lekhnitskii stress function approach was used for obtaining the analytical solution for multi-layered filament-wound composite pipes under bending loading. The analytical solution for the design of spoolable composite tubes was presented by [7]. The prediction of bending strength and failure mode for

filament-wound composite pipes was given by [6]. The multi-parametric investigation of stress distribution as a function of the inner layer material properties, its thickness, the number of layers, lay-up and the magnitude of bending load was carried out by [2], [5].

The study is focused on stress analysis of multi-layered thick-walled fibre reinforced composite pipes subjected to bending loading. The research focuses on the pipes with multi layered outer part and thin homogeneous inner layer. It provides analytical solution (within the framework developed [6]) and comparative study of stresses distribution in the pipes with inner homogeneous layer and inner composite layer of 0^0 fibre orientation. The investigation of stress distribution as a function of the inner layer material properties was carried out.

16.2 Stress analysis

Consider a multi-layered fibre reinforced filament-wound composite pipe with r_0 inner radius and r_a outer radius subjected to bending load. Each layer of the pipe consists of two laminae with principal material directions symmetrical to the axial direction. Consequently, each layer (two adjacent lay-ups) is assumed to behave as an orthotropic unit. For each orthotropic layer we have the constitutive equation for strains in terms of stresses [6]:

$$\begin{bmatrix} \varepsilon_r \\ \varepsilon_\theta \\ \varepsilon_z \\ \gamma_{r\theta} \end{bmatrix} = \begin{bmatrix} S_{11} & S_{12} & S_{13} & 0 \\ S_{12} & S_{22} & S_{23} & 0 \\ S_{13} & S_{23} & S_{33} & 0 \\ 0 & 0 & 0 & S_{44} \end{bmatrix} \begin{bmatrix} \sigma_r \\ \sigma_\theta \\ \sigma_z \\ \tau_{r\theta} \end{bmatrix} \tag{16.1}$$

where S_{ij} are compliance constants and r, θ and z denoted as radial, hoop and axial coordinates. The compliance constants can be obtained from:

$$(S_{ij}) = \left(Q_{ij}\right)^{-1} (a_{ij}) \, (P_{ij}) \, , \tag{16.2}$$

where matrix (a_{ij}) can be obtained from engineering constants; matrices (P_{ij}) and $\left(Q_{ij}\right)$ are the coordinate transformation matrices between the on-axis and the cylindrical axis.

The components of the stress field [6] could be presented in the form:

$$\sigma_r = (Br^{-1+\beta} - Cr^{-1-\beta} + A\eta r)\sin\theta, \quad \sigma_\theta = [B(1+\beta)r^{-1+\beta} - C(1-\beta)r^{-1-\beta} + 3A\eta r]\sin\theta, \tag{16.3}$$

$$\tau_{r\theta} = -(Br^{-1+\beta} - Cr^{-1-\beta} + A\eta r)\cos\theta, \quad \sigma_z = (s_1 Br^{-1+\beta} + s_2 Cr^{-1-\beta} + s_3 Ar]\sin\theta, \tag{16.4}$$

where A, B, C are unknown constants and

$$s_{1,2} = \mp\frac{S_{13} + S_{23}(1 \pm \beta)}{S_{33}}, \quad s_3 = 1 - \frac{(S_{13} + S_{23})\eta}{S_{33}},$$

$$\beta = \sqrt{1 + \frac{R_{11} + 2R_{12} + R_{44}}{R_{22}}}, \quad \eta = \frac{S_{23} - S_{13}}{R_{11} + 2R_{12} + R_{44} - 3R_{22}}, \quad R_{ij} = S_{ij} - \frac{S_{i3}S_{j3}}{S_{33}} \quad (i, j = 1, 2, 4)$$

Radial and hoop displacement have the following form:

$$u_r = (p_1 Br^{\beta} + p_2 Cr^{-\beta} + p_3 Ar^2)\sin\theta, \quad u_\theta = (q_1 Br^{\beta} + q_2 Cr^{-\beta} + q_3 Ar^2)\cos\theta, \tag{16.5}$$

and

$$p_{1,2} = \frac{R_{13} + R_{12}(1 \pm \beta)}{\beta}, \qquad p_3 = \frac{(R_{11} + 3R_{12})\eta + S_{13}}{2},$$

$$q_{1,2} = \frac{R_{11} + R_{12} \mp R_{22}\beta(1 \pm \beta)}{\beta}, \quad q_3 = \frac{(R_{11} + R_{12} - 6R_{22})\eta + S_{13} - 2S_{23}}{2},$$

Material properties in laminated multi-layered tube vary from layer to layer, however it is required that the stress and displacement continuity conditions be satisfied at the layer interfaces [3]. As the tube is subjected to no inner or outer pressure the boundary conditions have the following form:

$$\sigma_r^{(1)}(r_0) = 0, \qquad \sigma_r^{(N)}(r_a) = 0. \tag{16.6}$$

For perfectly bonded layers all displacements must be continuous from layer to layer. For the displacements and stresses on the layer interfaces the continuity conditions are [8]:

$$u_r^{(k)}(r_k) = u_r^{(k+1)}(r_k), \quad u_\theta^{(k)}(r_k) = u_\theta^{(k+1)}(r_k), \quad \sigma_r^{(k)}(r_k) = \sigma_r^{(k+1)}(r_k) \quad k = \overline{1, N-1} \tag{16.7}$$

Substituting layer stresses 16.3, 16.4 into boundary conditions 16.6 and displacements 16.5 and layer stresses 16.3, 16.4 into continuity conditions 16.7 we obtain:

$$(B^{(1)} r_0^{-1+\beta} - C^{(1)} r_0^{-1-\beta} + A^{(1)} \eta^{(1)} r_0) \sin\theta = 0$$

$$(p_1^{(k)} B^{(k)} r_k^{\beta} + p_2^{(k)} C^{(k)} r_k^{-\beta} + p_3^{(k)} A^{(k)} r_k^2) \sin\theta = (p_1^{(k+1)} B^{(k+1)} r_k^{\beta} + p_2^{(k+1)} C^{(k+1)} r_k^{-\beta} + p_3^{(k+1)} A^{(k+1)} r_k^2) \sin\theta$$

$$(q_1^{(k)} B^{(k)} r_k^{\beta} + q_2^{(k)} C^{(k)} r_k^{-\beta} + q_3^{(k)} A^{(k)} r_k^2) \cos\theta = (q_1^{(k+1)} B^{(k+1)} r_k^{\beta} + q_2^{(k+1)} C^{(k+1)} r_k^{-\beta} + q_3^{(k+1)} A^{(k+1)} r_k^2) \cos\theta$$

$$(B^{(k)} r_k^{-1+\beta} - C^{(k)} r_k^{-1-\beta} + A^{(k)} \eta^{(k)} r_k) \sin\theta = (B^{(k+1)} r_k^{-1+\beta} - C^{(k+1)} r_k^{-1-\beta} + A^{(k+1)} \eta^{(k+1)} r_k^2) \sin\theta$$

for $k = \overline{1, N-1}$

$$\left(B^{(N)} r_a^{-1+\beta} - C^{(N)} r_a^{-1-\beta} + A^{(N)} \eta^{(N)} r_a\right) \sin\theta = 0 \tag{16.8}$$

The following relation must be satisfied for equilibrium for bending moment [8]:

$$\int_\theta \int_r \sigma_z r^2 \sin\theta dr d\theta = M \qquad r \in [r_0, r_a] \qquad \theta \in [0, 2\pi]. \tag{16.9}$$

Substituting axial layer stress 16.4 into the relation above we obtain:

$$\int_\theta \int_r \left(s_1 B r^{-1+\beta} + s_2 C r^{-1-\beta} + s_3 A r\right) \sin^2\theta dr d\theta = M. \tag{16.10}$$

Consequently, for a filament-wound tube with N layers the equilibrium for bending moment relation has the following form [2], [5]:

$$\sum_{m=1}^{N} s_1^{(1)} B^{(1)} \int_\theta \int_{r_0}^{r_1} r^{1+\beta} \sin^2\theta dr d\theta + s_1^{(m)} B^{(m)} \int_\theta \int_{r_{m-1}}^{r_m} r^{1+\beta} \sin^2\theta dr d\theta + s_1^{(N)} B^{(N)} \int_\theta \int_{r_{N-1}}^{r_a} r^{1+\beta} \sin^2\theta dr d\theta +$$

$$s_2^{(1)} C^{(1)} \int_\theta \int_{r_0}^{r_1} r^{1-\beta} \sin^2\theta dr d\theta + s_2^{(m)} C^{(m)} \int_\theta \int_{r_{m-1}}^{r_m} r^{1-\beta} \sin^2\theta dr d\theta + s_2^{(N)} C^{(N)} \int_\theta \int_{r_{N-1}}^{r_a} r^{1-\beta} \sin^2\theta dr d\theta + \tag{16.11}$$

$$s_3^{(1)} A^{(1)} \int_\theta \int_{r_0}^{r_1} r^3 \sin^2\theta dr d\theta + s_3^{(m)} A^{(m)} \int_\theta \int_{r_{m-1}}^{r_m} r^3 \sin^2\theta dr d\theta + s_3^{(N)} A^{(N)} \int_\theta \int_{r_{N-1}}^{r_a} r^3 \sin^2\theta dr d\theta = M$$

where

$$\int_0^{2\pi} \int_{r_0}^{r_1} r^{1+\beta} \sin^2\theta dr d\theta = \pi \frac{r_1^{2+\beta} - r_0^{2+\beta}}{2+\beta} \qquad \int_0^{2\pi} \int_{r_0}^{r_1} r^{1+\beta} \sin^2\theta dr d\theta = \pi \frac{r_1^{2+\beta} - r_0^{2+\beta}}{2+\beta} \tag{16.12}$$

$$\int_0^{2\pi} \int_{r_0}^{r_1} r^{1-\beta} \sin^2\theta dr d\theta = \pi \frac{r_1^{2-\beta} - r_0^{2-\beta}}{2-\beta} \qquad \int_0^{2\pi} \int_{r_0}^{r_1} r^3 \sin^2\theta dr d\theta = \pi \frac{r_1^4 - r_0^4}{4}$$

Substituting the integrals 16.12 into 16.10 we obtain the expression for bending moment equilibrium for filament-wound multi-layered tube:

$$s_1^{(1)}B^{(1)}\pi\frac{r_1^{2+\beta}-r_0^{2+\beta}}{2+\beta}+s_1^{(m)}B^{(m)}\pi\frac{r_m^{2+\beta}-r_{m-1}^{2+\beta}}{2+\beta}+s_1^{(N)}B^{(N)}\pi\frac{r_a^{2+\beta}-r_{N-1}^{2+\beta}}{2+\beta}+$$

$$s_2^{(1)}C^{(1)}\pi\frac{r_1^{2-\beta}-r_0^{2-\beta}}{2-\beta}+s_2^{(m)}C^{(m)}\pi\frac{r_m^{2-\beta}-r_{m-1}^{2-\beta}}{2-\beta}+s_2^{(N)}C^{(N)}\pi\frac{r_a^{2-\beta}-r_{N-1}^{2-\beta}}{2+\beta}+\qquad m=\overline{2,N-1} \tag{16.13}$$

$$s_3^{(1)}A^{(1)}\pi\frac{r_1^4-r_0^4}{4}+s_3^{(m)}A^{(m)}\pi\frac{r_m^4-r_{m-1}^4}{4}+s_3^{(N)}A^{(N)}\pi\frac{r_a^4-r_{N-1}^4}{4}=M$$

For the pipe of isotropic material $\eta=0$ and $\beta=2$. Consequently, the equilibrium for bending moment equation for the pipe with inner layer of homogeneous material is [2], [5]:

$$\sum_{m=1}^{N}s_1^{(1)}B^{(1)}\int_\theta\int_{r_0}^{r_1}r^3\sin^2\theta drd\theta+s_1^{(m)}B^{(m)}\int_\theta\int_{r_{m-1}}^{r_m}r^{1+\beta}\sin^2\theta drd\theta+s_1^{(N)}B^{(N)}\int_\theta\int_{r_{N-1}}^{r_a}r^{1+\beta}\sin^2\theta drd\theta+$$

$$s_2^{(1)}C^{(1)}\int_\theta\int_{r_0}^{\eta}r^{-1}\sin^2\theta drd\theta+s_2^{(m)}C^{(m)}\int_\theta\int_{r_{m-1}}^{r_m}r^{1-\beta}\sin^2\theta drd\theta+s_2^{(N)}C^{(N)}\int_\theta\int_{r_{N-1}}^{r_a}r^{1-\beta}\sin^2\theta drd\theta+ \tag{16.14}$$

$$s_3^{(1)}A^{(1)}\int_\theta\int_{r_0}^{r_1}r^3\sin^2\theta drd\theta+s_3^{(m)}A^{(m)}\int_\theta\int_{r_{m-1}}^{r_m}r^3\sin^2\theta drd\theta+s_3^{(N)}A^{(N)}\int_\theta\int_{r_{N-1}}^{r_a}r^3\sin^2\theta drd\theta=M$$

where

$$s_3^{(1)}A^{(1)}\int_0^{2\pi}\int_{r_0}^{r_1}r^3\sin^2\theta drd\theta=s_3^{(1)}A^{(1)}\pi\frac{r_1^4-r_0^4}{4}\qquad s_1^{(1)}B^{(1)}\int_0^{2\pi}\int_{r_0}^{r_1}r^3\sin^2\theta drd\theta=s_1^{(1)}B^{(1)}\pi\frac{r_1^4-r_0^4}{4} \tag{16.15}$$

$$s_2^{(1)}C^{(1)}\int_0^{2\pi}\int_{r_0}^{r_1}r^{-1}\sin^2\theta drd\theta=s_2^{(1)}C^{(1)}\pi\left(\ln(r_1)-\ln(r_0)\right).$$

Substituting the integrals 16.15 into 16.14 we obtain the expression for bending moment equilibrium for filament-wound multi-layered tube with homogeneous inner layer:

$$s_1^{(1)}B^{(1)}\pi\frac{r_1^4-r_0^4}{4}+s_1^{(m)}B^{(m)}\pi\frac{r_m^{2+\beta}-r_{m-1}^{2+\beta}}{2+\beta}+s_1^{(N)}B^{(N)}\pi\frac{r_a^{2+\beta}-r_{N-1}^{2+\beta}}{2+\beta}+$$

$$s_2^{(1)}C^{(1)}\pi\left(\ln(r_1)-\ln(r_0)\right)+s_2^{(m)}C^{(m)}\pi\frac{r_m^{2-\beta}-r_{m-1}^{2-\beta}}{2-\beta}+s_2^{(N)}C^{(N)}\pi\frac{r_a^{2-\beta}-r_{N-1}^{2-\beta}}{2-\beta}+$$

$$s_3^{(1)}A^{(1)}\pi\frac{r_1^4-r_0^4}{4}+s_3^{(m)}A^{(m)}\pi\frac{r_m^4-r_{m-1}^4}{4}+s_3^{(N)}A^{(N)}\pi\frac{r_a^4-r_{N-1}^4}{4}=M$$

As a result we derive the following system of equations solving which the stress in the tube can be obtained:

$$\left.\begin{array}{c}\text{Boundary condition}\\ \text{Continuity condition}\\ \text{Equilibrium for bending moment}\end{array}\right\}$$

16.3 Numerical results and discussion

To get the numerical results the software for bending stiffness and bending stress calculation was developed. As a numerical example we will consider the filament wound pipes of different designs made of carbon/epoxy composite (T300/LY5052) under bending load. The inner diameter of the pipes is 2cm and the outer diameter is 6cm. The bi-material pipe consists of inner steel and outer fibre composite layers. The comparative study of the stress distribution in the bi-material pipes with inner layer of homogeneous material (steel) and unidirectional inner layer of 0^0 fibre orientation was carried out. The properties of steel and composite are given in Table 16.1.

	Carbon/Epoxy unidirectional fibre composite (T300/LY5052) [1]	Steel
E_1(GPa)	135	205
E_2(GPa)	8	205
G_{12}(GPa)	3.8	77
ν_{12}	0.27	0.33
ν_{23}	0.49	0.33

Table 16.1: Properties of materials.

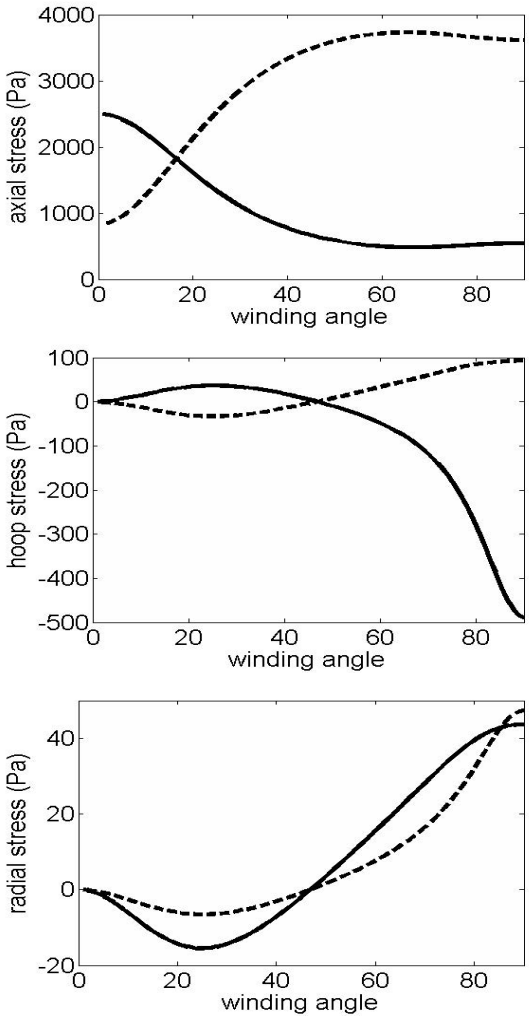

Figure 16.1: *Effect of the winding angle on the axial, hoop and radial stresses for the pipe with* $[0, a, -a]$ *lay-up (solid line - inner radius; dotted line - outer radius)*

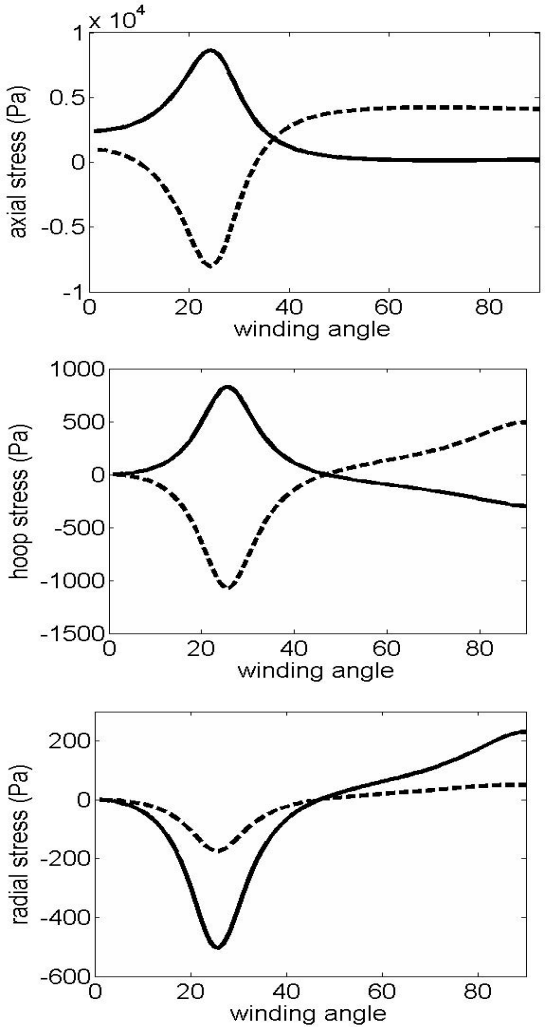

Figure 16.2: *Effect of the winding angle on the axial, hoop and radial stresses for the pipe with* $[steel, a, -a]$ *lay-up (solid line - inner radius; dotted line - outer radius)*

The effect of winding angle on axial and hoop stresses on inner and outer pipe surfaces is presented in Figures 16.1, 16.2. Axial stresses on inner surface are lower than on outer for pipes with inner steel and inner 0^0 fibre layer. The hoop stress in pipe with inner steel layer is higher on inner surface than on outer for winding angles from 40^0 till 90^0 and lower on inner surface than on outer for winding angles from 0^0 till 40^0. But for the pipe with inner 0^0 fibre layer the situation is vice versa. The hoop stress in pipe with inner 0^0 fibre layer is lower on inner surface than on outer for winding angles from 40^0 till 90^0 and higher on inner surface than on outer for winding angles from 0^0 till 40^0. Figures 16.3 - 16.4 give detailed trough the thickness distribution of axial and hoop stresses for a range or winding angles for the pipes with inner steel and 0^0 fibre layers.

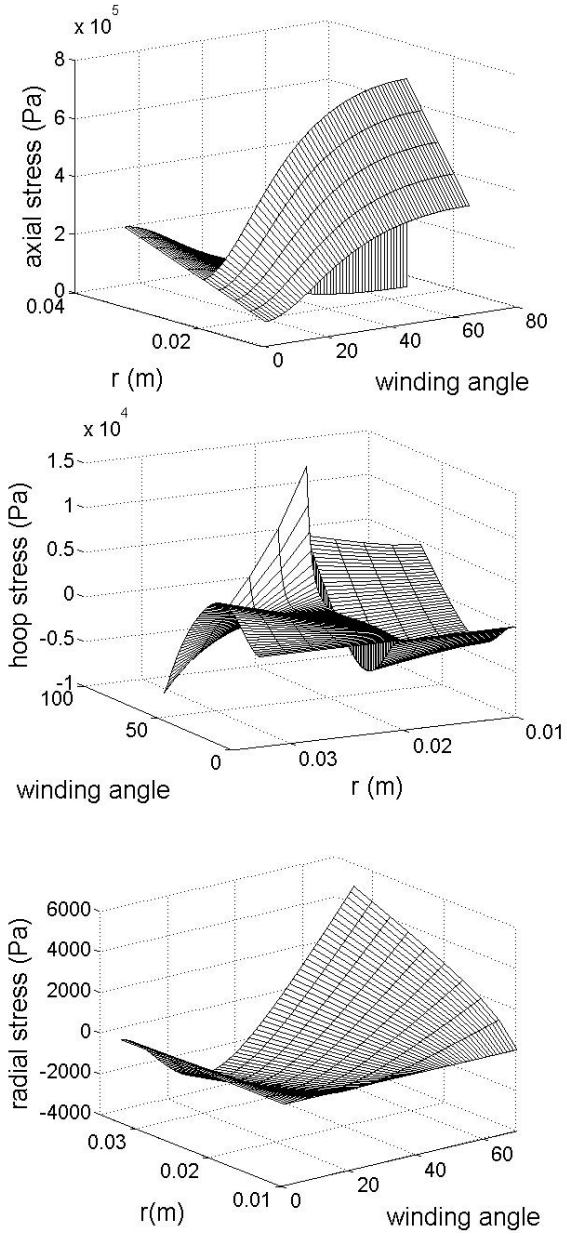

Figure 16.3: *Effect of the winding angle on the axial, hoop and radial stresses distribution through the wall thickness for the pipe with* $[0, a, -a]$ *lay-up*

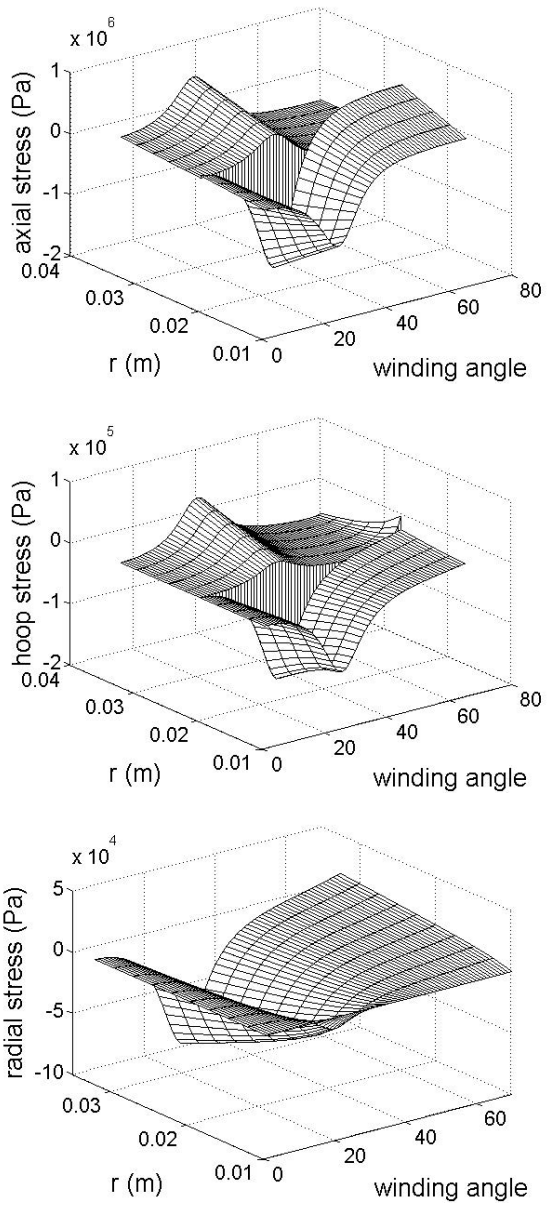

Figure 16.4: *Effect of the winding angle on the axial, hoop and radial stresses distribution through the wall thickness for the pipe with* $[steel, a, -a]$ *lay-up*

16.4 Conclusion

Due to the advantages over conventional materials in strength, stiffness, corrosion resistance and the ability to be tailored for the purpose the composite coiled tubing has a potential to replace the conventional, steel, coiled tubing. Coiled tube is thick walled tube which must withstand various loading conditions one of which is obviously bending loading. We consider fibre reinforced coiled tube as thick-walled multi-layered filament wound tube. Due to the manufacturing issues the inner pipe is used for multi-layered pull winding fibre reinforced tube production. In the paper the comparative study of stresses distribution in multi-layered fibre reinforced pipes with inner steel layer and inner 0^0 fibre layer is presented. The analysis show how the stresses depend on the material of inner layer

Acknowledgement

The financial support of Regionale Forskningsfond (Norway) via Prototech AS (Bergen) is gratefully acknowledged.

References

[1] H. Bakaiyan, H. Hosseini and E. Ameri, *Analysis of multi-layered filament-wound composite pipes under combined internal pressure and thermomechanical loading with thermal variations*, Composite Structures, 88 (2009), 532–541.

[2] I. A. Guz, M. V. Menshykova and J. K. Paik, *Thick-walled composite tubes for offshore applications:an example of stress and failure analysis for filament-wound multi-layered pipes*, Ships and Offshore Structures, 12, 3, (2015),304-322.

[3] C. Herakovich, *Mechanics of fibrous composites*,John Wiley and Sons, Inc, 1998.

[4] S. G. Lekhnitskii, *Theory of elasticity of an anisotropic body*, MIR Publishers 1981, Moskow,1998.

[5] M. V. Menshykova and I. A. Guz , *Stress analysis of layered thick walled composite pipes subjected to bending loading*, International Journal of Mechanical Sciences, 88 (2014), 289–299.

[6] T. Natsuki, H. Takayanagi and H. Tsuda, *Prediction of bending strength for filament-wound composite pipes*, Journal of Reinforced Plastics and Composites, 22, 8, (2003), 695–710.

[7] J. M. Starbuck and C. Eberle, Analytical solution for the design of spoolable composite tubing. In *Proceedings of the Third International Conference on Composite Materials for Offshore Operations*, Houston, TX, October 31 November 2, 2000.

[8] M. Xia, H. Takayanagi and K. Kemmochi, *Bending behaviour of filament-wound fiber-reinforced sandwich pipes*, Composite Structures, 56,(2002), 201–210.

Chapter 17

BDIES for the compressible Stokes system with variable viscosity mixed BVP in bounded domains

Sergey E. Mikhailov[1], **Carlos F. Portillo**[2]

[1] Department of Mathematics
Brunel University London
Kingston Lane
UB8 3PH, Uxbridge, Middlesex, UK.

[2] Department of Mathematical Sciences
Oxford Brookes University
Wheatley Campus
OX33 1HX, Wheatley, Oxfordshire, UK.

Abstract. *The mixed compressible Stokes system with variable coefficient models the motion of a laminar compressible viscous fluid in a bounded domain. The mixed boundary value problem related to the Stokes system is reduced to two different BDIES which are equivalent to the original boundary value problem, see [2, 10, 11]. These Boundary Integral Equation Systems can be expressed in terms of surface and volume parametrix-based potential type operators whose properties are also analysed in appropriate Sobolev spaces. The invertibility and Fredholm properties related to the matrix operator that defines the BDIES are also presented.*

17.1 Introduction

Boundary integral equations and the hydrodynamic potential theory for the Stokes system with constant viscosity have been extensively studied by numerous authors, e.g., [6, 7, 4, 14, 15, 5, 16].

Although the compressible Stokes System with variable viscosity has been extensively studied, it has not yet been reduced to BDIES following a similar approach as in [2]. In contrast to [2], the BVP approached in this chapter consists of a system of four equations with four unknowns: the three component velocity field and the scalar pressure field.

In the case of constant viscosity, fundamental solutions for both, velocity and pressure, are available. Notwithstanding, these fundamental solutions are not available in the variable coefficient case for which a *parametrix* (Levi function), (see e.g., [2, 10, 11, 12]) is needed in order to derive the (BDIES).

However, a parametrix for a certain PDE is not unique and neither is it in the case of a PDE system. Therefore, the choice of an appropriate parametrix is not a trivial decision at all. In

[11], we develop BDIES for the mixed imcompressible Stokes problem defined over a bounded domain. Equivalence between the BVP-BDIES is shown, however, invertibility results are not proved.

In this chapter, we derive two BDIES equivalent to the original mixed compressible Stokes system defined on a bounded domain. Furthermore, mapping properties of the hydrodynamic surface and volume potentials are shown. The main results are the equivalence theorems and the invertibility theorems of the operators defined by the BDIES.

17.2 Preliminaries

Let $\Omega = \Omega^+$ be a *bounded* and simply connected domain and let $\Omega^- := \mathbb{R}^3 \setminus \overline{\Omega}^+$. We will assume that the boundary $S := \partial\Omega$ is simply connected, closed and infinitely differentiable, $S \in \mathcal{C}^\infty$. Furthermore, $S := \overline{S}_N \cup \overline{S}_D$ where both S_N and S_D are non-empty, connected disjoint manifolds of S. The border of these two submanifolds is also infinitely differentiable, $\partial S_N = \partial S_D \in \mathcal{C}^\infty$.

Let $\boldsymbol{v}$ be the velocity vector field; p the pressure scalar field and $\mu \in \mathcal{C}^\infty(\Omega)$ be the variable kinematic viscosity of the fluid such that $\mu(\boldsymbol{x}) > c > 0$.

The Stokes operator is defined as

$$\begin{aligned}\mathcal{A}_j(p,\boldsymbol{v})(\boldsymbol{x}) :&= \frac{\partial}{\partial x_i}\sigma_{ji}(p,\boldsymbol{v})(\boldsymbol{x}) \\ &= \frac{\partial}{\partial x_i}\left(\mu(\boldsymbol{x})\left(\frac{\partial v_j}{\partial x_i} + \frac{\partial v_i}{\partial x_j} - \frac{2}{3}\delta_i^j \mathrm{div}\boldsymbol{v}\right)\right) - \frac{\partial p}{\partial x_j},\ j,i \in \{1,2,3\},\end{aligned} \tag{17.1}$$

where δ_i^j is Kronecker symbol. Here and henceforth we assume the Einstein summation in repeated indices from 1 to 3. We also denote the Stokes operator as $\boldsymbol{\mathcal{A}} = \{\mathcal{A}_j\}_{j=1}^3$. Ocassionally, we may use the following notation for derivative operators: $\partial_j = \partial_{x_j} := \dfrac{\partial}{\partial x_j}$ with $j = 1,2,3$; $\nabla := (\partial_1, \partial_2, \partial_3)$.

For a compressible fluid $\mathrm{div}\boldsymbol{v} = g$, which gives the following stress tensor operator and the Stokes operator, respectively, to

$$\begin{aligned}\sigma_{ji}(p,\boldsymbol{v})(\boldsymbol{x}) &= -\delta_i^j p(\boldsymbol{x}) + \mu(\boldsymbol{x})\left(\frac{\partial v_i(\boldsymbol{x})}{\partial x_j} + \frac{\partial v_j(\boldsymbol{x})}{\partial x_i} - \frac{2}{3}\delta_i^j g\right), \\ \mathcal{A}_j(p,\boldsymbol{v})(\boldsymbol{x}) &= \frac{\partial}{\partial x_i}\left(\mu(\boldsymbol{x})\left(\frac{\partial v_j}{\partial x_i} + \frac{\partial v_i}{\partial x_j} - \frac{2}{3}\delta_i^j g\right)\right) - \frac{\partial p}{\partial x_j},\ j,i \in \{1,2,3\}.\end{aligned}$$

In what follows $H^s(\Omega)$, $H^s(S)$ are the Bessel potential spaces, where $s \in \mathbb{R}$ is an arbitrary real number (see, e.g., [7, 8]). We recall that H^s coincide with the Sobolev–Slobodetski spaces W_2^s for any non-negative s. Let $H_K^s := \{g \in H^1(\mathbb{R}^3) : \mathrm{supp}(g) \subseteq K\}$ where K is a compact subset of $\mathbb{R}^3$. In what follows we use the bold notation: $\boldsymbol{H}^s(\Omega) = [H^s(\Omega)]^3$ for 3-dimensional vector spaces. We denote by $\widetilde{\boldsymbol{H}}^s(\Omega)$ the subspace of $\boldsymbol{H}^s(\mathbb{R}^3)$, $\widetilde{\boldsymbol{H}}^s(\Omega) := \{\boldsymbol{g} :\ \boldsymbol{g} \in \boldsymbol{H}^s(\mathbb{R}^3),\ \mathrm{supp}\,\boldsymbol{g} \subset \overline{\Omega}\}$; similarly, $\widetilde{\boldsymbol{H}}^s(S_1) = \{\boldsymbol{g} \in \boldsymbol{H}^s(S),\ \mathrm{supp}\,\boldsymbol{g} \subset \overline{S}_1\}$ is the Sobolev space of functions having support in $S_1 \subset S$.

We will also make use of the following space, (cf. e.g. [3, 2])

$$\boldsymbol{H}^{1,0}(\Omega;\boldsymbol{\mathcal{A}}) := \{(p,\boldsymbol{v}) \in L_2(\Omega) \times \boldsymbol{H}^1(\Omega) : \boldsymbol{\mathcal{A}}(p,\boldsymbol{v}) \in \boldsymbol{L}_2(\Omega)\},$$

endowed with the norm

$$\| (p,\boldsymbol{v}) \|_{\boldsymbol{H}^{1,0}(\Omega;L)} := \left(\| p \|^2_{L_2(\Omega)} + \| \boldsymbol{v} \|^2_{\boldsymbol{H}^1(\Omega)} + \| \boldsymbol{\mathcal{A}}(p,\boldsymbol{v}) \|^2_{\boldsymbol{L}_2(\Omega)}\right)^{1/2}.$$

The operator $\boldsymbol{\mathcal{A}}$ acting on $(p,\boldsymbol{v})$ is well defined in the weak sense provided $\mu(\boldsymbol{x})\in L^\infty(\Omega)$ as

$$\langle\boldsymbol{\mathcal{A}}(p,\boldsymbol{v}),\boldsymbol{u}\rangle_\Omega := -\mathcal{E}((p,\boldsymbol{v}),\boldsymbol{u}),\qquad \forall\boldsymbol{u}\in\widetilde{\boldsymbol{H}}^1(\Omega),$$

where the form $\mathcal{E}:\left[L^2(\Omega)\times\boldsymbol{H}^1(\Omega)\right]\times\widetilde{\boldsymbol{H}}^1(\Omega)\longrightarrow\mathbb{R}$ is defined as

$$\mathcal{E}\left((p,\boldsymbol{v}),\boldsymbol{u}\right) := \int_\Omega E\left((p,\boldsymbol{v}),\boldsymbol{u}\right)(\boldsymbol{x})\,dx, \tag{17.2}$$

and the function $E\left((p,\boldsymbol{v}),\boldsymbol{u}\right)$ is defined as

$$\begin{aligned} E\left((p,\boldsymbol{v}),\boldsymbol{u}\right)(\boldsymbol{x}) :=\ & \frac{1}{2}\mu(\boldsymbol{x})\left(\frac{\partial u_i(\boldsymbol{x})}{\partial x_j}+\frac{\partial u_j(\boldsymbol{x})}{\partial x_i}\right)\left(\frac{\partial v_i(\boldsymbol{x})}{\partial x_j}+\frac{\partial v_j(\boldsymbol{x})}{\partial x_i}\right)\\ & -\frac{2}{3}\mu(\boldsymbol{x})\mathrm{div}\boldsymbol{v}(\boldsymbol{x})\,\mathrm{div}\boldsymbol{u}(\boldsymbol{x})-p(\boldsymbol{x})\mathrm{div}\boldsymbol{u}(\boldsymbol{x}). \end{aligned}\tag{17.3}$$

For sufficiently smooth functions $(p,\boldsymbol{v})\in\boldsymbol{H}^{s-1}(\Omega^\pm)\times H^s(\Omega^\pm)$ with $s>3/2$, we can define the classical traction operators on the boundary S as

$$T_i^\pm(p,\boldsymbol{v})(\boldsymbol{x}) := \gamma^\pm\sigma_{ij}(p,\boldsymbol{v})(\boldsymbol{x})\,n_j(\boldsymbol{x}), \tag{17.4}$$

where $n_j(\boldsymbol{x})$ denote components of the unit outward normal vector $\boldsymbol{n}(\boldsymbol{x})$ to the boundary S of the domain Ω and $\gamma^\pm(\,\cdot\,)$ denote the trace operators from inside and outside Ω.

Traction operators (17.4) can be continuously extended to the *canonical* traction operators $\boldsymbol{T}^\pm:\boldsymbol{H}^{1,0}(\Omega^\pm,\boldsymbol{\mathcal{A}})\to\boldsymbol{H}^{-1/2}(S)$ defined in the weak form similar to [3, 9, 2] as

$$\begin{aligned}\langle\boldsymbol{T}^\pm(p,\boldsymbol{v}),\boldsymbol{w}\rangle_S := \pm\int_{\Omega^\pm}\left[\boldsymbol{\mathcal{A}}(p,\boldsymbol{v})\boldsymbol{\gamma}^{-1}\boldsymbol{w}+E\left((p,\boldsymbol{v}),\boldsymbol{\gamma}^{-1}\boldsymbol{w}\right)\right]\,dx,\\ \forall\,(p,\boldsymbol{v})\in\boldsymbol{H}^{1,0}(\Omega^\pm,\boldsymbol{\mathcal{A}}),\ \forall\,\boldsymbol{w}\in\boldsymbol{H}^{1/2}(S).\end{aligned}$$

Here the operator $\boldsymbol{\gamma}^{-1}:\boldsymbol{H}^{1/2}(S)\to\boldsymbol{H}^1(\mathbb{R}^3)$ denotes a continuous right inverse of the trace operator $\boldsymbol{\gamma}:\boldsymbol{H}^1(\mathbb{R}^3)\to\boldsymbol{H}^{1/2}(S)$.

Furthermore, if $(p,\boldsymbol{v})\in\boldsymbol{H}^{1,0}(\Omega,\boldsymbol{\mathcal{A}})$ and $\boldsymbol{u}\in\boldsymbol{H}^1(\Omega)$, the following first Green identity holds, cf. [3, 9, 2, 11],

$$\langle\boldsymbol{T}^+(p,\boldsymbol{v}),\boldsymbol{\gamma}^+\boldsymbol{u}\rangle_S = \int_\Omega[\boldsymbol{\mathcal{A}}(p,\boldsymbol{v})\boldsymbol{u}+E\left((p,\boldsymbol{v}),\boldsymbol{u}\right)(\boldsymbol{x})]dx. \tag{17.5}$$

Applying the identity (17.5) to the pairs $(p,\boldsymbol{v}),(q,\boldsymbol{u})\in\boldsymbol{H}^{1,0}(\Omega,\boldsymbol{\mathcal{A}})$ with exchanged roles and subtracting the one from the other, we arrive at the second Green identity, cf. [8, 9],

$$\begin{aligned}&\int_\Omega\left[\mathcal{A}_j(p,\boldsymbol{v})u_j-\mathcal{A}_j(q,\boldsymbol{u})v_j+q\,\mathrm{div}\,\boldsymbol{v}-p\,\mathrm{div}\,\boldsymbol{u}\right]\,dx=\\ &\langle\boldsymbol{T}^+(p,\boldsymbol{v}),\boldsymbol{\gamma}^+\boldsymbol{u}\rangle_S-\langle\boldsymbol{T}^+(q,\boldsymbol{u}),\boldsymbol{\gamma}^+\boldsymbol{v}\rangle_S.\end{aligned}\tag{17.6}$$

Now we are ready to define the mixed BVP for which we aim to derive equivalent BDIES and investigate the existence and uniqueness of their solutions.

For $\boldsymbol{f}\in\boldsymbol{L}_2(\Omega)$, $g\in L^2(\Omega)$, $\boldsymbol{\varphi}_0\in\boldsymbol{H}^{1/2}(S_D)$ and $\boldsymbol{\psi}_0\in\boldsymbol{H}^{-1/2}(S_N)$, find $(p,\boldsymbol{v})\in\boldsymbol{H}^{1,0}(\Omega,\boldsymbol{\mathcal{A}})$ such that:

$$\boldsymbol{\mathcal{A}}(p,\boldsymbol{v})(\boldsymbol{x}) = \boldsymbol{f}(\boldsymbol{x}),\ \ \boldsymbol{x}\in\Omega, \tag{17.7a}$$

$$\mathrm{div}(\boldsymbol{v})(\boldsymbol{x}) = g(\boldsymbol{x}),\ \ \boldsymbol{x}\in\Omega, \tag{17.7b}$$

$$r_{S_D}\boldsymbol{\gamma}^+\boldsymbol{v}(\boldsymbol{x}) = \boldsymbol{\varphi}_0(\boldsymbol{x}),\ \boldsymbol{x}\in S_D, \tag{17.7c}$$

$$r_{S_N}\boldsymbol{T}^+(p,\boldsymbol{v})(\boldsymbol{x}) = \boldsymbol{\psi}_0(\boldsymbol{x}),\ \boldsymbol{x}\in S_N. \tag{17.7d}$$

Such problems arise when modeling the behaviour of a compressible (or incompressible when $g = 0$) fluid flowing in a rigid open container (such is the case with the water flowing in a river when S_D is the surface of the river bed and S_N is the free surface of the water, [1]. Applying the first Green identity it is easy to prove the following uniqueness result.

Theorem 3. *Mixed BVP* (17.7) *has at most one solution in the space* $\boldsymbol{H}^{1,0}(\Omega, \boldsymbol{\mathcal{A}})$.

17.3 Parametrix and Remainder

When $\mu(\boldsymbol{x}) = 1$, the operator $\boldsymbol{\mathcal{A}}$ becomes the constant-coefficient Stokes operator $\mathring{\boldsymbol{\mathcal{A}}}$, for which we know an explicit fundamental solution defined by the pair of fields $(\mathring{q}^k, \mathring{\boldsymbol{u}}^k)$, where $\mathring{u}^k_j$ represent components of the incompressible velocity fundamental solution and $\mathring{q}^k$ represent the components of the pressure fundamental solution (see e.g. [6, 5, 4]).

$$\mathring{q}^k(\boldsymbol{x}, \boldsymbol{y}) = \frac{(x_k - y_k)}{4\pi|\boldsymbol{x} - \boldsymbol{y}|^3},$$
$$\mathring{u}^k_j(\boldsymbol{x}, \boldsymbol{y}) = -\frac{1}{8\pi}\left\{\frac{\delta^k_j}{|\boldsymbol{x} - \boldsymbol{y}|} + \frac{(x_j - y_j)(x_k - y_k)}{|\boldsymbol{x} - \boldsymbol{y}|^3}\right\}, \quad j, k \in \{1, 2, 3\}.$$

Therefore, $(\mathring{q}^k, \mathring{\boldsymbol{u}}^k)$ satisfy

$$\mathring{\mathcal{A}}_j(\mathring{q}^k, \mathring{\boldsymbol{u}}^k)(\boldsymbol{x}) = \sum_{i=1}^{3} \frac{\partial^2 \mathring{u}^k_j}{\partial x_i^2} - \frac{\partial \mathring{q}^k}{\partial x_j} = \delta^k_j \delta(\boldsymbol{x} - \boldsymbol{y}).$$

Let us denote $\mathring{\sigma}_{ij}(p, \boldsymbol{v}) := \sigma_{ij}(p, \boldsymbol{v})|_{\mu=1}$. Then, in the particular case $\mu = 1$, the stress tensor $\mathring{\sigma}_{ij}(\mathring{q}^k, \mathring{\boldsymbol{u}}^k)(\boldsymbol{x} - \boldsymbol{y})$ reads as

$$\mathring{\sigma}_{ij}(\mathring{q}^k, \mathring{\boldsymbol{u}}^k)(\boldsymbol{x} - \boldsymbol{y}) = \frac{3}{4\pi}\frac{(x_i - y_i)(x_j - y_j)(x_k - y_k)}{|\boldsymbol{x} - \boldsymbol{y}|^5},$$

and the boundary traction becomes

$$\begin{aligned}\mathring{T}_i(\boldsymbol{x}; \mathring{q}^k, \mathring{\boldsymbol{u}}^k)(\boldsymbol{x}, \boldsymbol{y}) :&= \mathring{\sigma}_{ij}(\mathring{q}^k, \mathring{\boldsymbol{u}}^k)(\boldsymbol{x} - \boldsymbol{y})\, n_j(\boldsymbol{x}) \\ &= \frac{3}{4\pi}\frac{(x_i - y_i)(x_j - y_j)(x_k - y_k)}{|\boldsymbol{x} - \boldsymbol{y}|^5}\, n_j(\boldsymbol{x}).\end{aligned}$$

Let us define a pair of functions $(q^k, \boldsymbol{u}^k)_{k=1,2,3}$ as

$$q^k(\boldsymbol{x}, \boldsymbol{y}) = \frac{\mu(\boldsymbol{x})}{\mu(\boldsymbol{y})}\mathring{q}^k(\boldsymbol{x}, \boldsymbol{y}) = \frac{\mu(\boldsymbol{x})}{\mu(\boldsymbol{y})}\frac{x_k - y_k}{4\pi|\boldsymbol{x} - \boldsymbol{y}|^3}, \quad j, k \in \{1, 2, 3\}. \tag{17.8}$$

$$u^k_j(\boldsymbol{x}, \boldsymbol{y}) = \frac{1}{\mu(\boldsymbol{y})}\mathring{u}^k_j(\boldsymbol{x}, \boldsymbol{y}) = -\frac{1}{8\pi\mu(\boldsymbol{y})}\left\{\frac{\delta^k_j}{|\boldsymbol{x} - \boldsymbol{y}|} + \frac{(x_j - y_j)(x_k - y_k)}{|\boldsymbol{x} - \boldsymbol{y}|^3}\right\}, \tag{17.9}$$

Then,

$$\sigma_{ij}(\boldsymbol{x}; q^k, \boldsymbol{u}^k)(\boldsymbol{x}, \boldsymbol{y}) = \frac{\mu(\boldsymbol{x})}{\mu(\boldsymbol{y})}\mathring{\sigma}_{ij}(\mathring{q}^k, \mathring{\boldsymbol{u}}^k)(\boldsymbol{x} - \boldsymbol{y}),$$
$$T_i(\boldsymbol{x}; q^k, \boldsymbol{u}^k)(\boldsymbol{x}, \boldsymbol{y}) := \sigma_{ij}(\boldsymbol{x}; q^k, \boldsymbol{u}^k)(\boldsymbol{x}, \boldsymbol{y})\, n_j(\boldsymbol{x}) = \frac{\mu(\boldsymbol{x})}{\mu(\boldsymbol{y})}\mathring{T}_i(\boldsymbol{x}; \mathring{q}^k, \mathring{\boldsymbol{u}}^k)(\boldsymbol{x}, \boldsymbol{y}).$$

Substituting (17.9)-(17.8) in the Stokes system with variable coefficient (17.1) gives

$$\mathcal{A}_j(\boldsymbol{x}; q^k, \boldsymbol{u}^k)(\boldsymbol{x}, \boldsymbol{y}) = \delta^k_j \delta(\boldsymbol{x} - \boldsymbol{y}) + R_{kj}(\boldsymbol{x}, \boldsymbol{y}), \tag{17.10}$$

where

$$R_{kj}(\boldsymbol{x},\boldsymbol{y}) = \frac{1}{\mu(\boldsymbol{y})}\frac{\partial \mu(\boldsymbol{x})}{\partial x_i}\mathring{\sigma}_{ij}(\mathring{q}^k,\mathring{\boldsymbol{u}}^k)(\boldsymbol{x}-\boldsymbol{y}) = \mathcal{O}(|\boldsymbol{x}-\boldsymbol{y}|)^{-2})$$

is a weakly singular remainder. This implies that $(q^k,\boldsymbol{u}^k)$ is a parametrix of the operator $\boldsymbol{\mathcal{A}}$.

17.3.1 Volume and surface potentials

Let us define the parametrix-based Newton-type and remainder vector potentials

$$\mathcal{U}_k\boldsymbol{\rho}(\boldsymbol{y}) = \mathcal{U}_{kj}\rho_j(\boldsymbol{y}) := \int_\Omega u^k_j(\boldsymbol{x},\boldsymbol{y})\rho_j(\boldsymbol{x})dx,$$
$$\mathcal{R}_k\boldsymbol{\rho}(\boldsymbol{y}) = \mathcal{R}_{kj}\rho_j(\boldsymbol{y}) := \int_\Omega R_{kj}(\boldsymbol{x},\boldsymbol{y})\rho_j(\boldsymbol{x})dx, \quad \boldsymbol{y}\in\mathbb{R}^3,$$

for the velocity, and the scalar Newton-type pressure and remainder potentials

$$\mathcal{Q}\boldsymbol{\rho}(\boldsymbol{y}) = \mathcal{Q}_j\rho_j(\boldsymbol{y}) := \int_\Omega q^j(\boldsymbol{x},\boldsymbol{y})\rho_j(\boldsymbol{x})dx, \tag{17.11}$$

$$\boldsymbol{\mathcal{Q}}\rho(\boldsymbol{y}) = \mathcal{Q}_j\rho(\boldsymbol{y}) := \int_\Omega q^j(\boldsymbol{x},\boldsymbol{y})\rho(\boldsymbol{x})dx, \tag{17.12}$$

$$\mathcal{R}^\bullet\boldsymbol{\rho}(\boldsymbol{y}) = \mathcal{R}^\bullet_j\rho_j(\boldsymbol{y}) := 2\,v.p.\int_\Omega \frac{\partial \mathring{q}^j(\boldsymbol{x},\boldsymbol{y})}{\partial x_i}\frac{\partial\mu(\boldsymbol{x})}{\partial x_i}\rho_j(\boldsymbol{x})dx - \frac{4}{3}\rho_j\frac{\partial\mu}{\partial y_j},\ \boldsymbol{y}\in\mathbb{R}^3, \tag{17.13}$$

for the pressure. The integral in (17.13) is understood as a 3D strongly singular integral in the Cauchy sense.

For the velocity, let us also define the parametrix-based single layer potential, double layer potential and their respective direct values on the boundary, as follows:

$$V_k\boldsymbol{\rho}(\boldsymbol{y}) = V_{kj}\rho_j(\boldsymbol{y}) := -\int_S u^k_j(\boldsymbol{x},\boldsymbol{y})\rho_j(\boldsymbol{x})\,dS(\boldsymbol{x}),\ \ \boldsymbol{y}\notin S,$$
$$W_k\boldsymbol{\rho}(\boldsymbol{y}) = W_{kj}\rho_j(\boldsymbol{y}) := -\int_S T_j(\boldsymbol{x};q^k,\boldsymbol{u}^k)(\boldsymbol{x},\boldsymbol{y})\rho_j(\boldsymbol{x})\,dS(\boldsymbol{x}),\ \ \boldsymbol{y}\notin S,$$
$$\mathcal{V}_k\boldsymbol{\rho}(\boldsymbol{y}) = \mathcal{V}_{kj}\rho_j(\boldsymbol{y}) := -\int_S u^k_j(\boldsymbol{x},\boldsymbol{y})\rho_j(\boldsymbol{x})\,dS(\boldsymbol{x}),\ \ \boldsymbol{y}\in S,$$
$$\mathcal{W}_k\boldsymbol{\rho}(\boldsymbol{y}) = \mathcal{W}_{kj}\rho_j(\boldsymbol{y}) := -\int_S T_j(\boldsymbol{x};q^k,\boldsymbol{u}^k)(\boldsymbol{x},\boldsymbol{y})\rho_j(\boldsymbol{x})\,dS(\boldsymbol{x}),\ \ \boldsymbol{y}\in S.$$

For pressure in the variable coefficient Stokes system, we will need the following single-layer and double layer potentials:

$$\mathcal{P}\boldsymbol{\rho}(\boldsymbol{y}) = \mathcal{P}_j\rho_j(\boldsymbol{y}) := -\int_S \mathring{q}^j(\boldsymbol{x},\boldsymbol{y})\rho_j(\boldsymbol{x})dS(\boldsymbol{x}),$$
$$\Pi\boldsymbol{\rho}(\boldsymbol{y}) = \Pi_j\rho_j(\boldsymbol{y}) := -2\int_S \frac{\partial\mathring{q}^j(\boldsymbol{x},\boldsymbol{y})}{\partial n(\boldsymbol{x})}\mu(\boldsymbol{x})\rho_j(\boldsymbol{x})dS(\boldsymbol{x}),\ \boldsymbol{y}\notin S.$$

Let us also denote

$$\mathcal{W}'_k\boldsymbol{\rho}(\boldsymbol{y}) = \mathcal{W}'_{kj}\rho_j(\boldsymbol{y}) := -\int_S T_j(\boldsymbol{y};q^k,\boldsymbol{u}^k)(\boldsymbol{x},\boldsymbol{y})\rho_j(\boldsymbol{x})\,dS(\boldsymbol{x}),\ \ \boldsymbol{y}\in S,$$
$$\mathcal{L}^\pm_k\boldsymbol{\rho}(\boldsymbol{y}) := T^\pm_k(\Pi\boldsymbol{\rho},\boldsymbol{W}\boldsymbol{\rho})(\boldsymbol{y}), \quad \boldsymbol{y}\in S,$$

where $T^\pm_k$ are the traction operators for the *compressible* fluid.

17.3.2 Mapping properties

The following corollary reflects the mapping property of the vector operator $\mathring{\boldsymbol{\mathcal{Q}}}$ which transforms a scalar function into a vector as opposed as the scalar operator $\mathring{\mathcal{Q}}$, which transforms a vector function into a scalar function, whose mapping properties are already well known, see e.g. [4, Lemma 5.6.6.] for the constant coefficient case and presented in the previous theorem for the variable coefficient case.

Corollary 2. *The following operators are continuous*

$$\mathring{\mathcal{Q}}_k : \widetilde{H}^s(\Omega) \to \boldsymbol{H}^{s+1}(\Omega), \quad s \in \mathbb{R}, \tag{17.14}$$

$$\mathring{\mathcal{Q}}_k : H^s(\Omega) \to \boldsymbol{H}^{s+1}(\Omega), \quad s > -1/2. \tag{17.15}$$

Theorem 4. *The following operators, with $s > 1/2$,*

$$\mathcal{R}_{ik} : \boldsymbol{H}^s(\Omega) \to \boldsymbol{H}^s(\Omega), \qquad \mathcal{R}^\bullet_k : \boldsymbol{H}^s(\Omega) \to \boldsymbol{H}^{s-1}(\Omega),$$

$$\gamma^+\mathcal{R}_{ik} : \boldsymbol{H}^s(\Omega) \to \boldsymbol{H}^{s-1/2}(S), \qquad T^\pm_{ik}(\mathcal{R}^\bullet, \mathcal{R}) : \boldsymbol{H}^{1,0}(\Omega; \boldsymbol{\mathcal{A}}) \to \boldsymbol{H}^{-1/2}(S)$$

are compact.

The theorems in the remainder of this section are well known for the constant coefficient case, see e.g. [5, 4]. Then by relations 1.10 - 1.16 given in [11], we obtain their counterparts for the variable-coefficient case.

Theorem 5. *The following operators are continuous*

$$(\mathcal{P}, \boldsymbol{V}) : \boldsymbol{H}^{-1/2}(S) \longrightarrow \boldsymbol{H}^{1,0}(\Omega; \boldsymbol{\mathcal{A}}), \tag{17.16}$$

$$(\Pi, \boldsymbol{W}) : \boldsymbol{H}^{1/2}(S) \longrightarrow \boldsymbol{H}^{1,0}(\Omega; \boldsymbol{\mathcal{A}}), \tag{17.17}$$

$$(\mathcal{Q}, \boldsymbol{\mathcal{U}}) : \boldsymbol{L}^2(\Omega) \longrightarrow \boldsymbol{H}^{1,0}(\Omega; \boldsymbol{\mathcal{A}}), \tag{17.18}$$

$$(\mathcal{R}^\bullet, \boldsymbol{\mathcal{R}}) : \boldsymbol{H}^1(\Omega) \longrightarrow \boldsymbol{H}^{1,0}(\Omega; \boldsymbol{\mathcal{A}}), \tag{17.19}$$

$$(\frac{4\mu}{3} I, \boldsymbol{Q}) : L^2(\Omega) \longrightarrow \boldsymbol{H}^{1,0}(\Omega; \boldsymbol{\mathcal{A}}). \tag{17.20}$$

Theorem 6. *Let $\boldsymbol{\tau} \in \boldsymbol{H}^{1/2}(S)$. Then, the following jump relation holds:*

$$(\mathcal{L}^\pm_k - \widehat{\mathcal{L}}_k)\boldsymbol{\tau} =$$

$$\gamma^\pm \left(\mu \left[\partial_i \left(\frac{1}{\mu} \right) \mathring{W}_k(\mu\boldsymbol{\tau}) + \partial_k \left(\frac{1}{\mu} \right) \mathring{W}_i(\mu\boldsymbol{\tau}) - \frac{2}{3}\delta^k_i \partial_j \left(\frac{1}{\mu} \right) \mathring{W}_j(\mu\boldsymbol{\tau}) \right] \right) n_i. \tag{17.21}$$

where

$$\widehat{\mathcal{L}}_k(\boldsymbol{\tau}) := \mathring{\mathcal{L}}_k(\mu\boldsymbol{\tau}).$$

Corollary 3. *Let S_1 be a non empty submanifold of S with smooth boundary. Then, the operators*

$$r_{S_1}\widehat{\boldsymbol{\mathcal{L}}} : \widetilde{\boldsymbol{H}}^{1/2}(S_1) \longrightarrow \boldsymbol{H}^{-1/2}(S),$$

$$r_{S_1}(\boldsymbol{\mathcal{L}}^\pm - \widehat{\boldsymbol{\mathcal{L}}}) : \widetilde{\boldsymbol{H}}^{1/2}(S_1) \longrightarrow \boldsymbol{H}^{1/2}(S),$$

are continuous and the operators

$$r_{S_1}(\boldsymbol{\mathcal{L}}^\pm - \widehat{\boldsymbol{\mathcal{L}}}) : \widetilde{\boldsymbol{H}}^{1/2}(S_1) \longrightarrow \boldsymbol{H}^{-1/2}(S),$$

are compact.

Theorem 7. *The following pressure surface potential operators are continuous:*

$$\mathcal{P}_k : H^{s-\frac{3}{2}}(S) \to H^{s-1}(\Omega), \quad s \in \mathbb{R}, \tag{17.22}$$

$$\Pi_k : H^{s-1/2}(S) \to H^{s-1}(\Omega), \quad s \in \mathbb{R}. \tag{17.23}$$

17.4 The Third Green Identities

Let $B(\boldsymbol{y},\epsilon)\subset\Omega$ be a ball with a small enough radius ϵ and centre $\boldsymbol{y}\in\Omega$. In this new domain, the integrands of the operators $\boldsymbol{\mathcal{R}}$ and $\mathcal{R}^{\bullet}$ belong to $L^2(\Omega\setminus B(\boldsymbol{y},\epsilon))$. In addition, the parametrix $(q^k,\boldsymbol{u}^k)\in\boldsymbol{H}^{1,0}(\Omega\setminus B(\boldsymbol{y},\epsilon);\boldsymbol{\mathcal{A}})$ since we have removed the singularity. Therefore, we can apply the second Green identity (17.6) in the domain $\Omega\setminus B(\boldsymbol{y},\epsilon)$ to any $(p,\boldsymbol{v})\in\boldsymbol{H}^{1,0}(\Omega;\boldsymbol{\mathcal{A}})$ and to the parametrix $(q^k,\boldsymbol{u}^k)$, keeping in mind the relation (17.10) and applying the standard limiting procedures, i.e., $\epsilon\to 0$, see, e.g. [13], we obtain

$$\boldsymbol{v}+\boldsymbol{\mathcal{R}}\boldsymbol{v}-\boldsymbol{V}\boldsymbol{T}^{+}(p,\boldsymbol{v})+\boldsymbol{W}\boldsymbol{\gamma}^{+}\boldsymbol{v}=\boldsymbol{\mathcal{U}}\boldsymbol{\mathcal{A}}(p,\boldsymbol{v})+\boldsymbol{\mathcal{Q}}(\mathrm{div}(\boldsymbol{v})),\quad\text{in }\Omega. \tag{17.24}$$

Theorem 8. *An integral representation formula for the pressure p is given by*

$$p+\mathcal{R}^{\bullet}\boldsymbol{v}-\mathcal{P}\boldsymbol{T}(p,\boldsymbol{v})+\Pi\boldsymbol{\gamma}^{+}\boldsymbol{v}=\mathring{\mathcal{Q}}\boldsymbol{\mathcal{A}}(p,\boldsymbol{v})+\frac{4\mu}{3}div\boldsymbol{v},\quad in\ \Omega. \tag{17.25}$$

If the couple $(p,\boldsymbol{v})\in\boldsymbol{H}^{1,0}(\Omega;\boldsymbol{\mathcal{A}})$ is a solution of the Stokes PDEs (17.7a)-(17.7b) with variable coefficient, then (17.24) and (17.25) give

$$p+\mathcal{R}^{\bullet}\boldsymbol{v}-\mathcal{P}\boldsymbol{T}(p,\boldsymbol{v})+\Pi\boldsymbol{\gamma}^{+}\boldsymbol{v}=\mathring{\mathcal{Q}}\boldsymbol{f}+\frac{4\mu}{3}g\quad\text{in}\quad\Omega, \tag{17.26}$$

$$\boldsymbol{v}+\boldsymbol{\mathcal{R}}\boldsymbol{v}-\boldsymbol{V}\boldsymbol{T}^{+}(p,\boldsymbol{v})+\boldsymbol{W}\boldsymbol{\gamma}^{+}\boldsymbol{v}=\boldsymbol{\mathcal{U}}\boldsymbol{f}+\boldsymbol{\mathcal{Q}}g\quad\text{in}\quad\Omega. \tag{17.27}$$

We will also need the trace and traction of the third Green identities for $(p,\boldsymbol{v})\in\boldsymbol{H}^{1,0}(\Omega;\boldsymbol{\mathcal{A}})$ on S. We highlight that the traction operator is well defined applied to the third Green identities (17.26)-(17.27) by virtue of Theorem 5.

$$1/2\boldsymbol{\gamma}^{+}\boldsymbol{v}+\gamma^{+}\boldsymbol{\mathcal{R}}\boldsymbol{v}-\boldsymbol{\mathcal{V}}\boldsymbol{T}^{+}(p,\boldsymbol{v})+\boldsymbol{\mathcal{W}}\gamma^{+}\boldsymbol{v}=\boldsymbol{\gamma}^{+}\boldsymbol{\mathcal{U}}\boldsymbol{f}+\boldsymbol{\gamma}^{+}\boldsymbol{\mathcal{Q}}g, \tag{17.28}$$

$$1/2\boldsymbol{T}^{+}(p,\boldsymbol{v})+\boldsymbol{T}^{+}(\mathcal{R}^{\bullet},\boldsymbol{\mathcal{R}})\boldsymbol{v}-\boldsymbol{\mathcal{W}}'\boldsymbol{T}^{+}(p,\boldsymbol{v})+\boldsymbol{\mathcal{L}}^{+}\gamma^{+}\boldsymbol{v}=\widetilde{\boldsymbol{T}}^{+}(g,\boldsymbol{f}) \tag{17.29}$$

where

$$\widetilde{\boldsymbol{T}}^{+}(g,\boldsymbol{f}):=\boldsymbol{T}^{+}(\mathring{\mathcal{Q}}\boldsymbol{f}+\frac{4\mu}{3}g,\ \boldsymbol{\mathcal{U}}\boldsymbol{f}+\boldsymbol{\mathcal{Q}}g). \tag{17.30}$$

One can prove the following three assertions that are instrumental for proving the equivalence of the BDIES and the mixed PDE.

Theorem 9. *Let $\boldsymbol{v}\in\boldsymbol{H}^{1}(\Omega)$, $p\in L_2(\Omega)$, $g\in L_2(\Omega)$, $\boldsymbol{f}\in\boldsymbol{L}_2(\Omega)$, $\boldsymbol{\Psi}\in\boldsymbol{H}^{-1/2}(S)$ and $\boldsymbol{\Phi}\in\boldsymbol{H}^{1/2}(S)$ satisfy the equations*

$$p+\mathcal{R}^{\bullet}\boldsymbol{v}-\mathcal{P}\boldsymbol{\Psi}+\Pi\boldsymbol{\Phi}=\mathring{\mathcal{Q}}\boldsymbol{f}+\frac{4\mu}{3}g\ \ in\ \Omega, \tag{17.31}$$

$$\boldsymbol{v}+\boldsymbol{\mathcal{R}}\boldsymbol{v}-\boldsymbol{V}\boldsymbol{\Psi}+\boldsymbol{W}\boldsymbol{\Phi}=\boldsymbol{\mathcal{U}}\boldsymbol{f}+\boldsymbol{\mathcal{Q}}g\ \ in\ \Omega. \tag{17.32}$$

Then $(p,\boldsymbol{v})\in\boldsymbol{H}^{1,0}(\Omega,\boldsymbol{\mathcal{A}})$ and solve the equations $\boldsymbol{\mathcal{A}}(p,\boldsymbol{v})=\boldsymbol{f}$ and $div(\boldsymbol{v})=g$. Moreover, the following relations hold true:

$$\mathcal{P}(\boldsymbol{\Psi}-\boldsymbol{T}^{+}(p,\boldsymbol{v}))-\Pi(\boldsymbol{\Phi}-\gamma^{+}\boldsymbol{v})=0\quad in\ \Omega, \tag{17.33}$$

$$\boldsymbol{V}(\boldsymbol{\Psi}-\boldsymbol{T}^{+}(p,\boldsymbol{v}))-\boldsymbol{W}(\boldsymbol{\Phi}-\gamma^{+}\boldsymbol{v})=\boldsymbol{0}\quad in\ \Omega. \tag{17.34}$$

Lemma 2. *Let $S=\overline{S}_1\cup\overline{S}_2$, where S_1 and S_2 are open non-empty non-intersecting simply connected submanifolds of S with infinitely smooth boundaries. Let $\boldsymbol{\Psi}^{*}\in\widetilde{\boldsymbol{H}}^{-1/2}(S_1)$, $\boldsymbol{\Phi}^{*}\in\widetilde{\boldsymbol{H}}^{1/2}(S_2)$. If*

$$\mathcal{P}(\boldsymbol{\Psi}^{*})-\Pi(\boldsymbol{\Phi}^{*})=\boldsymbol{0},\qquad\boldsymbol{V}\boldsymbol{\Psi}^{*}(\boldsymbol{x})-\boldsymbol{W}\boldsymbol{\Phi}^{*}(\boldsymbol{x})=\boldsymbol{0},\quad in\ \Omega, \tag{17.35}$$

then $\boldsymbol{\Psi}^{*}=\boldsymbol{0}$, and $\boldsymbol{\Phi}^{*}=\boldsymbol{0}$, on S.

17.5 BDIES M11

We aim to obtain two different BDIES for mixed BVP (17.7). This is a well known procedure, see [2, 11, 10] and further references therein.

To this end, let the functions $\boldsymbol{\Phi}_0 \in \boldsymbol{H}^{1/2}(S)$ and $\boldsymbol{\Psi}_0 \in \boldsymbol{H}^{-1/2}(S)$ be some continuations of the boundary functions $\boldsymbol{\varphi}_0 \in \boldsymbol{H}^{1/2}(S_D)$ and $\boldsymbol{\psi}_0 \in \boldsymbol{H}^{-1/2}(S_N)$ from (17.7c) and (17.7d). Let us now represent

$$\gamma^+ \boldsymbol{v} = \boldsymbol{\Phi}_0 + \boldsymbol{\varphi}, \quad \boldsymbol{T}^+(p, \boldsymbol{v}) = \boldsymbol{\Psi}_0 + \boldsymbol{\psi} \text{ on } S, \tag{17.36}$$

where $\boldsymbol{\varphi} \in \widetilde{\boldsymbol{H}}^{1/2}(S_N)$ and $\boldsymbol{\psi} \in \widetilde{\boldsymbol{H}}^{-1/2}(S_D)$ are unknown boundary functions.

Let us now take equations (17.26) and (17.27) in the domain Ω and restrictions of equations (17.28) and (17.29) to the boundary parts S_D and S_N, respectively. Substituting there representations (17.36) and considering further the unknown boundary functions $\boldsymbol{\varphi}$ and $\boldsymbol{\psi}$ as formally independent of (segregated from) the unknown domain functions p and $\boldsymbol{v}$, we obtain the following system (M11) consisting of four boundary-domain integral equations for four unknowns, $(p, \boldsymbol{v}) \in \boldsymbol{H}^{1,0}(\Omega, \boldsymbol{\mathcal{A}})$, $\boldsymbol{\varphi} \in \widetilde{\boldsymbol{H}}^{1/2}(S_N)$ and $\boldsymbol{\psi} \in \widetilde{\boldsymbol{H}}^{-1/2}(S_D)$:

$$p + \mathcal{R}^\bullet \boldsymbol{v} - \mathcal{P}\boldsymbol{\psi} + \Pi\boldsymbol{\varphi} = F_0, \quad \text{in } \Omega, \tag{17.37a}$$

$$\boldsymbol{v} + \boldsymbol{\mathcal{R}}\boldsymbol{v} - \boldsymbol{V}\boldsymbol{\psi} + \boldsymbol{W}\boldsymbol{\varphi} = \boldsymbol{F}, \quad \text{in } \Omega, \tag{17.37b}$$

$$r_{S_D}\boldsymbol{\gamma}^+\boldsymbol{\mathcal{R}}\boldsymbol{v} - r_{S_D}\boldsymbol{\mathcal{V}}\boldsymbol{\psi} + r_{S_D}\boldsymbol{\mathcal{W}}\boldsymbol{\varphi} = r_{S_D}\boldsymbol{\gamma}^+\boldsymbol{F} - \boldsymbol{\varphi}_0, \quad \text{on } S_D, \tag{17.37c}$$

$$r_{S_N}\boldsymbol{T}^+(\mathcal{R}^\bullet, \boldsymbol{\mathcal{R}})\boldsymbol{v} - r_{S_N}\boldsymbol{\mathcal{W}}'\boldsymbol{\psi} + r_{S_N}\boldsymbol{\mathcal{L}}^+\boldsymbol{\varphi} = r_{S_N}\boldsymbol{T}^+(F_0, \boldsymbol{F}) - \boldsymbol{\psi}_0, \quad \text{on } S_N, \tag{17.37d}$$

where

$$F_0 = \mathring{\mathcal{Q}}\boldsymbol{f} + \frac{4}{3}g\mu + \mathcal{P}\boldsymbol{\Psi}_0 - \Pi\boldsymbol{\Phi}_0, \quad \boldsymbol{F} = \boldsymbol{\mathcal{U}}\boldsymbol{f} + \boldsymbol{\mathcal{Q}}g + \boldsymbol{V}\boldsymbol{\Psi}_0 - \boldsymbol{W}\boldsymbol{\Phi}_0. \tag{17.38}$$

By virtue of Lemma 9, $(F_0, \boldsymbol{F}) \in \boldsymbol{H}^{1,0}(\Omega, \boldsymbol{\mathcal{A}})$ and hence $\boldsymbol{T}(F_0, \boldsymbol{F})$ is well defined.

We denote the right hand side of BDIE system (17.37) as

$$\mathcal{F}^{11}_* := [F_0, \mathcal{F}^{11}] = [F_0, \boldsymbol{F}, r_{S_D}\boldsymbol{\gamma}^+\boldsymbol{F} - \boldsymbol{\varphi}_0, r_{S_N}\boldsymbol{T}^+(F_0, \boldsymbol{F}) - \boldsymbol{\psi}_0]^\top, \tag{17.39}$$

which implies $\mathcal{F} \in \boldsymbol{H}^{1,0}(\Omega, \boldsymbol{\mathcal{A}}) \times \boldsymbol{H}^{1/2}(S_D) \times \boldsymbol{H}^{-1/2}(S_N)$.

Note that BDIE system (17.37) can be split into the BDIE system (M11), of 3 vector equations (17.37b), (17.37c), (17.37d) for 3 vector unknowns, $\boldsymbol{v}$, $\boldsymbol{\psi}$ and $\boldsymbol{\varphi}$, and the scalar equation (17.37a) that can be used, after solving the system, to obtain the pressure, p. The system (M11) given by equations (17.37a)-(17.37d) can be written using matrix notation as

$$\mathcal{M}^{11}_* \mathcal{X} = \mathcal{F}^{11}_*, \tag{17.40}$$

where $\mathcal{X}$ represents the vector containing the unknowns of the system

$$\mathcal{X} = (p, \boldsymbol{v}, \boldsymbol{\psi}, \boldsymbol{\varphi})^\top \in L^2(\Omega) \times \boldsymbol{H}^1(\Omega) \times \widetilde{\boldsymbol{H}}^{-1/2}(S_D) \times \widetilde{\boldsymbol{H}}^{1/2}(S_N)$$

The matrix operator $\mathcal{M}^{11}_*$ is defined by

$$\mathcal{M}^{11}_* = \begin{bmatrix} I & \mathcal{R}^\bullet & -\mathcal{P} & \Pi \\ \boldsymbol{0} & \boldsymbol{I} + \boldsymbol{\mathcal{R}} & -\boldsymbol{V} & \boldsymbol{W} \\ \boldsymbol{0} & r_{S_D}\boldsymbol{\gamma}^+\boldsymbol{\mathcal{R}} & -r_{S_D}\boldsymbol{\mathcal{V}} & r_{S_D}\boldsymbol{\mathcal{W}} \\ \boldsymbol{0} & r_{S_N}\boldsymbol{T}^+(\mathcal{R}^\bullet, \boldsymbol{\mathcal{R}}) & -r_{S_N}\boldsymbol{\mathcal{W}}' & r_{S_N}\boldsymbol{\mathcal{L}} \end{bmatrix}.$$

We note that the mapping properties of the operators involved in the matrix imply the continuity of the operator

$$\begin{aligned} \mathcal{M}^{11}_* : L^2(\Omega) \times \boldsymbol{H}^1(\Omega) \times \widetilde{\boldsymbol{H}}^{-1/2}(S_D) \times \widetilde{\boldsymbol{H}}^{1/2}(S_N) \\ \longrightarrow L^2(\Omega) \times \boldsymbol{H}^1(\Omega) \times \boldsymbol{H}^{1/2}(S_D) \times \boldsymbol{H}^{-1/2}(S_N). \end{aligned}$$

Remark 2. *The term* $\mathcal{F}_*^{11} = 0$ *if and only if* $(\boldsymbol{f}, g, \boldsymbol{\Phi}_0, \boldsymbol{\Psi}_0) = \boldsymbol{0}$.

Theorem 10 (Equivalence Theorem)**.** *Let* $\boldsymbol{f} \in \boldsymbol{L}_2(\Omega)$, $g \in L_2(\Omega)$ *and let* $\boldsymbol{\Phi}_0 \in \boldsymbol{H}^{-1/2}(S)$ *and* $\boldsymbol{\Psi}_0 \in \boldsymbol{H}^{-1/2}(S)$ *be some fixed extensions of* $\boldsymbol{\varphi}_0 \in \boldsymbol{H}^{1/2}(S_D)$ *and* $\boldsymbol{\psi}_0 \in \boldsymbol{H}^{-1/2}(S_N)$ *respectively.*

(i) If some $(p, \boldsymbol{v}) \in \boldsymbol{H}^{1,0}(\Omega; \boldsymbol{\mathcal{A}})$ *solve the mixed BVP* (17.7)*, then*

$$(p, \boldsymbol{v}, \boldsymbol{\psi}, \boldsymbol{\varphi}) \in \boldsymbol{H}^{1,0}(\Omega; \boldsymbol{\mathcal{A}}) \times \widetilde{\boldsymbol{H}}^{-1/2}(S_D) \times \widetilde{\boldsymbol{H}}^{1/2}(S_N),$$

where

$$\boldsymbol{\varphi} = \gamma^+ \boldsymbol{v} - \boldsymbol{\Phi}_0, \quad \boldsymbol{\psi} = \boldsymbol{T}^+(p, \boldsymbol{v}) - \boldsymbol{\Psi}_0 \quad \text{on } S, \tag{17.41}$$

solve BDIE system (17.37)*.*

(ii) If $(p, \boldsymbol{v}, \boldsymbol{\psi}, \boldsymbol{\varphi}) \in \boldsymbol{H}^{1,0}(\Omega; \boldsymbol{\mathcal{A}}) \times \widetilde{\boldsymbol{H}}^{-1/2}(S_D) \times \widetilde{\boldsymbol{H}}^{1/2}(S_N)$ *solve the BDIE system* (17.37) *then* $(p, \boldsymbol{v})$ *solve mixed BVP* (17.7) *and* $\boldsymbol{\psi}, \boldsymbol{\varphi}$ *satisfy* (17.41)*.*

(iii) The BDIE system (17.37) *is uniquely solvable in* $\boldsymbol{H}^{1,0}(\Omega; \boldsymbol{\mathcal{A}}) \times \widetilde{\boldsymbol{H}}^{-1/2}(S_D) \times \widetilde{\boldsymbol{H}}^{1/2}(S_N)$.

Theorem 11. *The operator*

$$\begin{aligned} \mathcal{M}_*^{11} : & L_2(\Omega) \times \boldsymbol{H}^1(\Omega) \times \widetilde{\boldsymbol{H}}^{-1/2}(S_D) \times \widetilde{\boldsymbol{H}}^{1/2}(S_N) \\ & \longrightarrow L_2(\Omega) \times \boldsymbol{H}^1(\Omega) \times \boldsymbol{H}^{1/2}(S_D) \times \boldsymbol{H}^{-1/2}(S_N) \end{aligned} \tag{17.42}$$

is continuously invertible.

Theorem 12. *The operator*

$$\mathcal{M}_*^{11} : \boldsymbol{H}^{1,0}(\Omega; \boldsymbol{\mathcal{A}}) \times \widetilde{\boldsymbol{H}}^{-1/2}(S_D) \times \widetilde{\boldsymbol{H}}^{1/2}(S_N) \tag{17.43}$$

$$\longrightarrow \boldsymbol{H}^{1,0}(\Omega; \boldsymbol{\mathcal{A}}) \times \boldsymbol{H}^{1/2}(S_D) \times \boldsymbol{H}^{-1/2}(S_N) \tag{17.44}$$

is continuously invertible.

The last three vector equations of the system (M11) are segregated from p. Hence, we can define the new system given by equations (17.37b), (17.37c), (17.37d) which can be written using matrix notation as

$$\mathcal{M}^{11} \mathcal{Y} = \mathcal{F}^{11}, \tag{17.45}$$

where $\mathcal{Y}$ represents the vector containing the unknowns of the system

$$\mathcal{Y} = (\boldsymbol{v}, \boldsymbol{\psi}, \boldsymbol{\varphi})^\top \in \boldsymbol{H}^1(\Omega) \times \widetilde{\boldsymbol{H}}^{-1/2}(S_D) \times \widetilde{\boldsymbol{H}}^{1/2}(S_N)$$

The matrix operator $\mathcal{M}^{11}$ is defined by

$$\mathcal{M}^{11} = \begin{bmatrix} \boldsymbol{I} + \boldsymbol{\mathcal{R}} & -\boldsymbol{V} & \boldsymbol{W} \\ r_{S_D} \boldsymbol{\gamma}^+ \boldsymbol{\mathcal{R}} & -r_{S_D} \boldsymbol{\mathcal{V}} & r_{S_D} \boldsymbol{\mathcal{W}} \\ r_{S_N} \boldsymbol{T}^+(\boldsymbol{\mathcal{R}}^\bullet, \boldsymbol{\mathcal{R}}) & -r_{S_N} \boldsymbol{\mathcal{W}}' & r_{S_N} \boldsymbol{\mathcal{L}} \end{bmatrix}$$

Corollary 4. *The operator*

$$\mathcal{M}^{11} : \boldsymbol{H}^1(\Omega) \times \widetilde{\boldsymbol{H}}^{-1/2}(S_D) \times \widetilde{\boldsymbol{H}}^{1/2}(S_N) \longrightarrow \boldsymbol{H}^1(\Omega) \times \boldsymbol{H}^{1/2}(S_D) \times \boldsymbol{H}^{-1/2}(S_N)$$

is continuous and continuously invertible.

17.6 Further Work

Immediate further work will focus on the numerical implementation of the proposed BDIES.

References

[1] R. Brown, I. Mitrea, M. Mitrea and M. Wright, Mixed Boundary Value Problems for the Stokes System, *Transactions of the American Mathematical Society*, **362**, (2009) 1211–1230.

[2] O. Chkadua, S.E. Mikhailov and D. Natroshvili, Analysis of direct boundary-domain integral equations for a mixed BVP with variable coefficient, I: Equivalence and invertibility, *J. Integral Equations Appl.* **21** (2009), 499–543.

[3] M. Costabel, Boundary integral operators on Lipschitz domains: Elementary results, *SIAM J. Math. Anal.* **19** (1988), 613–626.

[4] G.C. Hsiao and W.L. Wendland, *Boundary Integral Equations*, Springer, Berlin, 2008.

[5] M. Kohr and W.L. Wendland, Variational boundary integral equations for the Stokes system, *Applicable Anal.* **85** (2006), 1343–1372.

[6] O.A. Ladyzhenskaya, *The Mathematical Theory of Viscous Incompressible Flow*, Gordon & Breach, New York, 1969.

[7] J.L. Lions and E. Magenes, *Non-Homogeneous Boundary Value Problems and Applications*, Springer, Berlin, 1973.

[8] W. McLean, *Strongly Elliptic Systems and Boundary Integral Equations*, Cambridge University Press, 2000.

[9] S.E. Mikhailov, Traces, extensions and co-normal derivatives for elliptic systems on Lipschitz domains, *J. Math. Anal. Appl.* **378** (2011), 324–342.

[10] S.E. Mikhailov, Localized boundary-domain integral formulations for problems with variable coefficients, *Engineering Analysis with Boundary Elements* **26** (2002), 681–690.

[11] S.E. Mikhailov, and C.F. Portillo, BDIE system to the mixed BVP for the Stokes equations with variable viscosity, *Integral Methods in Science and Engineering*, Theoretical and Computational Advances, C. Constanda and A. Kirsh, eds., Springer, Boston (2015), 401–412.

[12] S.E. Mikhailov and C.F. Portillo, A New Family of Boundary-Domain Integral Equations for a Mixed Elliptic BVP with Variable Coefficient, in *Proceedings of the 10th UK Conference on Boundary Integral Methods*, Brighton University Press, (2015), 76–84.

[13] C. Miranda, *Partial Differential Equations of Elliptic Type*, 2nd edn., Springer, 1970.

[14] B. Reidinger and O. Steinbach, A symmetric boundary element method for the Stokes problem in multiple connected domains, *Math. Meth. Appl. Sci.* **26** (2003), 77–93.

[15] O. Steinbach, *Numerical Approximation Methods for Elliptic Boundary Value Problems*, Springer, Berlin, 2007.

[16] W.L. Wendland and J. Zhu, The boundary element method for three dimensional Stokes flow exterior to an open surface, *Mathematical and Computer Modelling* **6** (1991), 19–42.

Chapter 18

MHD combined convection flow in a lid-driven cavity with sinusoidal wavy wall

F. Sidre Oğlakkaya and Canan Bozkaya

Department of Mathematics,
Middle East Technical University
06800, Ankara, Turkey

Abstract. *In this study, a numerical analysis is conducted to understand the influence of a magnetic field on the mixed convection flow and the thermal distribution in a lid-driven cavity with a uniformly heated vertical sinusoidal wavy right surface. Specifically, we consider the two-dimensional, steady, incompressible and laminar flow of electrically conducting fluid in an electrically insulated cavity under the effect of a horizontally applied external magnetic field. The horizontal walls of the cavity are considered to be adiabatic while the isothermal sidewalls are maintained at different temperatures T_h and T_c with $T_h > T_c$. Furthermore, the left wall moves upward at a constant speed, while the other walls remain stationary. The coupled nonlinear equations of the mass, momentum and energy governing the present problem are discretized using the dual reciprocity boundary element method (DRBEM) which is a boundary only nature technique treating the nonlinear terms by the use of radial basis functions. The validity of the DRBEM code is ascertained by comparing the present results with previously published results. The influence of Rayleigh number, Hartmann number and the number of wavy surface undulation on the flow structure and the heat transfer characteristics are analyzed in details. The obtained results illustrate that the average Nusselt number increases with an increase in Rayleigh number and the number of undulation, while it decreases for higher values of Hartmann number.*

18.1 Literature Survey

The study of mixed convection and heat transfer in lid-driven cavities under the effect of magnetic field has attracted many researchers due to its interaction with many engineering and industrial applications, such as nuclear reactors, cooling of electronic devices, food processing, lubrication and drying technologies. Mixed convection in cavities occurs as a result of the interaction of two opposite mechanism, namely shear and buoyancy forces. The shear flow is generated by the motion of a lid and the buoyant flow is due to the thermal nonhomegeneity of cavity walls. On the other hand, when the fluid is electrically conducting, the flow and the temperature

distributions can be controlled by the application of an external magnetic field to the convective system. There are many studies on the solution of the MHD mixed convection flow in regular cavities with flat walls [2]-[5]. On the other hand, the mixed convective heat transfer for more complex geometries with irregular surfaces is also great importance since irregular surfaces are often encountered in many engineering applications, such as solar collectors, underground cable systems and cooling system of micro-electronic devices. It is worth mentioning that the irregular cavities with a form of wavy surfaces can be used to control the heat transfer efficiency since the changes in surface fluctuation have a great impact on the surface temperature. Although there are many studies given in the literature of natural convection flow in cavities with wavy surfaces (e.g. [7], [8], [9]), there have been few studies on the mixed convection flow in lid-driven cavities with irregular surfaces. Rahman et al. [6] investigated the influence of the uniform magnetic field with Joule heating effects in a lid-driven cavity with heated semi-circular wall. They observed that, the flow strength and temperature distribution are affected by the magnetic field and Joule parameter. Wang and Chen [10] solved the forced convection flow in a wavy-wall channel and analyzed its effect on Nusselt number for various values of Reynolds number. The effect of sinusoidal wavy wall on mixed convection heat transfer in a lid-driven cavity was investigated in the work of Al-Amiri et al. [11]. Their results revealed that the average Nusselt number increases with an increase in the amplitude of the wavy surface and Reynolds number. Later, Mekroussi et al. [12] worked on the same mixed convection problem in an inclined lid-driven cavity with a wavy wall. They found that the heat transfer was enhanced with an increase in the number of undulation as well as the inclination angle of the cavity. Nasrin and Parvin [13] conducted a study to analyze the mixed convection flow in a lid-driven cavity with a sinusoidal wavy bottom surface in the presence of a transverse magnetic field. In all these works, a domain decomposition method (e.g. finite element and/or finite volume methods) was employed for the discretization of the governing equation.

The aim of the present work is to investigate numerically the influence of both the wavy hot wall and the externally applied magnetic field on mixed convection flow in a lid-driven cavity with a wavy right surface by using a boundary only discretization technique, namely DRBEM. Thus, the coupled nonlinear governing equations are discretized by using DRBEM in which all the terms except the Laplacian are treated as nonhomogeneity and these terms are approximated by means of radial basis functions. Hence the solution is obtained with a less computational cost compared to domain decomposition techniques. Therefore, the present study focuses on incorporating the use of DRBEM with the effect of physical controlling parameters including Rayleigh and Hartmann numbers and the number of undulation along the hot wavy surface.

18.2 Statement of the Problem and the Governing Equations

In this study, we consider the two dimensional MHD mixed convection flow in a square lid-driven cavity of height ℓ with a sinusoidal wavy right wall (see Figure 18.1). The horizontal walls of the cavity are assumed to be adiabatic while the isothermal side walls are maintained at constant temperatures T_h and T_c with $T_h > T_c$. Furthermore, the left wall of the cavity moves upwards with a constant speed U_0, while the other walls remain stationary. A uniform magnetic field of strength B_0 is applied in horizontal direction normal to the moving wall and the gravity acts in the negative y-direction. The magnetic Reynolds number is assumed to be small so that the induced magnetic field is neglected. Moreover, the flow generated inside the cavity is assumed to be steady, laminar and it obeys the Boussinesq approximation while the effects of the radiation, joule heating and viscous dissipation are neglected. Air is selected as the working fluid which yields Prandtl number of 0.71. Thus, the dimensionless equations governing this flow can be written as follows [13]

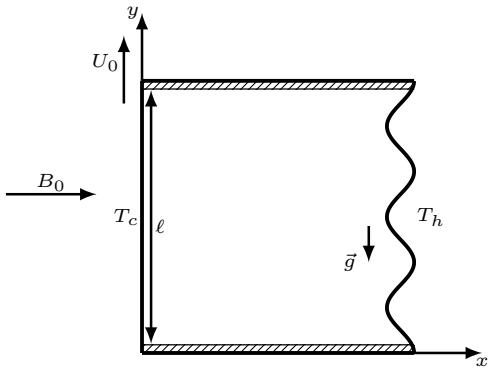

Figure 18.1: Geometry of the physical problem.

$$\frac{\partial U}{\partial X}+\frac{\partial V}{\partial Y}=0 \tag{18.1}$$

$$U\frac{\partial U}{\partial X}+V\frac{\partial U}{\partial Y}=-\frac{\partial P}{\partial X}+\frac{1}{Re}\left(\frac{\partial^2 U}{\partial X^2}+\frac{\partial^2 U}{\partial Y^2}\right), \tag{18.2}$$

$$U\frac{\partial V}{\partial X}+V\frac{\partial V}{\partial Y}=-\frac{\partial P}{\partial Y}+\frac{1}{Re}\left(\frac{\partial^2 V}{\partial X^2}+\frac{\partial^2 V}{\partial Y^2}\right)+\frac{Ra}{Re^2 Pr}\theta-\frac{Ha^2}{Re}V \tag{18.3}$$

$$U\frac{\partial \theta}{\partial X}+V\frac{\partial \theta}{\partial Y}=\frac{1}{RePr}\left(\frac{\partial^2 \theta}{\partial X^2}+\frac{\partial^2 \theta}{\partial Y^2}\right) \tag{18.4}$$

by defining the dimensionless variables

$$X=\frac{x}{\ell}, \quad Y=\frac{y}{\ell}, \quad U=\frac{u}{U_0}, \quad V=\frac{v}{U_0}, \quad P=\frac{p}{\rho U_0^2}, \quad \theta=\frac{T-T_c}{T_h-T_c}.$$

Here, (U,V) is the velocity field, P is the pressure, θ is the temperature. The dimensionless parameters are the Reynolds, Prandtl, Rayleigh and Hartmann numbers, which are given respectively as follows:

$$Re=\frac{U_0\ell}{\nu}, \quad Pr=\frac{\nu}{\alpha}, \quad Ra=\frac{g\beta(T_h-T_c)\ell^3}{\nu\alpha}, \quad Ha=B_0\ell\sqrt{\sigma/\mu}$$

in which the parameters α, β, ν, σ and μ are the thermal diffusivity, thermal expansion coefficient, kinematic viscosity, electrical conductivity and dynamic viscosity of the fluid, respectively.

The physical dimensionless form of the boundary conditions are

$$\begin{array}{ll} \text{At the horizontal walls:} & U=V=0,\ \partial\theta/\partial n=0 \\ \text{At sliding left wall:} & U=0,\ V=1,\ \theta=0 \\ \text{At wavy right wall:} & U=V=0,\ \theta=1. \end{array} \tag{18.5}$$

The shape of the wavy right wall is taken as sinusoidal which is defined by $X=1-A[1-cos(2n\pi Y)]$ where A is the dimensionless amplitude of the wavy surface and n is the number of undulation.

Then, the equations (18.1)-(18.4) can be written in stream function, vorticity and temperature form as

$$\nabla^2\Psi=-\omega \tag{18.6}$$

$$\nabla^2\omega = Re\left(U\frac{\partial\omega}{\partial X} + V\frac{\partial\omega}{\partial Y}\right) + Ha^2\frac{\partial V}{\partial X} - \frac{Ra}{RePr}\frac{\partial\theta}{\partial X} \tag{18.7}$$

$$\nabla^2\theta = RePr\left(U\frac{\partial\theta}{\partial X} + V\frac{\partial\theta}{\partial Y}\right) \tag{18.8}$$

by defining the stream function Ψ and vorticity ω as

$$U = \frac{\partial\Psi}{\partial Y}, \quad V = -\frac{\partial\Psi}{\partial X}, \quad \omega = \frac{\partial V}{\partial X} - \frac{\partial U}{\partial Y}\,.$$

The corresponding boundary conditions for stream function and temperature become

$$\begin{array}{ll} \text{At the horizontal walls:} & \Psi = 0,\ \partial\theta/\partial n = 0 \\ \text{At sliding left wall:} & \partial\Psi/\partial Y = 0,\ \partial\Psi/\partial X = -1,\ \theta = 0 \\ \text{At wavy right wall:} & \Psi = 0,\ \theta = 1 \end{array} \tag{18.9}$$

and the unknown boundary conditions of the vorticity will be obtained from (18.6) by using a radial basis function approximation which is an advantage of DRBEM.

18.3 Numerical Method

The DRBEM is employed to transform the governing equations (18.6)-(18.8) into boundary integrals by using the fundamental solution of Laplace equation $u^* = 1/2\pi\ln(1/r)$. Hence, the Equations (18.6)-(18.8) are weighted with u^* and the application of the divergence theorem results in the following equations:

$$c_i D_i + \int_\Gamma \left(q^* D - u^*\frac{\partial D}{\partial n}\right) d\Gamma = -\int_\Omega b_D u^* d\Omega \tag{18.10}$$

where D is used for each unknown Ψ, ω and θ. Here $q^* = \partial u^*/\partial n$, Γ is the boundary of the domain Ω and the constant c_i depends only on the boundary geometry at the point i under consideration. All the terms on the right hand side of Equations (18.6)-(18.8) denoted by b_D are treated as inhomogeneity and they are approximated by using the radial basis functions $f_j = 1 + r_j$, which are linked through the particular solutions $\hat{u}_j$ of $\nabla^2\hat{u}_j = f_j$ [1]. That is, these approximations are given by $b_D \approx \sum_{j=1}^{N+L}\alpha_{D_j} f_j = \sum_{j=1}^{N+L}\alpha_{D_j}\nabla^2\hat{u}_j$ where the coefficients α_{D_j} are undetermined constants, N and L are the number of boundary and interior nodes, respectively. Thus, Equation (18.10) take the form

$$c_i D_i + \int_\Gamma (q^* D - u^*\frac{\partial D}{\partial n})d\Gamma = \sum_{j=1}^{N+L}\alpha_{D_j}\left[c_i\hat{u}_{ji} + \int_\Gamma (q^*\hat{u}_j - u^*\hat{q}_j)d\Gamma\right] \tag{18.11}$$

which contains only the boundary integrals and $\hat{q} = \partial\hat{u}_j/\partial n$. By discretizing the boundary with constant elements, the matrix-vector form of Equation (18.11) can be expressed in a compact way for each unknowns $D(=\Psi,\ \omega,\ \theta)$, as

$$HD - G\frac{\partial D}{\partial n} = (H\hat{U} - G\hat{Q})F^{-1}b_D. \tag{18.12}$$

The matrices $\hat{U}$ and $\hat{Q}$ are constructed by taking each of the vectors $\hat{u}_j$ and $\hat{q}_j$ as columns, respectively. The matrix F consists of vectors f_j of size $(N + L)$ as columns. The components of the matrices G and H are obtained by taking the integral of the fundamental solution u^* and its normal derivative along each boundary elements Γ_j, respectively. The DRBEM equations (18.12) are coupled so that they are solved iteratively. In each iteration, the required space derivatives of the unknowns Ψ, ω and θ, and also the unknown vorticity boundary conditions are obtained by using the coordinate matrix F [1].

18.4 Numerical Validation and Results

In the present study, the characteristics of the flow field and temperature distribution in the lid-driven cavity with a wavy right wall are investigated in order to understand the impact of various physical parameters such as Hartmann number ($Ha = 0, 25, 50, 100$), Rayleigh number ($Ra = 10^3, 10^4, 10^5, 10^6$) and number of undulation ($n = 0, 1, 2, 3$) by keeping Reynolds and Prandtl numbers fixed as $Re = 100$ and $Pr = 0.71$, respectively. The boundary of the cavity is discretized by using $N = 350$ constant boundary elements. The choice of this grid is based on the grid refinement study conducted for the case when $Ha = 50$, $Ra = 10^5$ and $n = 3$ in order to determine the appropriate grid size required for the optimal relationship between computational cost and numerical accuracy. The results are visualized in terms of $|\Psi|_{max}$, $|\theta|_{max}$ and the average Nusselt number $\overline{Nu}$ along the hot wall. Figure 18.2 displays that the grid of $N \approx 350$ boundary elements ensures the grid independence, and hence is used in the subsequent computations. Furthermore, in order to assess the validity of our numerical procedure, we have tested our algorithm for the mixed convection flow in a lid-driven cavity with a heated wavy bottom wall of three undulation given in the work of Amiri et al. [11]. It is observed that the present results $\Psi_{min} = -0.0928, -0.1351, -0.2997$ and $\overline{Nu} = 7.4325, 3.1515, 2.6646$ respectively at $Ri = 0.01, 1, 10$ are in good agreement with the numerical results of Al-Amiri et al. [11] $\Psi_{min} = -0.0919, -0.1278, -0.2564$ and $\overline{Nu} = 7.9331, 3.2711, 2.7192$ (calculated from the formula (18) given in [11]), respectively at $Ri = 0.01, 1, 10$.

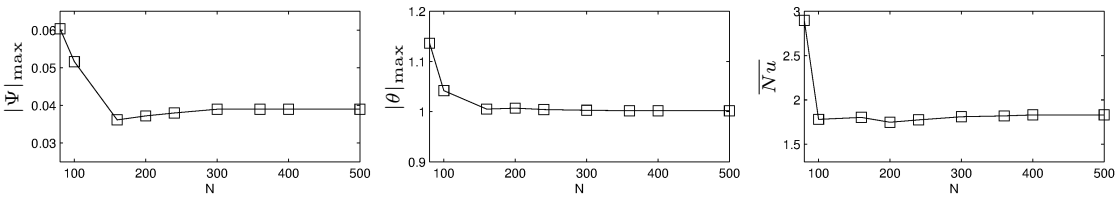

Figure 18.2: Grid dependency for $Ra = 10^5$, $Ha = 50$, $n = 3$

Figure 18.3 and 18.4 visualize the influence of Hartmann and Rayleigh numbers on the streamlines and isotherms, respectively, when the number of undulation $n = 3$. In the conduction case at $Ra = 10^3$, a clockwise rotating (negative) vortex in streamlines is formed along the vertical left wall due to its motion from bottom to top for each $Ha = 0$, 25, 50. However, the core of this vortex becomes weaker and extends vertically along the left wall as Ha increases. For higher values of Ra, the negative vortex extends vertically taking a more elliptical shape and it shrinks towards the left wall and finally it vanishes at $Ra = 10^6$, following the formation of a positive vortex in front of the heater at each Ha. The positive vortex extends towards the left wall and flow becomes dominated by this circulation as Ra increases at each Ha. The core of positive vortex extends vertically as Ha increases and it tends to become diagonal and finally horizontal as Ra increases. Moreover, the strength of the Ψ decreases as Ha increases due to the retarding effect of the magnetic field on the fluid flow, while it increases at higher values of Ra. On the other hand, the isotherms distribute uniformly in the cavity displaying almost similar behavior for each Ha at low values of Ra($= 10^3$ and 10^4) when the heat transfer is due to the conduction. By increase the buoyant force via increasing Ra, the flow becomes convection dominated. As a result, isotherms change their profiles from being vertical to almost horizontal on the center of the cavity forming a thermal boundary layer along the vertical walls as Ra increases. However, Ha has an opposite effect on isotherms, that is, the isotherms tend to go from horizontal to vertical (especially at $Ra = 10^5$) indicating the suppression of convective flow at higher Ha.

The effect of the shape of the wavy hot wall determined with different number of undulation is analyzed in terms of the variation of average Nusselt number $\overline{Nu}$ on the right hot wall with

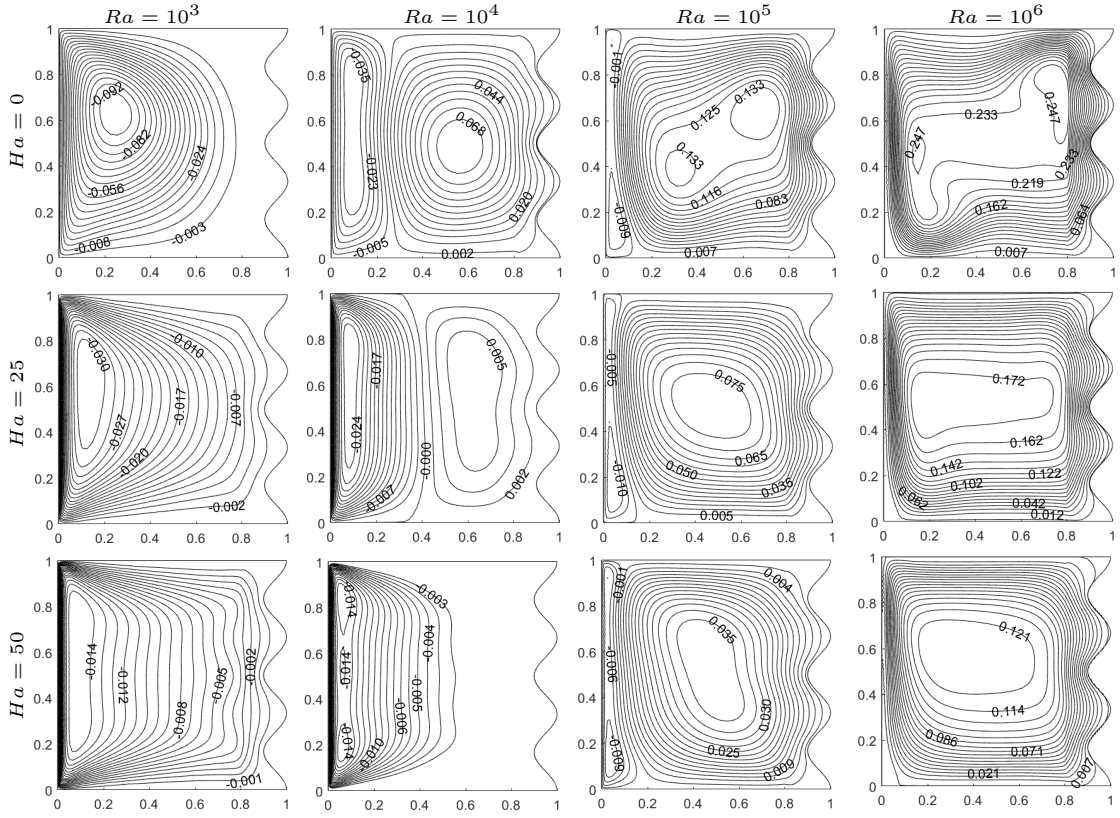

Figure 18.3: Effects of Ha and Ra numbers on streamlines at $n = 3$.

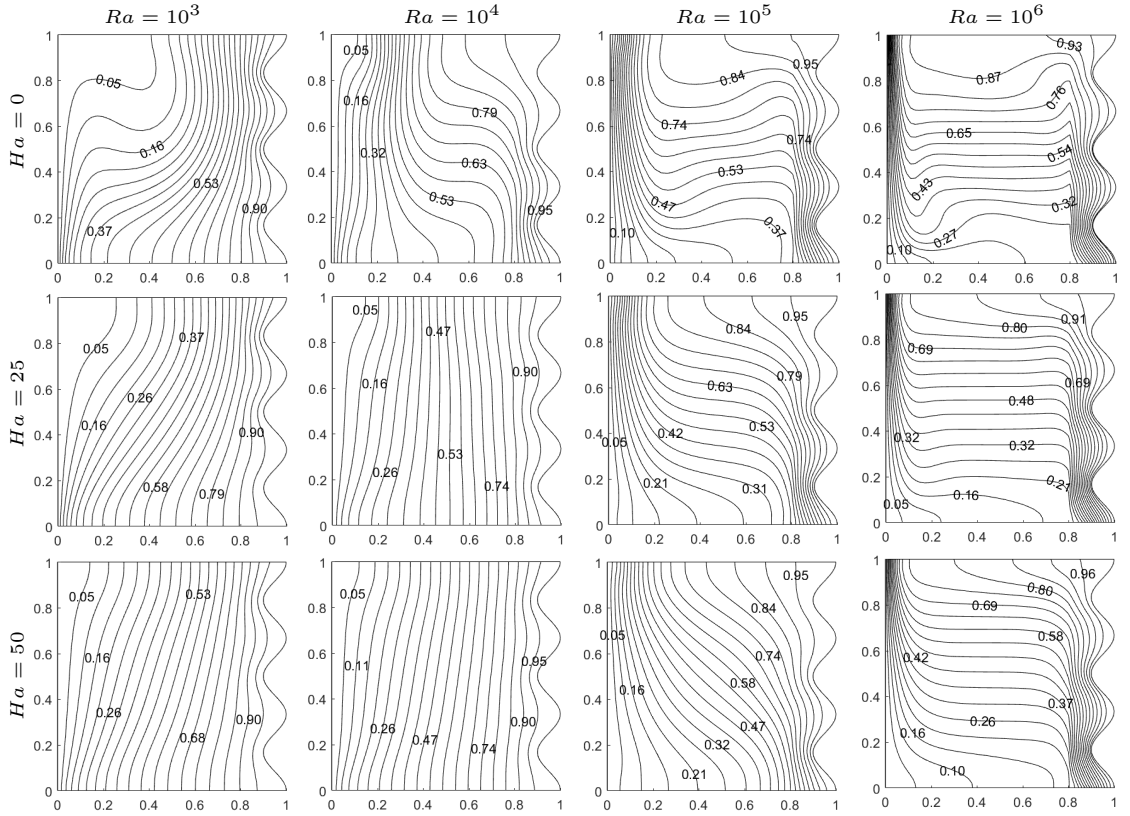

Figure 18.4: Effects of Ha and Ra numbers on isotherms at $n = 3$.

Hartmann and Rayleigh numbers. The average Nusselt number $\overline{Nu}$ along the hot wavy wall is evaluated by $\overline{Nu} = \frac{1}{S}\int Nu\, ds$ where $Nu = -S(\partial\theta/\partial n)$ is the local Nusselt number, S is the length of the wavy surface and s shows the integral calculated along the wavy line. The effect of the number of undulation n on the average Nusselt number at different values of Ra is shown in Figure 18.5 (a) $Ha = 0$, (b) $Ha = 10$, (c) $Ha = 25$, (d) $Ha = 50$. At each Ha, the $\overline{Nu}$ is increasing as Ra increases from $Ra = 10^4$ to 10^6 for all n since the heat transfer becomes dominated by convection for higher values of Ra. However, $\overline{Nu}$ decreases slightly when the flow is transferred from the conducting regime (i.e. $Ra = 10^3$) to the transition regime (from conduction to convective) at $Ra = 10^4$ regardless of the values of Ha and n. Moreover, the number of undulation has no significant effect on $\overline{Nu}$ at $Ra = 10^4$. It is well observed that, an increase in the number of undulation results in an increase in $\overline{Nu}$ at each Ha and Ra numbers, except at $Ra = 10^5$ when $Ha \geq 25$. That is, at $Ra = 10^5$ for high values of Ha ($Ha \geq 25$) the average Nusselt number decreases as n increases from $n = 2$ to $n = 3$, which indicates reduction of heat transfer inside the cavity. This results shows that at $Ra = 10^5$ the magnetic field of specific intensity plays a significant role in the heat transfer enhancement in the cavities with a wavy surface determined by various numbers of undulation.

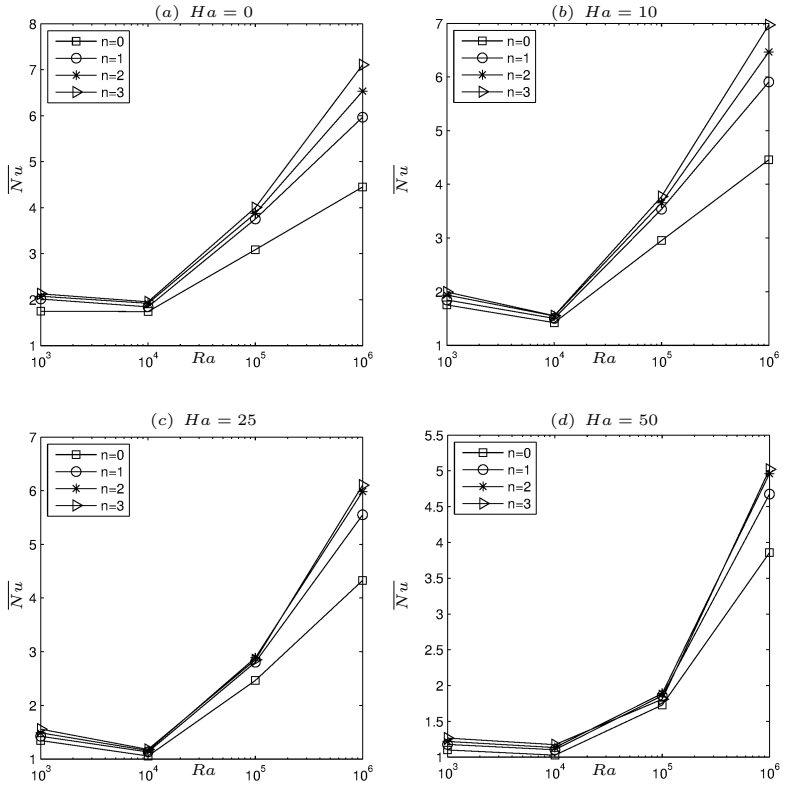

Figure 18.5: Variation of average Nusselt number with Rayleigh number at different numbers of undulation $n(= 0,\ 1,\ 2,\ 3)$ when (a) $Ha = 0$, (b) $Ha = 10$, (c) $Ha = 25$, (d) $Ha = 50$.

In Figure 18.6, the variation of average Nusselt number on the right wavy wall with Hartmann and Rayleigh numbers are shown for the cavity with a right wavy wall of $n = 3$ undulations. The average Nusselt number decreases as Ha increases at all Ra. Moreover, the rate of decrease in $\overline{Nu}$ increases with an increase in Ra. On the other hand, $\overline{Nu}$ increases as Ra increases from $Ra = 10^4$ to $Ra = 10^6$ at each Ha since the heat transfer is due to the convection. However, as mentioned before as Ra increases from $Ra = 10^3$ to $Ra = 10^4$, the $\overline{Nu}$ decreases especially for $Ha \geq 10$. The reason for this phenomena is that at $Ra = 10^4$, namely at the transition regime from conduction to convection, the buoyancy force is not strong enough to resist the magnetic field, and hence the heat transfer rate reduces.

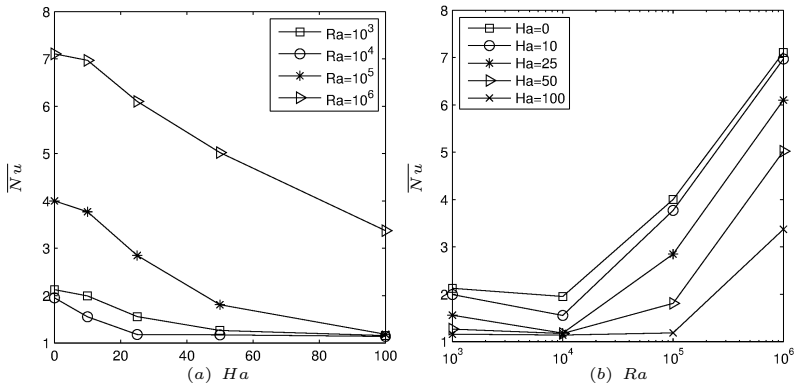

Figure 18.6: Effects of (a) Hartmann and (b) Rayleigh numbers on average Nusselt number at $n = 3$.

18.5 Conclusions

Mixed convection heat transfer in a lid driven cavity with a wavy hot right wall under the effect of a uniform horizontal magnetic field is solved numerically for various values of physical parameters. The governing equations are discretized using the DRBEM with appropriate number of constant boundary elements. The present results reveal that the flow behavior and the heat transfer enhancement are strongly affected by the presence of magnetic field and the shape of the cavity determined by various numbers of undulation along the hot right wall. The Hartmann and Rayleigh numbers have opposite effects on the flow and heat transfer rate. That is, the flow strength and the heat transfer rate increases as Ra increases (when $Ra \geq 10^4$), while they decrease for higher Hartmann numbers at fixed number of undulation. It is also observed that the heat transfer generally enhances with an increase in the number of undulation along the hot wall (except the case when $Ra = 10^5$, $Ha \geq 25$ as n increases from $n = 2$ to $n = 3$). Therefore, the lid-driven cavity with wavy wall of more undulations can be considered as an effective heat transfer mechanism at low Hartmann numbers.

References

[1] C. A. Brebbia, P. W. Patridge and L. C. Wrobel, *The Dual Reciprocity Boundary Element Method*, Computational Mechanics Publications, Southampton, Boston, 1992.

[2] S. Sivasankaran, A. Malleswaran, J. Lee and P. Sundar, *Hydro-magnetic combined convection in a lid-driven cavity with sinusoidal boundary conditions on both sidewalls*, Int. J. Heat Mass Transfer, 54 (2011), 512–525.

[3] A. C. Chamka, *Hydromagnetic combined convection flow in a vertical lid-driven cavity with internal generation or absorption*, Numer. Heat Transfer, Part A, 41 (2002), 529–546.

[4] F. Selimefendigil, H. F. Öztop, *MHD mixed convection and entropy generation of power law fluids in a cavity with a partial heater under the effect of a rotating cylinder*, Int. J. Heat Mass Transfer, 98 (2016), 40–51.

[5] B. Ghasemi, S. M. Aminossadati, *Comparison of mixed convection in a square cavity with an oscillating versus a constant velocity wall*, Numer. Heat Transfer, Part A, 54 (2008), 726–743.

[6] M. M. Rahman, H. F. Öztop, N. A. Rahim, N. A. Saidur and K. Al-Salem, *MHD mixed convection with Joule heating effect in a lid-driven cavity with a heated semi-circular source using the finite element technique*, Numer. Heat Transfer, Part A, 60 (2011), 543–560.

[7] L. Adjlout, O. Imine, A. Azzi, M. Belkadi, *Laminar natural convection in an inclined cavity with a wavy wall*, Int. J. Heat Mass Transfer, 45 (2002), 2141–2152.

[8] A. Misirlioğlu, A. C. Baytas, I. Pop, *Free convection in a wavy cavity filled with a porous medium*, Int. J. Heat Mass Transfer, 48 (2005), 1840–1850.

[9] P. K. Das, S. Mahmud, *Numerical investigation of natural convection inside a wavy enclosure*, Int. J. Therm. Sci., 42 (2003), 397–406.

[10] C. C. Wang and C. K. Chen, *Forced convection in a wavy wall channel*, Int. J. Heat Mass Transfer, 45 (2002), 2587–2595.

[11] A. Al-Amiri, K. Khanafer, J. Bull, I. Pop, *Effect of sinusoidal wavy bottom surface on mixed convection heat transfer in a lid-driven cavity*, Int. J. Heat Mass Transfer, 50 (2007), 1771–1780.

[12] S. Mekroussi, D. Nehari, Mohamed Bouzit, N. S. Chemloul, *Analysis of mixed convection in an inclined lid-driven cavity with a wavy wall*, J. Mech. Sci. Technol., 27 (7) (2013), 2181–2190.

[13] R. Nasrin and S. Parvin, *Hydromagnetic effect on mixed convection in a lid-driven cavity with sinusoidal corrugated bottom surface*, Int. Commun. Heat Mass Transfer, 38 (2011), 781–789.

Chapter 19

Adaptive time-stepping for surfactant-laden drops

Sara Pålsson, Chiara Sorgentone and Anna-Karin Tornberg

KTH Mathematics, Linné Flow Centre/Swedish e-Sceince Research Centre
100 44 Stockholm
Sweden

Abstract. *An adaptive time-stepping scheme is presented aimed at computing the dynamics of surfactant-covered deforming droplets. This involves solving a coupled system, where one equation corresponds to the evolution of the drop interfaces and one to the surfactant concentration. The first is discretised in space using a boundary integral formulation which can be treated explicitly in time. The latter is a convection-diffusion equation solved with a spectral method and is advantageously solved with a semi-implicit method in time. The scheme is adaptive with respect to drop deformation as well as surfactant concentration and the adjustment of time-steps takes both errors into account. It is applied and demonstrated for simulation of the deformation of surfactant-covered droplets, but can easily be applied to any system of equations with similar structure. Tests are performed for both 2D and 3D formulations and the scheme is shown to meet set error tolerances in an efficient way.*

19.1 Introduction

Simulation of micro-scale deforming droplets is a contemporary issue of increasing interest. One reason for this is the development of miniaturised equipment in the chemical and biological industries. At these small scales, the fluid flow is dominated by viscous forces, i.e. the Reynolds number is small. The flow can therefore be modelled by the linear Stokes equations which are quasi static. Furthermore, the surface to volume ratio is large and surface tension forces have a significant affect on droplet deformation.

Surface active agents (surfactants) are molecules which alter the surface tension of a droplet interface. The addition of surfactants can therefore significantly modify the dynamics of the droplet deformation [3, 12]. Surfactant-laden droplets are relevant to a range of applications, for example: creating drops through tip-streaming, preventing drop coalescence, and promoting/preventing droplet breakup [19]. This study considers insoluble surfactants, which exist only on the droplet interfaces and are not exchanged with the bulk-fluid.

As demonstrated in [3, 9, 13, 15], droplet deformation can be simulated using boundary integral methods (BIM). Other approaches include using level set methods to represent the interface coupled with an immersed interfaces method [21] or a finite element solver [5] for the fluid equations. Similarly, the surfactant convection-diffusion (C-D) equation on the droplet

interfaces can be treated with spectral methods [10] or finite element methods [7], among others. This study uses a BIM for the droplet deformation, coupled with a spectral method for the surfactant evolution.

An adaptive time-stepping method, specifically designed for simulating the deformation of surfactant-covered droplets, is presented. The BIM used to compute the flow velocity is a highly accurate method in space and in order to appropriately match the spatial and temporal errors, an adaptive time-stepping scheme is favourable. Due to the use of a BIM, there is only a first-order constraint on the time-step for the drop evolution. The time-discretisation to capture the dynamics of drop evolution is therefore straightforward and can be done with an explicit method, e.g. an explicit Runge-Kutta method (RK). To solve the C-D equation for the surfactant concentration is typically more involved due to the diffusion, which makes the equation stiff. One option is to use a high-order semi-implicit Runge-Kutta method ($IMEXRK$) [1], as in [10]. Another approach is to use a lower order scheme, such as Crank-Nicholson [3] or spectral deferred correction (SDC) methods [11].

To the knowledge of the authors, no adaptive schemes considering *both* surfactant concentration and drop deformation have been reported. This study develops an adaptive time-stepping scheme, capable of fulfilling the demands of a coupled system. The adaptivity is extended to both drop deformation and surfactant concentration, with the aim of minimising the number of Stokes evaluations needed. The scheme (a combination of an RK scheme for the drop evolution together with an $IMEXRK$ scheme for the surfactant concentration) is applied and demonstrated for the system of equations specific to the deformation of surfactant-covered droplets. However, it can easily be applied to any system of equations which couples an expensive BIM part and a C-D equation. It is demonstrated that the adaptive scheme may be applied to both 2D and 3D formulations.

This paper is organised as follows: in Section 19.2 the governing equations of droplet deformation and surfactant evolution are formulated; Section 19.3 describes the numerical method for time integration; examples and results are presented in Section 19.4.

19.2 Formulation

The problem motivating this study, which is also used to demonstrate results and comparisons, is the solution of Stokes equations for surfactant-covered deformable drops both in 2D and 3D. An example of a pair of deforming drops in a linear shear flow can be seen in Fig. 19.1. A brief explanation of this problem follows here, for more details see e.g. [15].

To obtain the velocity $\mathbf{u}$ with which to move the drop interfaces Γ, the Stokes equations are solved, here in non-dimensional form:

$$\begin{aligned} \Delta \mathbf{u}_0 &= \nabla p_0, \quad \nabla \cdot \mathbf{u}_0 = 0, \quad \text{for } \mathbf{x} \in \Omega_0, \\ \lambda_k \Delta \mathbf{u}_k &= \nabla p_k, \quad \nabla \cdot \mathbf{u}_k = 0, \quad \text{for } \mathbf{x} \in \Omega_k, \end{aligned} \tag{19.1}$$

where Ω_0 is the domain surrounding the drops and Ω_k the domain inside the drop k. Furthermore, the boundary condition on the drop interfaces is

$$(p_0 - p_k)\,\mathbf{n} + (\mathbf{e}_0 - \lambda_k \mathbf{e}_k) \cdot \mathbf{n} = \sigma \kappa \mathbf{n} - \nabla_s \sigma \text{ for } \mathbf{x} \in \Gamma, \tag{19.2}$$

which is a balance of the normal stresses. Here, $\lambda_k = \frac{\mu_k}{\mu_0}$ is the ratio of viscosity between the inner and outer fluids, p_k, p_0 pressure inside and outside the drops, $\mathbf{e}_k$, $\mathbf{e}_0$ strain tensors, κ mean curvature, $\mathbf{n}$ normal and σ surface tension coefficient. The interface is evolved in time by

$$\frac{d\mathbf{x}}{dt} = \mathbf{u}(\mathbf{x}, t), \text{ for } \mathbf{x} \in \Gamma. \tag{19.3}$$

The concentration, ρ, of insoluble surfactants on the interfaces Γ is described by the C-D equation

$$\frac{\partial \rho}{\partial t} = \frac{d\mathbf{x}}{dt} \cdot \nabla_s \rho - \nabla_s \cdot (\rho \mathbf{u}_s) - \rho \kappa u_n + \frac{1}{\mathrm{Pe}_\Gamma} \nabla_s^2 \rho, \tag{19.4}$$

see [18] for further details. Here, Pe_Γ is the Péclet number, $\mathbf{u}_s = \mathbf{u} - \mathbf{n}\,(\mathbf{u} \cdot \mathbf{n})$ and $u_n = \mathbf{u} \cdot \mathbf{n}$. In both the surfactant equation and interface condition, $\nabla_s = \nabla - \mathbf{n}\,(\mathbf{n} \cdot \nabla)$ is the surface gradient operator. Surfactant concentration ρ and velocity $\mathbf{u}$ are coupled through an equation of state. This study uses the linear equation of state

$$\sigma = 1 - E\rho, \tag{19.5}$$

where E is the so-called elasticity number. Different equations of state can be used, see [14] for further discussion. The diffusion term in (19.4) is preferably treated implicitly, as it is stiff and linear. The convection term, however, is non-stiff but non-linear and therefore difficult to solve implicitly. It is then advantageous to split the right hand side of the C-D equation (19.4) into two parts, treating the convection explicitly and the diffusion implicitly in time, i.e.

$$\frac{\partial \rho}{\partial t} = f_E + f_I, \text{ where } \begin{cases} f_E\,(\rho, \mathbf{u}, \mathbf{x}, t) = \frac{d\mathbf{x}}{dt} \cdot \nabla_s \rho - \nabla_s \cdot (\rho \mathbf{u}_s) - \rho \kappa u_n, \\ f_I\,(\rho, \mathbf{x}, t) = \frac{1}{\mathrm{Pe}_\Gamma} \nabla_s^2 \rho. \end{cases} \tag{19.6}$$

Although the time-stepping scheme was developed with surfactant-laden deforming drops as its focus, it can be applied to a variety of equations of a similar structure. In general terms, the aim of this paper is to find a good time-stepping scheme for the coupled system

$$\begin{cases} \frac{d\mathbf{x}}{dt} = \mathbf{u}\,(\mathbf{x}(t), \rho(t))\,, \\ \frac{d\rho}{dt} = f\,(\rho, \mathbf{u}, \mathbf{x}, t)\,, \end{cases} \tag{19.7}$$

corresponding to (19.3) and (19.4). Furthermore, the scheme must handle splitting of the function f in (19.7) into parts for implicit and explicit treatment, as is the case of (19.6). The explicit function f_E may be non-linear, and both f_E and f_I contain spatial derivatives.

In the following, it is assumed that an adequate spatial discretisation, $\mathbf{x}_h$, exists to compute both $\mathbf{u}_h$ and ρ_h to high accuracy for any time t.

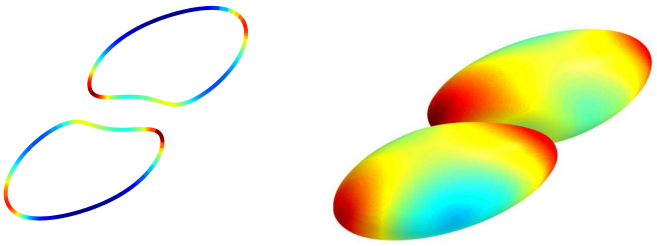

Figure 19.1: Deforming drops in 2D (left) and 3D (right), with concentration of insoluble surfactants in colour.

19.3 Numerical method

Given the formulation described in Section 19.2 $\mathbf{x}_h^i$ and ρ_h^i are computed at each time t_i. A BIM is used for computing $\mathbf{u}(\mathbf{x}_h^i, \rho_h^i, t_i)$, see [15] for a complete formulation. In the 2D case, the Sherman-Lauricella formulation of the BIM for Stokes equations [9] is used together with an

interpolatory special quadrature to evaluate the integrals when they are nearly-singular (close drop interactions) [13]. The surfactant equation (19.4) is solved in space with a pseudo-spectral collocation method. This is a spectrally accurate method, as the interface is one-dimensional and periodic and the discretisation equidistant with respect to arc length. In the 2D case, treating the implicit term f_I is trivial, since the surface Laplacian operator for the diffusion term has an explicit spectral representation. The convection term includes non-linear terms, thus zero-padding is needed to prevent aliasing.

The problem in 3D is more complicated and expensive to solve: it has an increased number of degrees of freedom, methods for keeping the point distribution optimal become much more expensive and the specialised quadrature methods for singular (self-self interaction) and nearly-singular integrals are different. An accurate discretisation of the drops' surfaces and surfactant concentration in 3D is based on Spherical Harmonic Expansion [2, 17]; the special quadrature needed for singular integrals uses analytical properties of the Spherical Harmonics [4], whilst the nearly-singular quadrature is based on an interpolation technique, adapting and optimising an approach proposed by [22]. In 3D, to compute the implicit part of a time-step for the surfactant evolution (19.4) involves solving a system $Ay = b$, where $y = \rho_h^{i+1}$ and $A = I - dt\frac{1}{\mathrm{Pe}}\nabla_s^2$. In practice this will be solved with a spectral method for the spherical harmonic coefficients.

For both the 2D and 3D case, each BIM computation is significantly more expensive than solving the C-D equation for the surfactants. To minimise computational costs, it is therefore necessary to reduce the number of BIM evaluations whilst also maintaining error levels below a desired threshold. The system (19.7) is spatially resolved with a high fidelity, using a method of lines approach.

In the example case presented (Stokes flow) the drop evolution described by (19.3) can be solved explicitly in time. Three Runge-Kutta schemes are investigated: explicit midpoint (*RKMID*, 2nd order), Kutta's method (*RK3*, 3rd order) and Bogacki-Shampine (*RKBS*, 3rd order). All three are made adaptive by comparing to a lower order scheme, see their Butcher tableaux in Table 19.1.

RKMID
(Explicit midpoint, 2nd order)

0		
1/2	1/2	
	0	1
	1	0

RKBS
(Bogacki-Shampine, 3rd order)

0				
1/2	1/2			
3/4	0	3/4		
1	2/9	1/3	4/9	
	2/9	1/3	4/9	
	7/24	1/4	1/3	1/8

RK3
(Kutta's method, 3rd order)

0			
1/2	1/2		
1	−1	2	
	1/6	4/6	1/6
	0	1	

Table 19.1: Butcher tableaux for explicit schemes for $\mathbf{x}$.

The variables $\mathbf{x}$ and ρ depend on each other through the surface tension described by (19.5). How the equations are coupled determines which schemes for ρ are applicable. There are several ways of coupling equations: for example through Strang splitting [20], by using an SDC approach [11] or by using Runge-Kutta methods with the same stages for both equations. Strang splitting consists of solving one equation with half a time-step twice, and the other with one whole time-step. Generally, these two half time-steps can be collapsed into one whole, thus increasing the efficiency of the scheme, but for adaptive time-steps this is not the case. The benefit of Strang splitting is that it leaves the choice of scheme for ρ free, as it is computed independently of the scheme of $\mathbf{x}$. As it is second order, using higher order methods for $\mathbf{x}$ and ρ will not increase the overall order of the scheme.

Following the approach by [16], where an adaptive *SDC* scheme was used to simulate vesicles, the authors tried to employ a similar method. However, it became computationally expensive in comparison to the other schemes investigated to achieve higher order for the specific coupled problem in this study.

When coupling two Runge-Kutta methods with the same stages, it is possible to interchange information between the equations at each stage. This will give the overall method the order of the lowest-order scheme used in the coupling. However, this adds the constraint that the two equations in (19.7) must be treated with similar methods. This splitting is referred to as stage-splitting.

Implicit midpoint (2^{nd} order)

0		
1/2	0	1/2
	0	1

Explicit midpoint (2^{nd} order)

0		
1/2	1/2	
	0	1

Table 19.2: Butcher tableaux for *IMEX2* scheme for ρ. Implicit midpoint used for f_I and explicit midpoint for f_E.

Equation (19.4) is solved using an implicit-explicit Runge-Kutta method (*IMEXRK*), see [1]. The *IMEXRK* schemes exist in different orders, for this study a second order (*IMEX2*) scheme is used. This scheme consists of an implicit midpoint rule for f_I and an explicit midpoint rule for f_E, as shown in Table 19.2. The benefit of this scheme is that it uses the same stages as both *RKMID* and *RK3*, making both Strang splitting and stage-splitting applicable. Whilst possible to use higher order *IMEXRK* schemes, this proves impractical as the stages increase in complexity and can no longer easily be matched with the schemes for $\mathbf{x}$ in stage-splitting. Moreover, Strang splitting is not suitable, as the splitting itself is only second order.

How to couple *IMEX2* with an explicit scheme from Table 19.1 through stage-splitting is shown in Fig. 19.2 for the *RKMID+IMEX2* case. The coupling for *RK3+IMEX2* follows similarly. The *RKBS* scheme, however, has an additional stage at $t_{i+3/4}$, for which $\rho_h^{i+3/4}$ is needed. To obtain this stage an additional semi-implicit time-step from $\rho_h^{i+1/2}$ to $\rho_h^{i+3/4}$ is taken. Note that every semi-implicit time-step for ρ_h will boil down to solving a linear system. The cost of this depends on the nature of f_I, but will in general be cheaper than a BIM evaluation.

For the scheme to be adaptive, the local errors of both $\mathbf{x}_h^{i+1}$ and ρ_h^{i+1} are measured. For $\mathbf{x}$ the standard approach of comparing to a lower order scheme $\tilde{\mathbf{x}}_h^{i+1}$ is used, since this does not need extra evaluations, as shown in Table 19.1. For ρ, one option is to use a similar approach and compare to a first order *IMEXRK* (*IMEX1*) approximation, $\tilde{\rho}_h^{i+1}$, referred to as *IMEX1*-adaptivity. Another option is to use a constraint on ρ, in the case of insoluble surfactants the mass must be conserved on the interface, i.e.

$$\frac{d}{dt}\left(\int_{\Gamma(t)} \rho(t) dS\right) = 0.$$

This can be used to approximate a local error in conservation of mass, the change in mass between time-steps, and is referred to as conservation-adaptivity. Although not applicable to all systems, such constraints are common in the case where the second equation in (19.7) corresponds to a C-D equation in an isolated system.

The total error of a time-step $i+1$ is computed as

$$r^{i+1} = \max\left(\frac{\|\mathbf{x}_h^{i+1} - \tilde{\mathbf{x}}_h^{i+1}\|_\infty}{\|\mathbf{x}_h^{i+1}\|_\infty},\ r_\rho^{i+1}\right),$$

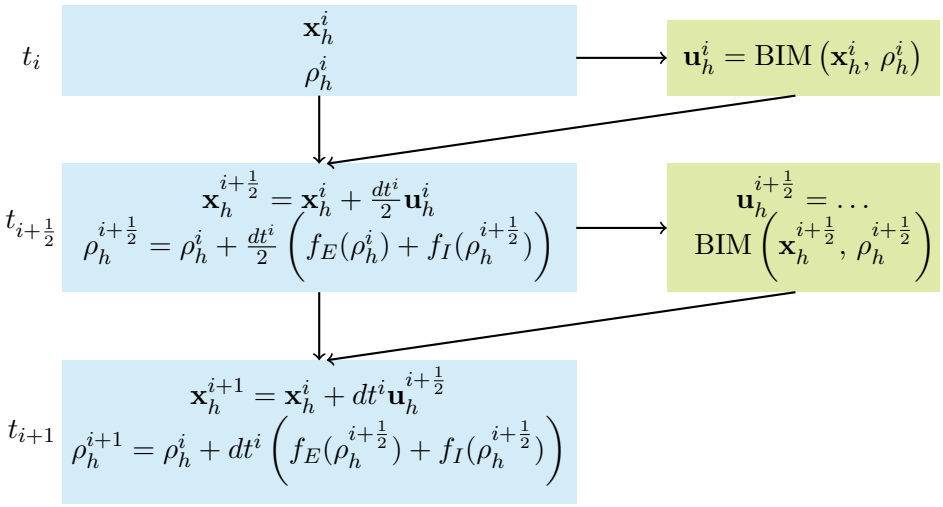

Figure 19.2: Schematic over *RKMID+IMEX2* scheme.

where either $r_\rho^{i+1} = \frac{\|\rho_h^{i+1} - \tilde{\rho}_h^{i+1}\|_\infty}{\|\rho_h^{i+1}\|_\infty}$ or $r_\rho^{i+1} = \frac{|\int_{\Gamma^{i+1}} \rho_h^{i+1} dS - \int_{\Gamma^i} \rho_h^i dS|}{|\int_{\Gamma^i} \rho_h^i dS|}$. If r^{i+1} is larger than a set tolerance, tol, the time-step $t_i \to t_{i+1}$ will be retaken with a smaller time-step size. This new time step, dt_{new}^i, is chosen using the fact that $r_{i+1} = O(dt^2)$ since $\tilde{\mathbf{x}}_h^{i+1}$ and $\tilde{\rho}_h^{i+1}$ are evaluated using first order methods. Thus, as the new time-step is required to meet the set tolerance, i.e. $r_{new}^{i+1} < tol$,

$$\left(\frac{dt_{new}^i}{dt^i}\right)^2 \approx \frac{tol}{r^{i+1}},$$

which in turn gives

$$dt_{new}^i = dt^i \cdot \left(0.9\frac{tol}{r^{i+1}}\right)^{\frac{1}{2}}. \tag{19.8}$$

Here, 0.9 is a safety factor to ensure dt_{new}^i sufficiently small [6]. Moreover, after each successful time-step, the next time-step size dt will be updated with the same formula.

It is important not to measure the time-step error too conservatively, i.e. taking too small time-steps, as this will mean a lot of extra work to reach an accuracy not requested. A good estimate should generate a solution which is close to the set tolerance in error.

19.4 Results

The different schemes included in this investigation are: 1. *RKMID+IMEX2* with Strang splitting, 2. *RKMID+IMEX2* with stage-splitting, 3. *RK3+IMEX2* with stage-splitting and 4. *RKBS+IMEX2* with stage-splitting. The schemes will be investigated using both *IMEX1*-adaptivity and conservation-adaptivity for the second equation in (19.7) together with the standard lower order scheme comparison for the first.

Results and comparisons of the methods are demonstrated by studying one drop with viscosity ratio $\lambda = 1$ in a linear shear flow, $\mathbf{u}_\infty = G\,(0, x_2)$, $G = 0.2$. The drop is initially an ellipse/ellipsoid with aspect ratio 2. The results are in agreement for both initially uniform and non-uniform ρ. The simulations are run to time $T = 1$. All errors are computed in the max norm against a reference solution $(\mathbf{x}_{ref}, \rho_{ref})$, which is computed with a fixed time-step

$dt = 10^{-5}$ *RKMID+IMEX2* scheme. The spatial discretisation is accurate enough for the time error to dominate in all simulations.

Despite the different methods used in the 2D and 3D cases respectively, computing $\mathbf{u}_h^i$ dominates the computational cost in both. However, whilst in 2D each *IMEX* computation is cheap, in 3D it involves solving a linear system. Therefore, for 3D it becomes more important to minimise the number of *IMEX* evaluations than in 2D.

First, the performance of the schemes in 2D is investigated by studying the order of the schemes when keeping the size of time-steps constant. The interface errors, compared to $\mathbf{x}_{ref}$, are shown in Fig. 19.3 (left). All four schemes are second order in time, w.r.t. $\mathbf{x}$, despite *RK3*, *RKBS* being third order. This is not surprising, as they are coupled with a second order *IMEX2* scheme.

For a constant dt, *RKMID+IMEX2* gives a significantly larger error in $\mathbf{x}$ than the other three schemes and the splitting used does not affect the error. Contrary, for ρ the error is similar for all three schemes with stage-splitting, see Fig. 19.3 (left, solid lines) whilst Strang-splitting gives a slightly smaller error. The conservation error is the smallest for *RKMID+IMEX2* with stage-splitting. Taking the errors of both $\mathbf{x}$ and ρ into consideration, the schemes are all on the same

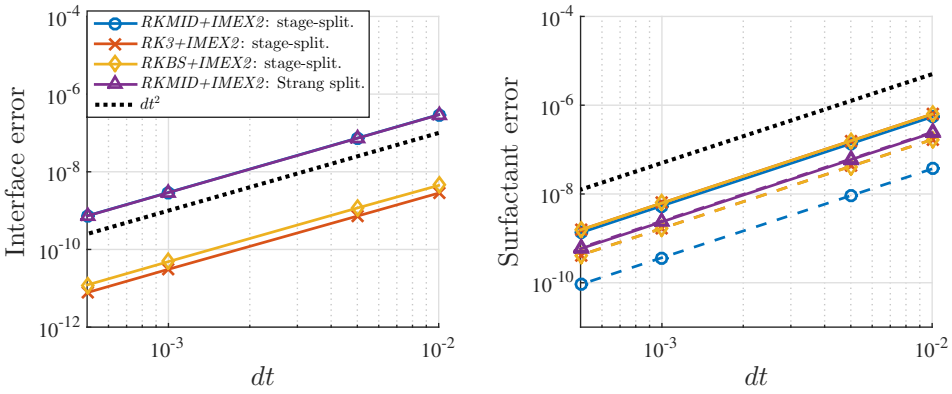

Figure 19.3: For fixed time-step sizes dt, max norm error in interface position (left) and max norm error in surfactant concentration (right, solid lines) and surfactant mass conservation (right, dashed lines) (in 2D).

level. Furthermore, the total number of Stokes evaluations needed for one time-step for each scheme is displayed in Table 19.3. The number of Stokes evaluations needed for the Strang splitting scheme is double that of *RK3*, *RKBS* and three times that of *RKMID*, all three with stage-splitting. This is due to the fact that the two $\frac{dt}{2}$ time-steps cannot be collapsed into one without a large overhead when considering an adaptive scheme. For the remainder of this study, only the schemes with stage-splitting will be investigated further, as they are much cheaper.

Scheme	Number of Stokes evaluations
Stage-splitting *RKMID+IMEX2*	2
Stage-splitting *RK3+IMEX2*	3
Stage-splitting *RKBS+IMEX2*	3
Strang splitting *RKMID+IMEX2*	6

Table 19.3: Number of Stokes evaluations for one time-step.

With regards to adaptivity, both *IMEX1*- and conservation-adaptivity is investigated, for

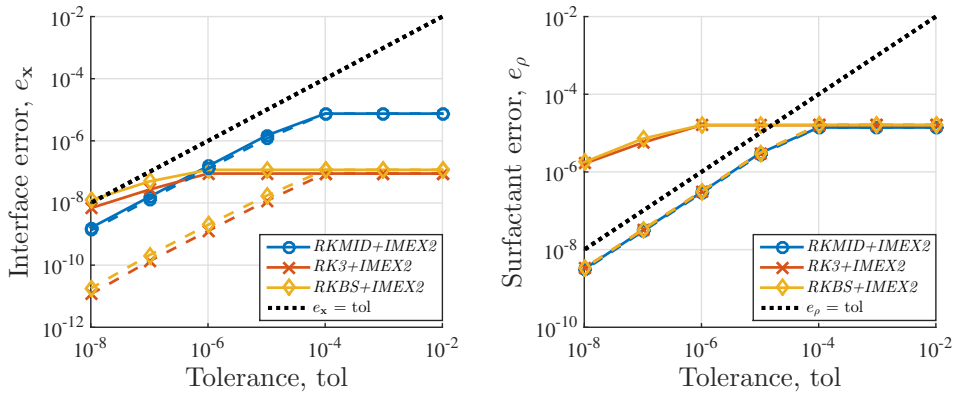

Figure 19.4: Error for interface and surfactants (max norm) with adaptive methods (2D). Dashed lines represent schemes with conservation-adaptivity, and solid lines *IMEX1*-adaptivity.

2D in Fig. 19.4 and 3D Fig. 19.5. For *RKMID+IMEX2* these two approaches do not differ significantly in error, neither for $\mathbf{x}$ nor ρ, as shown in Fig. 19.4. Moreover, at all times the errors are below the set tolerance. This is not the case for *RK3+IMEX2* and *RKBS+IMEX2*. With *IMEX1*-adaptivity, these schemes achieve an error almost three orders of magnitude below set tolerance for $\mathbf{x}$, whilst following the tolerance levels for ρ well. For conservation-adaptivity, *RK3+IMEX2* and *RKBS+IMEX2* do not meet the tolerance set for ρ, and can therefore be disregarded as possible schemes. All schemes show the same behaviour in both 2D and 3D. For all runs a maximum time-step size was set, which results in the flattening of the curves that can be seen in Fig. 19.4 and Fig. 19.5.

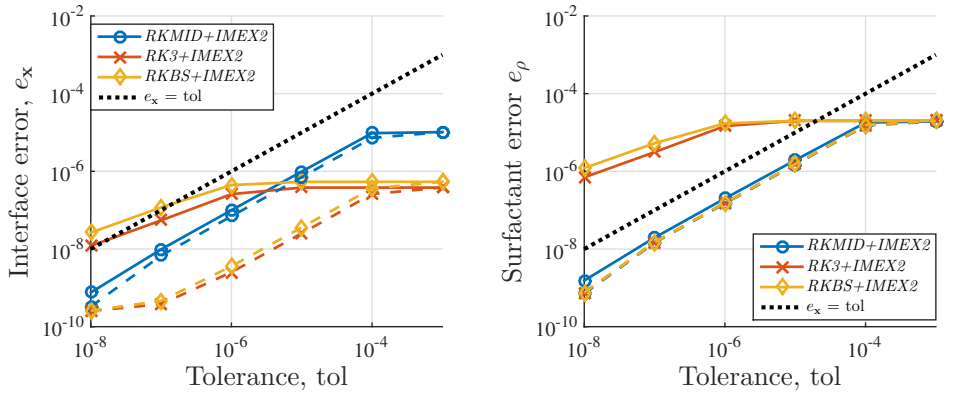

Figure 19.5: Error for interface and surfactants (max norm), 3D. Conservation-adaptivity represented by dashed lines and *IMEX1*-adaptivity by solid lines.

In Fig. 19.6 the cost as number of Stokes evaluations for each set tolerance is shown for both the 2D and 3D case. Here, *RK3+IMEX2* and *RKBS+IMEX2* with conservation-adaptivity are not considered since they do not meet the expected tolerances. Of the remaining schemes, *RKMID+IMEX2* is cheaper than the others, with either adaptivity option.

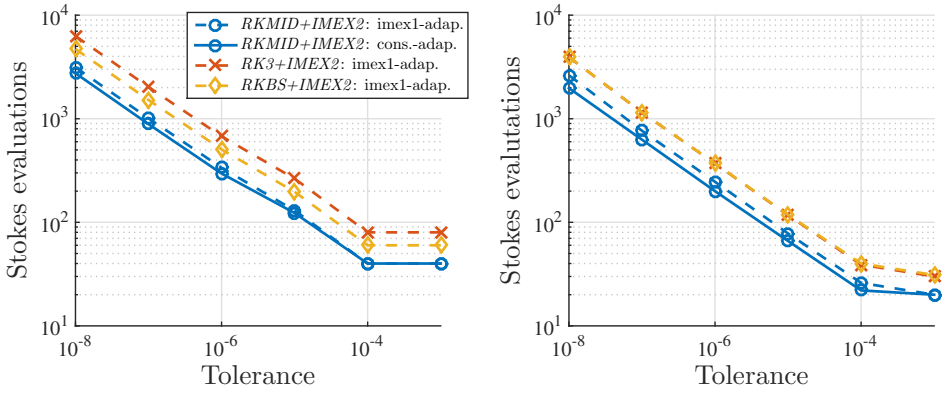

Figure 19.6: Number of Stokes evaluation of tolerance set, left: 2D, right: 3D.

19.5 Conclusions

In this study, several methods for time-stepping, coupling and controlling the temporal errors through adaptivity was investigated. The tests have been performed on a system of equations describing surfactant-covered deforming droplets in Stokes flow, but can generalised to any system of ODEs containing an expensive equation evaluated through a BIM together with a "cheaper" equation. Special care has been taken such that the second equation can be handled semi-implicitly in time, as is the case for the surfactant C-D equation.

For the drop evolution, second and third order explicit schemes have been considered, and for the surfactant concentration a semi-implicit Runge-Kutta scheme of second order is used. As the cost of each BIM evaluation is high, the aim of the scheme was to minimise the number of BIM computations while still meeting the set tolerance in both $\mathbf{x}$ and ρ. It is shown that Strang splitting introduces extra costs, compared to a stage-splitting approach.

The study contained two ways of measuring adaptivity. Whilst for *RKMID+IMEX2* the two approaches gave similar results, for *RK3+IMEX2* and *RKBS+IMEX2* conservation-adaptivity under-predicts the errors and *IMEX1*-adaptivity strongly over-predicts the error. Moreover, using *IMEX1*-adaptivity introduces an additional system to be solved each time-step for the surfactant concentration. Thus, the most cost-efficient scheme to meet the set error tolerances is the *RKMID+IMEX2* scheme with stage-splitting and conservation-adaptivity.

Acknowledgement

This work has been supported by the Göran Gustafsson Foundation for Research in Natural Sciences and Medicine and by the Knut and Alice Wallenberg foundation under grant no. 2013-0339.

References

[1] U. M. Ascher, S. J. Ruuth and R. J. Spiteri, *Implicit-explicit Runge-Kutta methods for time-dependent partial differential equations*, Applied Numerical Mathematics, 25(2-3) (1997), 151–167.

[2] K. Atkinson and W. Han, *Spherical harmonics and approximations on the unit sphere: an introduction* (Vol 2044), Springer Science & Business Media, 2012.

[3] I. B. Bazhlekov, P. D. Anderson and H. E. Meijer, *Numerical investigation of the effect of insoluble surfactants on drop deformation and breakup in simple shear flow*, Journal of Colloid and Interface Science, 298(1), (2006), 369–394.

[4] I. G. Graham and I. H. Sloan, *Fully discrete spectral boundary integral methods for Helmholtz problems on smooth closed surfaces in* $\mathcal{R}^3$, Numerische Mathematik, 92(2) (2002), 289–323.

[5] P. Hansbo, M. G. Larson and S. Zahedi, *A cut finite element method for a Stokes interface problem*, Applied Numerical Mathematics, 85 (2014), 90–114.

[6] E. Hairer, S.P. Nørsett and G. Wanner, *Solving Ordinary Differential Equations I, Nonstiff Problems*, Springer, Berlin, 1993.

[7] P. Hansbo, M. G. Larson and S. Zahedi, *Characteristic cut finite element methods for convection–diffusion problems on time dependent surfaces*, Computer Methods in Applied Mechanics and Engineering, 293 (2015), 431–461.

[8] S. Khatri and A. K. Tornberg, *A numerical method for two phase flows with insoluble surfactants*, Computers & Fluids, 49(1) (2011), 150–165.

[9] M. C. A. Kropinski, *An efficient numerical method for studying interfacial motion in two-dimensional creeping flows*, Journal of Computational Physics, 171(2) (2001), 479–508.

[10] M. C. A. Kropinski and E. Lushi, *Efficient numerical methods for multiple surfactant-coated bubbles in a two-dimensional Stokes flow*, Journal of Computational Physics, 230(12), (2011), 4466–4487.

[11] A. T. Layton and M. L. Minion, *Conservative multi-implicit spectral deferred correction methods for reacting gas dynamics*, Journal of Computational Physics, 194(2) (2004), 697–715.

[12] W. J. Milliken, H. A. Stone and L. G. Leal, *The effect of surfactant on the transient motion of Newtonian drops*, Physics of Fluids A: Fluid Dynamics, 5(1) (1993), 69–79.

[13] R. Ojala and A. K. Tornberg, *An accurate integral equation method for simulating multi-phase Stokes flow*, Journal of Computational Physics, 298 (2015), 145–160.

[14] Y. Pawar and K. J. Stebe, *Marangoni effects on drop deformation in an extensional flow: the role of surfactant physical chemistry. I. Insoluble surfactants*, Physics of Fluids, 8(7) (1996), 1738–1751.

[15] C. Pozrikidis, *Boundary integral and singularity methods for linearized viscous flow*, Cambridge University Press, Cambridge, UK, 1992.

[16] B. Quaife and G. Biros, *Adaptive time stepping for vesicle suspensions*, Journal of Computational Physics, 306 (2016), 478–499.

[17] A. Rahimian, S. K. Veerapaneni, D. Zorin and G. Biros, *Boundary integral method for the flow of vesicles with viscosity contrast in three dimensions*, Journal of Computational Physics, 298 (2015), 766–786.

[18] H. A. Stone, *A simple derivation of the time-dependent convective-diffusion equation for surfactant transport along a deforming interface*, Physics of Fluids A: Fluid Dynamics, 2(1) (1990), 111–112.

[19] H. A. Stone and L. G. Leal, *The effects of surfactants on drop deformation and breakup*, Journal of Fluid Mechanics, 220 (1990), 161–186.

[20] G. Strang, *On the construction and comparison of difference schemes*, SIAM Journal on Numerical Analysis, 5(3) (1968), 506–517.

[21] J. J. Xu, Z. Li, J. Lowengrub and H. Zhao, *A level-set method for interfacial flows with surfactant*, Journal of Computational Physics, 212(2) (2006), 590–616.

[22] L. Ying, G. Biros and D. Zorin, *A high-order 3D boundary integral equation solver for elliptic PDEs in smooth domains*, Journal of Computational Physics, 219(1) (2006), 247–275.

Chapter 20

Boundary elements and mesh refinements for the wave equation

David Stark[1] **and Heiko Gimperlein**[1,2]

[1] Maxwell Institute for Mathematical Sciences and Department of Mathematics,
Heriot-Watt University,
Edinburgh, EH14 4AS,
United Kingdom.

[2] Institut für Mathematik,
Universität Paderborn,
Warburger Str. 100,
33098 Paderborn,
Germany.

Abstract. *We discuss time domain boundary element methods for singular geometries, in particular graded meshes and adaptive mesh refinements. First, we discuss edge and corner singularities for a Dirichlet problem for the wave equation. Time independent graded meshes lead to efficient approximations, as confirmed by numerical experiments for wave scattering from screens. We briefly discuss adaptive mesh refinement procedures based on a posteriori error estimates. A modified MOT scheme provides an efficient preconditioner (or stand-alone solver) for the space-time systems obtained for the Galerkin discretisations.*

20.1 Introduction

Boundary element methods provide an efficient, extensively studied numerical scheme for time-independent or time-harmonic scattering and emission problems. Unlike finite element discretisations, they reduce the computation from the three dimensional domain to its two dimensional boundary. Recently, boundary elements have been explored for the simulation of transient phenomena, with applications e.g. to environmental noise [2] or electromagnetic scattering [9]. Galerkin time domain boundary element methods prove to be stable and accurate in long–time computations and are competitive with frequency domain methods for realistic problems [3].

Here we discuss recent work on adaptive mesh refinements and graded meshes for singular geometries, as motivated by the sound emission on tires [2].

20.2 Problem description and time domain BEM

We consider the wave equation outside a scatterer Ω^- in $\mathbb{R}^3$, where Ω^- is a bounded polygon or a screen with connected complement $\Omega = \mathbb{R}^3 \setminus \overline{\Omega^-}$. The acoustic sound pressure field u due to an incident field or sources on $\Gamma = \partial\Omega$ satisfies the linear wave equation for $(t, \mathbf{x}) \in \mathbb{R} \times \Omega$:

$$\partial_t^2 u(t,\mathbf{x}) - \Delta u(t,\mathbf{x}) = 0$$

with Dirichlet boundary conditions $u(t,\mathbf{x}) = f(t,\mathbf{x})$ for $\mathbf{x} \in \Gamma$, and $u(t,\mathbf{x}) = 0$ for $t \le 0$.

A single-layer ansatz for u,

$$u(t,\mathbf{x}) = \int_\Gamma \frac{\phi(t-|\mathbf{x}-\mathbf{y}|,\mathbf{y})}{4\pi|\mathbf{x}-\mathbf{y}|} ds_y, \tag{20.1}$$

results in an equivalent weak formulation as an integral equation of the first kind in space-time anisotropic Sobolev spaces [7, 3]:
Find $\phi \in H^1_\sigma(\mathbb{R}^+, \widetilde{H}^{-\frac{1}{2}}(\Gamma))$ such that for all $\psi \in H^1_\sigma(\mathbb{R}^+, \widetilde{H}^{-\frac{1}{2}}(\Gamma))$

$$\int_0^\infty \int_\Gamma (V\phi(t,\mathbf{x}))\partial_t\psi(t,\mathbf{x})\; ds_x\; d_\sigma t = \int_0^\infty \int_\Gamma f(t,\mathbf{x})\partial_t\psi(t,\mathbf{x})\; ds_x\; d_\sigma t\;, \tag{20.2}$$

where $d_\sigma t = e^{-2\sigma t} dt$ and

$$V\phi(t,\mathbf{x}) = \int_\Gamma \frac{\phi(t-|\mathbf{x}-\mathbf{y}|,\mathbf{y})}{4\pi|\mathbf{x}-\mathbf{y}|} ds_y\;.$$

A theoretical analysis requires $\sigma > 0$, but practical computations use $\sigma = 0$.

For the definition of the Sobolev spaces, we focus on the case where $\Gamma = \partial\Omega$. For $\sigma > 0$, $s, r \in \mathbb{R}$ the space $H^s_\sigma(\mathbb{R}^+, H^r(\Gamma))$ consists of distributions ϕ on $\mathbb{R}^+ \times \Gamma$, vanishing at $t = 0$, such that in local coordinates the space–time Fourier–Laplace transform $\mathcal{F}\phi$ satisfies

$$\|\phi\|_{s,r,\Gamma} = \left(\int\int |\omega + i\sigma|^{2s} (|\omega + i\sigma|^2 + |\xi|^2)^r |\mathcal{F}\phi(\omega + i\sigma, \xi)|^2 \; d\xi \; d\omega \right)^{\frac{1}{2}} < \infty\;.$$

For the case of a screen, where $\partial\Gamma \neq \emptyset$, more care is required to define spaces $H^s_\sigma(\mathbb{R}^+, \widetilde{H}^r(\Gamma))$ and $H^s_\sigma(\mathbb{R}^+, H^r(\Gamma))$ of distributions which vanish outside Γ, resp. which extend to a larger set. See for example [3] for a detailed discussion.

We study time dependent boundary element methods to solve (20.2), based on approximations by piecewise polynomial ansatz and test functions from the space $V^{p,q}_{h,\Delta t}$ spanned by

$$\phi_i(t,\mathbf{x}) = \widetilde{\Lambda}_i(t)\Lambda_i(\mathbf{x})\;. \tag{20.3}$$

Here, Λ_i a piecewise polynomial shape function of degree p in space and $\widetilde{\Lambda}_i$ a corresponding shape function of degree q in time. For $p \ge 1$, resp. $q \ge 1$, the shape functions are assumed to be continuous.

We obtain a numerical scheme for the weak formulation (20.2): Find $\phi_{h,\Delta t} \in V^{p,q}_{h,\Delta t}$ such that for all $\psi_{h,\Delta t} \in V^{p,q}_{h,\Delta t}$

$$\int_0^\infty \int_\Gamma \big(V\phi_{h,\Delta t}(t,\mathbf{x})\big)\partial_t\psi_{h,\Delta t}(t,\mathbf{x})\; ds_x\; dt = \int_0^\infty \int_\Gamma f(t,\mathbf{x})\partial_t\psi_{h,\Delta t}(t,\mathbf{x})\; ds_x\; dt\;. \tag{20.4}$$

From $\phi_{h,\Delta t}$, the sound pressure $u_{h,\Delta t}$ is obtained in Ω by evaluating the integral in (20.1) numerically.

20.3 Error estimate and adaptive mesh refinements

Computable error indicators are a key ingredient to design adaptive mesh refinements. We recall from [3]:

Theorem: Let $\phi, \phi_{h,\Delta t} \in H_0^1([0,T], H^{-\frac{1}{2}}(\Gamma))$ be the solutions to (20.2) resp. (20.4). Assume that $R = \dot{f} - V\dot{\phi}_{h,\Delta t} \in H^0([0,T], H^1(\Gamma))$. Then

$$\|\phi - \phi_{h,\Delta t}\|^2_{0,-\frac{1}{2},\Gamma} \lesssim \max\{\Delta t, h\}(\|\partial_t R\|_{L^2([0,T],L^2(\Gamma))} + \|\nabla R\|_{L^2([0,T],L^2(\Gamma))})^2.$$

The error indicators

$$\eta(\triangle) = \max\{\Delta t, h\}\Big\{ \sum_i \int_{t_i}^{t_{i+1}} \int_\Delta (\partial_t R)^2 + \sum_i \int_{t_i}^{t_{i+1}} \int_\Delta (\nabla R)^2 \Big\}$$

lead to

Adaptive Algorithm:
Input: Mesh $\mathcal{T} = \mathcal{T}_0$, refinement parameter $\theta \in (0,1)$, tolerance $\epsilon > 0$, data f.

1. Solve $V\dot{\varphi}_{h,\Delta t} = \dot{f}$ on $\mathcal{T}$.
2. Compute the error indicators $\eta(\triangle)$ in each triangle $\triangle \in \mathcal{T}$.
3. Find $\eta_{max} = \max_\triangle \eta(\triangle)$.
4. Stop if $\sum_i \eta^2(\triangle_i) < \epsilon^2$.
5. Mark all $\triangle \in \mathcal{T}$ with $\eta(\triangle_i) > \theta\eta_{max}$.
6. Refine each marked triangle into 4 new triangles to obtain a new mesh $\mathcal{T}$
7. Go to 1.

Output: Approximation of $\dot{\varphi}$.

20.4 Graded meshes

The realistic scattering and diffraction of waves in $\mathbb{R}^3$ is crucially affected by geometric singularities of the scatterer,as solutions of the wave equation exhibit well-known singularities at non-smooth boundary points of the domain. For such geometric singularities, graded meshes adapted to the geometry are known to provide optimal convergence rates for time independent problems. We have generalised to time-independent theory to the transient setting [4] and illustrate the improved convergence rates in numerical experiments below.

Our computations are mainly conducted on the square $[-1,1]^2$. To define β-graded meshes, due to symmetry, it suffices to consider a β-graded mesh on $[-1,0]$. We define $y_k = x_k = -1 + (\frac{k}{N_l})^\beta$ for $i = 1, \ldots, N_l$ and for a constant $\beta \geq 0$. The nodes of the β-graded mesh are therefore $(x_k, y_l),\ k,l = 1, \ldots, N_l$. We note that for $\beta = 1$ we would have a uniform mesh.

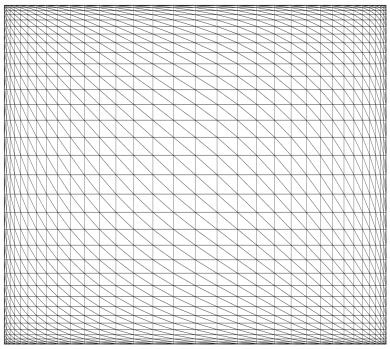

Figure 20.1: β-graded mesh with $n = 20$ triangles per side and $\beta = 2$

20.5 Numerical results

Experiment 1: If Γ is a screen, the density ϕ exhibits edge and corner singularities. Motivated by recent work by Müller and Schwab for 2d FEM, in [4] we adapt a classical analysis by von Petersdorff for time-independent problems and obtain the precise singular behaviour of ϕ near $\partial\Gamma$: $\phi(t, \mathbf{x}) \sim \text{dist}(\mathbf{x}, \partial\Gamma)^{-1/2}$ near an edge, $\phi(t, \mathbf{x}) \sim \text{dist}(\mathbf{x}, \partial\Gamma)^{-0.703}$ near a right-angled corner. Time-independent graded meshes provide a quasi- optimal approximation of these singularities. The numerical experiment depicted in Figure 20.2 compares the convergence in energy norm on graded and uniform meshes for $\Gamma = [0, 1]^2 \times \{0\}$ and illustrates the theoretically predicted convergence of order DOF^{-1}, resp. $\sim DOF^{-1/2}$ [4]. Graded meshes are relevant in industrial-

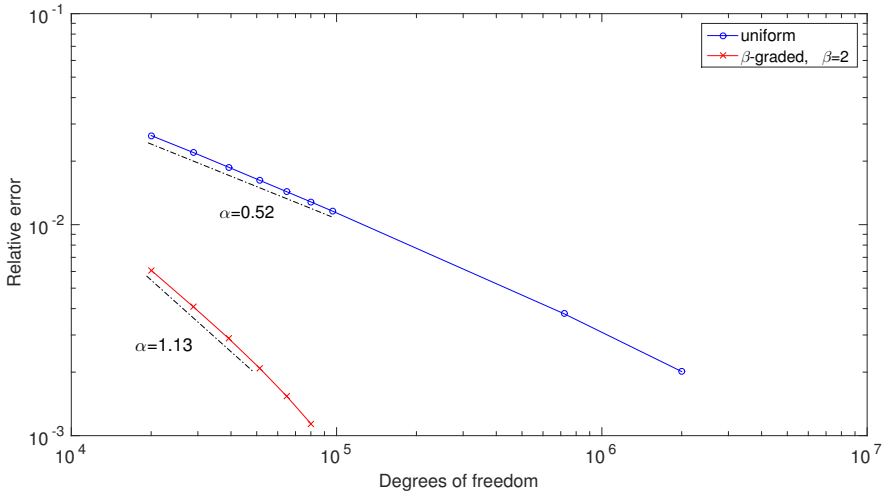

Figure 20.2: Energy convergence for graded vs. uniform meshes.

scale engineering problems. In particular, [4] shows the use of graded meshes to accurately compute the sound amplification in the singular horn geometry between a vibrating tire and the road.

Experiment 2: We use provably reliable residual error indicators, as well as heuristic ZZ and hierarchical indicators to steer adaptive mesh refinements. Figure 20.3 shows that the residual indicators converge at the same rate as the energy error for an example problem with $\Gamma = S^2$. Theoretical results establish the reliability and (weak) efficiency of the residual error indicators (see [3]) and compare the adaptive methods obtained from the different error indicators.

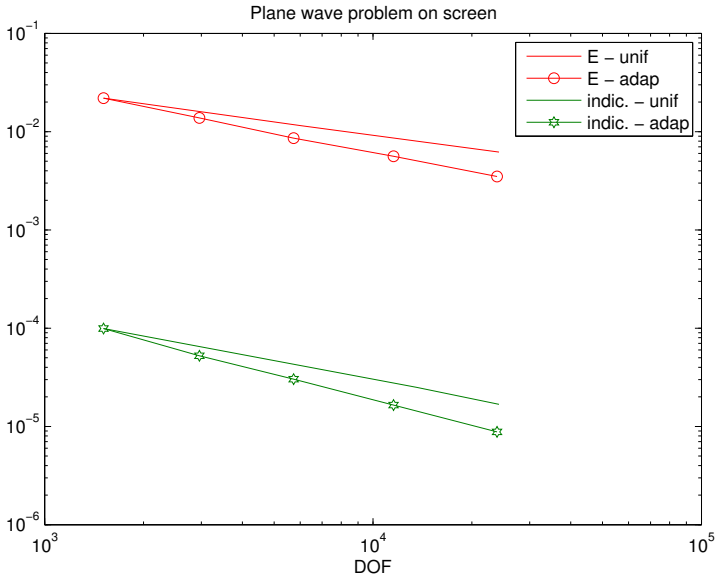

Figure 20.3: Uniform vs adaptive for plane wave problem on $[0, 0.5]^2$ screen.

Geometry	DOF	Energy	MOT	Error
sphere	320	8.5692	8.5470	.26%
	1280	8.6059	8.6059	$\ll 1\%$
icosahed.	320	20.538	21.480	4.6%
	1280	19.879	20.143	1.3%
screen	288	0.4233	0.4497	6.2%
	1250	0.4589	0.4716	2.8%

Table 20.1: relative errors in energy: modified MOT vs. GMRES with residual 10^{-9}.

Experiment 3: To obtain provably stable methods and a rigorous error analysis, we require conforming Galerkin discretisations. In general, the discretised equation (20.4) corresponds to a lower Hessenberg linear system in space-time, with one band above the diagonal. Motivated by adaptivity and C^∞ temporal basis functions, there has been much recent interest in works by by Sauter-Veit [6], Merta et al. [8], Schanz and others in efficient solvers. We present an approximate time-stepping scheme [5], based on extrapolation, which becomes exact for $\Delta t \to 0$. It may be used as either a preconditioner or standalone solver. Table 1 compares one step of this method to the (essentially exact) solution of the space-time system as obtained from GMRES [5].

20.6 Conclusions

In this paper we have outlined the use of time domain boundary element methods with mesh refinements for singular geometries. Time-independent graded meshes allow to resolve the edge and corner singularities in the scattering from polygonal scatterers or screens. Adaptive mesh refinement procedures based on a posteriori error estimates allow to address more general singularities in the solution. The numerical solution of the resulting systems is aided by a modified MOT scheme, which provides an efficient preconditioner (or stand-alone solver) for the space-time systems.

Acknowledgement

H. G. acknowledges support by ERC Advanced Grant HARG 268105 and the EPSRC Impact Acceleration Account.

References

[1] A. Bamberger and T. Ha Duong, *Formulation variationnelle espace-temps pour le calcul par potentiel retard de la diffraction d'une onde acoustique*, Math. Meth. Appl. Sci. 8 (1986), 405–435, 598–608.

[2] L. Banz, H. Gimperlein, Z. Nezhi and E. P. Stephan, *Time domain BEM for sound radiation of tires*, Comput. Mech. **58** (2016), 45–57.

[3] H. Gimperlein, M. Maischak and E. P. Stephan, *Adaptive time domain boundary element methods and engineering applications*, survey, Journal of Integral Equations and Applications, to appear (2016).

[4] H. Gimperlein, F. Meyer, C. Özdemir, D. Stark and E. P. Stephan, *Boundary elements with mesh refinements for the wave equation*, in preparation (2017).

[5] H. Gimperlein and D. Stark, *Extrapolation as preconditioner for time domain boundary element methods*, preprint (2016).

[6] S. Sauter and A. Veit, *Adaptive time discretization for retarded potentials*, Numer. Math. **132** (2016), 569–595.

[7] F.-J. Sayas, *Retarded Potentials and Time Domain Boundary Integral Equations: a road-map*, Springer Series in Comp. Math. 50, Springer, 2016.

[8] A. Veit, M. Merta, J. Zapletal and D. Lukas, *Efficient solution of time-domain boundary integral equations arising in sound-hard scattering*, Internat. J. Numer. Methods Engrg. **107** (2016), 430–449.

[9] A. E. Yilmaz, J.-M. Jin and E. Michielssen, *Time domain adaptive integral method for surface integral equations*, IEEE Trans. Antennas Propagation 52 (2004), 2692–2708.

Chapter 21

Evaluation of discontinuity in IGABEM modelling of 3D acoustic fields

Yi Sun[1,2], Jon Trevelyan[2], Gabriel Hattori[2] and Chihua Lu[1]

[1] Department of Vehicle Engineering
Wuhan University of Technology
122 Luoshi Road, Hongshan District
Wuhan, China

[2] School of Engineering and Computing Sciences
Durham University
DH1 3LE, South Road
Durham, UK

Abstract. *The use of non-uniform rational B-splines (NURBS) as basis functions to discretise the solution variables as well as the problem geometry in a boundary element formulation has become known as the isogeometric boundary element method (IGABEM); this is a popular topic in the field of numerical analysis. IGABEM has been shown to offer improved convergence properties over the conventional boundary element method (BEM) algorithms based on piecewise polynomial approximation spaces [1]. Using the IGABEM formulation, the NURBS information from computer aided design (CAD) can be used directly in boundary element analysis without geometry clean-up or mesh generation [2]. However this analysis has been performed only for smooth acoustic solutions while in most real-world engineering design and analysis acoustic problems, geometric corners and discontinuities in boundary conditions raise the possibility of weak discontinuities in the solution field.*

In the current work we consider such problems. The motivation is to study acoustic problems at low frequency within the passenger compartment of an automobile, and this problem is characterised by panels with piecewise continuous impedance boundaries.

We develop a discontinuous IGABEM formulation based on NURBS and compare its performance against conventional BEM scheme. Continuous and discontinuous formulations are also compared. In this paper, a three dimentional model is presented to illustrate the potential of the proposed method for integrated engineering design and analysis.

21.1 Introduction

The noise, vibration and harshness (NVH) performance has become one of the most important quality indicators of a product in vehicle industry. This is mainly due to the more and more strict

noise emission regulations and increasing demand of comfort from the consumers. Whereas, the demand of lightweight and low-energy brings many limits for acoustic engineers in their design, which will inevitably lead to limitations on the improvement of the noise and vibration properties of the vehicle. In addition, the evaluation of the NVH performance is now mostly conducted by testing the real car, which is usually done after the design process and will extend the entire design time. To overcome these problems, a calculation method which can offer more precise prediction on compartment acoustics is required, especially in the early design stage.

The Boundary Element Method is widely used in solving acoustic problems in the vehicle industry [3, 4]. The BEM provides a useful technique to analyse problems governed by partial differential equations [5]. In the BEM, integrals are evaluated only on the boundary instead of the whole domain, which means volumetric problems are reduced to surface problems. This will dramatically reduce the complexity of the mesh generation process and the entire analysis time. However, geometry preparation and mesh generation are still time-consuming if the problem has a large number of degrees of freedom (DOF). Especially for problems in the machine industry, mesh generation and refinement can take up to 80% of the total analysis time [2], which slows down the product development process.

The idea of Isogeometric Analysis (IGA) based on NURBS was first put forward by Hughes [2]. The concept is using the splines employed in CAD geometry to capture the exact geometry for analysis. NURBS are the most widely-used geometry representation in CAD and have been shown to bring advantageous properties in the analysis process. By taking the basis functions generated from NURBS, IGA can bridge the gap between CAD and CAE, and offer precise and efficient geometric modelling. Compared to the conventional BEM, the discretisation in the isogeometric boundary element method (IGABEM) is conducted based on CAD mapping instead of conventional piecewise polynomials. Analogously, the associated shape functions in the BEM are also replaced by basis functions in the IGABEM. Research on the IGABEM has progressed rapidly in recent years [6, 7, 8, 9]. A two dimensional elastostatic problem based on the IGABEM was presented by Simpson [9]. Then Marussig [10] implemented the IGABEM in three dimensions with a hierarchical matrix which reduced the calculation time for large problems. Particularly, in the area of acoustic application, Scott [8] put forward acoustic problems using the IGABEM with T-splines. Further Peake proposed an extended isogeometric boundary element method (XIBEM) for two-dimensional Helmholtz problems [6] and then extended it to three dimensional acoustic problems [11]. It should be noticed that these analyses have been performed only for smooth acoustic solutions while in real industry acoustic problems, particularity in the vehicle industry, the boundary conditions are mostly discontinuous, the material performance of the vehicle body and windows being obviously different.

We present a discontinuous IGABEM formulation based on a three dimensional model in this work. The model is characterised with piecewise continuous impedance boundaries to capture the material difference. Performance comparisons are made between the proposed method and the conventional BEM to show its potential application in industry. Continuous and discontinuous formulations are compared.

21.2 B-Splines and NURBS

The knot vector is the fundamental description of the basis functions of a B-spline. It is a set of non-decreasing and independent coordinates, written

$$\Xi = \{\xi_1, \xi_2, ..., \xi_{n+p+1}\}\,,\ \xi_i \in \mathbb{R} \tag{21.1}$$

where real number ξ_i is named a knot, i is the knot index, $i = 1, 2, ..., n + p + 1$, ξ_i is the ith knot in the parameter space, p is the polynomial degree, and n is the number of basis functions

which define the B-spline. The half-open interval $[\xi_i, \xi_{i+1})$ is called a knot span which can be zero length since the knots may be duplicated. Based on the knot vector, the B-spline basis functions can be built by using the Cox-de Boor recurrence formula [12, 13]:

$$p = 0 : N_{i,0} = \begin{cases} 1 & \xi_i \leq \xi < \xi_{i+1} \\ 0 & \text{otherwise} \end{cases} \tag{21.2}$$

$$p > 0 : N_{i,p}(\xi) = \frac{\xi - \xi_i}{\xi_{i+p} - \xi_i} N_{i,p-1}(\xi) + \frac{\xi_{i+p+1} - \xi}{\xi_{i+p+1} - \xi_{i+1}} N_{i+1,p-1}(\xi) \tag{21.3}$$

B-spline curves [14] are built by using a linear combination of B-spline basis functions. A pth-degree piecewise polynomial B-spline curve $C^b(\xi)$ is given by

$$C^b(\xi) = \sum_{i=1}^{n} N_{i,p}(\xi) \mathbf{A}_i \tag{21.4}$$

where $\mathbf{A}_i$ are the control points which could be position vectors, and $N_{i,p}(\xi)$ denotes the ith basis function on the point ξ_i. It should be noted that the concepts of control points and basis functions are similar to nodal coordinates and shape functions in BEM, respectively.

A B-spline surface $S^b(\xi, \eta)$ is a tensor product surface of two B-splines. Given a net of control points $\mathbf{A}_{i,j} (i = 1, 2, ..., n; j = 1, 2, ..., m)$, polynomial degrees p and q, two knot vectors $\Xi = [\xi_1, \xi_2, ..., \xi_{n+p+1}]$ and $H = [\eta_1, \eta_2, ..., \eta_{m+q+1}]$, a B-spline surface is defined as

$$S^b(\xi, \eta) = \sum_{i=1}^{n} \sum_{j=1}^{m} N_{i,p}(\xi) M_{j,q}(\eta) \mathbf{A}_{i,j} \tag{21.5}$$

where $N_{i,p}(\xi)$ and $M_{j,q}(\eta)$ represent univariate B-spline basis functions of degree p and q, associated with knot vectors Ξ and H, respectively.

NURBS are developed from B-splines but the introduction of weights enables the exact representation of geometric entities like circular arcs and spheres. Thus, a pth degree NURBS curve is given by

$$C(\xi) = \sum_{i=1}^{n} R_{i,p}(\xi) \mathbf{A}_i \tag{21.6}$$

where $\mathbf{A}_i$ denotes the control points, and $R_{i,p}(\xi)$ are the NURBS basis functions derived from the B-spline basis. The NURBS basis functions $R_{i,p}(\xi)$ of polynomial degree p are expressed as

$$R_{i,p}(\xi) = \frac{N_{i,p}(\xi) w_i}{W(\xi)} \tag{21.7}$$

with

$$W(\xi) = \sum_{i=1}^{n} N_{i,p}(\xi) w_i \tag{21.8}$$

and $W(\xi)$ denotes the weighting function generated by defining a weight ω_i for every control point. $R_{i,p}(\xi)$ are piecewise rational functions. If all the weights are equal to 1, then $R_{i,p}(\xi) = N_{i,p}(\xi)$, and the NURBS degenerate into B-splines. The definition of a NURBS surface $S(\xi, \eta)$ is then completely analogous to a B-spline surface, given as

$$S(\xi, \eta) = \sum_{i=1}^{n} \sum_{j=1}^{m} R_{ij,pq}(\xi, \eta) \mathbf{A}_{i,j} \tag{21.9}$$

with

$$R_{i,j,p,q}(\xi, \eta) = \frac{N_{i,p}(\xi) M_{j,q}(\eta) w_{i,j}}{\sum_{i=1}^{n} \sum_{j=1}^{m} N_{i,p}(\xi) M_{j,q}(\eta) w_{i,j}} \tag{21.10}$$

It should be noted that these same NURBS basis functions can also be used to represent the field variables.

21.3 Boundary integral equation

Given a domain Ω with boundary Γ, the acoustic waves within the domain are governed by the well-known Helmholtz equation:

$$\nabla^2\phi(\mathbf{x}) + k^2\phi(\mathbf{x}) = 0, \quad \mathbf{x} \in \Omega \tag{21.11}$$

where ∇^2 is the Laplacian operator, $\phi(\mathbf{x})$ is the acoustic potential at the field point $\mathbf{x}$, λ is the wavelength, and $k = 2\pi/\lambda$ is the wave number.

Using Green's second identity and the Green's function, the boundary integral equation (BIE) for the Helmholtz equation can be written as:

$$C(\mathbf{s})\phi(\mathbf{s}) + \int_\Gamma \frac{\partial G(\mathbf{s},\mathbf{x})}{\partial n}\phi(\mathbf{x})d\Gamma(\mathbf{x}) = \int_\Gamma G(\mathbf{s},\mathbf{x})\frac{\partial \phi(\mathbf{x})}{\partial n}d\Gamma(\mathbf{x}) \tag{21.12}$$

where $\mathbf{s}$ is a collocation point, $C(\mathbf{s})$ is the jump term at the collocation point, and $\partial\phi(\mathbf{x})/\partial n$ is the acoustic velocity on the boundary. $G(\mathbf{s},\mathbf{x})$ and $\partial G(\mathbf{s},\mathbf{x})/\partial n$ are the Green's function and corresponding derivative given by

$$G(\mathbf{s},\mathbf{x}) = \frac{e^{ikr}}{4\pi r} \tag{21.13}$$

$$\frac{\partial G(\mathbf{s},\mathbf{x})}{\partial n} = \frac{e^{ikr}}{4\pi r^2}(ikr - \frac{\partial r}{\partial n}) \tag{21.14}$$

where

$$r = |\mathbf{x} - \mathbf{s}| \tag{21.15}$$

In the conventional BEM, the boundary Γ is discretised into E non-overlapping boundary elements on which the geometric, acoustic potential and velocity are appoximated with polynomial, isoparametric elements, thus the boundary can be expressed as:

$$\Gamma = \bigcup_{e=1}^{E} \Gamma_e \tag{21.16}$$

The elements represent the geometry through the mapping:

$$\Gamma_e = \mathbf{F}(\xi), \quad \xi \in [-1, 1] \tag{21.17}$$

Then Eq.(21.12) can be written as a discretised form:

$$C(\mathbf{s})\phi(\mathbf{s}) + \sum_{e=1}^{E}\sum_{j=1}^{J}\int_{-1}^{1}\frac{\partial G(\mathbf{s},\boldsymbol{\xi})}{\partial n}N_{ej}(\boldsymbol{\xi})\phi_{ej}(\boldsymbol{\xi})J_e(\boldsymbol{\xi})d\boldsymbol{\xi} = \sum_{e=1}^{E}\sum_{j=1}^{J}\int_{-1}^{1}G(\mathbf{s},\boldsymbol{\xi})\frac{\partial \phi_{ej}(\boldsymbol{\xi})}{\partial n}N_{ej}(\boldsymbol{\xi})J_e(\boldsymbol{\xi})d\boldsymbol{\xi} \tag{21.18}$$

where J is the number of shape functions on the element, N_{ej} are the shape functions for the element, ϕ_{ej} and $\partial\phi_{ej}/\partial n$ are the acoustic potential and velocity on the node, respectively. $J_e(\xi)$ is the Jacobian from the mapping in Eq.(21.17).

Taking the collocation point $\mathbf{s}$ to lie at each node in turn, a set of equations relating all potential and velocity coefficient can be obtained:

$$\mathbf{H}\boldsymbol{\phi} = \mathbf{G}\frac{\partial \boldsymbol{\phi}}{\partial n} \tag{21.19}$$

where the fully populated matrix $\mathbf{H}$ contains all integrals of the left-hand two terms of Eq.(21.12), and matrix $\mathbf{G}$ is assembled by integrals of the right-hand terms of Eq.(21.12). $\boldsymbol{\phi}$ and $\partial\boldsymbol{\phi}/\partial n$ are vectors containing acoustic potential and normal derivative coefficients, respectively.

By reordering all the unknowns and related coefficients to the left-hand side and all the knowns and related coefficients to the right-hand side, we can get a final matrix in this form:

$$\mathbf{A}\mathbf{x} = \mathbf{b} \tag{21.20}$$

where $\mathbf{A}$ is an unsymmetric and fully populated square matrix, the vector $\mathbf{x}$ contains all unknown potential and velocity coefficients while the vector $\mathbf{b}$ is calculated from all known coefficient and their associated terms. The complex matrix is a linear system which can be solved directly.

21.4 IGABEM for acoustics

In IGABEM, NURBS basis functions are employed to represent the geometry, ϕ and $\partial\phi/\partial n$. The boundary is divided into E non-overlapping isogeometric patches Γ_e, analogously to conventional BEM in Eq.(21.16). Note that a local coordinate system $\mathbf{u} = (u, v)$ is defined on each patch Γ_e as follows:

$$\Gamma_e = \mathbf{U}(\eta), \quad \eta \in [0, 1) \tag{21.21}$$

Thus the total Jacobian is expressed as:

$$J_U = \left| \frac{\partial \mathbf{x}}{\partial \boldsymbol{\eta}} \frac{\partial \boldsymbol{\eta}}{\partial \boldsymbol{\xi}} \right| \tag{21.22}$$

where the first component is the mapping from global coordinates to the local coordinates on each patch, and the second term is the mapping from local coordinates to the parametric space. The reason for this additional local mapping is that the B-splines and NURBS are defined in the interval $[0, 1)$ while the integration is performed in the mapping defined in Eq.(21.17).

The acoustic potential and velocity can be discretised in terms of a NURBS interpolation, respectively:

$$\phi(\mathbf{x}) = \sum_{j=1}^{J} R_{j,p}(u(\mathbf{x}), v(\mathbf{x}))\widetilde{\phi}_{j,p} \tag{21.23}$$

$$\frac{\partial \phi(\mathbf{x})}{\partial n} = \sum_{j=1}^{J} R_{j,p}(u(\mathbf{x}), v(\mathbf{x}))\widetilde{q}_{j,p} \tag{21.24}$$

where J is the number of control points, $\widetilde{\phi}_{j,p}$ and $\widetilde{q}_{j,p}$ are potentials and derivatives associated with control points. It is important to note that $\widetilde{\phi}_{j,p}$ and $\widetilde{q}_{j,p}$ are no longer the nodal potentials and derivatives since the control points may not lie on the geometry. Then the final isogeometric boundary integral equation can be written by substituting Eq.(21.23) and Eq.(21.24) into Eq.(21.12):

$$\begin{aligned} C(\mathbf{s})\phi(\mathbf{s}) + \sum_{e=1}^{E}\sum_{j=1}^{J}\int_{-1}^{1} \frac{\partial G(\mathbf{s}, \boldsymbol{\xi})}{\partial n} R^e_{j,p}(\boldsymbol{\xi})\phi^e_{j,p}(\boldsymbol{\xi}) J_{U_e}(\boldsymbol{\xi}) d(\boldsymbol{\xi}) \\ = \sum_{e=1}^{E}\sum_{j=1}^{J}\int_{-1}^{1} G(\mathbf{s}, \boldsymbol{\xi}) \frac{\partial \phi^e_{j,p}(\boldsymbol{\xi})}{\partial n} R^e_{j,p}(\boldsymbol{\xi}) J_{U_e}(\boldsymbol{\xi}) d(\boldsymbol{\xi}) \end{aligned} \tag{21.25}$$

where $\boldsymbol{\xi} = \boldsymbol{\xi}(\boldsymbol{\eta})$.

In general, the control points are no longer able to be taken as the collocation points in IGABEM, since they may not lie on the geometry boundary (except flat patches). Alternatively, the Greville abscissae [15, 16] may be used to define the position of collocation points as:

$$\xi'_g = \frac{\xi_{g+1} + \xi_{g+2} + ... + \xi_{g+p}}{p}, \quad g = 1, 2, ..., n \tag{21.26}$$

where n denotes the number of control points, p is the degree.

After defining the collocation points in the geometry, the integral boundary equations defined in Eq.(21.25) can be assembled in matrix form analogously to conventional BEM.

21.4.1 Discontinuous isogeometric boundary patch

In order to give a square system, the number of collocation points must equal the number of unknowns. In a discontinuous model, the control points lying on a discontinuous element boundary may have two or more degrees of freedom, i.e, one for each patch of which it is a member. In order to guarantee a suitable number of collocation points, the simplest scheme is to locate them internally in each patch as shown in Fig.21.1(b). The discontinuous IGABEM patches can allow the potential fields to become discontinuous at the interfaces between patches. This is a consideration for vehicle industry applications in which a discontinuity exists between different materials.

Additionally, since the collocation points lie within the patches, at points where the boundary is smooth, the jump term $C(\mathbf{s})$ of all points is equal to $1/2$.

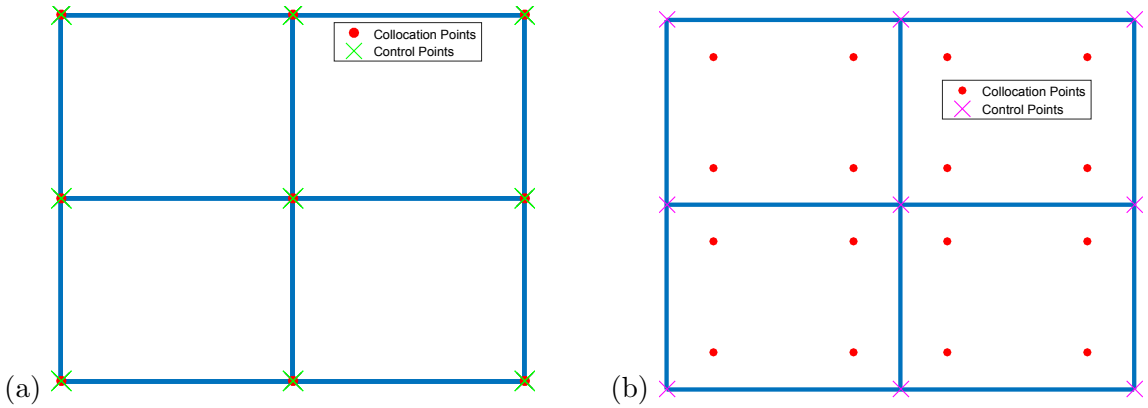

Figure 21.1: Isogeometric patches in 3D: (a) continuous basis functions, and (b) discontinuous basis functions.

21.5 Numerical example

This section presents a numerical example to verify the accuracy of the proposed discontinuous IGABEM and evaluate the performance between the IGABEM and BEM, continuous and discontinuous approaches. The problem is defined in Figure 21.2. The cubic domain is constructed by 10 piecewise continuous impedance patches on which different boundary conditions are applied. Patch 1 is the small square patch on the front surface. Patch 2 is the patch on the back surface opposite to patch 1. The size of patch 1 and patch 2 are 3×3 and 1×1, respectively. The wavelength is 5 in this case. Fig. 21.2 also shows the control points $(*)$ and collocation points $(\cdot)$ on the front surface of the cube. In this example, the collocation points are equally-spaced over the boundary.

There are three forms of boundary condition in acoustic problem:

- Dirichlet condition: the acoustic potential is known over the boundary:

$$\phi(\mathbf{x}) = \overline{\phi}(\mathbf{x}) \tag{21.27}$$

- Neumann condition: the acoustic velocity is known over the boundary:

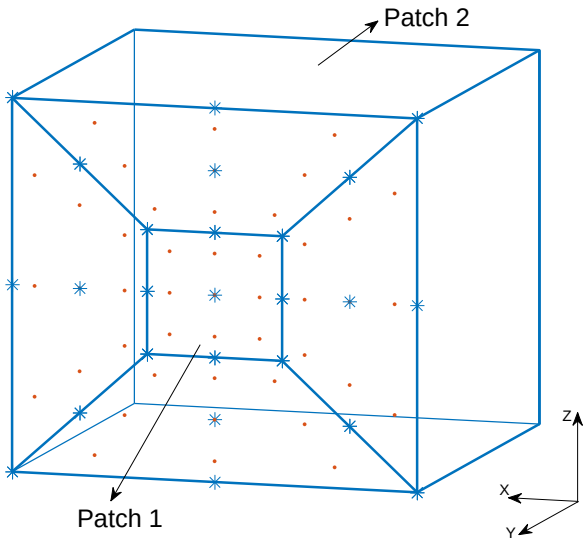

Figure 21.2: A 3D cubic model with piecewise continuous impedance boundaries.

$$\frac{\partial \phi(\mathbf{x})}{\partial n} = \overline{q} \tag{21.28}$$

- Robin condition: the derivative of the potential is presented as a linear function of the potential:

$$\alpha \frac{\partial \phi(\mathbf{x})}{\partial n} = \beta \phi(\mathbf{x}) + \gamma \tag{21.29}$$

In this example, a Neumann condition with $\frac{\partial \phi(\mathbf{x})}{\partial n} = 0$, $\frac{\partial \phi(\mathbf{x})}{\partial n} = 1$ is applied on patch 1 and patch 2, respectively, and a Robin condition with $\alpha = 1, \beta = -2, \gamma = 1 + i$ is applied on the remaining patches.

The $L^2(\Gamma)$ norm of the potential was calculated over the entire boundary as:

$$\| \phi \|_{L^2(\Gamma)} = \sqrt{\int_\Gamma |\phi|^2 \, d\Gamma} \tag{21.30}$$

We define an error metric evaluated as

$$Error = \frac{\| \phi - \phi_{ref} \|_{L^2(\Gamma)}}{\| \phi_{ref} \|_{L^2(\Gamma)}} \tag{21.31}$$

where $\| \phi_{ref} \|_{L^2(\Gamma)}$ is the $L^2(\Gamma)$ norm of the reference solution obtained from the converged result of the conventional BEM analysis using quadratic shape functions.

Fig.21.3 shows the accuracy and convergence comparison between the proposed method and the discontinuous BEM as well as a comparision between continuous BEM and IGABEM; it is clear that IGABEM offers a significant advantage over BEM in accuracy per DOF. Also, the discontinuous IGABEM converges faster than discontinuous BEM. However, discontinuous IGABEM did not show any improvement compared to continuous IGABEM for this set of boundary conditions, which may be due to the discontinuity of the boundary conditions not being sharp enough in this example. Work is in progress to examine other situations.

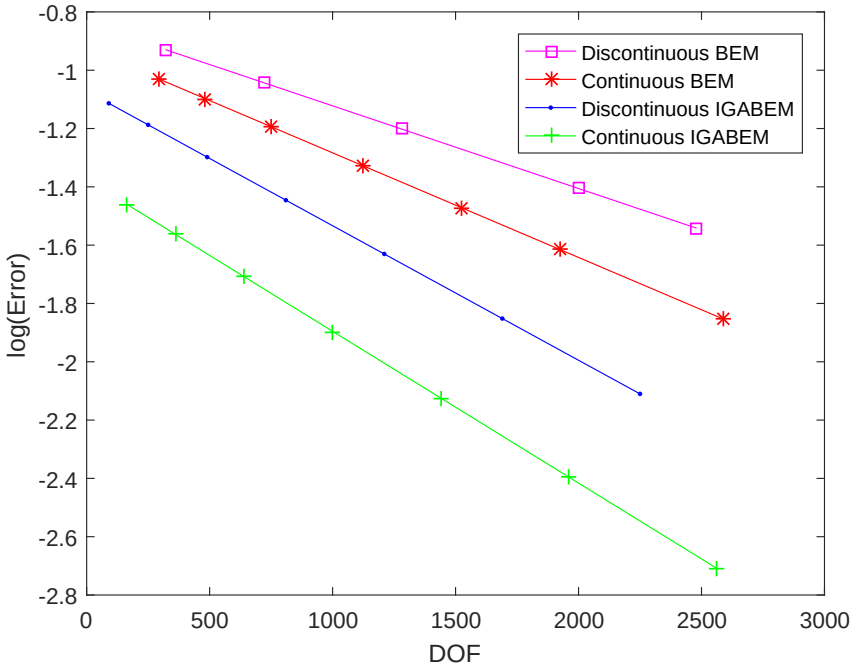

Figure 21.3: Comparison between BEM and IGABEM (continuous and discontinuous).

21.6 Conclusions

A discontinuous IGABEM for acoustic problems has been introduced for the first time in the literature. The discontinuous boundary patch has the ability to naturally capture discontinuous boundary conditions. The evaluation of discontinuity in IGABEM modelling of three dimentional acoustic problems has also been presented and compared to the conventional BEM approach.It has been shown that the IGABEM presents lower errors and converges faster than the equivalent problem with conventional BEM. However, the continuous IGABEM presents consistently better results than the discontinuous IGABEM for the example studied. This can be attributed to the fact that the problem as posed does not present high discontinuities at the boundaries.

Future works include using increased boundary discontinuities, and also the model of the interior of an automobile, where the difference between materials provides a real application for the proposed method. Further, combining this method with a Participation Factor Panel (PFP) method will find the vehicle panel which contributes most to the sound pressure at a given location.

Acknowledgement

Yi Sun would like to thank the China Scholarship Council (CSC) for the support given to the PhD research.

References

[1] R. Simpson, M. Scott, M. Taus, D. Thomas, H. Lian, *Acoustic isogeometric boundary element analysis*, Comput. Meth. Appl. Mech. Eng., 269 (2014), 265–290.

[2] T. Hughes, J. Cottrell, Y. Bazilevs, *Isogeometric analysis: CAD, finite elemens, NURBS, exact geometry and mesh refinement*, Comput. Meth. Appl. Mech. Eng., 194 (2005), 4135–4195.

[3] J. He, X. Jin, Q. Zhang, Powertrain mount system optimization based on interior noise analysis. In *2010 2nd International Conference on Future Computer and Communication*, Wuhan, China, 2010.

[4] L. Franzoni, J. Rouse, T. Duvall, *A broadband energybased boundary element method for predicting vehicle interior noise*, J. Acoust. Soc. Am., 115(5) (2004), 2538–2538.

[5] S. Kirkup, *The Boundary Element Method in Acoustics: A Development in Fortran*, Hebden Bridge: Integrated Sound Software, 1998.

[6] M. Peake, J. Trevelyan, G. Coates, *Extended isogeometric boundary element method (XIBEM) for two-dimensional helmholtz problems*, Comput. Meth. Appl. Mech. Eng., 259 (2013), 93–102.

[7] K. Li, X. Qian, *Isogeometric analysis and shape optimization via boundary integral*, Comput. Aided Des., 43(11) (2011), 1427–1437.

[8] M. Scott, R. Simpson, J. Evans, S. Bordas, T. Hughes, T. Sederberg, *Isogeometric boundary element analysis using unstructured T-splines*, Comput. Meth. Appl. Mech. Eng., 254 (2013), 197–221.

[9] R. Simpson, S. Bordas, H. Lian, J. Trevelyan, *An isogeometric boundary element method for elastostatic analysis: 2D implementation aspects*, Comput. Struct., 118 (2013), 2–12.

[10] B. Marussig, J. Zechner, G. Beer, T. P. Fries, *Fast isogeometric boundary element method based on independent field approximation*, Comput. Meth. Appl. Mech. Eng., 284 (2015), 458-488.

[11] M. Peake, J. Trevelyan, G. Coates, *Extended isogeometric boundary element method (XIBEM) for three-dimensional medium-wave acoustic scattering problems*, Comput. Meth. Appl. Mech. Eng., 284 (2015), 762–780.

[12] M. G. Cox, *The numerical evaluation of B-splines*, IMA J. Appl. Math., 10 (1972), 134–149.

[13] C. De Boor, *On calculating with B-splines*, J. Approx. Theory., 6 (1972), 50–62.

[14] L. Piegl, W. Tiller, *The NURBS Book*, Springer-Verlag Berlin Heidelberg, 1997.

[15] T. Greville, *Numerical procedures for interpolation by spline functions*, J. SIAM: Series B, Numer. Anal., (1964), 53–68.

[16] R. Johnson, *Higher order B-spline collocation at the Greville abscissae*, Appl. Numer. Math., 52 (2005), 63–75.

Chapter 22

Acceleration of IGABEM for 3D elastostatics using Proper Generalised Decomposition inside a black-box Fast Multipole Method

Jon Trevelyan[1], **and Shengze Li**[2]

[1] School of Engineering & Computing Sciences,
Durham University
South Road
Durham DH1 3LE

[2] College of Aerospace Science & Engineering,
National University of Defence Technology
Changsha
China

Abstract. *The Boundary Element Method is an ideal and natural choice for the isogeometric analysis of solids in 3D. Such analysis has been abbreviated IGABEM. Recently, Simpson and Liu presented an IGABEM scheme accelerated by a black-box Fast Multipole Method (bbFMM) for the solution of the Helmholtz equation. Here Chebyshev interpolation is used to describe the far-field behaviour of any arbitrary kernel removing the reliance on multipole expansions specific to particular kernels. The largest computational expense in the bbFMM lies in the computation of the multipole-to-local (M2L) operators. This step involves computing the far-field contribution at the Chebyshev nodes for all FMM cells in the interaction list of each cell at each level. In bbFMM works, this stage is accelerated by a Singular Value Decomposition (SVD) to generate a compressed, low-rank approximation to the M2L operator. We present an improvement to the process by replacing the SVD compression by an alternative based on the Proper Generalised Decompostion (PGD). The final solution accuracy is not significantly affected.*

We present numerical aspects of the PGD-accelerated bbFMM IGABEM scheme, including a discussion of the number of PGD modes required to acheive prescribed accuracy. Analysis of the computational performance shows the bbFMM to reduce the complexity of IGABEM from $\mathcal{O}(n^2)$ to $\mathcal{O}(n)$ and the PGD to provide improvements over SVD. For smaller problems, the use of PGD to compress the M2L operation effectively offsets the overheads involved in using FMM.

22.1 Introduction

Isogeometric analysis, first proposed by Hughes et al. [1], offers a number of advantages over conventional (i.e. piecewise polynomial) finite element and boundary element formulations. Key among these are the promise of deeper integration of analysis within Computer Aided Design (CAD) systems, greatly simplified meshing and remeshing processes, and, perhaps most important of all, improved convergence properties. The essential idea is to use the basis functions used in traditional spline-based CAD models as the approximation space for a numerical scheme to solve a partial differential equation. Most popular are the Non-uniform Rational B-splines (NURBS) and T-splines. Following the initial paper, the concept has rapidly expanded from elasticity [1, 2] to various applications such as fluid dynamics [3, 4], electromagnetics [5] and vibration [6]. Early work on IGA was initially based on NURBS [7], and then extended to T-splines [8] and PHT-splines [9, 10, 11].

While isogeometric analysis with the Finite Element Method (IGAFEM) has gained this popularity, it should be noted that the common boundary representation using NURBS in CAD can only be used directly for IGAFEM analysis of plates and shells. There remains a requirement to supply such an algorithm with a *volumetric* NURBS definition in order to analyse a 3D solid object, and this is not a straightforward process. In order to overcome this difficulty, researchers have turned to the Boundary Element Method (BEM) and developed an isogeometric form, IGABEM. Here the boundary-only nature of the model means that the analysis of a solid can be conducted without a volumetric NURBS representation of the geometry, and this is a major advantage over IGAFEM for this large and important class of problems.

IGABEM has been explored in various areas including elastostatics [12, 13, 14], shape optimisation [15, 16], acoustics [17, 18, 19, 20] and fracture mechanics [21]. However, for large systems, the dense and nonsymmetric matrix produced by BEM codes remains in IGABEM. This presents great challenges in computational complexity for 3D problems if they have a large number of DOF. Matrix compression techniques can reduce the complexity to $\mathcal{O}(n \log n)$ or, better still, $\mathcal{O}(n)$. Popular techniques include the Fast Multipole Method (FMM) [22] and Adaptive Cross Approximation (ACA) [23]. These methods approximate the far-field kernel interactions through efficient hierarchical data structures, which allow for use of matrix-vector multiplication with almost linear complexity. There are no detailed comparisons of the two approaches, but we note that ACA has the benefit of simplicity of implementation, especially in a pre-existing BEM code.

In this paper we focus on the FMM. In most works on this method, the far-field interactions are expressed in terms of multipole expansions specific to the kernel for the PDE at hand. In order to provide a more general, kernel-independent implementation, the black-box FMM (bbFMM) [24] was developed for the matrix compression with a fast $\mathcal{O}(n)$ algorithm. This is based on approximation using Chebyshev interpolations. In this paper we present such a scheme applied to IGABEM, and accelerate the most numerically intensive stage of the bbFMM using a Proper Generalised Decomposition (PGD) [25], which provides a quasi-optimal reduced basis using an iterative procedure with a low computational effort ($\mathcal{O}(2mn)$ for an $m \times n$ system).

22.2 Formulation

22.2.1 IGABEM

We start with the classical boundary integral equation for elasticity, i.e.

$$\mathbf{C}(\mathbf{s})\mathbf{u}(\mathbf{s}) + \int_\Gamma \mathbf{T}(\mathbf{s},\mathbf{x})\mathbf{u}(\mathbf{x})\mathrm{d}\Gamma(\mathbf{x}) = \int_\Gamma \mathbf{U}(\mathbf{s},\mathbf{x})\mathbf{t}(\mathbf{x})\mathrm{d}\Gamma(\mathbf{x}), \tag{22.1}$$

to solve the equations of linear elasticity for a problem subject to boundary conditions

$$u_i = \bar{u}_i \quad \text{on } \Gamma_{u_i} \subset \Gamma, \tag{22.2}$$

$$t_i = \bar{t}_i \quad \text{on } \Gamma_{t_i} \subset \Gamma, \tag{22.3}$$

where $\mathbf{s} \in \Gamma$ denotes the source point and $\mathbf{x} \in \Gamma$ the field point, $\mathbf{u} \in \mathbb{R}^3$ the displacement field, $\mathbf{t} \in \mathbb{R}^3$ the traction field, $\mathbf{U}(\mathbf{s}, \mathbf{x}) = [U_{ij}]$ the displacement fundamental solutions kernel, $\mathbf{T}(\mathbf{s}, \mathbf{x}) = [T_{ij}]$ the traction fundamental solutions kernel, $\mathbf{C}(\mathbf{s}) = [C_{ij}]$ the jump term, $\bar{u}_i$ and $\bar{t}_i$ the prescribed displacements and tractions, i and j the indices running from 1 to 3 in three dimensions and the integral on the left hand side is taken in the Cauchy Principal Value (CPV) sense sections.

In the IGABEM formulation we consider the geometry to be defined in terms of NURBS surfaces,

$$\mathbf{x}(\boldsymbol{\xi}) = \sum_{a=1}^{n_a} R_{a,p}(\boldsymbol{\xi}) \mathbf{P}_a, \tag{22.4}$$

and the displacements and tractions to be defined in the same space of functions, i.e.

$$\mathbf{u}(\boldsymbol{\xi}) = \sum_{a=1}^{n_a} R_{a,p}(\boldsymbol{\xi}) \tilde{\mathbf{u}}_a, \tag{22.5}$$

$$\mathbf{t}(\boldsymbol{\xi}) = \sum_{a=1}^{n_a} R_{a,p}(\boldsymbol{\xi}) \tilde{\mathbf{t}}_a, \tag{22.6}$$

where $\mathbf{P}_a$ is a set of control point coordinates, $\tilde{\mathbf{u}}_a, \tilde{\mathbf{t}}_a$ are sets of unknown coefficients, and $R_{a,p}$ the NURBS basis functions, for polynomial degree p and in parametric coordinate $\boldsymbol{\xi} = (\xi_1, \xi_2)$, which may be found in Piegl & Tiller [7].

22.2.2 Black box Fast Multipole Method

The Fast Multipole Method provides an alternative to the conventional $\mathcal{O}(n^2)$ problem of finding node-to-node interactions through the kernel functions $\mathbf{U}(\mathbf{s}, \mathbf{x}), \mathbf{T}(\mathbf{s}, \mathbf{x})$. First the nodes are subdivided in a hierarchichal, octree structure over multiple levels. The subdivision into progressively smaller clusters stops when a minimum number of nodes is reached, at which level the cell is called a 'leaf'. Nodes in adjacent clusters are deemed too close to allow the approximation of the kernel, and the corresponding matrix terms are calculated in the conventional manner. However, nodes in well separated clusters are amenable to the kernel behaviour being approximated through a set of multipole expansions. Figure 22.1 illustrates the procedure though, for clarity, considers a 2D case, i.e. a quadtree cell hierarchy rather than the 3D octree hierarchy considered in the current work.

These multipole expansions, from cells at one level in the hierarchy to their parent cell, and vice versa, can be approximated using Chebyshev interpolation as illustrated in the Figure. In this way, an arbitrary kernel function can be considered, removing the need for kernel-specific multipole expansions. Full details of the approach are not given here, but the bbFMM is described by Fong & Darve [24].

The most numerically intensive component of the bbFMM execution is the evaluation of the so-called Moment to Local (or M2L) operators; these are illustrated using the long red arrows in Figure 22.1. The operators are used to describe the kernel behaviour between Chebyshev points in all non-adjacent cells at the same level in the octree hierarchy. In order to accelerate this part of a bbFMM code, researchers have to date approximated the M2L operators using a reduction method based on the Singular Value Decomposition (SVD) [24, 20]. We proceed now to present an alternative based on the PGD.

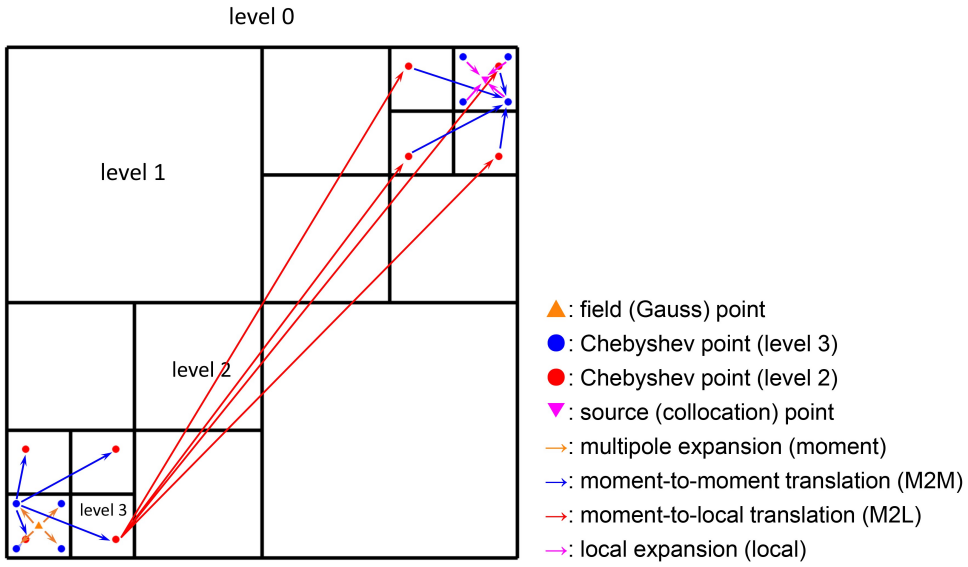

Figure 22.1: A quadtree based bbFMM scheme.

22.2.3 PGD acceleration

The Proper Generalised Decomposition [25] is based on the representation of a function by a combination of the information in each direction. That is, an arbitrary d-dimensional function may be written in the form

$$u(x_1, \ldots, x_d) = \sum_{i=1}^{n} f_i^1(x_1) f_i^2(x_2) \cdots f_i^d(x_d). \tag{22.7}$$

Specifically for the acceleration of the M2L process, we seek the low rank approximation $\widetilde{\mathbf{K}}(\bar{\mathbf{s}}, \bar{\mathbf{x}})$ to the kernel matrix $\mathbf{K}(\bar{\mathbf{s}}, \bar{\mathbf{x}})$ that contains the kernels relating a source point $\bar{\mathbf{s}}$ and field point $\bar{\mathbf{x}}$ in different cells at the same level. The notation $\mathbf{K}$ is used in a generic fashion such that it might denote either $\mathbf{U}(\mathbf{s}, \mathbf{x})$ or $\mathbf{T}(\mathbf{s}, \mathbf{x})$ as required. We use an iterative procedure in which the k^{th} approximation is written

$$\begin{aligned} \widetilde{\mathbf{K}}^k(\bar{\mathbf{s}}, \bar{\mathbf{x}}) &= \widetilde{\mathbf{K}}^{k-1}(\bar{\mathbf{s}}, \bar{\mathbf{x}}) + \mathbf{S}_k(\bar{\mathbf{s}}) \circ \mathbf{X}_k(\bar{\mathbf{x}}) \\ &= \sum_{i=1}^{k-1} \mathbf{S}_i(\bar{\mathbf{s}}) \circ \mathbf{X}_i(\bar{\mathbf{x}}) + \mathbf{S}_k(\bar{\mathbf{s}}) \circ \mathbf{X}_k(\bar{\mathbf{x}}), \end{aligned} \tag{22.8}$$

where the operator $\circ$ denotes a Hadamard product, and the functions $\mathbf{S}_k(\bar{\mathbf{s}})$ and $\mathbf{X}_k(\bar{\mathbf{x}})$ are the only unknowns. In order to solve this non-linear problem, an alternating direction scheme is used. An initial guess can always be made to generate the first approximation, $\widetilde{\mathbf{K}}^1(\bar{\mathbf{s}}, \bar{\mathbf{x}})$, based on the essential $1/r^2$ and $1/r$ behaviour, respectively, of the $\mathbf{T}$ and $\mathbf{U}$ kernels.

$$\widetilde{\mathbf{K}}^1(\bar{\mathbf{s}}, \bar{\mathbf{x}}) = \mathbf{S}_1(\bar{\mathbf{s}}) \circ \mathbf{X}_1(\bar{\mathbf{x}}). \tag{22.9}$$

Since the $\mathbf{T}$ kernel is of order $1/r^2$ and the $\mathbf{U}$ kernel is of order $1/r$, a suitable initial approximation is the following choice:

$$\mathbf{S}_1^t(\bar{\mathbf{s}}) = \left[\frac{1}{||\bar{\mathbf{s}} - \bar{\mathbf{x}}^*||}\right], \tag{22.10}$$

$$\mathbf{X}_1^t(\bar{\mathbf{x}}) = \left[\frac{1}{||\bar{\mathbf{s}}^* - \bar{\mathbf{x}}||}\right], \tag{22.11}$$

$$\mathbf{S}_1^u(\bar{\mathbf{s}}) = \left[\frac{1}{\sqrt{||\bar{\mathbf{s}} - \bar{\mathbf{x}}^*||}}\right], \tag{22.12}$$

$$\mathbf{X}_1^u(\bar{\mathbf{x}}) = \left[\frac{1}{\sqrt{||\bar{\mathbf{s}}^* - \bar{\mathbf{x}}||}}\right]. \tag{22.13}$$

The iterative sequence used to calculate the kth enrichment is stopped at iteration P, when:

$$\tilde{\epsilon}(P) > \frac{||\mathbf{S}_k^P(\bar{\mathbf{s}}) \circ \mathbf{X}_k^P(\bar{\mathbf{x}}) - \mathbf{S}_k^{P-1}(\bar{\mathbf{s}}) \circ \mathbf{X}_k^{P-1}(\bar{\mathbf{x}})||}{||\mathbf{S}_k^{P-1}(\bar{\mathbf{s}}) \circ \mathbf{X}_k^{P-1}(\bar{\mathbf{x}})||}, \tag{22.14}$$

where $||\cdot||$ denotes the L^2-norm and $\tilde{\epsilon}(P)$ is a suitable threshold value. After some enrichment steps, the PGD process will stop once the following criterion is satisfied (with threshold $\epsilon(k)$):

$$\epsilon(k) > \frac{||\mathbf{S}_k(\bar{\mathbf{s}}) \circ \mathbf{X}_k(\bar{\mathbf{x}})||}{||\mathbf{S}_1(\bar{\mathbf{s}}) \circ \mathbf{X}_1(\bar{\mathbf{x}})||} \tag{22.15}$$

22.3 Results

We start by considering the influence of the number of Chebyshev nodes used in the kernel interpolation. Accuracy will increase with the number of Chebyshev nodes, but this comes at some computational cost. The relative error is given as:

$$E_c = \frac{||\mathbf{K}^c - \mathbf{K}^d||}{||\mathbf{K}^d||} \times 100\%, \tag{22.16}$$

where $\mathbf{K}^c$ denotes the kernel interpolated by Chebyshev nodes and $\mathbf{K}^d$ is the kernel evaluated directly. The relative errors in the traction and displacement kernels, approximated using different number of Chebyshev nodes, are illustrated in Fig. 22.2. It can be seen that with an increasing number of nodes, the accuracy is consistently improved; once around 9 nodes are used, convergence is apparent. We next consider the improvement in efficiency gained by adopting the PGD in place of the SVD compression. A problem of a thick-walled cylinder is chosen, shown in Fig. 22.3, under an internal pressure of 1MPa. The right, left and bottom surface have prescribed direction displacement constraints in the direction normal to each surface. The height is 1m, inner radius 0.4m and outer radius 1m. The control points and geometry are displayed in the figure. An octree structure with the result of von-Mises stress for a 78 DOF model is presented in Fig. 22.4. In Figure 22.5 we display a comparison of the CPU time requirements for both approaches in constructing the M2L operators. Once a problem size of around 100 DOF is reached, the PGD exhibits $\mathcal{O}(n^2)$ complexity while the SVD exhibits $\mathcal{O}(n^3)$ for this stage of the bbFMM process. This is a significant improvement that improves the overall run-time, as demonstrated in Figure 22.6. The run-time is shown for increasing model size, these models being generated using a standard knot insertion algorithm [7]. All runs were executed on a 2.80GHz quadcore processor with 8 parallel threads, though no parallel coding was implemented. The figure clearly shows the use of the FMM to give $\mathcal{O}(n)$ complexity, in comparison with $\mathcal{O}(n^2)$ for conventional

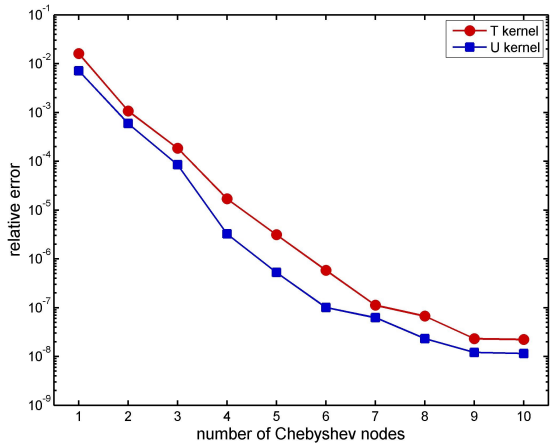

Figure 22.2: Relative error E_c as a function of the number of Chebyshev nodes.

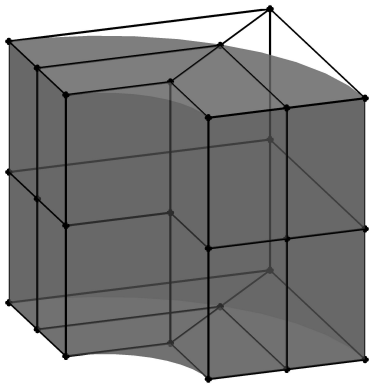

Figure 22.3: Quarter cylinder geometry with NURBS control points.

IGABEM, and also that the PGD acceleration has particular benefits, effectively offsetting the overheads of using the FMM, for smaller models. In this way the $\mathcal{O}(n)$ behaviour applies for the entire range of problem sizes, though it should be noted that for larger problems there may be expected to be some departure from this since the M2L operator requires $\mathcal{O}(n^2)$ operations and the linear solver will require at least this; however, for the problem sizes tested (up to over 100,000 DOF) this departure has not yet become apparent.

It appears that the use of PGD in preference to the SVD has little benefit for problem sizes greater than around 10^4 degrees of freedom. By modifying the PGD approach, further gains can be made across the entire range of problem sizes. This is the subject for a future publication.

22.4 Conclusions

An IGABEM algorithm has been presented for linear elasticity in 3D. It is accelerated with the bbFMM using a low-rank approximation to the Moment-to-Local operators produced using Proper Generalised Decomposition in preference to the Singular Value Decomposition. This reduces the complexity of the M2L construction from $\mathcal{O}(n^3)$ to $\mathcal{O}(n^2)$. The performance of the scheme is enhanced across the range of model sizes tested, with negligible loss in accuracy,

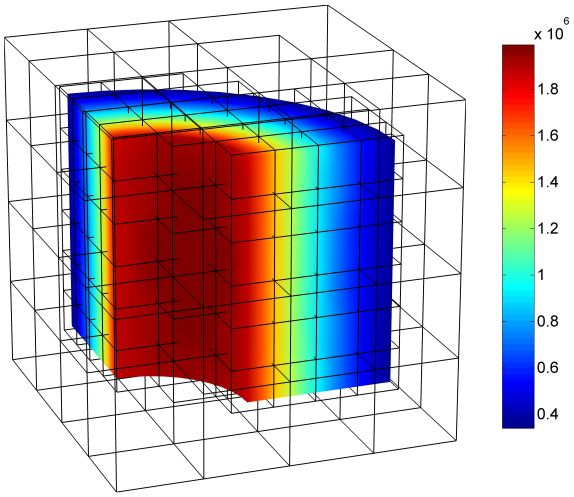

Figure 22.4: Octree structure of the quarter cylinder model showing contours of von-Mises stress (MPa).

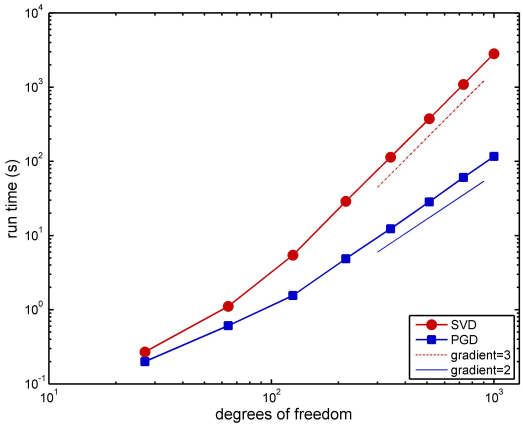

Figure 22.5: CPU time for computation of M2L operators.

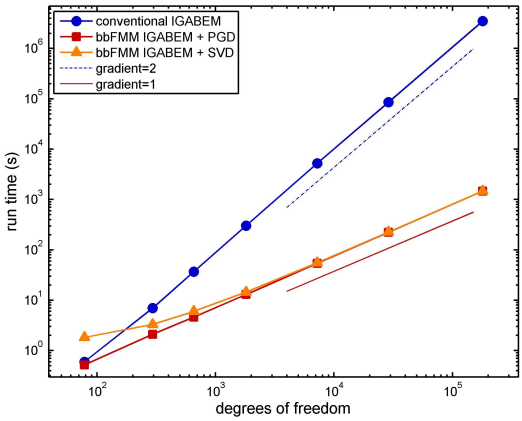

Figure 22.6: Comparison of overall run-time - cylinder problem.

so that the method becomes a highly promising approach for the efficient and accurate stress analysis of solids in an industrial setting.

References

[1] T. J. R. Hughes, J. Cottrell and Y. Bazilevs, *Isogeometric analysis: CAD, finite elements, NURBS, exact geometry and mesh refinement*, Comp. Meth. Appl. Mech. Engrg., 194 (2005), 4135–4195.

[2] D. Schillinger, L. Dede, M. A. Scott, J. A. Evans, M. J. Borden, E. Rank and T. J. R. Hughes, *An isogeometric design-through-analysis methodology based on adaptive hierarchical refinement of NURBS, immersed boundary methods, and T-spline CAD surfaces*, Comput. Methods Appl. Mech. Engrg., 249–252 (2012), 116–150.

[3] Y. Bazilevs, V. M. Calo, T. J. R. Hughes and Y. Zhang, *Isogeometric fluid-structure interaction: theory, algorithms, and computations*, Comput. Mech., 43 (2008), 3–37.

[4] Y. Bazilevs, M.-C. Hsu and M. Scott, *Isogeometric fluid-structure interaction analysis with emphasis on non-matching discretizations, and with application to wind turbines*, Comput. Methods Appl. Mech. Engrg., 249–252 (2012), 28–41.

[5] A. Buffa, G. Sangalli and R. Vazquez, *Isogeometric analysis in electromagnetics: B-splines approximation*, Comput. Methods Appl. Mech. Engrg., 199 (2010), 1143–1152.

[6] J. Cottrell, A. Reali, Y. Bazilevs and T. Hughes, *Isogeometric analysis of structural vibrations*, Comput. Methods Appl. Mech. Engrg., 195 (2006), 5257–5296.

[7] L. Piegl and W. Tiller, *The NURBS Book*, Springer Berlin Heidelberg, 1995.

[8] Y. Bazilevs, V. Calo, J. Cottrell, J. Evans, T. Hughes, S. Lipton, M. Scott and T. Sederberg, *Isogeometric analysis using T-splines*, Comput. Methods Appl. Mech. Engrg., 199 (2010), 229–263.

[9] N. Nguyen-Thanh, J. Kiendl, H. Nguyen-Xuan, R. Wüchner, K. Bletzinger, Y. Bazilevs and T. Rabczuk, *Rotation free isogeometric thin shell analysis using PHT-splines*, Comput. Methods Appl. Mech. Engrg., 200 (2011), 3410–3424.

[10] N. Nguyen-Thanh, H. Nguyen-Xuan, S. Bordas and T. Rabczuk, *Isogeometric analysis using polynomial splines over hierarchical T-meshes for two-dimensional elastic solids*, Comput. Methods Appl. Mech. Engrg., 200 (2011), 1892–1908.

[11] P. Wang, J. Xu, J. Deng and F. Chen, *Adaptive isogeometric analysis using rational PHT-splines*, Comput.-Aided Des., 43 (2011), 1438–1448.

[12] R. Simpson, S. Bordas, J. Trevelyan and T. Rabczuk, *A two-dimensional isogeometric boundary element method for elastostatic analysis*, Comput. Methods Appl. Mech. Engrg., 209–212 (2012), 87–100.

[13] M. Scott, R. Simpson, J. Evans, S. Lipton, S.P.A. Bordas, T.J.R. Hughes and T. Sederberg, *Isogeometric boundary element analysis using unstructured T-splines*, Comput. Methods Appl. Mech. Engrg., 254 (2013), 197–221.

[14] Y. Wang and D. Benson, *Multi-patch nonsingular isogeometric boundary element analysis in 3D*, Comput. Methods Appl. Mech. Engrg., 293 (2015), 71–91.

[15] K. Li and X. Qian, *Isogeometric analysis and shape optimization via boundary integral*, Comput.-Aided Des., 43 (2011), 1427–1437.

[16] H. Lian, P. Kerfriden and S. P. A. Bordas, *Implementation of regularized isogeometric boundary element methods for gradient-based shape optimization in two-dimensional linear elasticity*, Int. J. Numer. Methods Eng., 106 (2016), 972–1017.

[17] M. Peake, J. Trevelyan and G. Coates, *Extended isogeometric boundary element method (XIBEM) for two-dimensional Helmholtz problems*, Comput. Methods Appl. Mech. Engrg., 259 (2013), 93–102.

[18] R. Simpson, M. Scott, M. Taus, D. Thomas and H. Lian, *Acoustic isogeometric boundary element analysis*, Comput. Methods Appl. Mech. Engrg., 269 (2014), 265–290.

[19] M. Peake, J. Trevelyan and G. Coates, *Extended isogeometric boundary element method (XIBEM) for three-dimensional medium-wave acoustic scattering problems*, Comput. Methods Appl. Mech. Engrg., 284 (2015), 762–780.

[20] R. Simpson and Z. Liu, *Acceleration of isogeometric boundary element analysis through a black-box fast multipole method*, Eng. Anal. Boundary Elem., 66 (2016), 168–182.

[21] X. Peng, E. Atroshchenko, P. Kerfriden and S.P.A. Bordas, *Isogeometric boundary element methods for three dimensional static fracture and fatigue crack growth*, Comput. Methods Appl. Mech. Engrg., 316 (2017), 151–185.

[22] V. Rokhlin, *Rapid solution of integral equations of classical potential theory*, J. Comput. Phys., 60 (1985), 187–207.

[23] M. Bebendorf and R. Kriemann, *Fast parallel solution of boundary integral equations and related problems*, Comput. Visual Sci. 8 (2005) 121–135.

[24] W. Fong and E. Darve, *The black-box fast multipole method*, J. Comp Phys. 228 (2009) 8712–8725.

[25] F. Chinesta, A. Ammar, A. Leygue and R. Keunings, *An overview of the Proper Generalized Decomposition with applications in computational rheology*, J Non-Newt Fluid Mech. 166 (2011) 578–592.

ISBN 978-0-9931112-9-7 (paperback)
ISBN 978-1-912253-00-5 (eBook)